

**Self-Interference Mitigation in Full-Duplex Systems: Signal Modeling,  
Rate Optimization, and Application**

BY

MD ATIQUL ISLAM

B.Sc., Islamic University of Technology, 2015

M.Sc., University of Illinois at Chicago, 2021

THESIS

Submitted as partial fulfillment of the requirements  
for the degree of Doctor of Philosophy in Electrical and Computer Engineering  
in the Graduate College of the  
University of Illinois at Chicago, 2022

Chicago, Illinois

Defense Committee:

Besma Smida, Chair and Advisor

Natasha Devroye

Rashid Ansari

Erdem Koyuncu

George C. Alexandropoulos, National and Kapodistrian University of Athens

Copyright by  
MD ATIQUL ISLAM  
2022

To my parents for their constant love and support

## ACKNOWLEDGMENTS

First and foremost, I am extremely grateful to my advisor, Dr. Besma Smida, for her invaluable guidance, continuous support, and tutelage during the course of my Ph.D. journey. She has always inspired me with her extraordinary mentorship, immense knowledge, and unmatched patience. This dissertation would not exist without her vision, unwavering research, and financial support.

I acknowledge my committee members: Dr. Natasha Devroye, Dr. Rashid Ansari, and Dr. Erdem Koyuncu of the University of Illinois at Chicago (UIC); and Dr. George. C. Alexandropoulos of the University of Athens for agreeing to be a part of my Ph.D. dissertation committee. I am indeed grateful for the time and efforts they put into reviewing and evaluating this thesis and my research prospect in general.

Furthermore, I extend my sincere gratitude to my research collaborators, Dr. George. C. Alexandropoulos and Dr. Natasha Devroye, once again. I heartily appreciate their contributions of ideas that motivated my research and made this journey productive.

I would also like to thank all the staff from the Electrical and Computer Engineering department at UIC for their constant help and support every step toward completing this degree.

Finally, I am genuinely and deeply indebted to my parents, siblings, and friends for their tremendous understanding and unconditional support all these years.

MAI

## PREFACE

This dissertation is an original intellectual product of the author, M. A. Islam. The presented work has been conducted under the supervision of Dr. Besma Smida at the University of Illinois at Chicago, USA. The research effort has partly been supported by the National Science Foundation (NSF) CAREER award #1620902. The results of these works have previously appeared (or are appearing) as journal and conference articles. The copyright permissions for reusing the published materials have been presented in Appendix E.

MD ATIQUL ISLAM  
July 13, 2022

## CONTRIBUTION OF AUTHORS

In work *A comprehensive self-interference model for single-antenna full-duplex communication systems*, Md Atiqul Islam performed the derivation and prepared the manuscripts with the support of Besma Smida.

In the works *Joint Analog and Digital Transceiver Design for Wideband Full Duplex MIMO Systems*, *A unified beamforming and A/D self-interference cancellation design for full duplex MIMO radios*, *Simultaneous downlink data transmission and uplink channel estimation with reduced complexity full duplex MIMO radios*, *Simultaneous Data Communication and Channel Estimation in Multi-User Full Duplex MIMO Systems*, *Direction-Assisted Beam Management in Full Duplex Millimeter Wave Massive MIMO Systems*, *Integrated Sensing and Communication with Millimeter Wave Full Duplex Hybrid Beamforming*, and *Simultaneous Multi-User MIMO Communications and Multi-Target Tracking with Full Duplex Radios*, Md Atiqul Islam derived the technical details with the support from George C. Alexandropoulos and Besma Smida. Md Atiqul Islam wrote the manuscripts with inputs from George C. Alexandropoulos and Besma Smida.

In the work *On Deep Learning Assisted Self-Interference Estimation in a Full-Duplex Relay Link*, Konstantin Muranov and Md Atiqul Islam both contributed to the conceptual ideas for SI cancellation. They wrote the manuscript with the input from Besma Smida and Natasha Devroye.

## CONTRIBUTION OF AUTHORS (Continued)

In the works *Full duplex hybrid A/D beamforming with reduced complexity multi-tap analog cancellation* and *Full Duplex Massive MIMO Architectures: Recent Advances, Applications, and Future Directions*, Md Atiqul Islam worked on the technical details with the support from George C. Alexandropoulos and Besma Smida. The manuscripts were prepared by George C. Alexandropoulos, Md Atiqul Islam, and Besma Smida.

## TABLE OF CONTENTS

<u>CHAPTER</u>	<u>PAGE</u>
<b>1 INTRODUCTION . . . . .</b>	<b>1</b>
1.1 Background and Motivation . . . . .	1
1.1.1 Full Duplex Wireless Communication . . . . .	1
1.1.2 Self-Interference Cancellation for Full Duplex Radios . . . . .	4
1.2 Contribution of the Thesis . . . . .	7
1.2.1 Self-Interference Cancellation for Single-antenna Full Duplex Systems . . . . .	7
1.2.2 Unified Analog and Digital Transceiver Design for Wideband Full Duplex MIMO Systems . . . . .	9
1.2.3 Simultaneous Data Communication and Channel Estimation in Single- and Multi-User FD MIMO Systems . . . . .	10
1.2.4 Self-interference Cancellation for FD massive MIMO Systems with Hybrid Beamformers . . . . .	11
1.2.5 Direction-Assisted Beam Management in Full Duplex Millimeter Wave Massive MIMO Systems . . . . .	13
1.2.6 Integrated Sensing and Communication with Millimeter Wave Full Duplex Hybrid Beamforming . . . . .	14
<b>2 SELF-INTERFERENCE CANCELLATION FOR SINGLE-ANTENNA FULL DUPLEX SYSTEMS . . . . .</b>	<b>16</b>
2.1 Introduction . . . . .	16
2.2 FD Transceiver Model And Self-interference characterization . . . . .	19
2.2.1 Self-interference Model at the Transmitter . . . . .	20
2.2.2 Self-interference Model at the Receiver . . . . .	23
2.3 Proposed Digital Estimation and Cancellation of Self-interference Signal . . . . .	26
2.4 Performance Simulation and Analysis . . . . .	30
2.4.1 Simulation Parameters . . . . .	30
2.4.2 SI Cancellation Capability and SINR . . . . .	32
2.5 Machine Learning for Self-Interference Cancellation in Full Duplex Systems . . . . .	34
2.5.1 Proposed DNN Architecture of SI Cancellation . . . . .	35
2.5.2 Performance Evaluation of the Proposed DNN-assisted SI Cancellation . . . . .	37
2.6 Concluding Remarks . . . . .	39

## TABLE OF CONTENTS (Continued)

<u>CHAPTER</u>		<u>PAGE</u>
<b>3</b>	<b>UNIFIED ANALOG AND DIGITAL TRANSCEIVER DESIGN FOR WIDEBAND FULL DUPLEX MIMO SYSTEMS . . . . .</b>	40
3.1	Introduction . . . . .	41
3.1.1	Related works on FD MIMO SI Cancellation . . . . .	43
3.1.2	Contributions . . . . .	45
3.2	System and Signal Models . . . . .	47
3.2.1	Downlink TX and RX Signal Modeling . . . . .	47
3.2.2	Uplink TX and RX Signal Modeling . . . . .	52
3.3	Join Digital TX/RX Beamforming and Wideband Analog Cancellation . . . . .	55
3.3.1	Wideband FD MIMO Analog SI Canceller . . . . .	55
3.3.2	Digital TX/RX Beamforming and Wideband Analog SI Cancellation . . . . .	58
3.4	TSVD-based Adaptive MIMO Digital SI Cancellation . . . . .	63
3.4.1	Proposed Digital SI Cancellation . . . . .	64
3.5	Simulation Results and Discussion . . . . .	66
3.5.1	Simulation Parameters . . . . .	67
3.5.2	Analog SI Mitigation Capability . . . . .	68
3.5.3	Achievable Downlink Rate . . . . .	72
3.5.4	Performance of the Digital SI Canceller . . . . .	73
3.5.5	Average FD Rate . . . . .	75
3.5.6	Impact of Channel Estimation Error on the FD Rate . . . . .	77
3.5.7	Interference Suppression Ratio for Different Signal Waveforms . . . . .	78
3.6	Concluding Remarks . . . . .	79
<b>4</b>	<b>SIMULTANEOUS CONTROL AND DATA COMMUNICATION IN SINGLE- AND MULTI-USER FD MIMO SYSTEMS . . . . .</b>	81
4.1	Introduction . . . . .	81
4.1.1	Contributions . . . . .	83
4.2	System and Signal Models . . . . .	84
4.2.1	Channel Modeling . . . . .	85
4.2.2	Signal Modeling at the BS and UE Nodes . . . . .	86
4.3	Proposed SCDC Scheme . . . . .	87
4.3.1	Proposed CSI Acquisition and Beamforming . . . . .	87
4.3.2	Channel Estimation Error and Average DL Rate . . . . .	89
4.4	Proposed Joint Optimization Framework . . . . .	92
4.5	Evaluation of SCDC Scheme for Single-user FD MIMO System . . . . .	94
4.5.1	Simulation Parameters . . . . .	95
4.5.2	Achievable DL Rate and CSI Estimation Performances . . . . .	96
4.6	Evaluation of SCDC Scheme for Multi-user FD MIMO System . . . . .	98
4.6.1	Compared FD and HD MIMO Designs . . . . .	99
4.6.2	Simulation Parameters . . . . .	100

## TABLE OF CONTENTS (Continued)

<u>CHAPTER</u>		<u>PAGE</u>
	4.6.3 Analog Cancellor Complexity and Achievable DL Rate . . . . .	100
	4.7 Concluding Remarks . . . . .	103
<b>5</b>	<b>SELF-INTERFERENCE CANCELLATION FOR FULL DUPLEX MASSIVE MIMO SYSTEMS WITH HYBRID BEAMFORMERS</b>	<b>104</b>
	5.1 Introduction . . . . .	105
	5.1.1 Contributions . . . . .	105
	5.2 System Model and Proposed Architecture . . . . .	106
	5.2.1 System Model . . . . .	106
	5.2.2 Proposed FD HBF Hardware Architecture . . . . .	108
	5.2.3 Partially Connected HBF . . . . .	108
	5.2.4 Multi-Tap Analog Cancellation . . . . .	110
	5.2.5 Received Signal Models . . . . .	112
	5.3 Joint Design Problem Formulation . . . . .	114
	5.3.1 Exhaustive Search . . . . .	117
	5.3.2 Sub-rate Optimization Based RF Precoder and Combiner . . . . .	118
	5.3.3 Complexity Analysis . . . . .	122
	5.4 Simulation Results and Discussion . . . . .	124
	5.4.1 Channel Models . . . . .	124
	5.4.2 Simulation Parameters . . . . .	126
	5.4.3 Hardware Complexity, Self-Interference Mitigation Capability, and Achievable Rates . . . . .	127
	5.5 Concluding Remarks . . . . .	131
<b>6</b>	<b>DIRECTION-ASSISTED BEAM MANAGEMENT IN FULL DUPLEX MILLIMETER WAVE MASSIVE MIMO SYSTEMS</b>	<b>132</b>
	6.1 Introduction . . . . .	133
	6.1.1 Contributions . . . . .	134
	6.2 System and Signal Models . . . . .	134
	6.2.1 Channel Model . . . . .	136
	6.2.2 Received Signal Model . . . . .	137
	6.3 DoA Estimation and DL Data Transmission . . . . .	138
	6.3.1 UL/DL Channel Evolution Properties . . . . .	139
	6.3.2 Proposed FD-Based SDDT Protocol . . . . .	140
	6.3.3 UL DoA Estimation . . . . .	141
	6.3.4 DoA-Assisted Analog Beamforming and DL Rate . . . . .	143
	6.4 Proposed SDDT Optimization Framework . . . . .	143
	6.5 Numerical Results . . . . .	146
	6.5.1 Simulation Parameters . . . . .	146
	6.5.2 Compared HD Massive MIMO Designs . . . . .	147
	6.5.3 DoA Estimation Error and Average DL Rate . . . . .	149
	6.6 Concluding Remarks . . . . .	151

## TABLE OF CONTENTS (Continued)

<u>CHAPTER</u>		<u>PAGE</u>
<b>7</b>	<b>INTEGRATED SENSING AND COMMUNICATION WITH MIL- LIMETER WAVE FULL DUPLEX HYBRID BEAMFORMING .</b>	<b>152</b>
7.1	Introduction . . . . .	153
7.1.1	Contributions . . . . .	154
7.2	System and Signal Models . . . . .	155
7.2.1	Radar Signal Reception Model . . . . .	157
7.2.2	DL Signal Reception Model . . . . .	159
7.3	DoA, Delay, and Doppler Shift Estimation . . . . .	160
7.3.1	Radar Target DoA Estimation . . . . .	160
7.3.2	Delay and Doppler Shift Estimation . . . . .	162
7.4	Proposed ISAC Optimization Framework . . . . .	163
7.5	Numerical Results and Discussion . . . . .	166
7.5.1	Simulation Parameters . . . . .	166
7.5.2	Radar Target Parameters . . . . .	168
7.5.3	Radar Target Sensing performance . . . . .	168
7.6	Concluding Remarks . . . . .	172
<b>8</b>	<b>CONCLUSION . . . . .</b>	<b>173</b>
	<b>APPENDICES . . . . .</b>	<b>176</b>
	<b>Appendix A . . . . .</b>	<b>177</b>
	<b>Appendix B . . . . .</b>	<b>178</b>
	<b>Appendix C . . . . .</b>	<b>180</b>
	<b>Appendix D . . . . .</b>	<b>184</b>
	<b>Appendix E . . . . .</b>	<b>186</b>
	<b>CITED LITERATURE . . . . .</b>	<b>194</b>
	<b>VITA . . . . .</b>	<b>210</b>

## LIST OF TABLES

<u>TABLE</u>		<u>PAGE</u>
I	WAVEFORM AND SYSTEM LEVEL PARAMETERS OF SINGLE-ANTENNA FULL DUPLEX SYSTEM . . . . .	30
II	SINGLE-ANTENNA FULL DUPLEX TRANSCEIVER COMPONENT PARAMETERS . . . . .	31
III	WIDEBAND FD MIMO SIMULATION PARAMETERS . . . . .	67
IV	COMPUTATIONAL COMPLEXITY OF PROPOSED SCHEME AND EXHAUSTIVE SEARCH . . . . .	123

## LIST OF FIGURES

<u>FIGURE</u>		<u>PAGE</u>
1	A simplified illustration denoting the time-frequency resource usage of TDD, FDD, and Full Duplex systems. . . . .	2
2	Generic FD transceiver architecture illustrating the boundaries and contents of the propagation, analog, and digital domains, as well as the self-interference and desired signal for both shared and multiple antenna configurations. . . . .	4
3	A detailed block diagram of a single-antenna full duplex direct conversion transceiver, where analog cancellation is achieved using IMT circuit. . . .	20
4	Residual self-interference power after digital cancellation with respect to different RF cancellation value and 25 dBm transmit Power . . . . .	32
5	The SINRs for different digital cancellation method with respect to the overall transmit power with antenna and RF cancellation of 60 dB . . . .	34
6	A two-layer Feed-Forward Neural Network. . . . .	36
7	Digital SI cancellation in dB w.r.t the number of on-line training epochs. . . . .	38
8	The considered three-node communication system and the proposed wideband FD MIMO architecture. The FD MIMO node $b$ incorporates processing blocks for analog SI cancellation and digital TX/RX beamforming, as well as for a digital cancellation block for treating the residual SI at the output of the TX RF chains. All these blocks are jointly optimized, realizing the desired wideband FD operation in a hardware-efficient way. The HD multi-antenna nodes $m_1$ and $m_2$ communicate with node $b$ in the downlink and uplink directions, respectively. . . . .	46
9	The proposed wideband analog SI canceller for the FD MIMO OFDM node $b$ for mitigating the $L_{SI}$ channel paths $[\mathbf{H}_{SI}[\ell]]_{j,i} \forall \ell = \{0, 1, \dots, L_{SI}-1\}$ between the output of the $i$ th TX RF chain and the input of the $j$ th RX RF chain with $i = \{1, 2, \dots, N_{TX,b}\}$ and $j = \{1, 2, \dots, N_{RX,b}\}$ . . . . .	56

## LIST OF FIGURES (Continued)

<u>FIGURE</u>		<u>PAGE</u>
10	Probability of the residual SI power after analog cancellation above RF saturation level $-40$ dBm with respect to DL transmit power in dBm and $N_{\text{RX},m_1} = N_{\text{TX},m_2} = 1$ . . . . .	69
11	Probability of residual SI after analog cancellation above RF saturation level $-40$ dBm with respect to DL transmit power in dBm and $N_{\text{RX},m_1} = N_{\text{TX},m_2} = 4$ . . . . .	70
12	Average downlink rate as a function of the downlink transmit power for $N_{\text{RX},b} = N_{\text{TX},b} = 4$ and $N_{\text{RX},m_1} = \{1, 4\}$ . . . . .	72
13	Digital SI cancellation value with respect to the number of training OFDM symbols for digital SI estimation. . . . .	73
14	Power Spectrum of the SI signal after SI cancellation in the RF and digital domains with $40$ dBm average TX power, $20$ MHz bandwidth, and $-100$ dBm receiver noise floor. . . . .	75
15	Average FD rate as a function of the downlink transmit power for $N_{\text{RX},b} = N_{\text{TX},b} = 4$ and $N_{\text{RX},m_1} = N_{\text{TX},m_2} = \{1, 4\}$ . . . . .	76
16	Average FD rate as a function of the transmit power and different channel estimation MSE for $N_{\text{RX},b} = N_{\text{TX},b} = 4$ and $N_{\text{RX},m_1} = N_{\text{TX},m_2} = \{1, 4\}$ . . . . .	77
17	Interference Suppression Ratio with respect to the transmit power and different signal waveforms for the considered FD MIMO system with $N_{\text{RX},b} = N_{\text{TX},b} = N_{\text{RX},m_1} = N_{\text{TX},m_2} = 4$ . . . . .	78
18	The considered multi-user FD MIMO system model for simultaneous DL data transmission and UL pilot-assisted channel estimation. BS node $b$ and all UE nodes deploy A/D SI cancellation with the former node $b$ realizing reduced complexity multi-tap analog cancellation. . . . .	85
19	(a) Proposed SCDC Scheme, (b) Sequential Beamforming with DL data transmission and UL CSI, and (c) Conventional HD Beamforming with UL training over two consecutive time slots. . . . .	88
20	Achievable DL rate of the proposed FD SCDC scheme for a single-user versus the DL transmit power in dBm for the case of limited UL transmit power at $5$ dBm. . . . .	95

## LIST OF FIGURES (Continued)

<u>FIGURE</u>		<u>PAGE</u>
21	MSE of UL channel estimation versus the UL transmit power for the case where the DL transmit power is 40dBm. . . . .	96
22	Achievable DL rate versus the UL transmit power for the case where the DL transmit power is 40dBm. . . . .	98
23	Achievable DL Rate w.r.t DL transmit power for $N_b = 8$ , $K = 4$ , $f_d = 50\text{Hz}$ and different analog canceller taps $N$ . . . . .	99
24	Achievable DL Rate of FD MU system w.r.t number of UEs $K$ for $N_b = 8$ , $P_b = 40\text{dBm}$ , $f_d = 50\text{Hz}$ and different analog canceller taps $N$ . . . . .	101
25	Achievable DL Rate w.r.t Doppler frequency $f_d$ for $N_b = 8$ , $P_b = 40\text{dBm}$ , $K = 4$ and different analog canceller taps $N$ . . . . .	102
26	The considered bidirectional communication system with the proposed FD HBF architecture in the MIMO node $k$ including $N$ -tap analog cancellation and A/D TX/RX beamforming. The HD multi-antenna nodes $q$ and $m$ communicate with node $k$ in the DL and UL directions, respectively.	107
27	Frobenius Norm of $\tilde{\mathbf{H}}_{k,k}$ vs Number of Analog Cancellation Taps for different Antenna Elements per RF Chain at Node $k$ . . . . .	125
28	Probability of avoiding RX RF chain saturation vs transmit power for different Antenna Elements per RF Chain at Node $k$ with $\alpha = 3$ . . . . .	127
29	Achievable DL rates vs the transmit powers in dBm for Proposed Sub-rate and Exhaustive Search Scheme with $N_k^{(A)} = M_k^{(A)} = 16$ antenna elements . . . . .	128
30	Achievable DL rates vs the transmit powers in dBm of Proposed Sub-rate Scheme with $N_k^{(A)} = M_k^{(A)} = \{64, 128\}$ antenna elements . . . . .	129
31	Average FD and HD rates vs the transmit powers in dBm for $N_k^{(A)} = M_k^{(A)} = \{16, 128\}$ antenna elements and different analog canceller taps at node $k$ . . . . .	130
32	The considered FD massive MIMO communication system operating at mmWave frequencies: an FD massive MIMO BS capable of analog BF communicates with a mobile single-antenna FD UE, where the latter node transmits training signals in the UL for DoA estimation. . . . .	135

## LIST OF FIGURES (Continued)

<u>FIGURE</u>		<u>PAGE</u>
33	(a) Proposed FD SDDT Scheme, (b) Conventional HD DoA with update after threshold, and (c) Conventional HD DoA estimation in each slot. . .	140
34	Error of LoS DoA estimation w.r.t the time slot index for the $64 \times 2$ FD massive MIMO node $b$ communicating with the mobile single-antenna FD UE $u$ transmitting UL training symbols with 10dBm transmit power.	146
35	MSE of the DoA estimation with respect to UL transmit power in dBm for the $64 \times 2$ FD massive MIMO node $b$ communicating with the single-antenna FD UE $u$ transmitting training symbols in the UL direction. . .	148
36	Achievable DL rate with respect to DL transmit power in dBm for the $64 \times 2$ FD massive MIMO node $b$ communicating with the mobile single-antenna FD UE $u$ sending training symbols with 10dBm transmit power.	150
37	The considered FD massive MIMO ISAC system: the FD hybrid A/D beamforming BS communicates in the downlink with a mobile half duplex UE, while its reflected transmitted signals from radar targets/scatterers in the environment are received via hybrid combining and processed for DoA, range, and relative velocity estimations of the radar targets/scatterers.	155
38	Sensing parameter estimation performance for 6 radar targets with $N_b^{\text{RF}} = M_b^{\text{RF}} = 8, N_b^{\text{A}} = N_b^{\text{A}} = 16$ and transmit power of 30dBm. (a) DoA and range estimation, (b) Range and relative velocity estimation. . . . .	167
39	Sensing parameter estimation performance for 6 radar targets with $N_b^{\text{RF}} = M_b^{\text{RF}} = 8, N_b^{\text{A}} = N_b^{\text{A}} = 16$ and DL transmit power of 10dBm. (a) DoA and range estimation, (b) Range and relative velocity estimation. . . . .	169
40	DL rate with respect to transmit power in dBm for the $128 \times 128$ massive MIMO FD BS communicating with a 4 antenna UE RX node. . . . .	170
41	RMSE of the DoA Tracking for 4 radar targets with $N_{\text{RF}} = M_{\text{RF}} = 8, N_{\text{A}} = M_{\text{A}} = 16$ and DL transmit power of 30dBm. . . . .	171

## LIST OF ALGORITHMS

<u>ALGORITHM</u>	<u>PAGE</u>
1 Digital TX/RX Beamforming Maximizing DL Rate . . . . .	61
2 Digital TX/RX Beamforming Maximizing UL Rate . . . . .	62
3 Adaptive Digital SI cancellation using TSVD regularization . . . . .	65
4 Proposed FD MIMO SCDC Design . . . . .	93
5 Digital TX Precoder Design for FD massive MIMO systems . . . . .	119
6 Sub-rate Optimization based RF TX Precoder and RX Combiner Design	121
7 Proposed FD massive MIMO SDDT Design . . . . .	145
8 Delay and Doppler Shift Estimation . . . . .	161
9 FD ISAC Optimization . . . . .	165

## LIST OF ABBREVIATIONS

5G	Fifth Generation
ACK	ACKnowledgement
ADC	Analog-to-Digital-Converter
AWGN	Additive White Gaussian Noise
A/D	Analog and Digital
BB	BaseBand
BS	Base Station
BW	BandWidth
CSI	Channel State Information
DAC	Digital-to-Analog-Converter
DEMUX	DEMUltipleXers
DFT	Discrete Fourier transform
DL	DownLink
DNN	Deep Neural Network
DoA	Direction of Arrival
DoD	Direction of Departure
eMBB	enhanced Mobile BroadBand

## LIST OF ABBREVIATIONS (Continued)

FD	Full Duplex
FDD	Frequency Division Duplexing
HBF	Hybrid BeamFormer
HD	Half Duplex
IFFT	Inverse Fast Fourier Transform
IIP3	Third-order Input-referred Intercept Point
IpN	Interference-plus-Noise
IQ	In-phase Quadrature
ISAC	Integrated Sensing and Communication
LNA	Low Noise Amplifier
LPF	Low Pass Filter
LTE	Long Term Evolution
MAC	Multiple Access
MIMO	Multiple-Input Multiple-Output
mMTC	massive Machine Type Communications
mmWave	millimeter Wave
MSE	Mean Squared Error
MUSIC	MULTiple SInal Classification

## LIST OF ABBREVIATIONS (Continued)

MUX	MUltipleXers
NACK	Negative-ACKnowledgement
nLoS	non-Line-of-Sight
NOMA	Non-Orthogonal Multiple Access
NR	New Radio
OFDM	Orthogonal Frequency-Division Multiplexing
PA	Power Amplifier
PAPR	Peak-to-Average-Power-Ratio
PRB	Physical Resource Block
RF	Radio Frequency
RX	Receiver
SCDC	Simultaneous Communication of Data and Control
SDDT	Simultaneous DoA estimation and Data Transmission
SI	Self-Interference
SISO	Single-Input Single-Output
SNR	Signal-to-Noise-Ratio
SVD	Singular Value Decomposition
TDD	Time Division Duplexing

## LIST OF ABBREVIATIONS (Continued)

TDMA	Time Division Multiple Access
TSVD	Truncated Singular Value Decomposition
TX	Transmitter
UE	User Equipment
UL	UpLink
ULA	Uniform Linear Arrays
URLLC	Ultra-Reliable Low Latency Communications
VGA	Variable gain amplifier

## NOTATIONS

Vectors and matrices are denoted by boldface lowercase and boldface capital letters, respectively.

The following mathematical notations are used throughout this thesis:

$ x $	the absolute value of a scalar $x$
$[\mathbf{x}]_i$	the $i$ -th element of vector $\mathbf{x}$
$[\mathbf{X}]_{i,j}$	the $(i, j)$ th element of matrix $\mathbf{X}$
$[\mathbf{X}]_{(i,:)}$	the $i$ th row of matrix $\mathbf{X}$
$[\mathbf{X}]_{(:,j)}$	the $j$ th column of matrix $\mathbf{X}$
$\mathbf{X}^T$	the transpose of matrix $\mathbf{X}$
$\mathbf{X}^H$	the Hermitian transpose of matrix $\mathbf{X}$
$\mathbf{X}^*$	the conjugate of matrix $\mathbf{X}$
$\det(\mathbf{X})$	the determinant of matrix $\mathbf{X}$
$\text{diag}(\mathbf{x})$	denotes a diagonal matrix formed by the entries of the vector $\mathbf{x}$
$\text{sort}(\mathbf{X})$	rearranging the rows of $\mathbf{X}$ based on descending row vector norm
$\text{tr}(\mathbf{X})$	trace of matrix $\mathbf{X}$
$\ \mathbf{x}\ $	the Euclidean norm of $\mathbf{x}$
$\mathbf{x}^{\circ n}$	the Hadamard power operation of $\mathbf{x}$ to the factor $n$
$\mathbf{x} \odot \mathbf{y}$	denotes the Hadamard product of $\mathbf{x}$ and $\mathbf{y}$

## NOTATIONS (Continued)

$\mathbf{x} * \mathbf{y}$	convolution of $\mathbf{x}$ and $\mathbf{y}$
$\ \mathbf{x}\ _p$	the $l_p$ -norm of $\mathbf{x}$ , defined as $(\sum_k  \mathbf{x}(k) ^p)^{\frac{1}{p}}$
$\ \mathbf{X}\ _F$	Frobenius norm of $\mathbf{X}$
$\text{card}(\mathbb{X})$	cardinality of set $\mathbb{X}$
$\mathbb{C}$	the complex number set
$\mathbb{R}$	the set of real numbers
$\mathbb{E}\{\cdot\}$	the mathematical expectation of a random variable
$\mathbf{I}_n$	the $n \times n$ identity matrix for $n \geq 2$
$\mathbf{0}_n$	the $n \times n$ matrix with all elements as zero
$\Re(x)$	real part of $x$
$\Im(x)$	imaginary part of $x$
$j$	the imaginary unit <i>i.e.</i> , $j = \sqrt{-1}$

## SUMMARY

Future wireless networks are converging towards a unified communication, sensing, and computing platform that enables various vertical applications. The ubiquity, ultra high speed, and low latency demanded by this omnipresent platform will require, among other factors, more efficient frequency spectrum usage as well as optimized co-design of the control and data planes. Full Duplex (FD) communication is proposed as one of the promising wireless candidates to meet such demand for fifth Generation (5G) New Radio (NR), its sixth Generation (6G) successor, and beyond, due to its inherent capability to enable simultaneous transmission and reception in the same frequency band at the same time. However, the fundamental challenge of FD communications is the Self-Interference (SI) signal induced to the Receiver (RX) chain of the FD node by its own Transmitter (TX).

This thesis investigates the applications of FD technologies for single-antenna, Multiple-Input Multiple-Output (MIMO), and massive MIMO wireless systems devising optimized signaling as well as SI suppression approaches. First, we provide a comprehensive signal model for single-antenna FD communication systems considering the effect of analog impairments induced by TX/RX Radio Frequency (RF) components and propose a novel orthogonalized digital SI mitigation technique as well as a Deep Neural Network (DNN) based cancellation architecture trained with Transfer Learning approach. Extending our work to wideband FD MIMO systems, a novel optimization framework is designed for unified Analog and Digital (A/D) Beamforming (BF) and low-complexity multi-tap wideband analog cancellation. Employing the FD MIMO

## SUMMARY (Continued)

architecture, we further devise a Simultaneous Communication of Data and Control (SCDC) protocol capable of uplink channel acquisition while maintaining optimized downlink transmission.

Furthermore, we study the FD massive MIMO systems with Hybrid BeamFormers (HBFs) operating at millimeter Wave (mmWave) frequencies, which requires low-complexity SI cancellation solutions. In contrast to the conventional FD massive MIMO analog cancellers that scale the complexity with the number of TX/RX antennas, making it infeasible in practical implementation, we propose a multi-tap analog canceller for hybrid FD Massive MIMO systems that radically reduces the required cancellation taps. Our sub-rate based optimization framework for analog beam management achieves a superior sum rate performance compared to conventional HD HBF systems. We also design a direction-Assisted beam management technique for mmWave FD massive MIMO systems utilizing its simultaneous transmission and reception capability and thus, reducing the beam training overhead.

Finally, we investigate mmWave FD massive MIMO radios as the key enabler for the emerging Integrated Sensing and Communication (ISAC) systems. FD ISAC system simultaneously transmits downlink data signals while the reflected transmission waveform is utilized to detect and track multiple radar targets. We propose a novel FD ISAC optimization framework through A/D beamforming and cancellation for precise estimation of radar target parameters, i.e. Direction of Arrival (DoA), range, and relative velocity, while maintaining maximized downlink rate. Through indicative numerical simulation, we validate the performance of our proposed FD approaches in comparison with state-of-the-art works.

# CHAPTER 1

## INTRODUCTION

### 1.1 Background and Motivation

Given the immense growth in the demand for data traffic, future wireless networks will require efficient utilization of the available frequency spectrum. The upcoming fifth generation (5G) wireless communication systems will have features, including enhanced Mobile Broad-Band (eMBB), Ultra-Reliable Low Latency Communications (URLLC), and massive Machine Type Communications (mMTC), that require network services with extreme demand on spectral efficiency, latency, and reliability [1, 2]. To meet such demands, 5G research communities have proposed techniques, including massive Multiple-Input Multiple-Output (MIMO) systems, mmWave spectrum sharing, Non-Orthogonal Multiple Access (NOMA), and Full Duplex (FD) Communications [1–6].

#### 1.1.1 Full Duplex Wireless Communication

Recently, in-band FD has been proposed as a candidate technology for 5G wireless systems because of the potential spectral efficiency gains due to simultaneous transmission and reception. All currently deployed wireless networks operate in Half Duplex (HD) manner, dividing transmission and reception within the same node either in time with Time Division Duplexing (TDD) or in frequency with Frequency Division Duplexing (FDD). However, FD systems are capable of simultaneously transmitting and receiving radio signals on the same center frequency at

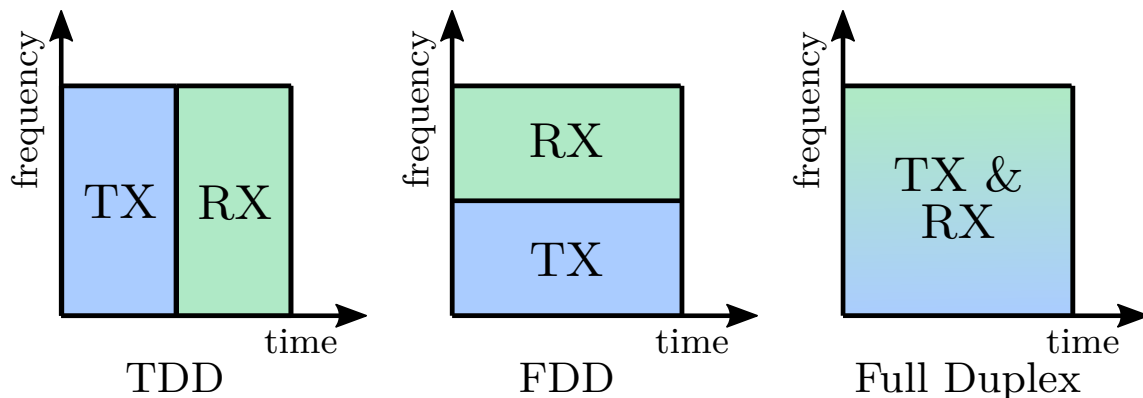


Figure 1. A simplified illustration denoting the time-frequency resource usage of TDD, FDD, and Full Duplex systems.

the same time. As neither the temporal nor spectral resources are shared between transmission and reception, the available time-frequency resource can be utilized for both, as illustrated in Figure 1. Thus, in-band FD systems are capable of increasing the attainable spectral efficiency of the conventional wireless networks by a factor close to two [4, 5].

In addition to the spectral efficiency improvement, the applications of FD systems can enable real-time sensing of spectrum occupancy for cognitive radios minimizing overhead and timing constraints [5] and reducing feedback delay (such as control information, Channel State Information (CSI) feedback, ACKnowledgement/Negative-ACKnowledgement (ACK/NACK) signals, resource allocation information, etc.) during data signal transmission [7]. In relay systems, FD employment can reduce end-to-end delay through simultaneous transmission and reception [8, 9]. Full duplex technology has also been considered in military jammer systems for the continuous detection of weak signals [10, 11], providing physical-layer security by adding

noise to the wireless channel [12]. Beyond physical-layer, FD techniques can be employed in the Multiple Access (MAC) Layer to detect collisions while transmitting in a contention-based network [3].

Moreover, recently FD technology has been considered a key enabler of the emerging Integrated Sensing and Communication (ISAC) for future wireless networks, where the previously competing sensing and communication operations are jointly optimized in the same hardware platform using a unified signal processing framework [13–17]. FD ISAC applications at millimeter Wave (mmWave) frequencies have the potential to provide high capacity communication links while simultaneously achieving high-resolution sensing, e.g., Direction of Arrival (DoA), range, and relative speed of radar targets/scatterers [18–21].

However, the inherent challenge of FD communications is the Self-Interference (SI) signal. Due to the simultaneous transmission and reception in the same frequency band, strong interference will induce to the Receiver (RX) chain of the FD node by its own Transmitter (TX). Contrary to the FDD systems, this SI can not be filtered out with a duplexer. If not suppressed, this strong SI signal can reduce or even completely abolish the FD system’s attainable capacity. Therefore, the principal research challenge for the FD communication systems is to develop techniques to cancel the SI signal. To appreciate the impact of the SI signal, consider the following example of a femto-cell base station with 30 dBm transmit power and a receiver noise floor of  $-100$  dBm. Assuming 20 dB isolation between TX and RX of the base station, the SI signal power at the RX is  $30 - 20 - (-100) = 110$  dB above the noise floor. Therefore,

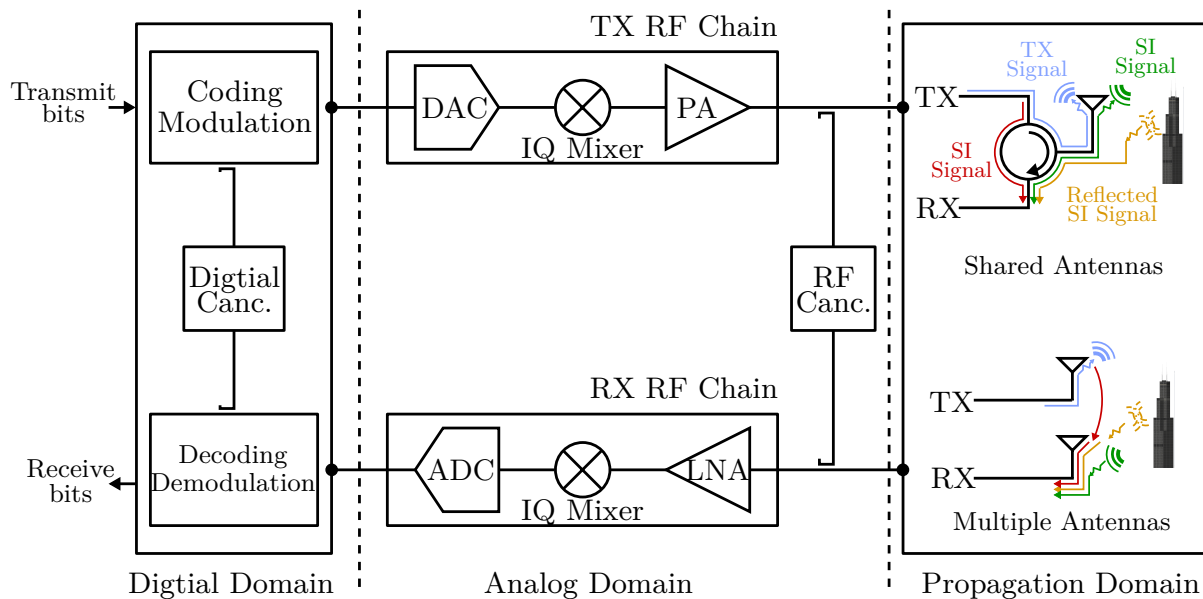


Figure 2. Generic FD transceiver architecture illustrating the boundaries and contents of the propagation, analog, and digital domains, as well as the self-interference and desired signal for both shared and multiple antenna configurations.

to maintain the link Signal-to-Noise Ratio (SNR), the FD base station must suppress 110 dB of SI signal, which is a daunting task.

### 1.1.2 Self-Interference Cancellation for Full Duplex Radios

In principle, SI cancellation should be straightforward as the transceiver knows its own transmit signal, and it can simply cancel it from the received signal, assuming the coupling SI channel up to the point of cancellation is known. However, in reality, obtaining accurate knowledge of the overall SI coupling channel is extremely challenging, as the SI signal goes through several stages of distortions while propagating from the TX to the RX of the FD node.

These distortions occur due to the analog impairments induced by the Radio Frequency (RF) components of the TX and RX chains rendering accurate SI cancellation rather cumbersome. In addition to the distortions, any SI cancellation attempt must ensure that

- The SI signal power entering the RX chain is not too high for the RX Low Noise Amplifier (LNA) to prevent RX chain saturation.
- The dynamic range of the Analog-to-Digital-Converters (ADCs) is high enough to capture the residual SI and the weak received signal of interest with sufficient precision.

To deal with the SI signal's adverse effect, in literature, the SI cancellation is performed in three stages: propagation domain suppression, analog/RF cancellation, and digital domain SI cancellation, as shown in Figure 2. In a shared antenna FD system, SI attenuation is achieved through circulator isolation [3, 5]. For multiple antenna systems, the antenna/propagation domain isolation approaches include: physically separating the RX antenna from the TX antenna to decrease the SI power by propagation attenuation [22–27]; use of spatial diversity of transmission so that SI signals add destructively and place a null at the receiving antenna location [28–32], orthogonal polarization [33–37], absorbers [38], utilizing reflective or physical boundaries [39], wavetraps [27], feed corrugations [40], employment of differential feeds [41, 42], hybrid coupler [43, 44], use of electrical balance isolator [45], auxiliary port cancellation [46], even-odd mode excitation [47], and use of lenses [48].

Following the limited antenna isolation, analog SI cancellation is employed at the RX input of the FD node to sufficiently suppress the strong SI signal. Every analog/RF cancellation method has to ensure that no RX RF components, i.e., LNAs, In-phase Quadrature (IQ) mixers, go

into saturation due to high SI input power, and the dynamic range of the ADCs is large enough to capture the residual SI as well as the weak desired signal, as mentioned above. Analog suppression is achieved by subtracting a processed copy of the transmitted signal from the RX RF chain input. In Single-Input Single-Output (SISO) FD system, the RF cancellation stage imitates the SI coupling channel between the TX and RX and destructively combines the cancellation signal at the RX input to suppress the SI [49–55]. In FD MIMO radios, the analog cancellation approach becomes challenging as each RX chain suffers from SI introduced by all the TX antennas. For wideband FD communication systems, the cancellation problem exacerbates due to the multipath SI signals reflected by the environment. Therefore, multi-tap RF cancellation is employed in FD MIMO systems, where each of the taps includes time delay or tunable bandpass filters, phase shifter, and attenuator [56–64].

Although antenna and analog domain suppression techniques are capable of preventing RX RF saturation, the residual SI signal is still large enough to overwhelm the weak desired signal. Therefore, digital domain SI cancellation techniques are employed at the RX baseband to suppress the residual SI below the noise floor, as shown in Figure 2. Digital domain cancellation is accomplished by residual SI channel modeling exploiting the fact that each FD node has knowledge of its ideal transmit signal in the digital domain. After appropriate filtering, the digital SI signal can be combined with the received signal after the ADC to provide further interference suppression. Therefore, the SI channel modeling approach must include the SI coupling paths along with the nonlinear distortions induced by practical RF components of the transceiver chain, specifically, the image effect due to gain and phase imbalance of the IQ mixers, and

nonlinearities by Power Amplifier (PA) and LNA. For single-antenna FD systems, baseband modeling of these nonlinear distortions is performed to provide appropriate digital cancellation [51, 65–67]. Akin to the analog canceller, FD MIMO operation increases the computational complexity of the digital cancellation as the number of linear, nonlinear components to be estimated increases with the number of TX/RX chains and multipath SI components [57, 68, 69]. Furthermore, FD systems in conjunction with massive MIMO radio operating in mmWave frequencies would require optimized SI cancellation and signaling design for specific applications.

## 1.2 Contribution of the Thesis

The thesis is devoted to formulating self-interference cancellation strategies and advanced transceiver design for single antenna full duplex as well as MIMO and massive MIMO FD systems and their applications. The key contributions of this thesis are as follows:

### 1.2.1 Self-Interference Cancellation for Single-antenna Full Duplex Systems

In Chapter 2, we focus on the SI suppression for single-antenna FD systems through extensive signal modeling and digital SI cancellation design. The contribution of this chapter is summarized below.

- We develop a comprehensive signal model for single-antenna FD communication systems based on direct-conversion transceiver structure. We consider the effect of TX and RX RF components, such as nonlinearities induced by PA and LNA, image signal component introduced by IQ mixers due to phase and gain imbalance, phase noise, receiver noise figure, as well as the multipath SI channels due to environmental reflections.

- We formulate an appropriate SI cancellation approach considering receiver chain RF and baseband nonlinearities along with TX impairments.
- The proposed technique employs orthogonalization of the digital SI design matrix using QR decomposition to alleviate the estimation and cancellation error.
- We evaluate our proposed approach and compare it with state-of-the-art digital SI cancellation methods using extensive waveform simulation. We show that our proposed SI modeling and cancellation approach outperforms the existing method for single-antenna FD systems.
- We provided a DNN-based SI cancellation approach with Transfer Learning that is capable of achieving superior digital SI suppression with limited number of training symbols and training epochs.

This chapter is based on the following published article:

- [C1] M. A. Islam and B. Smida, “A comprehensive self-interference model for single-antenna full-duplex communication systems,” in Proceedings of the IEEE International Conference on Communications (ICC), Shanghai, China, May 2019, pp. 1–7.
- [J1] K. Muranov, M. A. Islam, B. Smida, and N. Devroye, “On Deep Learning Assisted Self-Interference Estimation in a Full-Duplex Relay Link,” IEEE Wireless Communications Letters, vol. 10, no. 12, pp. 2762–2766, Sep. 2021.

### 1.2.2 Unified Analog and Digital Transceiver Design for Wideband Full Duplex MIMO Systems

In wideband FD MIMO system, the SI cancellation complexity increase exponentially with the number of RF chains and SI channel paths. Chapter 3 studies a novel low-complexity A/D SI cancellation and transceiver design for FD MIMO systems. The key concepts of this chapter is as follows.

- We develop a wideband FD MIMO communication system comprising of an FD MIMO node simultaneously communicating with two multi-antenna UpLink (UL) and DownLink (DL) nodes utilizing the same time and frequency resources.
- To suppress the strong SI signal due to simultaneous transmission and reception in FD MIMO systems, we propose a joint design of Analog and Digital (A/D) cancellation as well as transmit and receive beamforming capitalizing on baseband Orthogonal Frequency-Division Multiplexing (OFDM) signal modeling.
- Considering practical transmitter impairments, we present a multi-tap wideband analog canceller architecture whose number of taps does not scale with the number of transceiver antennas and multipath SI components.
- We also propose a novel adaptive digital cancellation based on truncated singular value decomposition that reduces the residual SI signal estimation parameters.

- To maximize the FD sum rate, a joint optimization framework is presented for A/D cancellation and digital beamforming. We validate our proposed approach through extensive waveform simulation.

The content of this chapter is based on the following published articles:

- [J2] M. A. Islam, G. C. Alexandropoulos, and B. Smida, “Joint Analog and Digital Transceiver Design for Wideband Full Duplex MIMO Systems,” IEEE Transactions on Wireless Communications, Jun. 2022.
- [C2] M. A. Islam, G. C. Alexandropoulos, and B. Smida, “A unified beamforming and A/D self-interference cancellation design for full duplex MIMO radios,” in Proceedings of the IEEE Annual International Symposium on Personal, Indoor and Mobile Radio Communications (PIMRC), Istanbul, Turkey, Sep. 2019, pp. 1–7.

### **1.2.3 Simultaneous Data Communication and Channel Estimation in Single- and Multi-User FD MIMO Systems**

In Chapter 4, we present a novel Simultaneous Communication of Data and Control (SCDC) scheme for single- and multi-user FD MIMO systems. The contribution of this chapter is summarized as follows.

- We develop a novel SCDC scheme for FD MIMO base station serving multiple single-antenna FD users. We consider the simultaneous DL beamformed data transmission and UL pilot-assisted channel estimation while achieving sufficient SI suppression.

- We present a joint design of the base station's transmit and receive beamforming matrices as well as the settings for the multiple analog taps and the digital SI canceller with the objective to maximize the DL rate.
- We evaluate the performance of the proposed SCDC transmission scheme and show that it outperforms its conventional half duplex counterpart and reduces the SI cancellation hardware complexity.

The materials of this chapter is based on the following published articles:

- [C3] M. A. Islam, G. C. Alexandropoulos, and B. Smida, "Simultaneous downlink data transmission and uplink channel estimation with reduced complexity full duplex MIMO radios," in Proceedings of the IEEE International Conference on Communications (ICC), Dublin, Ireland, Jun. 2020, pp. 1–6.
- [C4] M. A. Islam, G. C. Alexandropoulos, and B. Smida, "Simultaneous Data Communication and Channel Estimation in Multi-User Full Duplex MIMO Systems," in Proceedings of the IEEE ASILOMAR Conference on Signals, Systems and Computers, Pacific Grove, USA, Nov. 2020, pp. 1–6.

#### **1.2.4 Self-interference Cancellation for FD massive MIMO Systems with Hybrid Beamformers**

Hybrid A/D beamforming architectures have been lately considered as a candidate technology for realizing massive MIMO transceivers with very large number of antenna elements, but with much fewer numbers of Radio Frequency (RF) chains. Chapter 5 investigates FD

massive MIMO systems designing low-complexity A/D BeamFormers (BFs) and SI cancellation algorithms while maximizing FD sum rate. The key contribution of the chapter is as follows.

- We present a novel architecture for FD massive MIMO systems with hybrid A/D beamforming transceivers, including multi-tap analog cancellation with reduced number of taps and simple multiplexers for efficient signal routing among the transceiver RF chains.
- Capitalizing on the proposed transceiver architecture, we develop a joint design of analog cancellation and A/D beamforming with the objective to maximize the achievable FD rate performance.
- We also derive a novel sub-rate based RF TX/RX beamforming design that remove the computational complexity of analog beam selection compared to a conventional exhaustive search approach.
- Representative millimeter wave simulation results demonstrate the effectiveness of the proposed architecture and algorithmic framework for enabling simultaneous UL and DL communications with reduced complexity analog SI cancellation.

This chapter is based on the following published and submitted articles:

- [C5] G. C. Alexandropoulos, M. A. Islam, and B. Smida, “Full duplex hybrid A/D beamforming with reduced complexity multi-tap analog cancellation,” in Proceedings of the IEEE International Workshop on Signal Processing Advances in Wireless Communications (SPAWC), Atlanta, USA, Jun. 2020, pp. 1–5.

- [J3] George C. Alexandropoulos, M. A. Islam, and B. Smida, “Full Duplex Massive MIMO Architectures: Recent Advances, Applications, and Future Directions,” Under review in the IEEE Vehicular Technology Magazine, 2022.

### 1.2.5 Direction-Assisted Beam Management in Full Duplex Millimeter Wave Massive MIMO Systems

Recent applications of the Full Duplex (FD) technology focus on enabling simultaneous control communication and data transmission to reduce the control information exchange overhead, which impacts end-to-end latency and spectral efficiency. In Chapter 6, we present a DoA estimation strategy with simultaneous DL data transmission for FD massive MIMO systems. The chapter is summarized below.

- We present a DoA-assisted beam management framework for FD mmWave massive MIMO systems, where the BS is equipped with a large antenna array realizing DL analog BF and few digitally controlled receive antenna elements used for UL DoA estimation.
- Capitalizing on our FD hardware architecture for hybrid A/D BF, we propose a Simultaneous DoA estimation and Data Transmission (SDDT) scheme for boosting beam management in FD mmWave massive MIMO communications.
- Enabled by FD and leveraging channel reciprocity, we simultaneously estimate the UL dominant DoA and transmit analog beamformed data in the DL direction.
- We present a joint design of the DoA-assisted analog BF as well as the A/D SI cancellation units, targeting the maximization of the achievable DL rate.

- Our extensive simulation results considering a mmWave channel model showcase the FD-enabled gains of DoA-assisted beam management under various user mobility conditions.

The content of this chapter is based on the following published article:

- [C6] M. A. Islam, G. C. Alexandropoulos, and B. Smida, “Direction-Assisted Beam Management in Full Duplex Millimeter Wave Massive MIMO Systems,” in Proceedings of the IEEE Global Communications Conference (GLOBECOM), Madrid, Spain, Dec. 2021, pp. 1–6.

### **1.2.6 Integrated Sensing and Communication with Millimeter Wave Full Duplex Hybrid Beamforming**

In-band FD is being considered as a key enabling technology for ISAC applications due to its simultaneous transmission and reception capability. Chapter 7 investigates FD-based ISAC system operating at millimeter Wave (mmWave) frequencies, where a massive MIMO node employing hybrid A/D beamforming performs DL communication while sensing the radar targets in its coverage environment. The contribution of the chapter is summarized as follows.

1. We present a novel FD massive MIMO ISAC system operating at mmWave frequencies and realizing hybrid A/D beamforming, where OFDM waveforms are utilized for both DL communication and radar target sensing.
2. Unlike state-of-the-art works, we devise an ISAC optimization framework that is capable of estimating the DoA, range, and relative velocity of multiple radar targets, while maximizing the DL communication rate.

3. We also employ the ISAC system for a multi-user DL communication, where we propose a joint design of the A/D beamformers and a reduced complexity SI cancellation for the FD ISAC system, which targets at maximizing the multi-user DL communication rate and the precision of the radar target tracking.

The material of this chapter is based on the following published and submitted articles:

- [C7] M. A. Islam, G. C. Alexandropoulos, and B. Smida, “Integrated Sensing and Communication with Millimeter Wave Full Duplex Hybrid Beamforming,” in Proceedings of the IEEE International Conference on Communications (ICC), Seoul, South Korea, May 2022, pp. 1–6.
- [C8] M. A. Islam, G. C. Alexandropoulos, and B. Smida, “Simultaneous Multi-User MIMO Communications and Multi-Target Tracking with Full Duplex Radios,” Submitted in the IEEE Global Communications Conference (GLOBECOM), Dec. 2022, Rio de Janeiro, Brazil, pp. 1–6

Each chapter contains numerical evaluations of the proposed methods as well as comparisons with the state-of-the-art approaches. Finally, we conclude the thesis in Chapter 8.

## CHAPTER 2

# SELF-INTERFERENCE CANCELLATION FOR SINGLE-ANTENNA FULL DUPLEX SYSTEMS

Single-antenna full duplex communication technology has the potential to substantially increase spectral efficiency. However, limited propagation domain cancellation of single-antenna system results in a higher impact of receiver chain nonlinearities on the residual self-interference signal. In this chapter, we offer a comprehensive SI model for single-antenna full-duplex systems based on direct-conversion transceiver structure considering nonlinearities of all the transceiver RF components, in-phase/quadrature (IQ) imbalances, phase noise effect, and receiver noise figure. To validate our model, we also propose a more appropriate digital SI cancellation approach considering receiver chain RF and baseband nonlinearities. The proposed technique employs orthogonalization of the design matrix using QR decomposition to alleviate the estimation and cancellation error.

### 2.1 Introduction

Full-duplex technology is one of the emerging techniques to achieve higher spectral efficiency, where devices simultaneously transmit and receive at a single frequency. This novel paradigm

---

The content of this chapter is based on our published articles in [67] and [70]. Copyright © 2019, 2021 IEEE.

in improving spectrum usage can increase the throughput by a factor of two compared to the traditional bidirectional half-duplex, namely TDD and FDD. However, the implementation of full-duplex systems is constrained by the cancellation of SI, which is stemming from the transmitter to the receiver hindering the detection of the received signal.

Single-antenna FD system employs circulator or duplexer to route transmitted and received signal between TX/RX input and antenna. The circulators are supposed to provide very high isolation between the TX/RX RF chain input. However, practical circulators provide only about 15 – 20 dB isolation contributing to a direct path between TX and RX as circulator leakage. In addition to that, the mismatch between transmitter line impedance and antenna impedance induces another SI path to the RX front end due to the antenna reflection. While these two signals are considered to be the main coupling components of the SI, there are also weaker multipath components due to the reflections from the surrounding environment. Therefore, successful detection of the desired signal from the far node depends on the sufficient suppression of the SI signal in the analog/RF and digital cancellation stage.

Analog SI cancellation in a single-antenna FD system can be achieved using a complex feed-forward network, including multiple delay lines, tunable attenuator, and adaptive algorithm [51]. For a more compact solution, analog SI cancellation is performed using an electrical balance duplexer [45], or reconfigurable Impedance Mismatched Terminal (IMT) circuit [44, 50]. However, as mentioned in Chapter 1, antenna and analog domain suppression are not sufficient to mitigate the strong SI signal below the weak desired signal, and the residual SI is suppressed in the digital domain.

Digital domain cancellation is accomplished by SI regeneration using digital filters fitted to the detector input through the known transmit data. For digital cancellation techniques, the effect of transmitter and receiver PA nonlinearities is analyzed in [51,65], whereas the impact of IQ imbalances and resulting image components is investigated in [66]. Signal models, including the phase noise of transmitter and receiver oscillators, are presented in [71]. It was observed that the phase noise is a bottleneck for perfect SI cancellation while using two different oscillators for transmitter and receiver. A scenario with a common oscillator for both the transceiver sides is also analyzed in [72].

In previous literature, both single-antenna and separate-antenna full-duplex models are investigated. However, using single-antenna as a function of SI cancellation is more attractive because of twofold reasons: first, using two antenna full-duplex system may not achieve any higher throughput than using two antenna in half-duplex MIMO system spatially multiplexing two independent packets at the same time [51,73]; second, using single-antenna transceiver system results in a compact design. Existing single-antenna full-duplex antenna and analog cancellation methods typically achieve 50 – 60 dB cancellation [44,45,74], where separate-antenna system provides higher cancellation. For a practical receiver, this limited RF cancellation results in a higher effect of receiver RF and baseband (BB) nonlinearity on the SI signal.

The contribution of our work is as follows.

- We provide a comprehensive self-interference model for single-antenna full-duplex systems based on direct-conversion structure considering all the impairments including transmit-

ter and receiver IQ imbalances, nonlinear distortions in all the transceiver components, receiver noise figure, and phase noise effect of both transmitter and receiver IQ mixers.

- Through extensive circuit-level waveform simulation, we show the effect of receiver RF and BB second and third-order nonlinearity on the residual self-interference signal for limited antenna and RF cancellation.
- To tackle this effect, we propose an appropriate self-interference estimation and digital cancellation approach considering receiver chain nonlinearities, which outperforms the existing digital cancellation techniques. To reduce the estimation and cancellation error, we employ orthogonalization of the design matrix using QR decomposition method.

## 2.2 FD Transceiver Model And Self-interference characterization

In this section, we discuss the self-interference signal modeling for a single-antenna FD transceiver system based on the direct-conversion structure presented in Figure 3. In direct-conversion structure, RF and BB signal frequency translation is performed without any intermediate frequency stage, unlike superheterodyne structure [75]. The direct-conversion receiver structure allows signal amplification and filtering at the BaseBand (BB) stage, which reduces the power consumption and manufacturing cost. However, direct-conversion radios suffer from RF and BB impairments, such as IQ imbalances, nonlinear distortions, and phase noise effect [76]. Therefore, a detailed characterization of the self-interference signal is performed in the next subsections considering the RF and BB impairments.

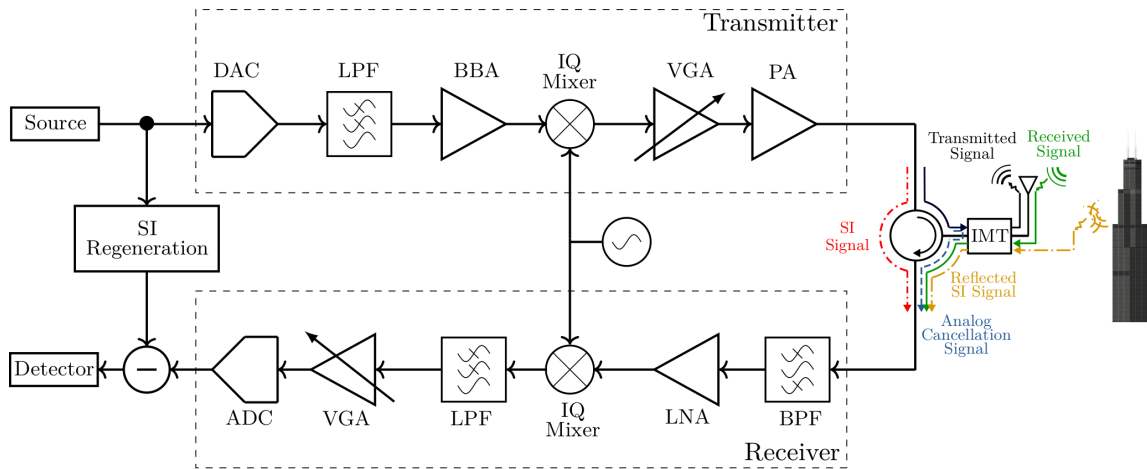


Figure 3. A detailed block diagram of a single-antenna full duplex direct conversion transceiver, where analog cancellation is achieved using IMT circuit.

### 2.2.1 Self-interference Model at the Transmitter

At the transmit chain, the impairments are mainly introduced by the RF front-end components, specifically IQ mixers and power amplifiers. Both baseband and bandpass modeling approach is taken into account for the following SI characterization.

After the Digital-to-Analog Converters (DACs), the I and Q components of the converted baseband signal  $x(t)$  are passed through the low-pass filters for further suppression of aliasing products. The I and Q signals are then fed into the IQ mixer for upconversion to the carrier frequency. As stated in [66], IQ imbalances in practical mixers add a mirror image of the original signal with certain image attenuation. The IQ mixers also induce phase noise to the signal. Let

$\gamma_{\text{TX}}, \lambda_{\text{TX}}$  be the complex gain of the linear and image signal components, respectively. Thus, the upconverted RF signal is given by

$$\begin{aligned} x_{\text{IQ}}(t) &\triangleq 2\Re\left\{(\gamma_{\text{TX}} x(t) + \lambda_{\text{TX}} \bar{x}(t))e^{j(\omega_c t + \theta_{\text{TX}})}\right\} \\ &= z(t)e^{j(\omega_c t + \theta_{\text{TX}})} + \bar{z}(t)e^{-j(\omega_c t + \theta_{\text{TX}})}, \end{aligned} \quad (2.1)$$

where  $z(t) = (\gamma_{\text{TX}}x(t) + \lambda_{\text{TX}}\bar{x}(t))$ ,  $\omega_c$  is the angular center frequency of the RF signal and  $\theta_{\text{TX}}(t)$  is the random phase noise process. Here,  $(\bar{\cdot})$  denotes the complex conjugate.

Before transmission, the upconverted signal goes through variable amplification stages (variable Gain Amplifier (VGA), PA driver) to meet the transmit power specifications. Then, for final amplification, the signal is fed into the power amplifier operating in its nonlinear region. Only the odd-order nonlinear terms are considered for PA, as the even-power harmonics lie out of band and will be cutoff by the RF Low Pass Filter (LPF) of the receiver [66] [51]. Considering the VGA gain as  $\beta_{\text{VGA}}$ , the PA nonlinear response is modeled based on the Hammerstein nonlinearity, given as

$$x_{\text{PA}}(t) \triangleq \left( \sum_{p \in \{1,3\}} \beta_{\text{PA},p} (\beta_{\text{VGA}} x_{\text{IQ}}(t))^p \right) * f(t), \quad (2.2)$$

where  $p$  is the order of the nonlinearity,  $f(t)$  is the memory polynomial, and  $(*)$  denotes the linear convolution. Here,  $\beta_{\text{PA},1}$  is the linear gain and  $\beta_{\text{PA},3}$  is the gain of third-order nonlinear distortions. We consider only up to the third-order distortion, as that is in practice always the

strongest nonlinearity at PA output [66]. A general definition of the nonlinear distortion gains is given as

$$\beta_{C,n} \triangleq \frac{\beta_{C,1}}{(\text{IIPn})^{n-1}}, \quad (2.3)$$

where  $\beta_{C,1}$  denotes the linear gain and  $n$  is the nonlinearity order of any component  $C = \{\text{PA}, \text{LNA}, \text{BB}\}$ . These nonlinear distortions are modeled using IIP2 and IIP3 figures (second and third order input-referred intercept points) of the PA [75].

In single-antenna system, the PA output is routed to the antenna using a circulator. In addition to routing signals between the transceiver and antenna, the circulator should also provide very high isolation between the TX and RX. Unfortunately, practical circulators provide only about 15 – 20 dB isolation contributing to a direct path between TX and RX as circulator leakage [51]. There is another path of SI due to the antenna reflection [50]. Because of the mismatch between transmitter line impedance and antenna impedance, a portion of the transmitted signal reflects back to the receiver front end. While these two signals are considered to be the main coupling components of the SI, there are also weaker multipath components due to the reflections from the surrounding environment. At the receiver input, the SI signal subjects to the RF cancellation. Letting  $\alpha_{\text{RF}}(t)$ ,  $h_{ch}(t)$  be the impulse response of the RF cancellation and the multipath channel response of the self-interference signal, respectively, the signal at the receiver input is given by

$$\begin{aligned} r(t) &\triangleq \alpha_{\text{RF}}(t) * h_{ch}(t) * x_{\text{PA}}(t) + d(t) + \eta_{th}(t) \\ &\stackrel{\text{(a)}}{=} \sum_{p \in \{1,3\}} h_p(t) * (x_{\text{IQ}}(t))^p + d(t) + \eta_{th}(t), \end{aligned} \quad (2.4)$$

where  $h_p(t) = \beta_{\text{PA},p} \beta_{\text{VGA}}^p (\alpha_{\text{RF}}(t) * f(t) * h_{\text{ch}}(t))$  and  $d(t), \eta_{th}$  are the desired signal and the thermal noise of the receiver, respectively. Here, (a) is defined using Equation 2.2.

### 2.2.2 Self-interference Model at the Receiver

As a direct-conversion receiver suffers from LNA nonlinearities, Mixer IQ imbalance, and BB nonlinearity, these impairments will have a significant effect on the self-interference signal, especially in higher transmit power case. Therefore, a detailed receiver chain SI modeling is performed considering all the receiver impairments.

At the first stage of the receiver, the signal is amplified by a nonlinear LNA. We model the LNA using the same Hammerstein model used in Equation 2.3. The LNA output is given by

$$\begin{aligned}
 r_{\text{LNA}}(t) &\triangleq \sum_{q \in \{1,3\}} \beta_{\text{LNA},q} (r(t))^q + \eta_{\text{LNA}}(t) \\
 &\stackrel{(b)}{=} \sum_{q \in \{1,3\}} \beta_{\text{LNA},q} \left( \sum_{p \in \{1,3\}} h_p(t) * (x_{\text{IQ}}(t))^p + d(t) + \eta_h(t) \right)^q + \eta_{\text{LNA}}(t) \quad (2.5) \\
 &\approx \sum_{q \in \{1,3\}} \beta_{\text{LNA},q} \left( \sum_{p \in \{1,3\}} h_p(t) * (x_{\text{IQ}}(t))^p \right)^q + c(t),
 \end{aligned}$$

where  $\eta_{\text{LNA}}(t)$  is the noise of the LNA and  $q$  is the order of the nonlinearity. Here, (b) is defined using Equation 2.4. For brevity, we only consider the linear operation of the receiver components for the desired signal and noise.

Therefore,  $c(t) = \beta_{\text{LNA},1} (d(t) + \eta_{th}(t)) + \eta_{\text{LNA}}(t)$ . Here,  $\beta_{\text{LNA},1}$  and  $\beta_{\text{LNA},q}$  are the linear gain and respective  $q$ th order nonlinear distortion gain of the LNA. Only odd order distortions are considered, as the even order RF LNA nonlinearities produce frequency components that are far away from  $\omega_c$  and will be filtered out by LPF [75], [76].

After the LNA, receiver IQ mixer downconverts the RF signal into baseband frequency and LPFs are used to filter out the high frequency terms. Practical IQ mixers induce random phase noise  $\theta_{\text{RX}}(t)$ , which is uncorrelated to  $\theta_{\text{TX}}(t)$  in case of independent oscillators [77]. However, in single-antenna FD system, same oscillator is shared by the transmitter and the receiver resulting in a common phase noise process,  $\theta(t)$ . Thus,  $\theta_{\text{TX}}(t) = \theta_{\text{RX}}(t) = \theta(t)$ . It is shown in previous literature that sharing oscillators suppresses the phase noise below the noise floor even in the case of transmission delay [72], [77]. So, the downconverted signal is written as

$$\begin{aligned}
r_{\text{IQ}}(t) &\triangleq \text{LPF}\{r_{\text{LNA}}(t)e^{-j(\omega_c t + \theta_{\text{RX}}(t))}\} \\
&= \text{LPF}\left\{\left(\sum_{q \in \{1,3\}} \beta_{\text{LNA},q} \left(\sum_{p \in \{1,3\}} h_p(t) * (x_{\text{IQ}}(t))^p\right)^q + c(t)\right) e^{-j(\omega_c t + \theta_{\text{RX}}(t))}\right\} \\
&= \text{LPF}\left\{\sum_{q \in \{1,3\}} \beta_{\text{LNA},q} \left(\sum_{p \in \{1,3\}} h_p(t) * (z(t)e^{j(\omega_c t + \theta_{\text{RX}}(t))} + \bar{z}(t)e^{-j(\omega_c t + \theta_{\text{RX}}(t))})^p\right)^q \right. \\
&\quad \left. \times e^{-j(\omega_c t + \theta_{\text{RX}}(t))}\right\} + c(t) \quad (2.6) \\
&= \sum_{q \in \{1,3\}} \beta_{\text{LNA},q} \binom{q}{\frac{q-1}{2}} (h_1(t) * z(t) + h_3(t) * 3z^2(t)\bar{z}(t))^{\frac{q+1}{2}} \\
&\quad \times (h_1(t) * \bar{z}(t) + h_3(t) * 3z(t)\bar{z}(t)^2)^{\frac{q-1}{2}} + c(t) \\
&= \sum_{q \in \{1,3\}} \beta_{\text{LNA},q} \binom{q}{\frac{q-1}{2}} \left(\sum_{p \in \{1,3\}} h_p(t) * u_p(t)\right)^{\frac{q+1}{2}} \left(\sum_{p \in \{1,3\}} h_p(t) * \bar{u}_p(t)\right)^{\frac{q-1}{2}} + c(t) \\
&= s_{\text{IQ}}(t) + c(t),
\end{aligned}$$

where

$$\begin{aligned}
s_{\text{IQ}}(t) &= \sum_{q \in \{1,3\}} \beta_{\text{LNA},q} \left( \frac{q}{\frac{q-1}{2}} \right) \left( \sum_{p \in \{1,3\}} h_p(t) * u_p(t) \right)^{\frac{q+1}{2}} \left( \sum_{p \in \{1,3\}} h_p(t) * \bar{u}_p(t) \right)^{\frac{q-1}{2}} \\
u_1(t) &= \gamma_{\text{TX}} x(t) + \lambda_{\text{TX}} \bar{x}(t) \\
u_3(t) &= 3 \left( \gamma_{\text{TX}}^2 \bar{\lambda}_{\text{TX}} x^3(t) + (\gamma_{\text{TX}}^2 \bar{\gamma}_{\text{TX}} + 2\gamma_{\text{TX}} \lambda_{\text{TX}} \bar{\lambda}_{\text{TX}}) x^2(t) \bar{x}(t) \right. \\
&\quad \left. + (2\gamma_{\text{TX}} \bar{\gamma}_{\text{TX}} \lambda_{\text{TX}} + \lambda_{\text{TX}}^2 \bar{\lambda}_{\text{TX}}) x(t) \bar{x}^2(t) + \lambda_{\text{TX}}^2 \bar{\gamma}_{\text{TX}} \bar{x}^3(t) \right).
\end{aligned} \tag{2.7}$$

The proof of Equation 2.6 is given in Appendix A. Receiver IQ mixer also induces the image component because of the IQ imbalance. Now, considering the effect of IQ imbalance, the IQ output signal is written as

$$r_{\text{IQIm}}(t) \triangleq \gamma_{\text{RX}} r_{\text{IQ}}(t) + \lambda_{\text{RX}} \bar{r}_{\text{IQ}}(t) + \eta_{\text{IQ}}(t), \tag{2.8}$$

where  $\gamma_{\text{RX}}, \lambda_{\text{RX}}$  are the linear and image component gain, and  $\eta_{\text{IQ}}(t)$  is the noise of the IQ mixer.

Baseband components shown in Figure 3, specifically amplifiers and analog-to-digital converters, also introduce some nonlinearities and DC offset to the BB signal. For simplification, up to second-order nonlinearity is considered. In our model, we use the complex representation of the baseband signal since it helps analytically by revealing how the distortion components

are spectrally distributed in relation to the original signal. Considering all the impairments, the complex baseband signal is written as

$$r_{\text{BB}}(t) \triangleq \sum_{m=0}^2 \beta_{\text{BB},r} r_{\text{IQIm}}^m(t) + \eta_{\text{BB}}(t), \quad (2.9)$$

where  $m$  is the order of the nonlinearity,  $\beta_{\text{BB},r}$  and  $\eta_{\text{BB}}(t)$  is the respective  $m$ th order baseband gain and the BB components noise, respectively. The first term of Equation 2.9 represents the DC offset introduced by the baseband components. At the end of the receiver chain, the ADC converts the analog baseband signal to digital domain. Considering the quantization noise,  $n_{\text{Quant}}[n]$  induced by the ADC, the digital signal at the ADC output is expressed as

$$\begin{aligned} y[n] &\triangleq r_{\text{BB}}[n] + \eta_{\text{Quant}}[n] \\ &= \sum_{m=0}^2 \beta_{\text{BB},r} \left( \gamma_{\text{RX}} s_{\text{IQ}}[n] + \lambda_{\text{RX}} \bar{s}_{\text{IQ}}[n] \right)^m + \beta_{\text{BB},1} \gamma_{\text{RX}} \beta_{\text{LNA},1} d[n] + \eta_T[n]. \end{aligned} \quad (2.10)$$

Here,  $\eta_T[n]$  represents the total noise of the receiver, including thermal noise, receiver noise figure, and quantization noise.

### 2.3 Proposed Digital Estimation and Cancellation of Self-interference Signal

In this section, we propose an appropriate digital cancellation approach with improved reference signal design for estimation based on the signal at the ADC output. To ensure the estimation accuracy, orthogonalization procedure is employed in estimation technique.

Based on Equation 2.10 and Equation 2.7,  $y[n]$  can be expressed as the combination of the linear SI signal  $x[n]$ , conjugate SI signal  $\bar{x}[n]$ , and their higher-order terms along with the

desired signal, and receiver noise floor. Although a detailed expansion of Equation 2.10 results in hundreds of residual SI terms, most of the higher-order terms are very weak. Therefore, they have an insignificant effect on the total self-interference power, thus can be ignored without compromising self-interference cancellation accuracy. Based on the specification in Table II, we keep the 13 stronger SI components that include a combination of  $x[n]$ ,  $\bar{x}[n]$ , and their higher-order terms and use those for cancellation of the self-interference signal. Hence, using vector-matrix notation, for  $N$  observed training samples, the ADC output signal is written as

$$\mathbf{Y} = \mathbf{\Psi}\mathbf{w} + \mathbf{d} + \boldsymbol{\eta}, \quad (2.11)$$

where  $\mathbf{Y} = [y[n] y[n+1] \dots y[n+N-1]]^T$ ,  $\mathbf{d} = \beta_{\text{BB},1}\gamma_{\text{RX}}\beta_{\text{LNA},1}[d[n] d[n+1] \dots d[n+N-1]]^T$ , and  $\boldsymbol{\eta} = [\eta_T[n] \eta_T[n+1] \dots \eta_T[n+N-1]]^T$ . The definition of the design matrix  $\mathbf{\Psi}$  with size  $N \times (2L + 3L^2 + 7L^3 + 1)$  is given as

$$\mathbf{\Psi} = [\mathbf{1} \ \Psi_x \ \Psi_{\bar{x}} \ \Psi_{x,x} \ \Psi_{x,\bar{x}} \ \Psi_{\bar{x},\bar{x}} \ \Psi_{x,x,x} \ \Psi_{x,x,\bar{x}} \ \Psi_{x,\bar{x},\bar{x}} \ \Psi_{\bar{x},\bar{x},\bar{x}} \ \Psi_{x,x,x^2\bar{x}} \ \Psi_{x,\bar{x},x^2\bar{x}} \ \Psi_{x,x,x\bar{x}^2}], \quad (2.12)$$

where  $L$  is the length of the total impulse response including multipath channel, analog cancellation, and PA memory polynomial.

Here, the horizontally concatenated basis matrices represent the 13 stronger SI terms formulated as

$$\begin{aligned}\Psi_{\mathbf{a}} &= [\Phi_{\mathbf{a}}(n) \ \Phi_{\mathbf{a}}(n-1) \ \dots \ \Phi_{\mathbf{a}}(n-L+1)] \\ \Psi_{\mathbf{a},\mathbf{b}} &= [\Phi_{\mathbf{b}}(n) \odot \Psi_{\mathbf{a}} \ \Phi_{\mathbf{b}}(n-1) \odot \Psi_{\mathbf{a}} \ \dots \ \Phi_{\mathbf{b}}(n-L+1) \odot \Psi_{\mathbf{a}}] \\ \Psi_{\mathbf{a},\mathbf{b},\mathbf{c}} &= [\Phi_{\mathbf{c}}(n) \odot \Psi_{\mathbf{a},\mathbf{b}} \ \Phi_{\mathbf{c}}(n-1) \odot \Psi_{\mathbf{a},\mathbf{b}} \ \dots \ \Phi_{\mathbf{c}}(n-L+1) \odot \Psi_{\mathbf{a},\mathbf{b}}],\end{aligned}\tag{2.13}$$

where  $\odot$  denotes element wise multiplication of the vector with all the columns of the matrix.

Here, the basis vectors are defined as

$$\begin{aligned}\Phi_{\mathbf{x}}(n) &= [x[n] \ x[n+1] \ \dots \ x[n+N-1]]^T, \quad \Phi_{\bar{\mathbf{x}}}(n) = \bar{\Phi}_{\mathbf{x}}(n), \\ \Phi_{\mathbf{x}^2\bar{\mathbf{x}}}(n) &= [x^2[n]\bar{x}[n] \ x^2[n+1]\bar{x}[n+1] \ \dots \ x^2[n+N-1]\bar{x}[n+N-1]]^T, \quad \Phi_{\mathbf{x}\bar{\mathbf{x}}^2}(n) = \bar{\Phi}_{\mathbf{x}^2\bar{\mathbf{x}}}(n).\end{aligned}\tag{2.14}$$

For instance, the matrix  $\Psi_{\mathbf{x},\bar{\mathbf{x}},\mathbf{x}^2\bar{\mathbf{x}}} \in \mathbb{C}^{N \times L^3}$  represent the SI term:  $9\beta_{\text{BB},1}\gamma_{\text{TX}}\beta_{\text{LNA},3}\gamma_{\text{RX}}\bar{\gamma}_{\text{TX}}$   $(\gamma_{\text{TX}}^2\bar{\gamma}_{\text{TX}} + 2\gamma_{\text{TX}}\lambda_{\text{TX}}\bar{\lambda}_{\text{TX}})(h_1[n] * x[n])(h_1[n] * \bar{x}[n])(h_3[n] * x^2[n]\bar{x}[n])$ . Here,  $\mathbf{w}$  is the  $(2L + 3L^2 + 7L^3 + 1) \times 1$  parameter vector. Our goal is to estimate the parameter  $\mathbf{w}$ , and then use it to reconstruct and cancel the self-interference signal at the detector input. Therefore, the error vector is defined as

$$\mathbf{e} = \mathbf{Y} - \Psi\hat{\mathbf{w}},\tag{2.15}$$

where  $\hat{\mathbf{w}}$  is the least square estimate, which can be obtained by solving for the  $\mathbf{w}$  that minimizes the power of the error vector as

$$\hat{\mathbf{w}} = \arg \min_{\mathbf{w}} \|\mathbf{e}\|^2 = \arg \min_{\mathbf{w}} \|\mathbf{Y} - \Psi\mathbf{w}\|^2.\tag{2.16}$$

The above ordinary least square problem has a closed-form solution with the usual assumption that the design matrix  $\Psi$  has independent columns. However, the columns of the matrix  $\Psi$  are higher-order polynomials of linear SI component  $x[n]$ , conjugate SI component  $\bar{x}[n]$ , and their interaction products. Therefore, the columns of the matrix  $\Psi$  are correlated; thus, there exists a high level of multicollinearity. To tackle this problem, we propose to orthogonalize the design matrix  $\Psi$  using QR decomposition. We use the traditional Gram-Schmidt orthogonalization procedure to find a QR decomposition of  $\Psi$  such that  $\Psi = \mathbf{QR}$ , where  $\mathbf{Q}$  has orthogonal columns and the same rank as  $\Psi$ . Here,  $\mathbf{R}$  is an upper triangular matrix with 1 on the diagonal. Using the QR decomposition, Equation 2.16 is written as

$$\hat{\mathbf{w}} = \arg \min_{\mathbf{w}} \|\mathbf{Y} - \mathbf{QR}\mathbf{w}\|^2. \quad (2.17)$$

Letting  $\boldsymbol{\mu} = \mathbf{R}\mathbf{w}$ , we can reformulate the above minimization problem and find the least square solution as

$$\begin{aligned} \hat{\boldsymbol{\mu}} &= \arg \min_{\boldsymbol{\mu}} \|\mathbf{Y} - \mathbf{Q}\boldsymbol{\mu}\|^2 \\ &= (\mathbf{Q}^H \mathbf{Q})^{-1} \mathbf{Q}^H \mathbf{Y}, \end{aligned} \quad (2.18)$$

where  $(\cdot)^H$  denotes the Hermitian transpose of the matrix. Using back substitution, we derive  $\hat{\mathbf{w}}$  from  $\hat{\boldsymbol{\mu}}$ .

It is to be noted that authors in [66] proposed a widely linear canceller considering only the effect of linear SI  $x[n]$  and conjugate SI  $\bar{x}[n]$ , a nonlinear approach considering third-order

TABLE I  
WAVEFORM AND SYSTEM LEVEL PARAMETERS OF SINGLE-ANTENNA FULL  
DUPLEX SYSTEM

Parameter	Value	Parameter	Value
Bandwidth	20 MHz	SNR Requirement	10 dB
Carrier Frequency	2.4 GHz	Thermal Noise Floor	-101.0 dBm
Constellation	16-QAM	RX Noise Figure	4.1 dB
Number of Subcarriers	64	Sensitivity Level	-86 dBm
Cyclic Prefix Length	16	Transmit Power	-5:25 dBm
Sample length	15.625 ns	ADC Bits	12
Symbol Length	4 $\mu$ s	PAPR	10 dB

nonlinear SI term  $x^2[n]\bar{x}[n]$  is provided in [51], and a joint cancellation technique cascading PA nonlinearity with transmitter IQ imbalance is proposed in [68] for MIMO cases, which is converted here into single antenna system. However, receiver nonlinearities and their effect are ignored in these previous models. Our proposed estimation approach takes these components into account for the formulation of the design matrix and provides required SI cancellation at the detector input.

## 2.4 Performance Simulation and Analysis

In this section, we perform a waveform simulation to evaluate the performance of the proposed digital cancellation strategy and compare it with the previous methods.

### 2.4.1 Simulation Parameters

The transceiver architecture provided in Figure 3 is followed explicitly to perform the waveform simulation. The simulator is implemented using MATLAB baseband equivalent model of

TABLE II  
SINGLE-ANTENNA FULL DUPLEX TRANSCEIVER COMPONENT PARAMETERS

Parameter	Value	Parameter	Value
PA Gain	27 dB	LNA Gain	20 dB
PA IIP3	13 dBm	LNA IIP3	−3 dBm
VGA (Tx) Gain	0:33 dB	BB IIP2	50 dBm
IRR (Tx)	30 dB	IRR (Rx)	30 dB

the components, which includes the impact of all the transceiver impairments. The waveform simulation is based on a 20 MHz OFDM-based system with 64 subcarriers per OFDM symbols as in IEEE802.11 systems. The additional parameters of the waveforms are shown in Table I. The system-level component parameters of the full-duplex transceiver are provided in Table II, which are taken from the datasheet of AD9361 transceiver made by Analog Devices [78]. We perform our simulation based on single-antenna full-duplex system with a circulator providing a stronger leakage signal to the receiver as the direct SI component and several multipath components [45]. Therefore, the SI channel is simulated as a Rician channel with a K-factor of 30 dB and 4 non-Line-of-Sight (nLOS) components, each delayed by one sample [24]. To emulate IEEE802.11 system, we use WLAN packet formatting, where each packet consists of 120 OFDM symbols. Around 8% of the total packet size are considered as training symbols, which are used to estimate and cancel the self-interference. We use 1000 Monte Carlo simulation runs to calculate the average cancellation performance. Here, we consider 15dB circulator isolation with variable RF cancellation values to show its impact on the digital cancellation.

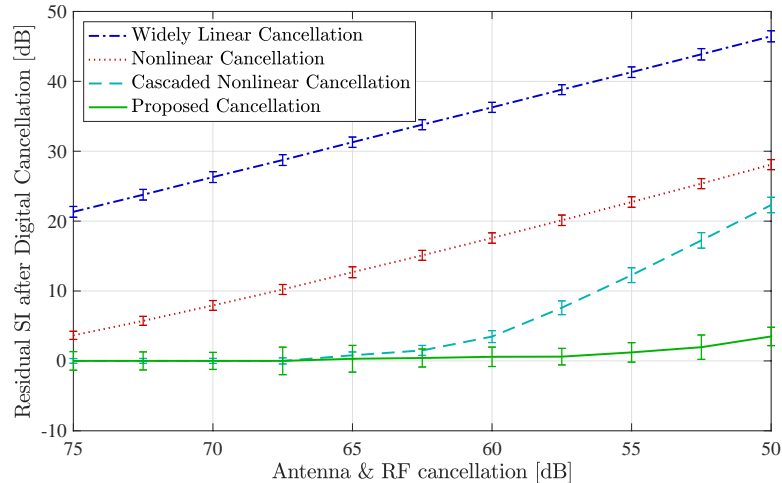


Figure 4. Residual self-interference power after digital cancellation with respect to different RF cancellation value and 25 dBm transmit Power

#### 2.4.2 SI Cancellation Capability and SINR

First, for variable antenna and RF cancellation, we compare the performance of the proposed digital cancellation technique with previous methods. In Figure 4, we represent the residual self-interference signal strength of several digital cancellation methods from the measured noise floor with respect to 50-75 dB antenna and RF cancellation for a transmit power of 25 dBm. We also include the error bars at one standard deviation from the mean of the cancellation value. We observe that a widely linear cancellation [66] scheme has a residual of 20-45 dB. Although considering the nonlinear cancellation [51] along with linear and widely linear methods increases the performance drastically, it has a residual of around 30 dB at an antenna and RF cancellation of 50 dB. For higher antenna and RF suppression, cascaded cancellation [68] performance is

comparable with our proposed method. However, below 65 dB cancellation, it has a sharp growth of the residual, leading almost 22 dB for 50 dB antenna and RF cancellation. In comparison with these methods, our proposed digital cancellation technique provides better performance contributing only around 3 dB residual at a very low RF cancellation. This performance boost is because of the inclusion of receiver chain second and third-order nonlinearities in our proposed method, whereas all the previous methods took only the transmitter PA nonlinearities into account, ignoring the receiver chain nonlinear distortions. However, that assumption provides comparable performance in case of high antenna and RF cancellation or linear receiver operation. As we observed, for practical transceivers such as AD9361, the receiver performance is not linear. Therefore, limited antenna and RF cancellation, typically below 65 dB, results in the higher self-interference signal power at the receiver input, which contributes to a stronger nonlinear effect of the receiver chain components. In this scenario, the proposed digital cancellation strategy outperforms the previous techniques.

In Figure 5, we show the performance of the digital cancellation methods with respect to the transmit power varying from  $-5$  dBm to 25 dBm while considering 60 dB antenna and RF cancellation. Here, signal-to-interference-plus-noise-ratio (SINR) is used as the figure-of-merit of the cancellation strategies. During the calculation of the SINR, the desired signal is naturally present with an SNR of 15 dB, which is the maximum achievable SINR. From Figure 5, we observed that our proposed method outperforms the previous techniques for all the transmit power cases. Nonlinear [51] and widely linear [66] methods sufficiently suppress the SI up to the transmit power of 15 and 10 dBm, respectively. Although the cascaded cancellation [68]

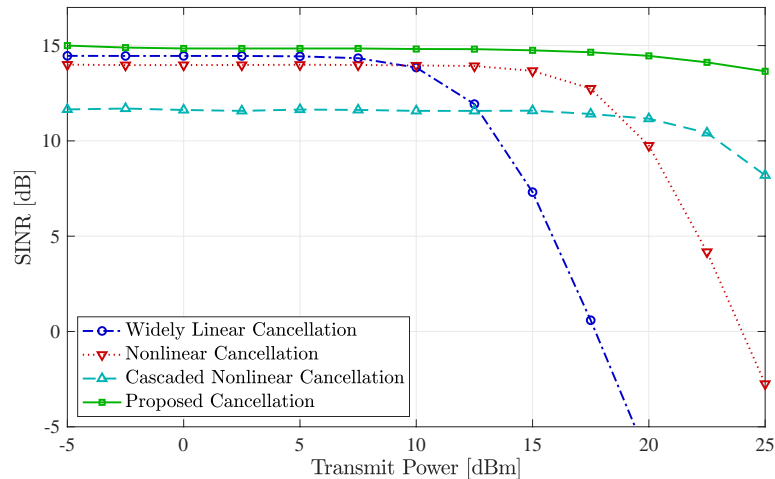


Figure 5. The SINRs for different digital cancellation method with respect to the overall transmit power with antenna and RF cancellation of 60 dB

method performs better than the previous methods for higher transmit power cases, it suffers from an overfitting problem resulting in higher estimation error in low transmit power cases. In our proposed model, we tackle this problem through orthogonalization of the design matrix, which reduces the estimation error. Thus, our proposed digital cancellation approach provides reliable and sufficient suppression of self-interference signal in a practical nonlinear receiver for a varying antenna and RF cancellation as low as 50 dB.

## 2.5 Machine Learning for Self-Interference Cancellation in Full Duplex Systems

In this section, we present a novel digital SI mitigation approach utilizing Machine Learning (ML) techniques, specifically, Deep Neural Networks (DNN). As described in previous sections, a key challenge in SI suppression is dealing with nonlinear SI induced at TX/RX RF compo-

nents. To estimate such nonlinear components, our proposed digital cancellation approach in Section 2.3 along with other the traditional cancellation methods require prior knowledge of the nonlinear model such as polynomial order [68, 69, 79]. In contrast, the DNN-based solutions [80–82], do not require prior knowledge of the nonlinear distortion model. It has been shown in [80] that utilization of DNN can reduce the computational complexity by as much as 36% relative to a non-DNN-based solution [69]. However, the existing DNN-based methods require *on-line* training of the DNN utilizing large amount of training sample to properly estimate time-invariant nonlinear distortion with the time-varying SI propagation channel.

This section we aim to improve the spectral efficiency by minimizing the amount of *on-line* DNN training, since it causes interruption of the data transmission, while successfully suppressing the residual SI in the digital domain.

### 2.5.1 Proposed DNN Architecture of SI Cancellation

A DNN is used for estimating the nonlinear components of the SI, while the linear SI is obtained using a Least Squares (LS) estimation technique. We propose a Transfer Learning based two-stage DNN training strategy that significantly reduces on-line training overhead. From Equation 2.10, we can take the SI signal at the ADC output and conceptually decompose it as  $y_{SI}[n] = y_{lin}[n] + y_{nl}[n]$ , where  $y_{lin}[n]$  represents the linear SI and  $y_{nl}[n]$  the nonlinear SI components. The linear part  $y_{lin}[n]$  is estimated utilizing LS approach, while the nonlinear SI components are estimated utilizing the DNN. The estimated signals are added to reconstruct the residual SI signal  $\hat{y}_{SI}[n] = \hat{y}_{lin}[n] + \hat{y}_{nl}[n]$ .

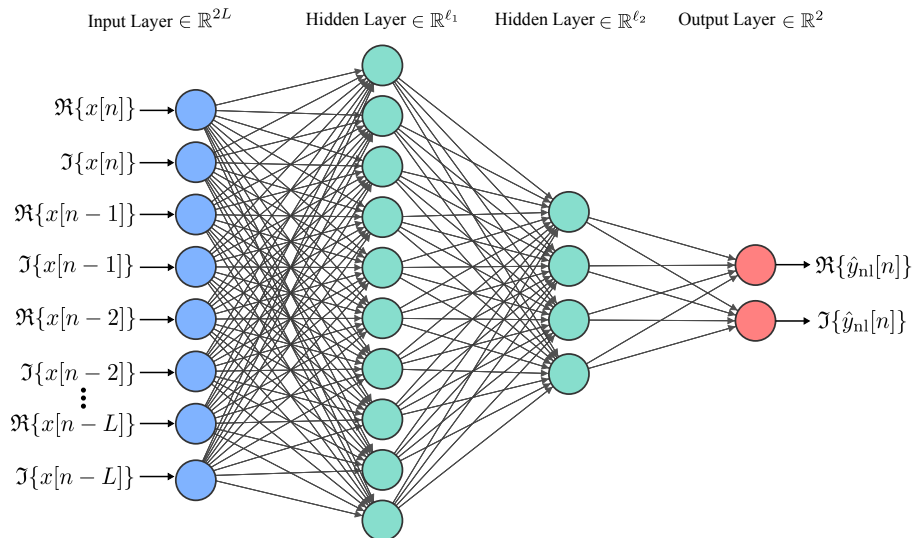


Figure 6. A two-layer Feed-Forward Neural Network.

For the considered DNN architecture, we consider a real valued feed-forward NN (FFNN) with a single input layer, two hidden layers, and an output layer as shown in Figure 6. The DNN has two nodes in the output layer, while the input layer consists of  $2L$  input nodes, which corresponds to the real and imaginary parts of the  $L$  delayed versions of the baseband transmitted signal  $x[n]$ . We denote  $\ell_i$  as the number of nodes in the  $i$ th hidden layer.

To overcome the DNN training limitations, we propose a two-phase training strategy based on the concept of *Transfer Learning*. First, we train our DNN model using training symbols generated at the FD relay node when there is no scheduled transmission between the source and destination nodes. We denote this stage as *pretraining*. During the actual source-destination transmission, we again perform training on the *pretrained* DNN model using a small number

of training symbols. This second stage is called *finetuning*, which is performed to compensate the SI channel and nonlinear characteristic mismatch between *pretraining* and actual transmission time. Using this two-stage approach, the proposed SI canceller can achieve improved SI suppression with a small amount of training symbols and processing time. *Transfer Learning* is widely used in computer vision [83].

### 2.5.2 Performance Evaluation of the Proposed DNN-assisted SI Cancellation

Considering a single-antenna FD system, we implement the proposed DNN-assisted SI cancellation approach. For brevity, we only consider the TX impairments in Equation 2.10, where the memory of the SI channel is  $L = 4$ .

**Training Samples:** We consider an off-line training with 8000 training sets, where each set consists of two input samples,  $\{\Re\{x[n]\}, \Im\{x[n]\}\}$ , and the corresponding output samples,  $\{\Re\{\hat{y}[n]\}, \Im\{\hat{y}[n]\}\}$ .

**Neural Network:** We considered the DNN with two hidden layers with  $\ell_1 = 10$  and  $\ell_2 = 4$  nodes, respectively, as shown in Figure 6. The number of input layer nodes is  $2L = 8$  (based on the SI channel memory,  $L = 4$ ). Each node employ Rectified Linear Unit (ReLU) activation function. We utilize the Adam minimization algorithm for training with Mean Squared Error (MSE) as the objective function. The DNN was implemented using the Keras framework with a TensorFlow backend.

**Pretraining:** The learning rate of  $\lambda = 0.001$ , and a mini-batch size of  $B = 12$ . All remaining parameters have their default values. We generated an off-line data set of 10 distinct

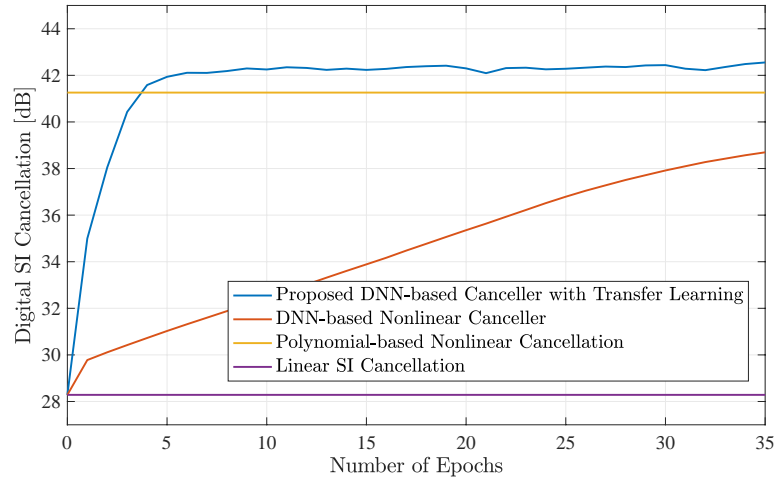


Figure 7. Digital SI cancellation in dB w.r.t the number of on-line training epochs.

training packets. Using each of the training packets, we train the DNN model until the training loss converges.

**Finetuning:** We dedicate a single data packet for *finetuning* the DNN model trained in the *pretrained* stage. For *finetuning*, we use 90% symbols of the packet, while the remaining 10% is used for validation. The optimization algorithm and the parameters are identical to the *pretraining* stage.

In Figure 7, we plot the digital SI cancellation value in dB with respect to the number of on-line training epochs. For comparison, we also provided the linear SI cancellation, polynomial-based SI cancellation from Section 2.3, and DNN-based nonlinear cancellation of [80]. It is shown in the figure that the proposed DNN-based SI cancellation with Transfer learning achieves 43dB of SI suppression at with only 4 on-line training epochs, while the DNN-based nonlinear

cancellation in [80] requires 35 epochs to provide 39dB of SI reduction. They also outperform the nonlinear polynomial and linear SI cancellation approaches, which provides 41dB and 28dB of SI suppression, respectively. Therefore, the transfer learning based canceller is capable of superior SI cancellation with limited number of training symbols and training epochs.

## 2.6 Concluding Remarks

In this chapter, we provided a detailed modeling of the self-interference signal considering transmitter PA nonlinearities, receiver chain second and third-order nonlinearities, DC offset, IQ imbalances, phase noise, and receiver noise figure. To validate the self-interference model, we proposed a digital cancellation approach considering receiver chain second and third-order nonlinearities and implemented a practical waveform simulator. Our comprehensive simulation showed that, in practical receiver, these nonlinearities have significant effect on the self-interference signal for an analog and RF cancellation of 65 dB or below. In this scenario, our proposed digital cancellation technique outperforms the existing cancellation methods by achieving up to 20 dB more self-interference cancellation. We also provided a DNN-based SI cancellation approach with Transfer Learning that is capable of achieving superior digital SI suppression with limited number of training symbols and training epochs.

## CHAPTER 3

### UNIFIED ANALOG AND DIGITAL TRANSCEIVER DESIGN FOR WIDEBAND FULL DUPLEX MIMO SYSTEMS

The exploitation of wideband MIMO systems provides an increased spectral performance due to plurality of TX/RX antennas. Therefore, application of FD technology in conjunction with wideband MIMO operation can meet the stringent throughput and latency requirements of beyond 5G wireless communication systems with limited spectrum resources. In this chapter, we propose a wideband FD MIMO communication system comprising of an FD MIMO node simultaneously communicating with two multi-antenna UL and DL nodes utilizing the same time and frequency resources. To suppress the strong SI signal due to simultaneous transmission and reception in FD MIMO systems, we provide a joint design of analog and digital cancellation as well as transmit and receive beamforming capitalizing on baseband OFDM signal modeling. Considering practical transmitter impairments, we present a multi-tap wideband analog canceller architecture whose number of taps does not scale with the number of transceiver antennas and multipath SI components. We also propose a novel adaptive digital cancellation based on truncated singular value decomposition that reduces the residual SI signal estimation param-

---

The content of this chapter is based on our published articles in [84] and [85]. Copyright © 2019, 2022 IEEE.

eters. To maximize the FD sum rate, a joint optimization framework is presented for A/D cancellation and digital beamforming.

### 3.1 Introduction

Future wireless communication systems need to accommodate the explosive growth in data traffic demand through efficient utilization of limited frequency spectrum. Recent advances in FD communication technology demonstrate the potential of a substantial spectral efficiency improvement over the conventional frequency- and time-division duplexing systems through simultaneous UL and DL communication in the same frequency and time resources [3, 5, 6, 49, 54, 85]. The exploitation of wideband MIMO systems provides further spectral performance boost due to enhanced spatial Degrees of Freedom (DoF) offered by the plurality of TX and RX antennas and larger bandwidths [51, 57–59, 68, 86, 87]. In addition, FD MIMO radios have recently been considered for certain physical-layer-based latency improvement through simultaneous communication of data and control signals [88–90]. Thus, enabling FD in conjunction with wideband MIMO operation can meet the stringent throughput and latency requirements of beyond 5G wireless communication systems with limited spectrum resources [6].

The simultaneous transmission and reception in wideband FD systems induce strong in-band SI signals at the FD receivers due to the inevitable limited isolation between the TX and RX blocks [3]. To suppress the strong SI signal, first, analog cancellation is employed at the input of the RX blocks at the FD node to ensure that none of the reception RF components (i.e., LNAs, IQ mixers) goes into saturation due to high SI power, while ensuring that the dynamic range of the ADCs is large enough to capture the residual SI and the naturally weak desired

signal with sufficient precision [54]. Compared to a narrowband FD SISO system, where a single direct SI coupling path exists between TX and RX, the wideband FD MIMO analog cancellation design is much more challenging. This happens because each RX chain suffers from the direct SI signals introduced by all the TX antennas as well as their multipath SI components created by environmental reflections [44, 50, 53–57, 60–64]. For an  $N_{\text{TX}} \times N_{\text{RX}}$  FD MIMO transceiver, the narrowband analog canceller requires  $N_{\text{TX}}N_{\text{RX}}$  taps to suppress the direct SI coupling paths, where each cancellation tap includes time delays, tunable bandpass filters, phase shifters, and attenuators. Considering a wideband communication with  $L$  multipath SI components being strong enough to run the RX RF chains into saturation, the same FD MIMO system would require an appropriate wideband analog canceller with  $N_{\text{TX}}N_{\text{RX}}L$  taps; such analog cancellers are hereinafter referred to as *full-tap* cancellers.

After the analog cancellation, digital domain SI mitigation techniques are applied at the RX baseband to suppress the residual SI signal below the noise floor, which is still large enough to overwhelm the weak desired signal [3, 5]. Digital cancellation is accomplished by reconstructing and reciprocally combining the residual SI signal at the FD RX through extensive SI channel modeling and exploiting the fact that each FD node has knowledge of its ideal transmit signal in the digital domain [51, 58]. Since the residual SI signal is impacted by TX hardware impairments, an appropriate SI channel model must include the SI coupling paths and the nonlinear distortions induced by the transceiver chain’s practical RF components, specifically the image effect due to the gain and phase imbalance of the IQ mixer and PA nonlinearities. For single-antenna FD systems, baseband modeling of these nonlinear distortions has been performed to provide

appropriate digital cancellation [51, 65–67]. Akin to the analog canceller, the wideband FD MIMO operation increases the computational complexity of the digital cancellation since the number of linear and nonlinear components to be estimated increases with the number of TX/RX chains and SI channel paths. Moreover, signal modeling in wideband FD MIMO systems requires multi-carrier designs (i.e. OFDM), as the channel becomes frequency selective due to larger bandwidth.

### 3.1.1 Related works on FD MIMO SI Cancellation

For narrowband or frequency-flat FD MIMO systems, full-tap analog cancellers connecting all TX outputs to RX inputs are usually employed, where the number of taps increases with the number of TX/RX RF chains [58, 87]. To reduce this hardware complexity, analog SI canceller designs exploiting AUXiliary (AUX) TX structures and/or joint design of TX/RX beamformers were studied in [60, 61], where the analog cancellation signals were injected into each of the RX inputs using separate TX RF chains. Although these techniques reduce the analog canceller hardware complexity, they are unable to suppress the nonlinear SI components due to the non-ideal RF front-end hardware rendering the RX chains into saturation [5]. In our previous work [85], we presented a unified low complexity A/D cancellation for narrowband FD MIMO systems. For wideband FD MIMO systems in [56, 57], full-tap analog cancellers with adaptive filters were utilized to provide sufficient analog SI cancellation. In [62], a full-tap wideband FD MIMO RF canceller was presented with a tunable time delay circuit, which employed reflected type phase shifters to emulate the true time delays of the SI channel. Recently, a full-tap beam-based RF cancellation approach was introduced in [63], which employed analog Least

Mean-Squared (LMS) loops as the adaptive filters for SI mitigation in FD massive MIMO systems. Those analog LMS loops include time delay generators, down-converters, LPFs, and up-converters. An integrated LMS adaptive wideband FD MIMO RF canceller was proposed in [64], where the time delay of the cancellation was generated using an  $N$ -path filter. However, the hardware complexity of all the above full-tap RF cancellers scales with the number of TX and RX RF chains as well as the number of SI multipath components, rendering the practical implementation of the analog SI cancellation unit a core design bottleneck.

Alleviating the need for analog SI cancellation, spatial suppression techniques were presented in [58, 86] for narrowband FD MIMO systems, where the SI suppression was solely handled by the digital TX/RX beamformers. However, those spatial suppression techniques were unable to cancel the SI in high TX power and often resulted in reductions of the data rates for both the UL and DL signals of interest. This stemmed from the fact that some of the available spatial DoFs were devoted to mitigating SI [59]. To avoid such issues, digital cancellation techniques exploiting SI signal modeling were utilized in practice to supplement the analog canceller in suppressing the SI signal. To achieve sufficient SI suppression, existing digital cancellation approaches capitalize on models for the PA impairments [57] and IQ mixer image effect [66], or rely on cascaded SI designs taking into account both nonidealities [68]. However, the number of estimation parameters of those models grows with the number of TX/RX RF chains and SI channel components. To reduce the number of parameters for the FD MIMO system, a digital canceller based on Principle Component Analysis (PCA) was provided in [69]. Furthermore, in [91–93], the authors considered FD MIMO OFDM signal modeling to design rate maximizing

TX/RX beamformers. However, these techniques assumed full-tap RF cancellers to achieve certain SI suppression levels.

### 3.1.2 Contributions

In this chapter, we present a joint A/D SI cancellation with TX/RX beamforming approach for wideband FD MIMO systems considering the effect of non-linear hardware distortions and multipath SI components. The main contributions of this chapter are summarized as follows:

- We propose a novel joint wideband analog SI cancellation and TX/RX beamforming approach for multi-user FD MIMO systems in the presence of TX RF chain impairments, where the multipath SI components are suppressed using reduced analog cancellations taps compared to existing FD MIMO solutions.
- A comprehensive OFDM signal modeling of the proposed FD MIMO system is derived, including baseband equivalent models of the TX RF chain impairments, corresponding wideband channels, and A/D SI cancellers.
- We present a novel adaptive digital canceller based on the Truncated Singular Value Decomposition (TSVD) that reduces the computational complexity of conventional digital SI cancellation while successfully suppressing the residual SI signal after analog cancellation below the RX noise floor.
- A joint optimization framework for A/D cancellation and TX/RX beamforming is presented to maximize the achievable sum-rate performance of the considered three-node wideband FD MIMO OFDM system.

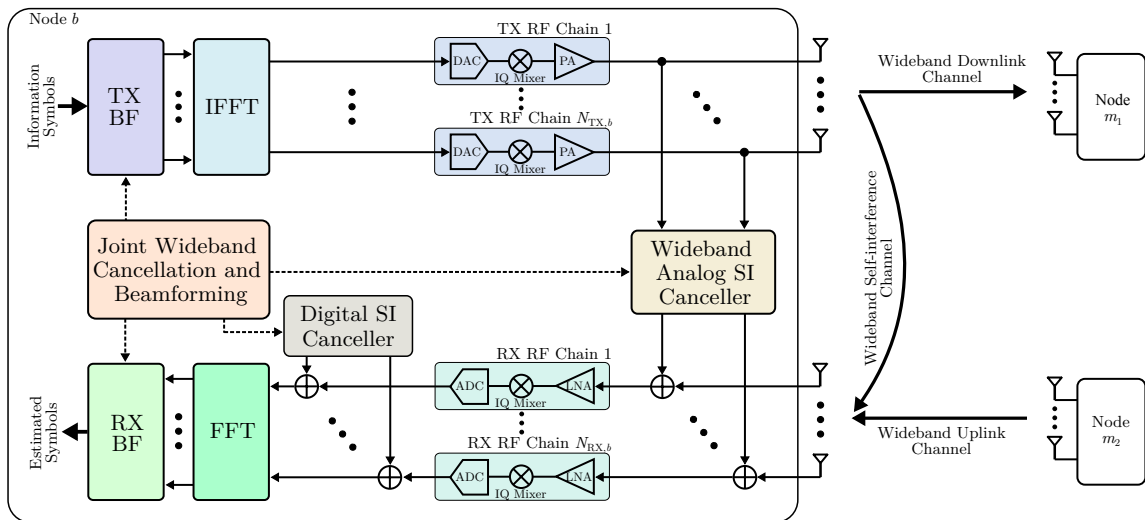


Figure 8. The considered three-node communication system and the proposed wideband FD MIMO architecture. The FD MIMO node  $b$  incorporates processing blocks for analog SI cancellation and digital TX/RX beamforming, as well as for a digital cancellation block for treating the residual SI at the output of the TX RF chains. All these blocks are jointly optimized, realizing the desired wideband FD operation in a hardware-efficient way. The HD multi-antenna nodes  $m_1$  and  $m_2$  communicate with node  $b$  in the downlink and uplink directions, respectively.

- Finally, we perform extensive waveform simulations to illustrate the proposed A/D SI cancellation performance and provide comparisons with the relevant state-of-the-art methods. It is demonstrated that our proposed wideband canceller in conjunction with TX/RX beamforming exhibits superior SI mitigation capability with reduced complexity (less than 50% analog taps) compared to the existing full-tap cancellers in the presence of TX hardware impairments.

## 3.2 System and Signal Models

We consider the three-node FD wireless communication system of Figure 8 comprising of an FD MIMO Base Station (BS) node  $b$  communicating concurrently with two HD multi-antenna nodes: node  $m_1$  in the downlink and node  $m_2$  in the uplink direction. The FD MIMO node  $b$  is assumed to be equipped with  $N_{\text{TX},b}$  TX and  $N_{\text{RX},b}$  RX antenna elements. Each TX antenna is attached to a dedicated RF chain that consists of a DAC, IQ mixer, and PA; similarly holds for the RX antennas and their attached RF chains, each containing LNA, IQ mixer, and ADC. The HD multi-antenna nodes  $m_1$  and  $m_2$  are assumed to have  $N_{\text{RX},m_1}$  and  $N_{\text{TX},m_2}$  antennas, respectively, with each of their antennas connected to a dedicated RF chain. All three nodes are considered capable of performing digital beamforming and OFDM operations with  $N_c$  subcarriers.

### 3.2.1 Downlink TX and RX Signal Modeling

During DL transmission, the FD MIMO node  $b$  sends  $d_b \leq \min\{N_{\text{TX},b}, N_{\text{RX},m_1}\}$  data streams multiplexed at each subcarrier  $n = \{0, 1, \dots, N_c - 1\}$  to the HD node  $m_1$ . The unit power symbol vector of  $n$ th subcarrier is denoted as  $\mathbf{s}_{b,n} \in \mathbb{C}^{d_b \times 1}$ , which, in practice, is selected from a discrete modulation set. The symbol vector  $\mathbf{s}_{b,n}$  is linearly precoded by the TX beamformer  $\mathbf{V}_{b,n} \in \mathbb{C}^{N_{\text{TX},b} \times d_b}$ . Without loss of generality, we assume that  $\mathbf{V}_{b,n}$  have unit norm columns. The precoded symbols are converted to time-domain samples using the Inverse Fast Fourier Transform (IFFT) operation. To prevent Inter-Symbol Interference (ISI), a cyclic prefix is appended in front of each IFFT block; in the subsequent analysis, we ignore the cyclic prefix for

simplicity. The output of the node  $b$  TX baseband block after the IFFT operation at a discrete time instant  $k$  is represented as

$$\mathbf{x}_b[k] \triangleq \frac{1}{\sqrt{N_c}} \sum_{n=0}^{N_c-1} \mathbf{v}_{b,n} \mathbf{s}_{b,n} e^{j\frac{2\pi nk}{N_c}}. \quad (3.1)$$

**Baseband Modeling of TX RF Chain Impairments:** As shown in Figure 8, the node  $b$  baseband samples in  $\mathbf{x}_b[k]$  are fed to the TX RF chains for upconversion and amplification. We introduce a baseband equivalent model for each of these RF chains incorporating IQ imbalances and PA nonlinearities [66], assuming that the RF chains are identical. Upon entering the TX RF chain of node  $b$ , each baseband sample goes through the IQ mixer for upconversion to the carrier frequency. In practical IQ mixers, a mirror image of the original signal with certain image attenuation is induced by the IQ phase and gain imbalances. Denoting the input at the  $i$ th ( $i = 1, 2, \dots, N_{\text{TX},b}$ ) TX RF chain of node  $b$  at time instant  $k$  as  $[\mathbf{x}_b[k]]_i$ , the IQ mixer output can be written as [66, eq. (8)]

$$[\mathbf{x}_b[k]]_i^{\text{IQ}} \triangleq \mu_1 [\mathbf{x}_b[k]]_i + \mu_2 [\mathbf{x}_b[k]]_i^*, \quad (3.2)$$

where  $\mu_1 \triangleq (1 + ge^{-j\theta})/2$  and  $\mu_2 \triangleq (1 - ge^{j\theta})/2$  with  $g$  and  $\theta$  are representing the gain and phase imbalances, respectively. It is noted that the Image Rejection Ratio, defined as  $\text{IRR} \triangleq |\mu_1/\mu_2|^2$ , represents the strength of the IQ induced conjugate term [94].

Before transmission, the upconverted signal is fed into the PA for amplification while satisfying the TX power constraint. Note that practical PAs exhibit varying degrees of nonlinearity.

However, we consider a quasi memoryless PA model of third-order nonlinearity, as it is the most dominant distortion in practice, and all the even-power harmonics lie out of the band and will be cut off by the RF low pass filter at the RXs [66, 75, 95]. For this PA model, the baseband equivalent of each  $i$ th PA output at time instant  $k$  is given using Equation 3.2 as

$$\begin{aligned}
[\mathbf{x}_b[k]]_i^{\text{PA}} &\triangleq \sum_{p=1,3} \nu_p \left| [\mathbf{x}_b[k]]_i^{\text{IQ}} \right|^{p-1} [\mathbf{x}_b[k]]_i^{\text{IQ}} \\
&= g_{1,i} [\mathbf{x}_b[k]]_i + g_{2,i} [\mathbf{x}_b[k]]_i^* + g_{3,i} [\mathbf{x}_b[k]]_i^3 \\
&\quad + g_{4,i} [\mathbf{x}_b[k]]_i^2 [\mathbf{x}_b[k]]_i^* + g_{5,i} [\mathbf{x}_b[k]]_i ([\mathbf{x}_b[k]]_i^*)^2 \\
&\quad + g_{6,i} ([\mathbf{x}_b[k]]_i^*)^3,
\end{aligned} \tag{3.3}$$

where  $p$  represents the nonlinearity order<sup>1</sup> and the six gain components  $g_{\ell,i}$  with  $\ell = 1, 2, \dots, 6$  are derived as

$$\begin{aligned}
g_{1,i} &\triangleq \mu_1 \nu_1, \quad g_{2,i} \triangleq \mu_2 \nu_1, \quad g_{3,i} \triangleq \mu_1^2 \mu_2^* \nu_3 \\
g_{4,i} &\triangleq (2|\mu_1|^2 \mu_1 + |\mu_2|^2 \mu_1) \nu_3, \\
g_{5,i} &\triangleq (2|\mu_1|^2 \mu_2 + |\mu_2|^2 \mu_2) \nu_3, \quad g_{6,i} \triangleq \mu_1^* \mu_2^2 \nu_3,
\end{aligned} \tag{3.4}$$

---

<sup>1</sup>Note that Equation 3.3 is general enough to model various degrees of nonlinearities in the TX RF chains; this can be accomplished by setting  $p$  to the desired nonlinearity order.

where  $\nu_1$  denotes the PA linear gain and  $\nu_3 \triangleq \nu_1/(\text{IIP3})^2$  is the gain of the third-order nonlinear distortions with IIP3 representing the third-order Input-referred Intercept Point of the PA [75].

Based on Equation 3.3 and after some algebraic manipulations, the baseband representation of the impaired transmitted signal from the  $N_{\text{TX},b}$  TX antennas of the FD MIMO node  $b$  in the DL direction can be expressed as

$$\tilde{\mathbf{x}}_b[k] \triangleq \mathbf{G}_{1,b}\mathbf{x}_b[k] + \mathbf{z}_b[k] = \mathbf{G}_b\psi_b[k], \quad (3.5)$$

where  $\mathbf{G}_{1,b} \triangleq \text{diag}\{g_{1,1}, g_{1,2}, \dots, g_{1,N_{\text{TX},b}}\}$  is the power allocation matrix of the linear components of the TX signal and  $\mathbf{z}_b[k]$  denotes its nonlinear part, which is given by

$$\begin{aligned} \mathbf{z}_b[k] \triangleq & \mathbf{G}_{2,b}\mathbf{x}_b^*[k] + \mathbf{G}_{3,b}(\mathbf{x}_b[k])^{\circ 3} + \mathbf{G}_{4,b}(\mathbf{x}_b[k])^{\circ 2} \odot \mathbf{x}_b^*[k] \\ & + \mathbf{G}_{5,b}\mathbf{x}_b[k] \odot (\mathbf{x}_b^*[k])^{\circ 2} + \mathbf{G}_{6,b}(\mathbf{x}_b^*[k])^{\circ 3}. \end{aligned} \quad (3.6)$$

In the latter expression,  $\mathbf{G}_{\ell,b} \triangleq \text{diag}\{g_{\ell,1}, g_{\ell,2}, \dots, g_{\ell,N_{\text{TX},b}}\}$  for  $\ell = 2, 3, \dots, 6$  representing the coefficient matrices for the nonlinear components of  $\tilde{\mathbf{x}}_b[k]$  is defined in the similar way to  $\mathbf{G}_{1,b}$ .

In Equation 3.5, we also introduce the notation  $\mathbf{G}_b \in \mathbb{C}^{N_{\text{TX},b} \times 6N_{\text{TX},b}}$  for the augmented power

allocation matrix, and the vertically arranged signal vector  $\boldsymbol{\psi}_b[k] \in \mathbb{C}^{6N_{\text{TX},b} \times 1}$  including the image and nonlinear components. The matrices are given by

$$\mathbf{G}_b \triangleq [\mathbf{G}_{1,b} \ \mathbf{G}_{2,b} \ \mathbf{G}_{3,b} \ \mathbf{G}_{4,b} \ \mathbf{G}_{5,b} \ \mathbf{G}_{6,b}], \quad (3.7)$$

$$\boldsymbol{\psi}_b[k] \triangleq \text{col}\{\mathbf{x}_b[k], \mathbf{x}_b^*[k], \mathbf{x}_b[k]^{\circ 3}, \mathbf{x}_b[k]^{\circ 2} \odot \mathbf{x}_b^*[k], \mathbf{x}_b[k] \odot (\mathbf{x}_b^*[k])^{\circ 2}, (\mathbf{x}_b^*[k])^{\circ 3}\}.$$

We finally make the practical assumption that the DL signal transmission is power limited to  $P_b$  such that  $\mathbb{E}\{\|\mathbf{G}_{1,b}\mathbf{x}_b[k] + \mathbf{z}_b[k]\|^2\} \leq P_b$ .

**DL Received Signal Model:** The transmitted DL signal  $\tilde{\mathbf{x}}_b[k]$  is received at the HD RX node  $m_1$  after passing through the wideband DL channel denoted by  $\mathbf{H}_{\text{DL}}[\ell] \in \mathbb{C}^{N_{\text{RX},m_1} \times N_{\text{TX},b}}$ ,  $\forall \ell = \{0, 1, \dots, L_{\text{DL}} - 1\}$ , where  $L_{\text{DL}}$  represents the number of DL channel paths. The received baseband signal  $\mathbf{y}_{m_1}[k] \in \mathbb{C}^{N_{\text{RX},m_1} \times 1}$  of node  $m_1$  at the discrete time instant  $k$  is mathematically expressed as

$$\mathbf{y}_{m_1}[k] \triangleq \sum_{\ell=0}^{L_{\text{DL}}-1} \mathbf{H}_{\text{DL}}[\ell] \tilde{\mathbf{x}}_b[k - \ell] + \mathbf{w}_{m_1}[k], \quad (3.8)$$

where  $\mathbf{w}_{m_1}[k]$  represents the Additive White Gaussian Noise (AWGN) vector at node  $m_1$  with covariance matrix  $\sigma_{m_1}^2 \mathbf{I}_{N_{\text{RX},m_1}}$ . It is to be noted that we assume no inter-node interference between nodes  $m_1$  and  $m_2$  due to appropriate node scheduling [96, 97].

The baseband received signal  $\mathbf{y}_{m_1}[k]$  is transformed to frequency domain using the Fast Fourier Transformation (FFT) operation, which is followed by RX beamforming for each sub-carrier to obtain the estimated symbol vectors denoted by  $\hat{\mathcal{S}}_{b,n}$ ,  $\forall n = \{0, 1, \dots, N_c - 1\}$ . Denoting

$n$ th subcarrier RX beamformer as  $\mathbf{u}_{m_1,n} \in \mathbb{C}^{d_b \times N_{\text{RX},m_1}}$ , the linearly processed estimated symbol vector is written as

$$\begin{aligned}
\widehat{\mathbf{s}}_{b,n} &\triangleq \mathbf{u}_{m_1,n} \left( \frac{1}{\sqrt{N_c}} \sum_{k=0}^{N_c-1} \mathbf{y}_{m_1}[k] e^{-\frac{j2\pi kn}{N_c}} \right) \\
&= \mathbf{u}_{m_1,n} \left( \frac{1}{\sqrt{N_c}} \sum_{k=0}^{N_c-1} \left( \sum_{\ell=0}^{L_{\text{DL}}-1} \mathbf{H}_{\text{DL}}[\ell] \tilde{\mathbf{x}}_b[k-\ell] + \mathbf{w}_{m_1}[k] \right) e^{-\frac{j2\pi kn}{N_c}} \right) \\
&= \mathbf{u}_{m_1,n} \left( \mathcal{H}_{\text{DL},n} \left( \mathbf{G}_{1,b} \mathbf{V}_{b,n} \mathbf{s}_{b,n} + \mathbf{z}_{b,n} \right) + \mathbf{w}_{m_1,n} \right), \tag{3.9}
\end{aligned}$$

where  $\mathcal{H}_{\text{DL},n} \triangleq \sum_{l=0}^{L_{\text{DL}}-1} \mathbf{H}_{\text{DL}}[l] e^{-\frac{j2\pi ln}{N_c}}$  is defined as  $n$ th subcarrier frequency domain representation of the wideband DL channel. Similarly,  $\mathbf{z}_{b,n}$  and  $\mathbf{w}_{m_1,n}$  represent the frequency transform of the TX nonlinear components vector  $\mathbf{z}_b[k]$  and the AWGN vector at node  $m_1$ , respectively.

The detailed derivation of Equation 3.9 is provided in Appendix B.

### 3.2.2 Uplink TX and RX Signal Modeling

Now, we model the UL signal transmitting from HD multi-antenna node  $m_2$  to the FD MIMO node  $b$ . Similar to the node  $b$  TX, the  $n$ th subcarrier symbol vector  $\mathbf{s}_{m_2,n} \in \mathbb{C}^{d_{m_2} \times 1}$  with  $d_{m_2} \leq \min(N_{\text{TX},m_2}, N_{\text{RX},b})$  is precoded by the unit norm TX beamformer  $\mathbf{V}_{m_2,n} \in \mathbb{C}^{N_{\text{TX},m_2} \times d_{m_2}}$ . The precoded symbol vectors are transformed to time domain samples  $\mathbf{x}_{m_2}[k] \in \mathbb{C}^{N_{\text{TX},m_2} \times 1}$  using FFT operation identical to Equation 3.1. The time domain samples are upconverted and amplified by the TX RF chains of node  $m_2$  following the similar operation of node  $b$  TX. Therefore, the TX output  $\tilde{\mathbf{x}}_{m_2}[k] \in \mathbb{C}^{N_{\text{TX},m_2} \times 1}$  at node  $m_2$  is expressed as

$$\tilde{\mathbf{x}}_{m_2}[k] \triangleq \mathbf{G}_{1,m_2} \mathbf{x}_{m_2}[k] + \mathbf{z}_{m_2}[k], \tag{3.10}$$

where  $\mathbf{G}_{1,m_2}$  is the power allocation matrix of the linear components of the TX signal and  $\mathbf{z}_{m_2}[k]$  denotes its nonlinear part, defined similarly as Equation 3.6. The UL signal transmission is power limited to  $P_{m_2}$  such that  $\mathbb{E}\{\|\mathbf{G}_{1,m_2}\mathbf{x}_{m_2}[k] + \mathbf{z}_{m_2}[k]\|^2\} \leq P_{m_2}$ .

**UL Received Signal Model:** The transmitted UL signal  $\tilde{\mathbf{x}}_{m_2}[k]$  is received at node  $b$  after passing through the wideband UL channel denoted by  $\mathbf{H}_{\text{UL}}[\ell] \in \mathbb{C}^{N_{\text{RX},b} \times N_{\text{TX},m_1}}$ ,  $\forall \ell = \{0, 1, \dots, L_{\text{UL}} - 1\}$ , where  $L_{\text{UL}}$  represents the number of UL channel paths. Due to FD operation, the transmitted signal  $\mathbf{x}_b[k]$  from node  $b$  TX is also received at the node  $b$  RX input after passing through the wideband SI channel denoted by  $\mathbf{H}_{\text{SI}}[\ell] \in \mathbb{C}^{N_{\text{RX},b} \times N_{\text{TX},b}}$ ,  $\forall \ell = \{0, 1, \dots, L_{\text{SI}} - 1\}$ , where  $L_{\text{SI}}$  is the number of SI channel delay taps. In addition to the UL and SI signals, the analog cancellation signal stemming from the output of the wideband analog SI canceller is fed into the RX inputs of node  $b$ , as shown in Figure 8. Therefore, similar to Equation 3.8, the received signal  $\mathbf{y}_b[k] \in \mathbb{C}^{N_{\text{RX},b} \times 1}$  is expressed as

$$\begin{aligned} \mathbf{y}_b[k] \triangleq & \sum_{\ell=0}^{L_{\text{UL}}-1} \mathbf{H}_{\text{UL}}[\ell] \tilde{\mathbf{x}}_{m_2}[k - \ell] + \sum_{\ell'=0}^{L_{\text{SI}}-1} \mathbf{H}_{\text{SI}}[\ell'] \tilde{\mathbf{x}}_b[k - \ell'] \\ & + \sum_{\ell''=0}^{L_{\text{C}}-1} \mathbf{C}_b[\ell''] \tilde{\mathbf{x}}_b[k - \ell''] + \mathbf{w}_b[k], \end{aligned} \quad (3.11)$$

where  $\mathbf{w}_b[k]$  is the AWGN vector at this node with covariance matrix  $\sigma_b^2 \mathbf{I}_{N_{\text{RX},b}}$ . In this expression,  $\mathbf{C}_b[\ell''] \in \mathbb{C}^{N_{\text{RX},b} \times N_{\text{TX},b}}$ ,  $\forall \ell'' = \{0, 1, \dots, L_{\text{C}} - 1\}$  represents the coefficients of the wideband analog SI canceller, which is modeled as an  $L_{\text{C}}$ th order Finite Impulse Response (FIR) filter and will be described in the following Sec. 3.3. Recall that the wideband analog canceller utilizes the TX RF chain output  $\tilde{\mathbf{x}}_b[k]$ , which contains the transmitter nonlinear impairments  $\mathbf{z}_b[k]$ , as

defined in Equation 3.6. Therefore, the analog canceller is capable of suppressing both linear and nonlinear SI components.

After the downconversion of the received signals at node  $b$ , the RF chain outputs are added with the digital SI cancellation signal. The resulting signals are then transformed to frequency domain using the FFT operation, as shown in Figure 8. Assuming that the digital cancellation signal at the time instant  $k$  is given by  $\mathbf{d}_b[k] \in \mathbb{C}^{N_{\text{RX},b} \times 1}$  and using Equation 3.1, Equation 3.5, as well as Equation 3.11, the frequency-domain received signal vector  $\mathbf{r}_{b,n} \in \mathbb{C}^{N_{\text{RX},b} \times 1}$  at the  $n$ th subcarrier of the FFT output can be expressed as

$$\begin{aligned}
\mathbf{r}_{b,n} &\triangleq \frac{1}{\sqrt{N_c}} \sum_{k=0}^{N_c-1} (\mathbf{y}_b[k] + \mathbf{d}_b[k]) e^{-\frac{j2\pi kn}{N_c}} \\
&= \frac{1}{\sqrt{N_c}} \sum_{\ell=0}^{L_{\text{UL}}-1} \mathbf{H}_{\text{UL}}[\ell] \sum_{k=0}^{N_c-1} \left( \mathbf{G}_{1,m_2} \left( \frac{1}{\sqrt{N_c}} \sum_{p=0}^{N_c-1} \mathbf{v}_{m_2,p} \mathbf{s}_{m_2,p} e^{\frac{j2\pi p(k-\ell)}{N_c}} \right) + \mathbf{z}_{m_2}[k-\ell] \right) e^{-\frac{j2\pi kn}{N_c}} \\
&\quad + \frac{1}{\sqrt{N_c}} \left( \sum_{\ell=0}^{L_{\text{SI}}-1} \mathbf{H}_{\text{SI}}[\ell] + \sum_{\ell=0}^{L_{\text{C}}-1} \mathbf{C}_b[\ell] \right) \left( \sum_{k=0}^{N_c-1} \mathbf{G}_{1,b} \left( \frac{1}{\sqrt{N_c}} \sum_{p=0}^{N_c-1} \mathbf{v}_{b,p} \mathbf{s}_{b,p} e^{\frac{j2\pi p(k-\ell)}{N_c}} \right) \right. \\
&\quad \left. + \sum_{k=0}^{N_c-1} \mathbf{z}_b[k-\ell] \right) e^{-\frac{j2\pi kn}{N_c}} + \frac{1}{\sqrt{N_c}} \sum_{k=0}^{N_c-1} \mathbf{d}_b[k] e^{-\frac{j2\pi kn}{N_c}} + \frac{1}{\sqrt{N_c}} \sum_{k=0}^{N_c-1} \mathbf{w}_b[k] e^{-\frac{j2\pi kn}{N_c}}, \quad (3.12) \\
&= \mathcal{H}_{\text{UL},n} (\mathbf{G}_{1,m_2} \mathbf{v}_{m_2,n} \mathbf{s}_{m_2,n} + \mathbf{z}_{m_2,n}) + (\mathcal{H}_{\text{SI},n} + \mathbf{C}_{b,n}) (\mathbf{G}_{1,b} \mathbf{v}_{b,n} \mathbf{s}_{b,n} + \mathbf{z}_{b,n}) + \mathbf{d}_{b,n} + \mathbf{w}_{b,n},
\end{aligned}$$

where

$$\begin{aligned}
\mathcal{H}_{\text{UL},n} &\triangleq \sum_{l=0}^{L_{\text{UL}}-1} \mathbf{H}_{\text{UL}}[l] e^{-\frac{j2\pi ln}{N_c}}, \quad \mathcal{H}_{\text{SI},n} \triangleq \sum_{l=0}^{L_{\text{SI}}-1} \mathbf{H}_{\text{SI}}[l] e^{-\frac{j2\pi ln}{N_c}}, \\
\mathbf{C}_{b,n} &\triangleq \sum_{l=0}^{L_{\text{C}}-1} \mathbf{C}_b[l] e^{-\frac{j2\pi ln}{N_c}}, \quad (3.13)
\end{aligned}$$

denote the frequency domain representations of the UL, SI channel, and the wideband analog SI canceller, respectively. Similarly,  $\mathbf{z}_{b,n}$ ,  $\mathbf{z}_{m_2,n}$ ,  $\mathbf{d}_{b,n}$ , and  $\mathbf{w}_{b,n}$  are defined as the  $n$ th subcarrier frequency transform of the TX nonlinear components vector  $\mathbf{z}_b[k]$  and  $\mathbf{z}_{m_2}[k]$ , digital cancellation signal vector  $\mathbf{d}_b[k]$ , and the AWGN vector  $\mathbf{w}_b[k]$ , respectively.

At the FFT output, the  $n$ th subcarrier symbol vector is linearly processed by the RX combiner  $\mathbf{U}_{b,n} \in \mathbb{C}^{d_{m_2} \times N_{\text{RX},b}}$  to obtain the estimated symbol vector  $\hat{\mathbf{s}}_{m_2,n} \in \mathbb{C}^{d_{m_2} \times 1}$ , which is derived as

$$\begin{aligned} \hat{\mathbf{s}}_{m_2,n} \triangleq & \mathbf{U}_{b,n} (\mathcal{H}_{\text{UL},n} (\mathbf{G}_{1,m_2} \mathcal{V}_{m_2,n} \mathbf{s}_{m_2,n} + \mathbf{z}_{m_2,n}) \\ & + (\mathcal{H}_{\text{SI},n} + \mathbf{C}_{b,n}) (\mathbf{G}_{1,b} \mathcal{V}_{b,n} \mathbf{s}_{b,n} + \mathbf{z}_{b,n}) + \mathbf{d}_{b,n} + \mathbf{w}_{b,n}). \end{aligned} \quad (3.14)$$

### 3.3 Join Digital TX/RX Beamforming and Wideband Analog Cancellation

In this section, we present the joint design of digital TX/RX beamforming with wideband analog SI cancellation. We first describe the proposed analog SI canceller for wideband FD MIMO OFDM radios and then present the mathematical formulation for the co-design of the analog cancellation matrix with the digital TX/RX beamformers.

#### 3.3.1 Wideband FD MIMO Analog SI Canceller

Upon signal reception at the FD MIMO node  $b$ , analog SI cancellation is applied to the signals received at the RX antennas before entering the RF chains, as shown in Figure 8. As previously described in the considered signal model, the wideband analog SI canceller intended for suppressing the multipath SI channel  $\mathbf{H}_{\text{SI}}[\ell]$  with  $\ell = \{0, 1, \dots, L_{\text{SI}} - 1\}$  is modeled as an

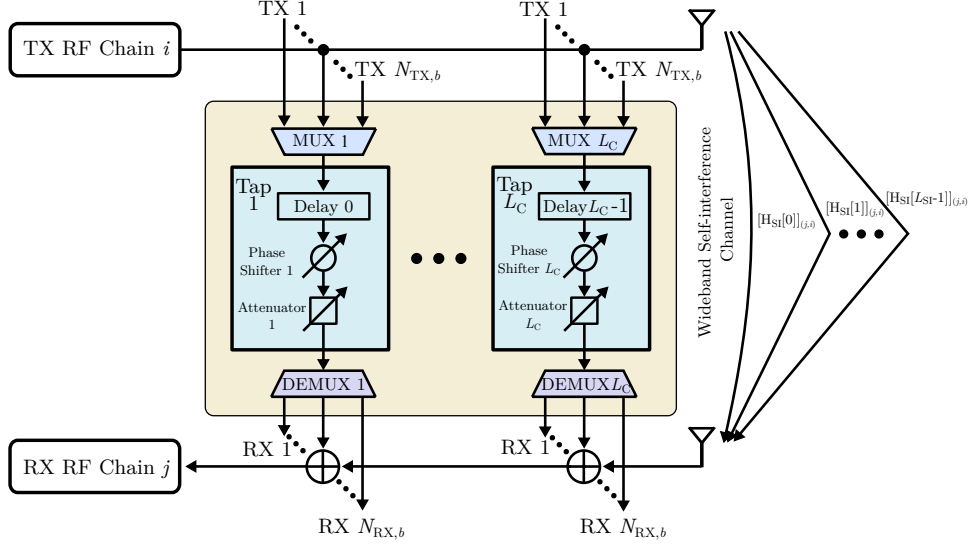


Figure 9. The proposed wideband analog SI canceller for the FD MIMO OFDM node  $b$  for mitigating the  $L_{\text{SI}}$  channel paths  $[\mathbf{H}_{\text{SI}}[\ell]]_{j,i} \forall \ell = \{0, 1, \dots, L_{\text{SI}} - 1\}$  between the output of the  $i$ th TX RF chain and the input of the  $j$ th RX RF chain with  $i = \{1, 2, \dots, N_{\text{TX},b}\}$  and  $j = \{1, 2, \dots, N_{\text{RX},b}\}$ .

$L_C$ th order FIR filter with the coefficients  $\mathbf{C}_b[\ell], \forall \ell = \{0, 1, \dots, L_C - 1\}$ . This filter takes the outputs of the TX RF chains as inputs and routes its outputs to the inputs of the RX RF chains. Note that the special case of  $L_C = 1$  was considered in [59,64,85] for suppressing narrowband SI signals. As will be shown in Sec. 3.5 with the performance evaluation results, such narrowband SI cancellers are not capable of suppressing the SI power below the maximum RX input power limit, and therefore, lead to RX RF chains' saturation. To avoid such saturation in wideband FD MIMO systems, full-tap wideband analog SI cancellation was utilized in [56,57] that requires  $L_C \geq L_{\text{SI}}$ . It is apparent that the hardware complexity of the full-tap cancellers scales with the number of TX/RX antenna elements as well as the multipath channel components.

The proposed wideband analog SI canceller for the FD MIMO OFDM node  $b$  is depicted in Figure 9. As illustrated in the figure, it consists of  $L_C$  analog taps, each including a delay line, a phase shifter, and an attenuator, to suppress the SI signal between the output of any  $i$ th TX RF chain and the input of any  $j$ th RX RF chain with  $i = \{1, 2, \dots, N_{\text{TX},b}\}$  and  $j = \{1, 2, \dots, N_{\text{RX},b}\}$ . It will be shown in the sequel that the proposed co-design of the analog SI canceller with the digital TX/RX beamformers allows choosing  $L_C < L_{\text{SI}}$ , thus reducing the hardware complexity of the canceller compared to the full-tap analog canceller case [56, 57] in state-of-the-arts. As shown in Figure 9, outputs of the TX RF chains are routed to the analog canceller via MULTipleXers (MUXs), and the outputs of the canceller are added to selected RX RF chains input using DEMultipleXers (DEMUXs). The analog canceller settings in Figure 9 are repeated for all the TX and RX RF chains resulting in  $N$ -tap wideband analog SI canceller. Therefore, for the  $\ell$ th filter delay, the baseband representation  $\mathbf{C}_b[\ell]$  of the  $N$ -tap analog canceller is modeled as

$$\mathbf{C}_b[\ell] \triangleq \mathbf{L}_3[\ell]\mathbf{L}_2[\ell]\mathbf{L}_1[\ell], \quad \forall \ell = \{0, 1, \dots, L_C - 1\}, \quad (3.15)$$

where  $\mathbf{L}_1[\ell] \in \mathbb{R}^{\frac{N}{L_C} \times N_{\text{TX},b}}$  and  $\mathbf{L}_3[\ell] \in \mathbb{R}^{N_{\text{RX},b} \times \frac{N}{L_C}}$  represent the MUX and DEMUX configurations of the  $\ell$ th order of the canceller, respectively, and they take the binary values 0 or 1. Therefore, it must hold that  $\sum_{j=1}^{N_{\text{TX},b}} [\mathbf{L}_1[\ell]]_{i,j} = 1$  and  $\sum_{i=1}^{N_{\text{RX},b}} [\mathbf{L}_3[\ell]]_{i,j} = 1, \forall i, j = \{1, 2, \dots, \frac{N}{L_C}\}$ . Here,  $\mathbf{L}_2[\ell] \in \mathbb{C}^{\frac{N}{L_C} \times \frac{N}{L_C}}$  is a diagonal matrix whose complex entries represent the attenuation and phase shift of the  $\ell$ th sample delayed canceller taps. For example, we consider a  $4 \times 4$  wideband MIMO system with  $\frac{N}{L_C} = 12$  available analog cancellation taps at the  $\ell$ th filter delay.

One possible MUX and DEMUX configuration of the  $\ell$ th order of the canceller can be written as  $\mathbf{L}_1[\ell] = [\mathbf{I}_4 \ \mathbf{I}_4 \ \mathbf{I}_4]^T$  and  $\mathbf{L}_3[\ell] = [\mathbf{I}_4 \ \mathbf{I}_4 \ \mathbf{I}_4]$ , respectively. Evidently, the above constraints are satisfied for the MUX and DEMUX configurations.

Compared to the narrowband [59, 64, 85] and full-tap wideband cancellers [56, 57], our proposed wideband analog SI canceller reduces the complexity in two ways: firstly, the analog canceller  $\mathbf{C}_b[\ell]$  has filter order  $L_C \leq L_{SI}$ , and secondly, the canceller is capable of selecting the minimum number of TX/RX antenna pairs, whose SI impact is to be suppressed to avoid the RX RF chains' saturation. Therefore, the hardware complexity of the proposed wideband analog SI canceller does not scale with the number of antennas nor with the number of multipath components. Assuming  $N$  as the total number of taps of the canceller  $\mathbf{C}_b[\ell]$ ,  $\forall \ell$ , it holds that  $N \leq N_{RX,b}N_{TX,b}L_C \leq N_{RX,b}N_{TX,b}L_{SI}$ .

### 3.3.2 Digital TX/RX Beamforming and Wideband Analog SI Cancellation

Suppose that the UL, DL, and SI wireless channels in the considered system of Figure 8 are estimated using pilot signals as  $\hat{\mathbf{H}}_{DL}[\ell]$ ,  $\hat{\mathbf{H}}_{UL}[\ell]$ , and  $\hat{\mathbf{H}}_{SI}[\ell]$ ,  $\forall \ell$ , respectively. Using these estimations and the representation for the analog canceller as well as digital TX/RX beamformers, estimates for the  $n$ th subcarrier achievable UL and DL rates can be respectively calculated as

$$\begin{aligned} \hat{\mathcal{R}}_{UL,n} &\triangleq \log_2 \left( \det \left( \mathbf{I}_{d_{m_2}} + \left\| \mathbf{u}_{b,n} \hat{\mathcal{H}}_{UL,n} \mathbf{G}_{1,m_2} \mathbf{v}_{m_2,n} \right\|^2 \hat{\mathcal{Q}}_{b,n}^{-1} \right) \right), \\ \hat{\mathcal{R}}_{DL,n} &\triangleq \log_2 \left( \det \left( \mathbf{I}_{d_b} + \left\| \mathbf{u}_{m_1,n} \hat{\mathcal{H}}_{DL,n} \mathbf{G}_{1,b} \mathbf{v}_{b,n} \right\|^2 \hat{\mathcal{Q}}_{m_1,n}^{-1} \right) \right), \end{aligned} \quad (3.16)$$

where  $\widehat{\mathbf{Q}}_{b,n}$  and  $\widehat{\mathbf{Q}}_{m_1,n}$  denote the estimated Interference-plus-Noise (IpN) covariances matrices at multi-antenna nodes  $b$  and  $m_1$ , respectively, which can be computed as

$$\begin{aligned}\widehat{\mathbf{Q}}_{b,n} &\triangleq \left\| \mathbf{u}_{b,n} \left( \widetilde{\mathbf{H}}_{\text{SI},n} (\mathbf{G}_{1,b} \mathbf{v}_{b,n} \mathbf{s}_{b,n} + \mathbf{z}_{b,n}) + \widehat{\mathbf{H}}_{\text{UL},n} \mathbf{z}_{m_2,n} + \mathbf{d}_n \right) \right\|^2 + \sigma_b^2 \left\| \mathbf{u}_{b,n} \right\|^2, \\ \widehat{\mathbf{Q}}_{m_1,n} &\triangleq \left\| \mathbf{u}_{m_1,n} \left( \widehat{\mathbf{H}}_{\text{DL},n} \mathbf{z}_{b,n} \right) \right\|^2 + \sigma_{m_1}^2 \left\| \mathbf{u}_{m_1,n} \right\|^2,\end{aligned}\quad (3.17)$$

where  $\widetilde{\mathbf{H}}_{\text{SI},n} \triangleq \left( \widehat{\mathbf{H}}_{\text{SI},n} + \mathbf{C}_{b,n} \right)$ . The latter expressions have been obtained from Equation 3.14 and Equation 3.9 assuming estimation of the TX impairments at RXs.

Extending the design approach of [85], we focus on the estimated achievable FD rate of  $n$ th subcarrier defined as the sum of  $\widehat{\mathcal{R}}_{\text{UL},n}$  and  $\widehat{\mathcal{R}}_{\text{DL},n}$ , and formulate the following general optimization problem for the joint design of the  $N$ -tap wideband analog SI canceller and the digital TX/RX beamformers:

$$\mathcal{OP}1 : \quad \max_{\substack{\mathbf{C}_b[\ell], \mathbf{v}_{b,n}, \mathbf{u}_{b,n}, \\ \mathbf{v}_{m_2,n}, \mathbf{u}_{m_1,n}, \mathbf{d}_b,n}} \widehat{\mathcal{R}}_{\text{UL},n} + \widehat{\mathcal{R}}_{\text{DL},n} \quad (3.18)$$

$$\text{s.t.} \quad \text{constraints on } \mathbf{C}_b[\ell], \forall \ell \text{ structure}, \quad (C1)$$

$$\mathbb{E}\{\|\mathbf{G}_{1,b} \mathbf{v}_{b,n} \mathbf{s}_{b,n} + \mathbf{z}_{b,n}\|^2\} \leq P_b, \quad (C2)$$

$$\mathbb{E}\{\|\mathbf{G}_{1,m_2} \mathbf{v}_{m_2,n} \mathbf{s}_{m_2,n} + \mathbf{z}_{m_2,n}\|^2\} \leq P_{m_2}, \quad (C3)$$

$$\mathbf{v}_{b,n}, \mathbf{u}_{b,n}, \mathbf{v}_{m_2,n}, \mathbf{u}_{m_1,n} : \text{unit norm columns}, \quad (C4)$$

$$\left\| \widetilde{\mathbf{H}}_{\text{SI},n} (\mathbf{G}_{1,b} \mathbf{v}_{b,n} \mathbf{s}_{b,n} + \mathbf{z}_{b,n}) \right\|^2 < \lambda_b \mathbf{I}_{N_{\text{RX},b}}, \quad (C5)$$

where (C1) represents the analog SI canceller settings as in Equation 3.15, constraints (C2), (C3) relate to the average transmit power at node  $b$  and  $m_2$ , respectively, (C4) enforces the unit norm

condition of the considered beamformers, and (C5) imposes the threshold residual power level,  $\lambda_b$  at the RX antenna input to avoid RF chain saturation at node  $b$ . The threshold power is limited by the ADC dynamic range. Note that our motivation is to reduce the analog SI cancellation taps while maximizing FD rate. Therefore, we propose the joint design of reduced  $N$ -tap analog canceller and the digital TX/RX beamformers to satisfy the RF saturation constraint after analog cancellation while boosting the FD sum rate.

The optimization problem in  $\mathcal{OP1}$  is a nonconvex problem with nonconvex constraints. We propose to solve  $\mathcal{OP1}$  in a decoupled way, where two subproblems are formulated and solved subject to the constraints. First, we solve for  $\mathbf{C}_b[\ell]$ ,  $\mathbf{v}_{b,n}$ , and  $\mathbf{u}_{m_1,n}$  that maximize the instantaneous DL rate subject to the relevant constraints for these unknown variables and the constraint to ensure that RF saturation is satisfied at all node  $b$  RXs. More specifically, we formulate the following optimization subproblem for the design

$$\begin{aligned} \mathcal{OP2} : \quad & \max_{\mathbf{C}_b[\ell], \mathbf{v}_{b,n}, \mathbf{u}_{m_1,n}} \widehat{\mathcal{R}}_{\text{DL},n} \\ & \text{s.t.} \quad (\text{C1}), (\text{C2}), (\text{C4}), (\text{C5}) \end{aligned}$$

We solve the problem  $\mathcal{OP2}$  adopting an alternating optimization approach. Specifically, supposing that the available number of analog canceller taps  $N$  and a realization of  $\mathbf{C}_b[\ell]$ ,  $\forall \ell$  satisfying the constraint (C1) are given, we seek for  $\mathbf{v}_{b,n}$  and  $\mathbf{u}_{m_1,n}$  maximizing the DL rate while meeting the constraints (C2), (C4) and the constraint (C5) for the residual SI after analog cancellation. The latter procedure is repeated for all allowable realizations of  $\mathbf{C}_b[\ell]$ ,  $\forall \ell$  for the given  $N$  in order to find the best variables  $\mathbf{C}_b[\ell]$ ,  $\mathbf{v}_{b,n}$ ,  $\mathbf{u}_{m_1,n}$  solving  $\mathcal{OP2}$ . For a given number of analog

---

**Algorithm 1** Digital TX/RX Beamforming Maximizing DL Rate
 

---

**Input:**  $\mathbf{C}_b[\ell], \forall \ell, P_b, \mu_1, \nu_1, \mu_2, \nu_3, \sigma_{m_1}^2$ , and  $n$ .

**Output:**  $\mathbf{V}_{b,n}, \mathbf{G}_{1,b}$ , and  $\mathbf{U}_{m_1,n}$ .

- 1: Obtain wireless channel estimates  $\widehat{\mathbf{H}}_{\text{DL}}[\ell]$  and  $\widehat{\mathbf{H}}_{\text{SI}}[\ell]$  using pilot signals.
  - 2: Get  $\widehat{\mathcal{H}}_{\text{DL},n}, \widehat{\mathcal{H}}_{\text{SI},n}$  and  $\mathbf{C}_{b,n}$  using Equation 3.13.
  - 3: Obtain  $\mathcal{D}_b$  including the  $N_{\text{TX},b}$  right-singular vectors of  $\widetilde{\mathcal{H}}_{\text{SI},n} = (\widehat{\mathcal{H}}_{\text{SI},n} + \mathbf{C}_{b,n})$  corresponding to the singular values in descending order.
  - 4: Set  $\alpha_{max} = \min\{N_{\text{RX},m_1}, N_{\text{TX},b}\}$ .
  - 5: **for**  $\alpha = \alpha_{max}, \alpha_{max} - 1, \dots, 2$  **do**
  - 6:   Set  $\mathcal{E}_b = [\mathcal{D}_b]_{(:,N_{\text{TX},b}-\alpha+1:N_{\text{TX},b})}$ .
  - 7:   Set  $\mathcal{F}_b$  as the right singular vectors of effective DL channel  $\widehat{\mathcal{H}}_{\text{DL},n}\mathcal{E}_b$ .
  - 8:   Set  $\mathbf{V}_{b,n} = \mathcal{E}_b\mathcal{F}_b$  and  $d_b = \alpha$ .
  - 9:   Set  $[\mathbf{G}_{1,b}]_{(i,i)} = \sqrt{P_b/N_{\text{TX},b}}, \forall i = 1, 2, \dots, N_{\text{TX},b}$ .
  - 10:   Obtain  $\mathbf{G}_{j,b}$  for  $j = 2, 3, \dots, 6$  using Equation 3.4.
  - 11:   **if**  $\left( \left\| \left[ \widetilde{\mathcal{H}}_{\text{SI},n} \mathbf{G}_{1,b} \mathbf{V}_{b,n} \right]_{(i,:)} \right\|^2 + \left| \left[ \widetilde{\mathcal{H}}_{\text{SI},n} \mathbf{z}_{b,n} \right]_i \right|^2 \right) < \lambda_b$   
     **then**
  - 12:       Stop the loop.
  - 13:   **end if**
  - 14: **end for**
  - 15: Set  $\mathbf{U}_{m_1,n}$  as row-wise placement of the  $d_b$  left singular vectors of the DL channel  $\widehat{\mathcal{H}}_{\text{DL},n}$  corresponding to the singular values in descending order.
  - 16: **if**  $\left( \left\| \left[ \widetilde{\mathcal{H}}_{\text{SI},n} \mathbf{G}_{1,b} \mathbf{V}_{b,n} \right]_{(i,:)} \right\|^2 + \left| \left[ \widetilde{\mathcal{H}}_{\text{SI},n} \mathbf{z}_{b,n} \right]_i \right|^2 \right) < \lambda_b$  **then**
  - 17:   Output  $\mathbf{V}_{b,n}, \mathbf{G}_{1,b}, \mathbf{U}_{m_1,n}$ , and stop the algorithm.
  - 18: **else**
  - 19:   Numbers of taps,  $N$  in analog canceller  $\mathbf{C}_b[\ell]$  is not capable of preventing RF saturation.
  - 20: **end if**
- 

cancellation taps  $N$ , we define the analog cancellation filter order  $L_C = \lceil \frac{N}{N_{\text{TX},b}N_{\text{RX},b}} \rceil$ . Now we formulate the analog canceller  $\mathbf{C}_b[\ell]$  as an orderly column-by-column placement of the reciprocal of wideband SI channel  $\widehat{\mathbf{H}}_{\text{SI}}[\ell]$  elements. Based on this analog canceller  $\mathbf{C}_b[\ell], \forall \ell$ , we follow the procedures summarized in Algorithm 1, solving for the beamformers maximizing the DL rate.

---

**Algorithm 2** Digital TX/RX Beamforming Maximizing UL Rate
 

---

**Input:**  $\mathbf{V}_{b,n}$ ,  $\tilde{\mathbf{H}}_{\text{SI},n}$ ,  $\mathbf{d}_{b,n}$ ,  $P_{m_2}$ ,  $\sigma_b^2$ , and  $n$ .

**Output:**  $\mathbf{V}_{m_2,n}$ ,  $\mathbf{G}_{1,m_2}$ , and  $\mathbf{U}_{b,n}$ .

- 1: Obtain UL channel estimates  $\hat{\mathbf{H}}_{\text{UL}}[\ell]$  using pilot signals, and its  $n$ -th subcarrier frequency domain presentation  $\hat{\mathbf{H}}_{\text{UL},n}$  using Equation 3.13.
  - 2: Obtain  $\mathcal{D}_{m_2}$  including the  $N_{\text{TX},m_2}$  right-singular vectors of  $\hat{\mathbf{H}}_{\text{UL},n}$  corresponding to the singular values in descending order.
  - 3: Set  $\mathbf{V}_{m_2,n} = [\mathcal{D}_{m_2}](:,1:d_{m_2})$ .
  - 4: Set  $[\mathbf{G}_{1,m_2}]_{(i,i)} = \sqrt{\frac{P_{m_2}}{N_{\text{TX},m_2}}}$ ,  $\forall i = 1, 2, \dots, N_{\text{TX},m_2}$ .
  - 5: Set  $\mathbf{\Sigma}_b = \tilde{\mathbf{H}}_{\text{SI},n} \left( \mathbf{G}_{1,b} \mathbf{V}_{b,n} \mathbf{V}_{b,n}^H \mathbf{G}_{1,b}^H + \mathbf{z}_{b,n} \mathbf{z}_{b,n}^H \right) \tilde{\mathbf{H}}_{\text{SI},n}^H + \hat{\mathbf{H}}_{\text{UL},n} \mathbf{z}_{m_2,n} \mathbf{z}_{m_2,n}^H \hat{\mathbf{H}}_{\text{UL},n}^H + \mathbf{d}_n \mathbf{d}_n^H + \sigma_b^2 \mathbf{I}_{N_{\text{RX},b}}$ .
  - 6: Set  $\mathbf{A}_b = \hat{\mathbf{H}}_{\text{UL},n} \mathbf{G}_{1,m_2} \mathbf{V}_{m_2,n} \mathbf{V}_{m_2,n}^H \mathbf{G}_{1,m_2}^H \hat{\mathbf{H}}_{\text{UL},n}^H \mathbf{\Sigma}_b^{-1}$ .
  - 7: Set  $\mathbf{U}_{b,n}$  as row-wise placement of the  $d_{m_2}$  eigenvectors of  $\mathbf{A}_b$  corresponding to  $d_{m_2}$  largest eigenvalues.
- 

Using  $\mathbf{C}_b[\ell]$ ,  $\forall \ell$ ,  $\mathbf{V}_{b,n}$ , and  $\mathbf{U}_{m_1,n}$  from the solution of  $\mathcal{OP}2$ , we transmit  $T$  precoded training symbols to obtain the digital cancellation signal  $\mathbf{d}_{b,n}$  following the procedures described in Sec. 3.4. Using the pilot estimated UL channel, DL beamformers, analog canceller, and digital cancellation signal, we propose to maximize the instantaneous UL rate for the solution of  $\mathcal{OP}2$ . In particular, we formulate the following optimization subproblem for the digital beamformers to maximize the UL rate:

$$\begin{aligned} \mathcal{OP}3 : \quad & \max_{\mathbf{V}_{m_2,n}, \mathbf{U}_{b,n}} \hat{\mathcal{R}}_{\text{UL},n} \\ & \text{s.t.} \quad (\text{C3}), (\text{C4}) \end{aligned}$$

The procedures to solve the optimization problem  $\mathcal{OP}3$  is provided in Algorithm 2.

### 3.4 TSVD-based Adaptive MIMO Digital SI Cancellation

To suppress the residual SI signal after analog cancellation, digital SI mitigation techniques are employed at the RX baseband of the FD node. The existing digital cancellation approaches utilize the SI signal modeling to estimate the linear and/or nonlinear SI components resulting from the FD TX RF chains to reconstruct the residual SI signal [57, 66, 68, 69]. However, for the considered wideband FD MIMO systems, the number of signal estimation parameters of those models increases with TX/RX RF chains and multipath SI channel components, which requires a large number of training signals. In this section, we propose a novel TSVD-based adaptive MIMO digital SI cancellation that reduces the computational complexity while successfully suppressing the residual SI signal.

At the node  $b$  RX, the baseband received signal  $\mathbf{y}_b[k]$  contains the desired signal from the UL TX node  $m_2$ , residual SI signal from node  $b$  after analog cancellation, and the AWGN vector. From Equation 3.5, Equation 3.7, and Equation 3.11, the residual SI signal with AWGN vector can be written as

$$\begin{aligned} \mathbf{y}_{\text{res}}[k] &\triangleq \sum_{\ell=0}^{L_{\text{SI}}-1} \mathbf{H}_{\text{res}}[\ell] \boldsymbol{\psi}_b[k-\ell] + \mathbf{w}_b[k] \\ &= \tilde{\mathbf{H}}_{\text{res}} \tilde{\boldsymbol{\psi}}_b[k] + \mathbf{w}_b[k], \end{aligned} \tag{3.19}$$

where  $\mathbf{H}_{\text{res}}[\ell] = (\mathbf{H}_{\text{SI}}[\ell] + \mathbf{C}_b[\ell]) \mathbf{G}_b$  is the residual SI channel and  $\boldsymbol{\psi}_b[k]$  is the vertically arranged TX precoded signal vector containing combination of  $\mathbf{x}_b[k]$ ,  $\mathbf{x}_b^*[k]$ , and their third-

order components as defined in Equation 3.7. Here the augmented residual SI channel  $\tilde{\mathbf{H}}_{\text{res}} \in \mathbb{C}^{N_{\text{RX},b} \times 6N_{\text{TX},b}L_{\text{SI}}}$  and the precoded signal vector  $\tilde{\boldsymbol{\psi}}_b[k] \in \mathbb{C}^{6N_{\text{TX},b}L_{\text{SI}} \times 1}$  are defined as

$$\begin{aligned} \tilde{\mathbf{H}}_{\text{res}} &\triangleq [\mathbf{H}_{\text{res}}[0] \ \mathbf{H}_{\text{res}}[1] \ \dots \ \mathbf{H}_{\text{res}}[L_{\text{SI}} - 1]] \\ \tilde{\boldsymbol{\psi}}_b[k] &\triangleq \text{col}\{\boldsymbol{\psi}_b[k], \boldsymbol{\psi}_b[k-1], \dots, \boldsymbol{\psi}_b[k-L_{\text{SI}}+1]\} \end{aligned} \quad (3.20)$$

The objective of the digital SI cancellation is to estimate the residual SI channel parameters of  $\tilde{\mathbf{H}}_{\text{res}}$  using training samples during no UL communication and utilize these estimated parameters to reconstruct the reciprocal of the residual SI signal during FD operation. The number of required training samples to estimate the precise residual SI channel parameters ( $N_{\text{RX},b} \times 6N_{\text{TX},b}L_{\text{SI}}$ ) increases with the number of FD MIMO node  $b$  antennas and the multipath SI components. To reduce the requirement of a large number of training signals and computational resources, we propose a novel TSVD-based adaptive digital SI cancellation approach for wideband FD MIMO systems.

### 3.4.1 Proposed Digital SI Cancellation

To design the digital SI cancellation, we utilize the precoded signal vector at the baseband of node  $b$  TXs. Supposing  $T$  training samples, the precoded signal matrix  $\mathbf{X}_b \in \mathbb{C}^{N_{\text{TX},b} \times T}$  is used to form the augmented signal matrix  $\tilde{\boldsymbol{\Psi}}_b \in \mathbb{C}^{6N_{\text{TX},b}L_{\text{SI}} \times T}$  using Equation 3.20. Therefore, based on Equation 3.19, the residual SI signal matrix  $\mathbf{Y}_{\text{res}} \in \mathbb{C}^{N_{\text{RX},b} \times T}$  with AWGN at the RX baseband of node  $b$  is expressed as

$$\mathbf{Y}_{\text{res}} = \tilde{\mathbf{H}}_{\text{res}} \tilde{\boldsymbol{\Psi}}_b + \mathbf{W}_b \quad (3.21)$$

---

**Algorithm 3** Adaptive Digital SI cancellation using TSVD regularization
 

---

**Input:**  $\mathbf{X}_b \in \mathbb{C}^{N_{\text{TX},b} \times T}$ ,  $\mathbf{Y}_{\text{res}} \in \mathbb{C}^{N_{\text{RX},b} \times T}$ ,  $\sigma_b^2$ .

**Output:**  $\hat{\mathbf{H}}_{\text{res}} \in \mathbb{C}^{N_{\text{RX},b} \times 6N_{\text{TX},b}L_{\text{SI}}}$ .

- 1: Obtain  $\tilde{\Psi}_b$  using Equation 3.20.
  - 2: Set  $L_p = 6N_{\text{TX},b}L_{\text{SI}}$ .
  - 3: Obtain SVD of  $\tilde{\Psi}_b = \mathbf{U}\mathbf{\Sigma}\mathbf{V}^H$ , where  $\mathbf{U} \in \mathbb{C}^{L_p \times L_p}$ ,  $\mathbf{V} \in \mathbb{C}^{T \times T}$ ,  $\mathbf{\Sigma} = \text{diag}\{\sigma_1, \sigma_2, \dots, \sigma_{L_p}\} \in \mathbb{C}^{L_p \times T}$ , and  $\sigma_1 \geq \sigma_2 \geq \dots \geq \sigma_{L_p} \geq 0$ .
  - 4: **for**  $p = 1, 2, \dots, L_p$  **do**
  - 5:     Set  $\Theta = \sum_{i=1}^p \frac{\mathbf{Y}_{\text{res}}[\mathbf{V}]_{(:,i)}[\mathbf{U}]_{(:,i)}^H}{\sigma_i}$ .
  - 6:     **if**  $\|\mathbf{Y}_{\text{res}} - \Theta\tilde{\Psi}_b\|^2 \leq \sigma_b^2 \mathbf{I}_{\text{RX},b}$  **then**
  - 7:         Set  $\hat{\mathbf{H}}_{\text{res}} = \Theta$ .
  - 8:         **Stop the algorithm.**
  - 9:     **end if**
  - 10: **end for**
  - 11: Set  $\hat{\mathbf{H}}_{\text{res}} = \Theta$ .
- 

Making use of the SI samples in Equation 3.21 and the notation  $\Theta \in \mathbb{C}^{N_{\text{RX},b} \times 6N_{\text{TX},b}L_{\text{SI}}}$ , the Least Squares (LS) estimation for  $\hat{\mathbf{H}}_{\text{res}}$  minimizing the power of the error matrix can be expressed as

$$\hat{\mathbf{H}}_{\text{res}} \triangleq \arg \min_{\Theta} \|\mathbf{Y}_{\text{res}} - \Theta\tilde{\Psi}_b\|^2. \quad (3.22)$$

The LS problem has a closed form solution as  $\hat{\mathbf{H}}_{\text{res}} = \mathbf{Y}_{\text{res}} \tilde{\Psi}_b^H (\tilde{\Psi}_b \tilde{\Psi}_b^H)^{-1}$ , assuming full row rank in  $\tilde{\Psi}_b$ . However,  $\tilde{\Psi}_b$ 's rows are high order polynomials of linear and conjugate SI samples, as well as their interaction products, and therefore correlated. In addition, the LS solution includes the effect of strong SI components along with less significant terms and is dominated by estimation error. To tackle the estimation error and reduce the parameter estimation model complexity, we propose the following TSVD-based digital SI cancellation method.

The main idea of the proposed adaptive digital SI cancellation method is to include the SI terms that have a strong effect on the residual SI signal while omitting the insignificant SI terms. We apply the TSVD regularization method to the estimation problem. First, we perform the SVD of the design matrix  $\tilde{\Psi}_b$  to obtain the singular values in an ascending manner. Now, we loop through the singular values of  $\tilde{\Psi}_b$  to find its best rank- $p$  approximant and the effective residual SI channel that can suppress the residual SI signal below the noise floor  $\sigma_b^2$ . The TSVD-based adaptive digital cancellation approach is described in Algorithm 3.

The proposed cancellation approach is adaptive because the values of  $p$  vary as the SI signal power changes. For higher SI power, the algorithm estimates more parameters resulting in a large  $p$  value. However, for low transmit power, the proposed approach omits the insignificant SI terms with small  $p$  values and reduces the estimation error. Using the residual channel estimate  $\hat{\mathbf{H}}_{\text{res}}$ , the digital cancellation signal  $\mathbf{d}_b[k]$  can be formed as

$$\mathbf{d}_b[k] \triangleq -\hat{\mathbf{H}}_{\text{res}} \tilde{\psi}_b[k], \quad (3.23)$$

which is applied to the received signals after the ADCs.

### 3.5 Simulation Results and Discussion

In this section, we present the performance evaluation of the proposed wideband FD MIMO scheme incorporating the impairments of the transceiver chains depicted in Figure 8. We also provide a performance comparison with the state-of-the-art A/D SI cancellation schemes relevant to the considered FD MIMO wideband communication system.

TABLE III  
WIDEBAND FD MIMO SIMULATION PARAMETERS

Parameter	Value	Parameter	Value
Signal Bandwidth	20MHz	Transmit Power	20 – 40 dBm
Subcarrier Spacing	312.5KHz	Node $b$ Noise Floor	–100 dBm
Sampling Time	50ns	Node $m_1$ Noise Floor	–90 dBm
Constellation	16-QAM	PA IIP3	15 dBm
No. of Subcarriers	64	TX IRR	30 dB
No. of Data Subcarriers	52	No. of ADC Bits	14
Cyclic Prefix Length	16	PAPR	10 dB

### 3.5.1 Simulation Parameters

We perform an extensive waveform simulation following the wideband FD MIMO architecture illustrated in Figure 8, where the practical transceiver components are incorporated using baseband equivalent models. We consider a  $4 \times 4$  FD MIMO BS node  $b$  (i.e.  $N_{\text{TX},b} = N_{\text{RX},b} = 4$ ), and two different cases for the number of antennas at HD nodes  $m_1$  and  $m_2$ : the single-antenna case (i.e.  $N_{\text{TX},m_1} = N_{\text{RX},m_2} = 1$ ) and the multi-antenna with  $N_{\text{RX},m_1} = N_{\text{TX},m_2} = 4$ . The generated wideband waveforms are OFDM signals with a BandWidth (BW) of 20 MHz. Both DL and UL channels are assumed to be wideband block Rayleigh fading channels with  $L_{\text{DL}} = L_{\text{UL}} = 4$  multipath components and an average pathloss of 100 dB. The SI channel at the FD MIMO node  $b$  is simulated as a wideband Rician fading channel with  $L_{\text{SI}} = 4$  multipath components, where the direct SI and the three considered reflected paths have 0, 50, 100, and 150ns delay as well as 40, 50, 60, and 70 dB pathlosses, respectively [24]. For the considered

waveform, the 50ns delay between consecutive SI paths constitutes to one sample delay of the OFDM signal. The additional parameters of the waveforms, along with other system-level parameters, are shown in Table III. To incorporate TX impairments at the FD MIMO node  $b$ , the TX IRR is considered 30 dB, which implies that the image signal power is 30 dB lower than the linear SI signal [66]. The quasi memoryless nonlinear PAs are assumed to have an IIP3 value of 15 dBm [78]. Each ADC at the RX RF chains of node  $b$  is considered to have a 14-bit resolution with an effective dynamic range of 60 dB for a Peak-to-Average-Power-Ratio (PAPR) of 10 dB [98]. Therefore, the residual SI power after analog cancellation at each RX RF chain of node  $b$  has to be below  $-40$  dBm to avoid RF saturation. Furthermore, to account for practical mismatch, the wideband analog canceller taps are considered non-ideal with steps of 0.02 dB for attenuation and  $0.13^\circ$  for phase, as in [59]. Thus, for each tap in our simulations, the phase setting has a random phase error uniformly distributed between  $-0.065^\circ$  and  $0.065^\circ$ . Considering a waveform with 312.5KHz subcarrier spacing, the phase error translates to a maximum of 0.578ns time delay error for each tap. We have used 1000 Monte Carlo simulation runs (1000 independent set of channels) to calculate the performance of all considered designs. In each run, we have performed pilot-assisted estimations of all involved wireless channels and considered 500 OFDM symbols transmitted from both nodes  $b$  and  $m_2$  to emulate one radio frame for packet-based FD MIMO communication system.

### 3.5.2 Analog SI Mitigation Capability

First, we evaluate the SI suppression capability of the proposed wideband FD MIMO analog SI canceller and compare it with the state-of-the-art SI cancellation approaches. As discussed

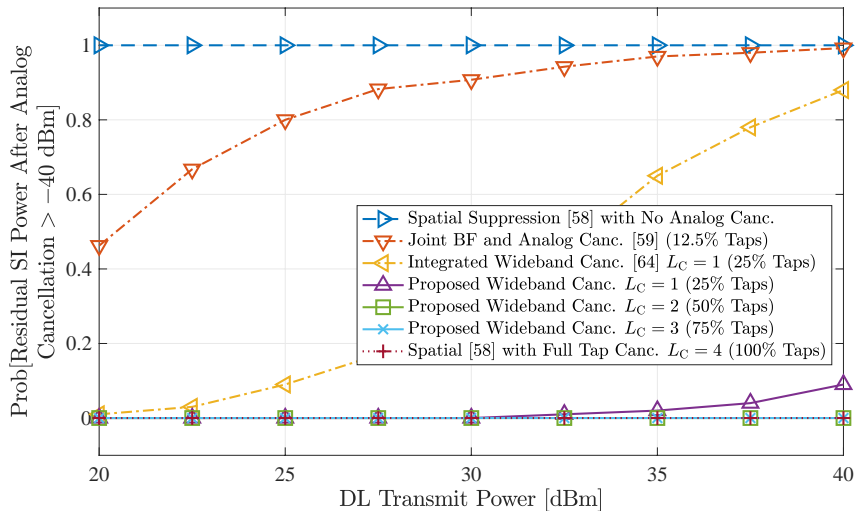


Figure 10. Probability of the residual SI power after analog cancellation above RF saturation level  $-40$  dBm with respect to DL transmit power in dBm and  $N_{\text{RX},m_1} = N_{\text{TX},m_2} = 1$ .

in Sec. 3.3, the performance indicator of the analog canceller is its ability to avoid RX RF chain saturation at the FD node. To reduce analog hardware complexity, most of the existing methods only deal with direct SI signals in analog cancellation and suppress the multipath components in the digital domain, assuming the insignificant impact of reflected SI components on RF chain saturation. However, for wideband FD MIMO systems, the multipath SI components can result in residual SI power above the RF saturation level for high transmit powers [99–101]. For example, we have considered a wideband SI channel with reflected paths having pathlosses as high as 70 dB, which results in an SI power of  $-30$  dBm at the RX input of FD MIMO node  $b$  for transmit power of 40 dBm. This residual SI power is above the RF chain saturation level

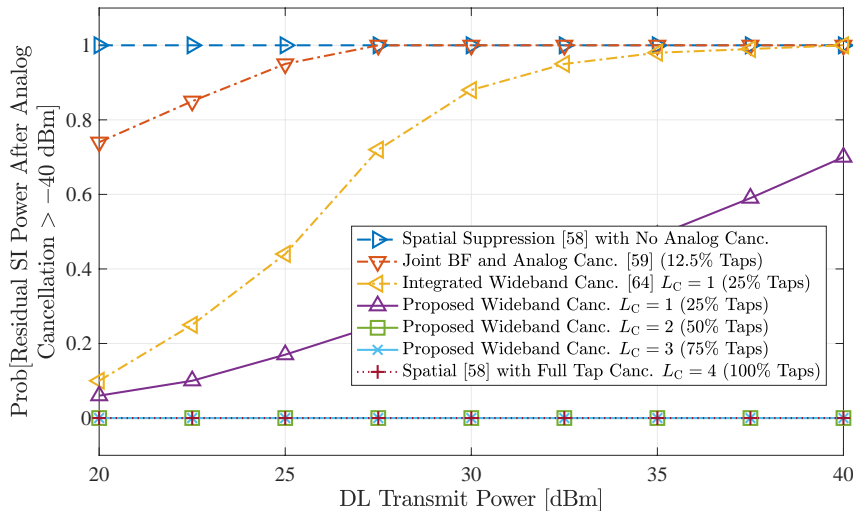


Figure 11. Probability of residual SI after analog cancellation above RF saturation level  $-40$  dBm with respect to DL transmit power in dBm and  $N_{\text{RX},m_1} = N_{\text{TX},m_2} = 4$ .

of  $-40$  dBm of the considered FD MIMO system, and therefore needs to be suppressed in the analog domain.

In Figure 10, we illustrate the probability of the residual SI signal power above the RF saturation level of  $-40$  dBm after proposed wideband analog cancellation with varying number of taps ( $L_C = 1, 2, 3$ ) as a function of DL transmit power ( $20 - 40$  dBm) for the considered  $4 \times 4$  wideband FD MIMO communication system with single-antenna HD users (i.e.  $N_{\text{RX},m_1} = N_{\text{TX},m_2} = 1$ ). For comparison, we also plot the analog SI cancellation performance of the “Spatial Suppression” [58], “Joint BF and Analog Cancellation” [59], and “Integrated Wideband Cancellation” [64] approaches. It is evident that the “Spatial Suppression” and “Joint BF and Analog Cancellation” approaches are unable to achieve enough analog SI suppression to avoid

RF saturation, as they only cancel parts of the direct SI components rendering high residual SI power. The “Integrated Wideband Cancellation” with  $L_C = 1$  is capable of achieving sufficient analog SI suppression for low transmit power of 20 dBm; however, for high transmit power cases, the FD MIMO node  $b$  RX RF chains go into saturation as the effect of multipath SI components becomes significant. In contrast, the proposed wideband analog cancellation approach with 25% taps ( $L_C = 1$ ) can provide sufficient RF suppression for transmit power up to 30 dBm. After a 50% reduction of taps compared to the “Spatial Suppression” with full-tap analog canceller, the proposed wideband cancellation with  $L_C = 2$  is capable of avoiding RF saturation for all DL transmit power values.

In Figure 11, we plot the probability of FD MIMO node  $b$  RX RF saturation for multi-antenna DL and UL users with  $N_{\text{RX},m_1} = N_{\text{TX},m_2} = 4$ . With the increment of DL RX antennas, the SI effect at the node  $b$  receiver grows substantially, as the TX transmits multiple streams simultaneously. For the considered multi-antenna case, the existing “Spatial Suppression” with no analog cancellation, “Joint BF and Analog Cancellation,” and “Integrated Wideband Cancellation” approaches provide inadequate SI cancellation performance rendering the RX RF chains into saturation. However, the proposed wideband cancellation with 50% taps is still capable of achieving enough SI suppression to avoid RX RF saturation. Therefore, the proposed wideband analog SI cancellation method with 50% fewer taps compared to the full-tap cancellers provides sufficient analog SI suppression avoiding RX RF chain saturation for considered single and multi-antenna users.

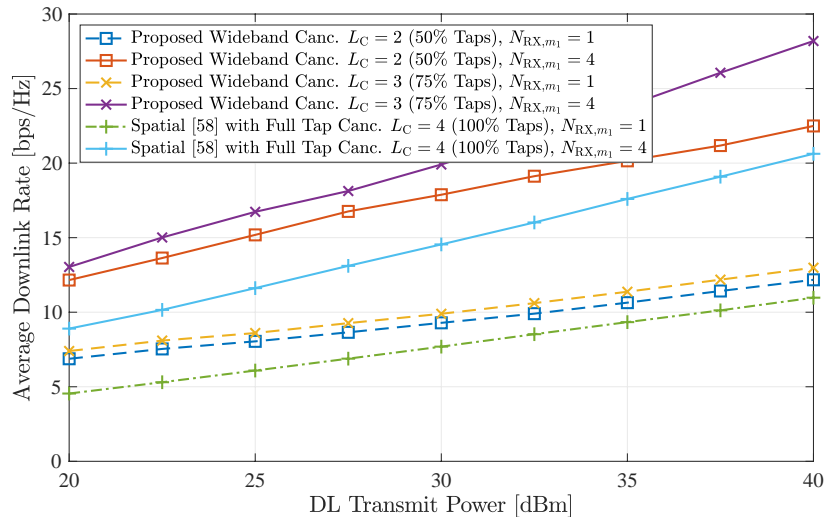


Figure 12. Average downlink rate as a function of the downlink transmit power for  $N_{RX,b} = N_{TX,b} = 4$  and  $N_{RX,m_1} = \{1, 4\}$ .

### 3.5.3 Achievable Downlink Rate

Figure 12 depicts the achievable DL rate of the proposed wideband FD MIMO system with  $N_{RX,b} = N_{TX,b} = 4$  and  $N_{RX,m_1} = \{1, 4\}$  as a function of DL transmit power. The DL rate is achieved after solving the  $\mathcal{OP}2$  using Algorithm 1 given the number of analog cancellation taps that can achieve sufficient SI suppression, as discussed in the previous section. We also plot the DL rate performance of the ‘‘Spatial suppression’’ approach with a full-tap analog canceller. It is evident from Figure 12 that the proposed wideband analog cancellation approach with only 50% taps ( $L_C = 2$ ) outperforms the existing full-tap approach for both single and multi-antenna user cases. Although the proposed approach with 75% taps ( $L_C = 3$ ) provides a

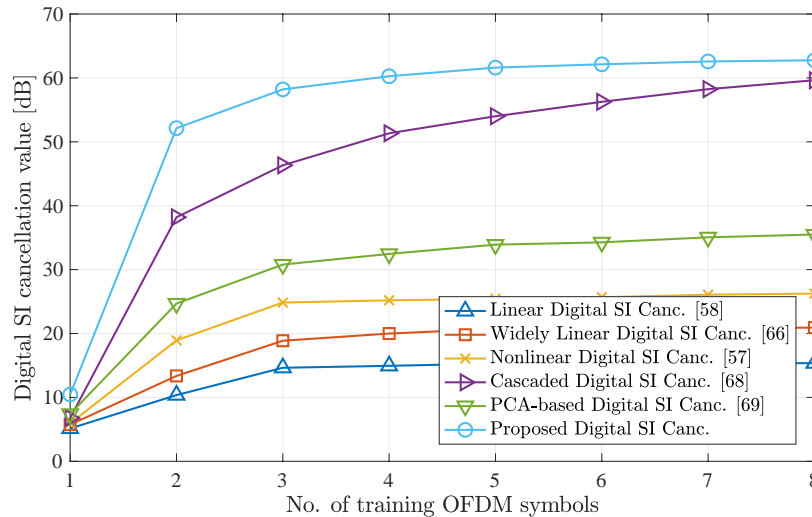


Figure 13. Digital SI cancellation value with respect to the number of training OFDM symbols for digital SI estimation.

substantial DL rate improvement compared to the scheme with 50% taps for multi-antenna user cases, their achievable DL rate is comparable for single-antenna users. Therefore, the proposed wideband cancellation approach provides a trade-off between the number of canceller taps and the achievable DL rate. It is to be noted that, in practical implementation, it is more desirable to reduce the analog canceller taps as much as possible, providing a cost-effective solution.

### 3.5.4 Performance of the Digital SI Canceller

The residual SI signal after analog SI cancellation is further suppressed in the digital domain. Here, we evaluate the performance of the proposed TSVD-based adaptive digital SI cancellation approach. As discussed before, the number of parameters to be estimated for the digital SI regeneration and cancellation increases with the number of antennas and multipath SI compo-

nents at node  $b$ . To estimate such a large number of parameters, a very high number of training samples is required resulting in an increased training overhead.

In Figure 13, we illustrate the amount of digital SI cancellation in dB with respect to the training OFDM symbols each including 64 subcarrier samples for the considered  $4 \times 4$  FD MIMO node  $b$  and multi-antenna users with  $N_{\text{RX},b} = N_{\text{TX},b} = N_{\text{RX},m_1} = N_{\text{TX},m_2} = 4$ . The digital SI estimation and cancellation are achieved for a transmit power of 40 dBm after applying the proposed wideband analog cancellation with 50% taps shown to avoid RF saturation. We compare our approach with “Linear Digital Cancellation” including only linear SI components [58], “Widely Linear Cancellation” considering linear and image effects [66], “Nonlinear Digital Cancellation” considering third-order nonlinear SI terms [57], “Cascaded Nonlinear Cancellation” providing joint cancellation technique cascading PA nonlinearity with transmitter IQ imbalance [68], and “PCA-based Nonlinear Cancellation” employing PCA transformation on SI estimation matrix [69]. It is evident that the linear, nonlinear, and widely linear cancellers achieve less than 30 dB SI cancellation, as they only consider parts of the significant SI components for digital cancellation. The PCA-based nonlinear canceller provides around 35 dB SI cancellation, as it omits some significant SI components to reduce estimating parameters. However, the proposed TSVD-based digital SI canceller achieves around 60 dB cancellation value with 4 OFDM symbols, while the cascaded nonlinear canceller requires more than double training symbols to provide a similar cancellation value. Therefore, the proposed TSVD-based digital canceller is capable of providing superior SI suppression performance with less computational resources, reducing the communication overhead.

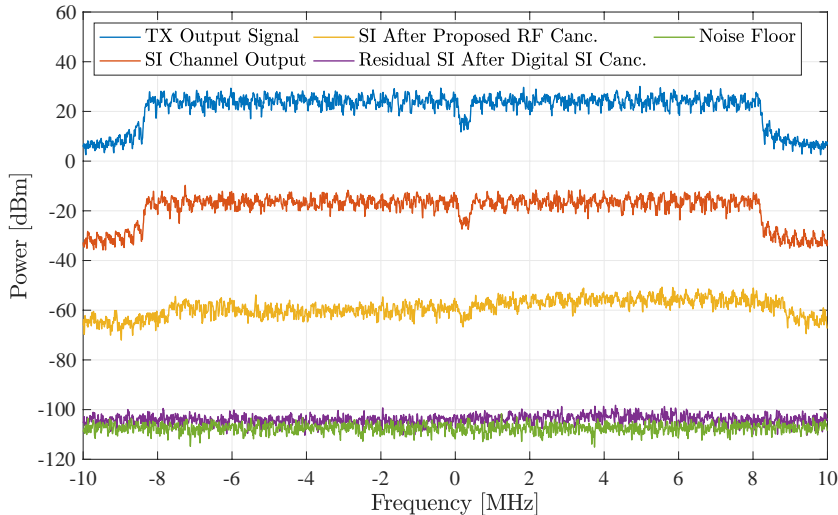


Figure 14. Power Spectrum of the SI signal after SI cancellation in the RF and digital domains with 40 dBm average TX power, 20 MHz bandwidth, and  $-100$  dBm receiver noise floor.

Figure 14 depicts the power spectrum of the SI signal after TX-RX isolation, proposed wideband RF cancellation with 50% taps, and TSVD-based digital SI cancellation for 40 dBm UL and DL transmit power and 20 MHz bandwidth with  $N_{\text{RX},b} = N_{\text{TX},b} = N_{\text{RX},m_1} = N_{\text{TX},m_2} = 4$ . It is shown that the combination of proposed wideband A/D SI cancellation approaches can achieve around 95 dB SI cancellation in addition to the 40 dB TX-RX isolation, and therefore successfully suppress the SI signal to the thermal noise floor for the wideband FD MIMO systems.

### 3.5.5 Average FD Rate

In Figure 15, we illustrate the FD rate of the proposed wideband A/D cancellation with respect to the DL and UL transmit power for  $N_{\text{RX},b} = N_{\text{TX},b} = 4$  and  $N_{\text{RX},m_1} = N_{\text{TX},m_2} = \{1, 4\}$ . For comparison, we also provide the FD rate for “Spatial Suppression” with full-tap

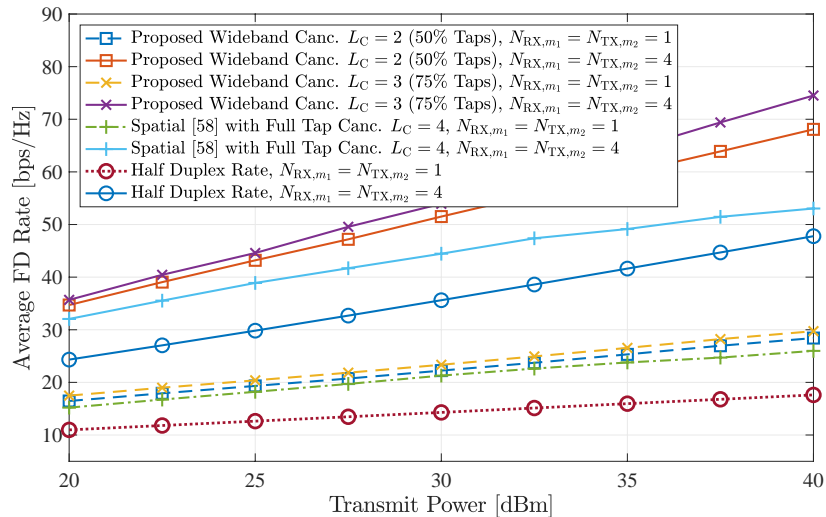


Figure 15. Average FD rate as a function of the downlink transmit power for  $N_{\text{RX},b} = N_{\text{TX},b} = 4$  and  $N_{\text{RX},m_1} = N_{\text{TX},m_2} = \{1, 4\}$ .

analog canceller and the achievable HD rate for the considered MIMO system. It is evident that the proposed digital and analog SI cancellation approach with 50% taps ( $L_C = 2$ ) outperforms the spatial suppression with full-tap analog canceller approach for both single and multi-antenna users cases. In addition, the proposed wideband A/D SI cancellation approach with  $L_C = 2$  can provide substantial rate improvement compared to the HD communication systems. Specifically, for a transmit power of 40 dBm and multi-antenna users case, the proposed wideband A/D SI cancellation approach can achieve  $1.45\times$  the FD rate compared to the HD system with a reduction of 50% analog taps compared to the state-of-the-art full-tap canceller.

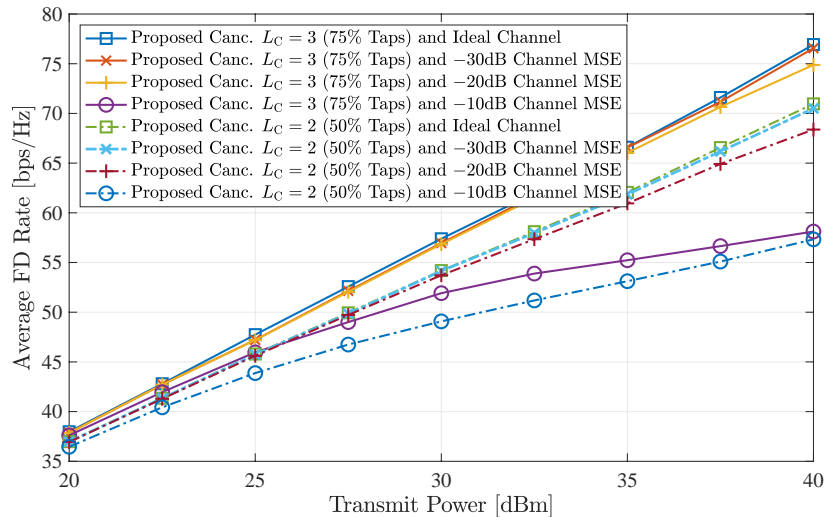


Figure 16. Average FD rate as a function of the transmit power and different channel estimation MSE for  $N_{RX,b} = N_{TX,b} = 4$  and  $N_{RX,m_1} = N_{TX,m_2} = \{1, 4\}$ .

### 3.5.6 Impact of Channel Estimation Error on the FD Rate

The impact of channel estimation error on the proposed FD system performance is depicted in Figure 16. We have plotted the average FD rate of the proposed wideband cancellation system with respect to the DL transmit power for  $N_{RX,b} = N_{TX,b} = 4$  and  $N_{RX,m_1} = N_{TX,m_2} = \{1, 4\}$  with different Mean Squared Errors (MSEs) for channel estimation of all considered channels (i.e. SI, DL, and UL) as well as analog cancellation taps. It is evident from the figure that, for channel estimation MSEs of  $-30\text{dB}$  and  $-20\text{dB}$ , the average FD rates are consistent with the FD rate of ideal channel knowledge for the proposed wideband A/D SI cancellation approach with both 50% and 75% taps. However, for the higher channel estimation error of  $-10\text{dB}$  MSE,

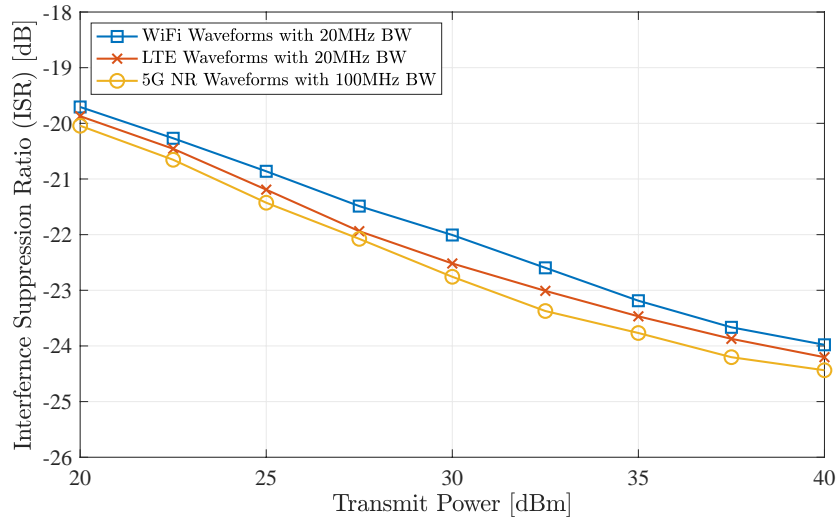


Figure 17. Interference Suppression Ratio with respect to the transmit power and different signal waveforms for the considered FD MIMO system with  $N_{RX,b} = N_{TX,b} = N_{RX,m_1} = N_{TX,m_2} = 4$ .

the FD rate is reduced at the large transmit powers of the proposed wideband FD system. This happens due to the utilization of increased DL DoFs in order to achieve the required SI cancellation, which will avoid RF saturation with non-ideal channels.

### 3.5.7 Interference Suppression Ratio for Different Signal Waveforms

In Figure 17, we illustrate Interference Suppression Ratio (ISR), which is defined as the average residual interference power versus the average SI power without cancellation, with respect to the transmit power for  $N_{RX,b} = N_{TX,b} = N_{RX,m_1} = N_{TX,m_2} = 4$  and different signal waveforms. In addition to the WiFi signal waveform with 20MHz BW and 312.5KHz subcarrier spacing as shown in Table III, we have also simulated Long Term Evolution (LTE) waveform with 20MHz

BW and 15KHz subcarrier spacing as well as 5G New Radio (NR) waveform with 100MHz BW and 60KHz subcarrier spacing, while considering multipath SI channel with  $L_C = 4$  as described in Sec. 3.5.1. It is to be noted that 5G NR and LTE waveforms' sample delays, which are 4.069ns and 32.552ns corresponding to the 60KHz and 15KHz subcarrier spacing, respectively, are not similar to the SI path delays (50ns delay between consecutive reflected paths). Therefore, for such waveforms, analog canceller experiences larger phase error corresponding to larger delay mismatch error. However, it is evident in Figure 17 that the proposed joint wideband A/D SI cancellation and TX/RX beamforming approach can achieve similar ISR performance for 100MHz 5G NR and 20MHz LTE waveforms to the previously considered WiFi waveforms. This is due to the higher RF saturation level of the wider-bandwidth 5G NR system. The node  $b$  RX noise floor for the 100MHz 5G NR system ( $-90\text{dBm}$ ) is higher than that of the WiFi case ( $-100\text{dBm}$ ). For an ADC dynamic range of 60dB, the RF saturation level in 5G NR case is  $-30\text{dBm}$ , whereas the WiFi waveforms have a saturation level at  $-40\text{dBm}$ . Therefore, the analog SI cancellation required in 5G NR cases is 10dB lower than WiFi waveforms. Although higher delay mismatch in the analog canceller 5G NR waveform results in slightly less SI cancellation, the residual SI is still well below the RF saturation level. Therefore, the proposed approach is capable of achieving the required SI cancellation for both LTE and 5G NR waveforms with large bandwidth.

### 3.6 Concluding Remarks

In this chapter, we have presented a reduced complexity wideband analog SI canceller jointly designed with digital TX/RX beamforming for practical FD MIMO systems with TX IQ imbal-

ances and PA nonlinearities maximizing the FD sum-rate performance. To suppress the residual linear SI signal along with its conjugate and nonlinear components below the noise floor, we proposed a novel adaptive digital SI cancellation technique reducing the number of estimation parameters. Our representative performance evaluation comparisons with existing wideband FD MIMO designs demonstrated that the proposed wideband A/D SI canceller achieves superior SI cancellation capability. Furthermore, we showed that the proposed optimization framework provided higher achievable rate performance with reduced hardware complexity for analog SI cancellation and computational resources of digital SI cancellation compared to the full-tap wideband FD MIMO radios.

## CHAPTER 4

### SIMULTANEOUS CONTROL AND DATA COMMUNICATION IN SINGLE- AND MULTI-USER FD MIMO SYSTEMS

Due to its capability of simultaneous transmission and reception, full duplex systems can be utilized for extracting control information while maintaining data communication with other nodes. In this chapter, we study Simultaneous Communication of Data and Control (SCDC) information signals in FD MIMO wireless systems. In particular, considering an FD MIMO base station serving multiple single-antenna FD users, novel single and multi-user communication schemes for simultaneous DL beamformed data transmission and UL pilot-assisted channel estimation is presented. Capitalizing on our FD MIMO hardware architecture in Chapter 3 with reduced complexity self-interference analog cancellation, we jointly design the base station's transmit and receive beamforming matrices as well as the settings for the multiple analog taps and the digital SI canceller with the objective to maximize the DL sum rate.

#### 4.1 Introduction

Multi-user FD MIMO communication technology has the potential of substantial spectral efficiency improvement and simplification of the control information exchange over conventional

---

The content of this chapter is based on our published articles in [88] and [90]. Copyright © 2020 IEEE.

TDD and FDD systems through concurrent UL and DL communication in the same frequency and time resources [3, 24, 49, 51, 58, 67, 85, 86, 102].

As described in Chapter 1, the main bottleneck of FD MIMO systems is the in-band SI signal at the reception side resulting from simultaneous transmission and reception, as well as limited TX and RX isolation. Therefore, a combination of propagation domain isolation, analog domain suppression, and digital SI cancellation techniques are adopted in practice to suppress the strong SI below the noise floor [58, 59, 86]. In FD MIMO systems, the suppression techniques are particularly challenging due to higher SI components, as a consequence of the increased number of transceiver antennas. In Chapter 3, we presented a unified approach with multi-tap analog cancellation and TX/RX beamforming, where the number of taps does not scale with the product of TX and RX antenna elements while maximizing the achievable rate performance under practical transceiver imperfections.

Recently, in [89, 103, 104], simultaneous DL data transmission and UL Channel State Information (CSI) reception has been considered at an FD MIMO Base Station (BS) serving multiple HD User Equipment (UE) nodes. In these studies, the UEs transmit training symbols through the UL channel in a Time Division Multiple Access (TDMA) manner, which are utilized by the BS to estimate the DL channels leveraging channel reciprocity, while at the same time transmitting the DL payload to UEs for whom the DL CSI is already available. However, the adopted multi-user models consider perfect analog cancellation that is based on conventional FD MIMO architectures with fully connected analog cancellation, interconnecting all TX antenna elements in the FD node with all its RX antennas.

### 4.1.1 Contributions

The main contributions of this chapter are summarized as follows:

- We propose a novel simultaneous communication of data and control information signals for single FD MIMO wireless systems.
- considering a FD MIMO base station serving multiple single-antenna FD users, a novel multi-user communication scheme for simultaneous DL beamformed data transmission and UL pilot-assisted channel estimation is presented.
- Exploiting channel reciprocity and relying on FD operation, the proposed system performs joint digital TX beamforming for DL communication and UL pilot-assisted CSI estimation.
- Considering realistic modeling for imperfect channel estimation and CSI delay error, we present a joint optimization framework for the DL rate optimization and the accurate CSI estimation.
- Our representative Monte Carlo simulation results for an example algorithmic solution for single-user SCDC scheme demonstrate that the proposed FD-based joint communication and control scheme provides  $1.4\times$  the downlink rate of its half duplex counterpart.
- We also showcase superior achievable DL rate performance for the multi-user SCDC scheme with more than 50% reduction in the analog cancellation hardware complexity compared to the conventional FD MIMO architectures with fully connected analog cancellation.

## 4.2 System and Signal Models

A multi-user MIMO communication is considered with a BS node  $b$  containing  $N_b$  TX and RX antennas, and  $K$  single-antenna FD UE nodes<sup>1</sup>, as shown in Figure 18. Each antenna is attached to a dedicated TX/RX RF chain at all the nodes. A multi-tap analog SI canceller is applied in the FD BS node  $b$ , whereas each UE node deploys a single-tap SI canceller. The FD BS node is capable of performing digital TX beamforming realized, for simplicity, with linear filters. We consider UL/DL channel reciprocity and focus on simultaneous data communication and channel estimation, where the DL is intended for information data communication while the UL is used for transmitting training signals from UEs to the BS. The UL CSI estimation is used for designing the DL precoder to digitally process the data signals before transmission.

We assume that, for every channel use, the BS node  $b$  transmits the complex-valued information data symbols  $\mathbf{s}_b \in \mathbb{C}^{m_b \times 1}$  (chosen from a discrete modulation set) using the unit norm digital precoding vector  $\mathbf{V}_b \in \mathbb{C}^{N_b \times m_b}$ , where the  $m_b$  is the number of data streams. In the UL direction, the  $K$  users simultaneously send orthogonal training symbols to the BS node  $b$ , which can be denoted as  $\mathbf{s}_K \in \mathbb{C}^{K \times 1}$ . The signal transmissions at both BS and UE nodes are power limited to  $P_b$  and  $P_k$ , respectively. Specifically, the DL signal is such that  $\mathbb{E}\{\|\mathbf{V}_b \mathbf{s}_b\|^2\} \leq P_b$ , whereas the UL signal from all  $K$  UEs is constrained as  $\mathbb{E}\{\|\mathbf{s}_K\|^2\} \leq P_K$ .

---

<sup>1</sup>It is to be noted that the single-user case can be achieved by setting the number of UEs  $K = 1$ .

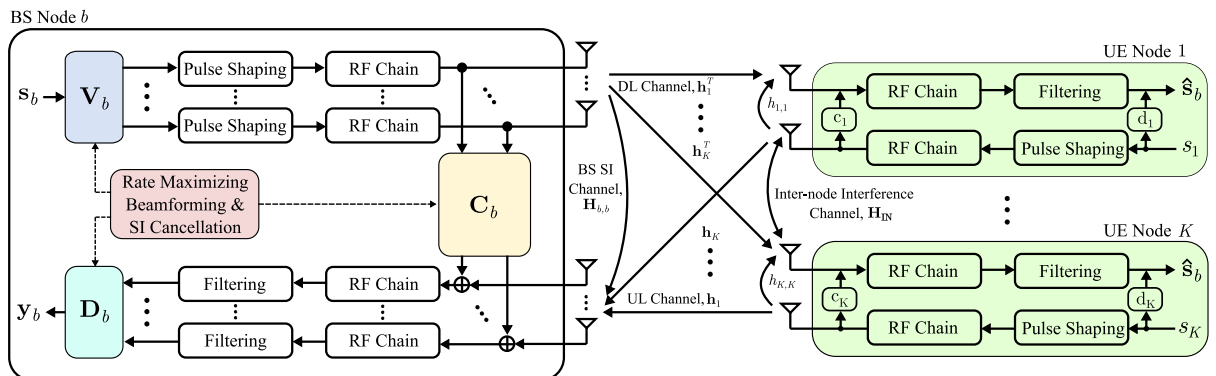


Figure 18. The considered multi-user FD MIMO system model for simultaneous DL data transmission and UL pilot-assisted channel estimation. BS node  $b$  and all UE nodes deploy A/D SI cancellation with the former node  $b$  realizing reduced complexity multi-tap analog cancellation.

#### 4.2.1 Channel Modeling

The Rayleigh faded DL channel from BS node  $b$  to UE node  $k$ , denoted by  $\mathbf{h}_k^T \in \mathbb{C}^{1 \times N_b}$ , is modeled as Independent and Identically Distributed (IID)  $\mathcal{CN}(0, l_K)$ , where  $l_K$  is the UL pathloss. Stacking all UE channel vectors, the DL channel for  $K$  users can be expressed as  $\mathbf{H} = [\mathbf{h}_1 \mathbf{h}_2 \cdots \mathbf{h}_K]^T \in \mathbb{C}^{K \times N_b}$ . Based on the UL/DL channel reciprocity, the Rayleigh faded UL channel is  $\mathbf{H}^T \in \mathbb{C}^{N_b \times K}$ . As all nodes are capable of FD operation, the simultaneous DL data and UL training transmission induce SI in the RXs of the BS and UEs, respectively. We consider the Rician fading model for the SI channels denoted by  $\mathbf{H}_{b,b} \in \mathbb{C}^{N_b \times N_b}$  for the BS and  $h_{k,k} \in \mathbb{C}, \forall k = 1, 2, \dots, K$ , for the UEs with Rician factor  $\kappa$  and pathlosses  $l_{b,b}$  and  $l_{k,k}$  at nodes  $b$  and  $k$ , respectively [24]. Using matrix notation, the SI channel for  $K$  users can be expressed

as  $\mathbf{H}_{K,K} = \text{diag}\{h_{1,1}, h_{2,2}, \dots, h_{K,K}\} \in \mathbb{C}^{K \times K}$ . Similarly, the inter-node interference channel between  $K$  users containing only off-diagonal elements is denoted as  $\mathbf{H}_{\text{IN}} \in \mathbb{C}^{K \times K} \mathcal{CN}(0, l_{\text{IN}})$ , where  $l_{\text{IN}}$  is the inter-node interference channel pathloss.

#### 4.2.2 Signal Modeling at the BS and UE Nodes

Because of FD operation, BS node  $b$  RXs receive the training symbols transmitted from  $K$  users as well as the SI signal induced by simultaneous data transmission. As shown in Figure 18, the SI is suppressed using low complexity analog SI cancellation, which is followed by a digital canceller in the baseband of BS node  $b$ . Denoting analog and digital SI cancellers as  $\mathbf{C}_b \in \mathbb{C}^{N_b \times N_b}$  and  $\mathbf{D}_b \in \mathbb{C}^{N_b \times N_b}$ , respectively, the received baseband signal at BS node  $b$ ,  $\mathbf{y}_b \in \mathbb{C}^{N_b \times 1}$ , can be expressed as

$$\begin{aligned} \mathbf{y}_b &\triangleq \mathbf{H}^T \mathbf{s}_K + (\mathbf{H}_{b,b} + \mathbf{C}_b + \mathbf{D}_b) \mathbf{V}_b \mathbf{s}_b + \mathbf{n}_b, \\ &= \mathbf{H}^T \mathbf{s}_K + \tilde{\mathbf{H}}_{b,b} \mathbf{V}_b \mathbf{s}_b + \mathbf{n}_b, \end{aligned} \quad (4.1)$$

where  $\mathbf{n}_b \in \mathbb{C}^{N_b \times 1}$  is the zero-mean AWGN with variance  $\sigma_b^2 \mathbf{I}_{N_b}$ . Here,  $\tilde{\mathbf{H}}_{b,b} \triangleq (\mathbf{H}_{b,b} + \mathbf{C}_b + \mathbf{D}_b)$  represents the residual SI channel after A/D SI cancellation.

Similarly, after A/D SI cancellation at each UE node, the precoded DL signal received at  $K$  user nodes,  $\mathbf{y}_K \in \mathbb{C}^{K \times 1}$  is written as

$$\begin{aligned} \mathbf{y}_K &\triangleq \mathbf{H} \mathbf{V}_b \mathbf{s}_b + (\mathbf{H}_{K,K} + \mathbf{C}_K + \mathbf{D}_K) \mathbf{s}_K + \mathbf{H}_{\text{IN}} \mathbf{s}_K + \mathbf{n}_K, \\ &= \mathbf{H} \mathbf{V}_b \mathbf{s}_b + \tilde{\mathbf{H}}_{K,K} \mathbf{s}_K + \mathbf{H}_{\text{IN}} \mathbf{s}_K + \mathbf{n}_K, \end{aligned} \quad (4.2)$$

where  $\mathbf{n}_K \in \mathbb{C}^{K \times 1}$  is the zero-mean AWGN with variance  $\sigma_K^2 \mathbf{I}_K$ .

Here,  $\mathbf{C}_K \triangleq \text{diag}\{c_{1,1}, c_{2,2}, \dots, c_{K,K}\} \in \mathbb{C}^{K \times K}$ ,  $\mathbf{D}_K \triangleq \text{diag}\{d_{1,1}, d_{2,2}, \dots, d_{K,K}\} \in \mathbb{C}^{K \times K}$ ,

where the diagonal elements of  $\mathbf{C}_K$  and  $\mathbf{D}_K$  represent the analog and digital SI canceller of each UE node, and  $\tilde{\mathbf{H}}_{K,K} \triangleq (\mathbf{H}_{K,K} + \mathbf{C}_K + \mathbf{D}_K)$  is the residual SI channel at all UE nodes.

### 4.3 Proposed SCDC Scheme

In this section, we present a multi-user FD MIMO based data communication and channel estimation scheme. First, we describe the CSI acquisition and DL beamforming scheme in Section 4.3.1. Then, in Section 4.3.2, we characterize the realistic channel estimation error, CSI delay error, and average achievable DL rate.

#### 4.3.1 Proposed CSI Acquisition and Beamforming

The proposed SCDC scheme is illustrated in Figure 19(a), where DL is dedicated for data transmission and UL is accessed to transmit training symbols. We assume a time division duplexing based data transmission, where the considered channels remains constant for all the channel uses in a time slot and the channels of successive time slots are temporally correlated [105, 106]. Each time slot contains  $T$  symbols (i.e.  $T$  channel uses). The proposed data transmission scheme and CSI acquisition scheme is described as follows:

1. For data transmission at any  $i$ th time slot, first, we obtain the UL channel estimate of  $(i-1)$ th time slot using  $T$  orthogonal training symbols sent from each UE, while maintaining simultaneous data transmission in the DL.
2. Using UL/DL reciprocity, we obtain the DL channel estimate at  $(i-1)$ th time slot from the UL channel estimate.

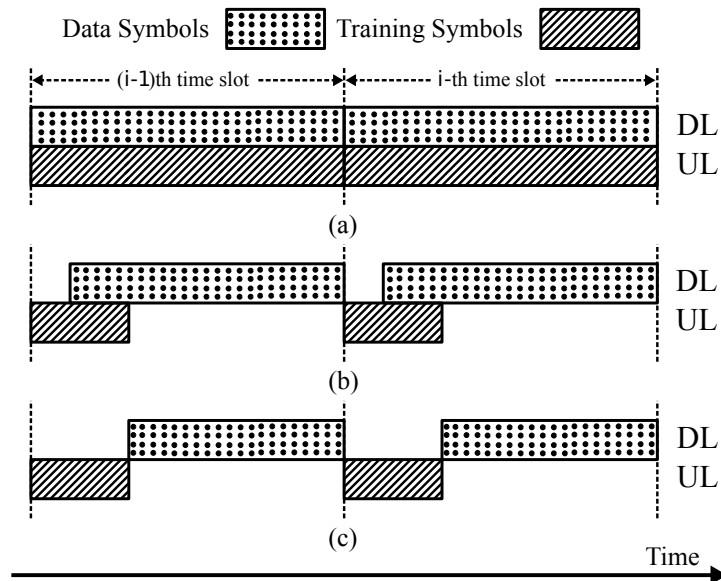


Figure 19. (a) Proposed SCDC Scheme, (b) Sequential Beamforming with DL data transmission and UL CSI, and (c) Conventional HD Beamforming with UL training over two consecutive time slots.

3. Based on the DL channel estimate, we derive the DL precoder  $\mathbf{V}_b[z]$  to process all the data streams at the  $i$ th time slot.

In Figure 19(b), the FD sequential beamforming approach of [104] is depicted, where the UEs access the UL channel in TDMA manner, and the BS initiates DL data transmission to the UEs with available CSI, instead of waiting for all the UEs to finish training. Figure Figure 19(c) represents the conventional HD MIMO scheme, where a fraction of the total channel uses is dedicated for UL training and the rest of each time slot is utilized for data transmission in DL direction.

### 4.3.2 Channel Estimation Error and Average DL Rate

To estimate the UL channel at  $(i-1)$ th time slot, the  $K$  users transmit orthogonal training symbols  $\mathbf{S}_K[i-1] \in \mathbb{C}^{K \times T}$ , such that  $\mathbb{E}[\mathbf{S}_K[i-1]\mathbf{S}_K^H[i-1]] = TP_K$ . Here, we utilize  $T$  training symbols in the UL direction for estimation, while maintaining DL data transmission enabled by FD. Therefore, the received training symbols at node  $b$  after A/D cancellation,  $\mathbf{Y}_b[i-1] \in \mathbb{C}^{N_b \times T}$ , can be expressed as

$$\begin{aligned} \mathbf{Y}_b[i-1] \triangleq & \mathbf{H}^T[i-1]\mathbf{S}_K[i-1] + \tilde{\mathbf{H}}_{b,b}[i-1]\mathbf{V}_b[i-1]\mathbf{S}_b[i-1] \\ & + \mathbf{N}_b[i-1], \end{aligned} \quad (4.3)$$

where  $\mathbf{H}^T[i-1]$ ,  $\tilde{\mathbf{H}}_{b,b}[i-1]$ ,  $\mathbf{V}_b[i-1]$ ,  $\mathbf{S}_b[i-1]$ , and  $\mathbf{N}_b[i-1]$  represent the UL channel, residual SI channel, DL precoder, transmit signal matrix, and AWGN noise matrix of node  $b$  RXs at  $(i-1)$ th time slot.

The considered MIMO channels  $\mathbf{H}[i-1]$  and  $\mathbf{H}[i]$  of the  $(i-1)$  and  $i$ th time slots, respectively, are assumed temporally correlated. Using the classical Jakes model, the correlation coefficient between DL channels  $\mathbf{H}[i-1]$  and  $\mathbf{H}[i]$  is defined as [106, Eq. (2.58)]

$$\rho \triangleq \mathbb{E}[\mathbf{H}^H[i]\mathbf{H}[i-1]] = J_0(2\pi f_d T_c), \quad (4.4)$$

where  $f_d$  is the Doppler frequency,  $T_c$  is the time difference between two consecutive time slots,  $J_0(\cdot)$  is the zero-th order Bessel function of the first kind. Using the Gauss-Markov error model, the time correlated DL channels in successive time slots can be expressed as [105]

$$\mathbf{H}[i-1] \triangleq \rho \mathbf{H}[i] + \sqrt{1 - \rho^2} \mathbf{E}[i], \quad (4.5)$$

where  $\mathbf{E}[i] \in \mathbb{C}^{K \times N_b}$  is the error matrix, whose entries are modeled as IID  $\mathcal{CN}(0, l_K)$ , and is independent of  $\mathbf{H}[i]$ . Due to reciprocity, similar time correlation, as in Equation 4.5, hold for all UL channels. Under this model, using UL/DL reciprocity, the received training signals at BS node  $b$  at the  $(i-1)$ th time slot can be written using Equation 4.3 as

$$\begin{aligned} \mathbf{Y}_b[i-1] &\triangleq \rho \mathbf{H}^T[i] \mathbf{S}_K[i-1] + \sqrt{(1 - \rho^2) P_K} \mathbf{E}_{UL}[i] \\ &+ \tilde{\mathbf{H}}_{b,b}[i-1] \mathbf{V}_b[i-1] \mathbf{S}_b[i-1] + \mathbf{N}_b[i-1], \end{aligned} \quad (4.6)$$

where  $\mathbf{E}_{UL}[i] \in \mathbb{C}^{N_b \times T}$  is the UL CSI delay error matrix modeled as IID  $\mathcal{CN}(0, l_K)$  and independent of  $\mathbf{N}_b[i-1]$ . Based on Equation 4.6, the UL channel  $\mathbf{H}^T[i]$  can be estimated using the Minimum Mean Squared Error (MMSE) estimator as [105]

$$\hat{\mathbf{H}}^T[i] \triangleq \frac{\rho \mathbf{Y}_b[i-1] \mathbf{S}_K^H[i-1]}{\sigma_b^2 + \sigma_{r,b}^2 + (1 - \rho^2) P_K l_K + \rho^2 T P_k}, \quad (4.7)$$

where  $\sigma_{r,b}^2 = \|\tilde{\mathbf{H}}_{b,b}[i-1]\mathbf{V}_b[i-1]\mathbf{S}_b[i-1]\|^2$  is the residual SI power after A/D cancellation at node  $b$ . From the UL estimate at the  $i$ th time slot, the relationship between the actual and estimated DL channels at the  $i$ th time slot, using the Gauss-Markov error model, can be written as [107]

$$\mathbf{H}[i] \triangleq \sqrt{1 - \tau_{\text{DL}}^2} \hat{\mathbf{H}}[i] + \tau_{\text{DL}} \mathbf{E}_{\text{DL}}[i], \quad (4.8)$$

where  $\mathbf{E}_{\text{DL}}[i]$  is the DL estimation error matrix having IID elements each modeled as  $\mathcal{CN}(0, l_K)$ , and  $\tau_{\text{DL}} \in [0, 1]$  is the Gauss-Markov error parameter that depends on the effective DL Signal-to-Noise-Ratio (SNR). The case  $\tau_{\text{DL}} = 0$  implies ideal DL CSI, whereas  $\tau_{\text{DL}} = 1$  signifies unavailable channel estimation. The Mean Squared Error (MSE) of the DL channel from Equation 4.7 at the BS node  $b$  is given by [105]

$$\text{MSE}_{\text{FD}} \triangleq \tau_{\text{DL}}^2 = \frac{\sigma_b^2 + \sigma_{r,b}^2 + (1 - \rho^2)P_K l_K}{\sigma_b^2 + \sigma_{r,b}^2 + (1 - \rho^2)P_K l_K + \rho^2 T P_k}, \quad (4.9)$$

Using the DL estimate  $\hat{\mathbf{H}}[i]$ , the achievable DL rate per channel use for the proposed SCDC scheme at the  $i$ th time slot can be derived as

$$\begin{aligned} \mathcal{R}_{\text{DL}}[i] \triangleq \log_2 \left( \det \left( \mathbf{I}_K + (1 - \tau_{\text{DL}}^2) P_b \hat{\mathbf{H}}[i] \mathbf{V}_b[i] \right. \right. \\ \left. \left. \times \mathbf{V}_b^{\text{H}}[i] \hat{\mathbf{H}}^{\text{H}}[i] \boldsymbol{\Sigma}_k[i]^{-1} \right) \right), \end{aligned} \quad (4.10)$$

where the interference-plus-noise covariance matrix:

$$\begin{aligned} \boldsymbol{\Sigma}_k[i] &\triangleq \sigma_K^2 \mathbf{I}_K + \tilde{\mathbf{H}}_{K,K}[i] \mathbf{s}_K[i] \mathbf{s}_K^H[i] \tilde{\mathbf{H}}_{K,K}^H[i] + \mathbf{H}_{\text{IN}}[i] \mathbf{s}_K[i] \\ &\quad \times \mathbf{s}_K^H[i] \mathbf{H}_{\text{IN}}^H[i] + \tau_{\text{DL}}^2 P_b l_K \mathbf{V}_b[i] \mathbf{V}_b^H[i]. \end{aligned} \quad (4.11)$$

#### 4.4 Proposed Joint Optimization Framework

In this section, we focus on the joint design of the digital TX precoder  $\mathbf{V}_b$ , the analog SI cancellers  $\mathbf{C}_b$  and  $c_k, \forall k = 1, \dots, K$ , as well as the digital cancellers  $\mathbf{D}_b$  and  $d_k, \forall k$  at BS node  $b$  and  $K$  UE nodes, respectively, maximizing the estimated achievable DL rate of  $i$ th time slot. It is to be noted that, for simplicity, we omit the time slot index in the subsequent optimization problem, as we are only dealing with variables at  $i$ th time slot, unless mentioned otherwise. Based on the estimated DL channel  $\hat{\mathbf{H}}$ , SI channels  $\hat{\mathbf{H}}_{b,b}$  and  $\hat{\mathbf{H}}_{K,K}$  at BS and UE nodes, respectively, the considered optimization problem is expressed as:

$$\begin{aligned} &\max_{\substack{\mathbf{V}_b, \mathbf{C}_b, \mathbf{D}_b \\ \mathbf{C}_K, \mathbf{D}_K}} \log_2 \left( \det \left( \mathbf{I}_K + (1 - \tau_{\text{DL}}^2) P_b \hat{\mathbf{H}} \mathbf{V}_b \mathbf{V}_b^H \hat{\mathbf{H}}^H \boldsymbol{\Sigma}_k^{-1} \right) \right) \\ \text{s.t.} \quad &P_b \| [(\hat{\mathbf{H}}_{b,b} + \mathbf{C}_b) \mathbf{V}_b]_{(j,:)} \|^2 \leq \lambda_b, \forall j = 1, 2, \dots, N_b, \\ &P_K \| [(\hat{\mathbf{H}}_{k,k} + \mathbf{C}_k)]_{(j,:)} \|^2 \leq \lambda_k, \forall j = 1, 2, \dots, K, \\ &\mathbb{E}\{\|\mathbf{V}_b \mathbf{s}_b\|^2\} \leq P_b, \text{ and } \mathbb{E}\{\|\mathbf{s}_K\|^2\} \leq P_K. \end{aligned} \quad (4.12)$$

In this formulation, the first constraint imposes the RX RF chain saturation threshold  $\lambda_b$  after analog cancellation at BS node  $b$ . As previously discussed, this threshold ensures proper recep-

---

**Algorithm 4** Proposed FD MIMO SCDC Design
 

---

**Input:**  $\widehat{\mathbf{H}}_{b,b}$ ,  $\widehat{\mathbf{H}}$ ,  $\widehat{\mathbf{H}}_{K,K}$ ,  $P_b$ ,  $P_K$ ,  $N$ , and  $N_b$ .

**Output:**  $\mathbf{V}_b$ ,  $\mathbf{C}_b$ ,  $\mathbf{C}_K$ ,  $\mathbf{D}_b$ , and  $\mathbf{D}_K$ .

- 1: Obtain the  $N$ -tap analog canceller  $\mathbf{C}_b$  using [59, Eq. 1].
  - 2: Obtain  $\mathbf{Q}_b$  including the  $N_b$  right-singular vectors of  $(\widehat{\mathbf{H}}_{b,b} + \mathbf{C}_b)$  corresponding to the singular values in descending order.
  - 3: Set  $\mathbf{C}_K = -\widehat{\mathbf{H}}_{K,K}$ .
  - 4: **for**  $\alpha = N_b, N_b - 1, \dots, 2$  **do**
  - 5:     Set  $\mathbf{F}_b = [\mathbf{Q}_b]_{(:, N_b - \alpha + 1 : N_b)}$ .
  - 6:     Set  $\mathbf{W}_b = \text{sort}(\widehat{\mathbf{H}}\mathbf{F}_b)$ , rearranging the rows of  $\widehat{\mathbf{H}}\mathbf{F}_b$  based on descending row vector norm.
  - 7:     Set  $\mathbf{Z}_b = [\mathbf{W}_b]_{(1:m_b, :)}$ .
  - 8:     Set  $\mathbf{G}_b = \beta_{\text{ZF}} \mathbf{Z}_b^H (\mathbf{Z}_b \mathbf{Z}_b^H)^{-1}$ , where  $\beta_{\text{ZF}}$  is the normalization constant that ensures  $\mathbb{E}[\text{tr}(\mathbf{G}_b \mathbf{G}_b^H)] = 1$ .
  - 9:     Set the DL precoder as  $\mathbf{V}_b = \mathbf{F}_b \mathbf{G}_b$ .
  - 10:     **if**  $P_b \|[(\widehat{\mathbf{H}}_{b,b} + \mathbf{C}_b)\mathbf{V}_b]_{(j,:)}\|^2 \leq \lambda_b, \forall j = 1, 2, \dots, N_b$ , and  $P_K \|[(\widehat{\mathbf{H}}_{k,k} + \mathbf{C}_k)]_{(j,:)}\|^2 \leq \lambda_k, \forall j = 1, 2, \dots, K$  **then**
  - 11:         Output  $\mathbf{V}_b$ ,  $\mathbf{C}_b$ ,  $\mathbf{C}_K$ ,  $\mathbf{D}_b = -(\widehat{\mathbf{H}}_{b,b} + \mathbf{C}_b)$ ,  $\mathbf{D}_K = -(\widehat{\mathbf{H}}_{K,K} + \mathbf{C}_K)$ , and stop the algorithm.
  - 12:     **end if**
  - 13: **end for**
  - 14: Set  $\mathbf{V}_b = [\mathbf{Q}_b]_{(:, N_b)}$ .
  - 15: **if**  $P_b \|[(\widehat{\mathbf{H}}_{b,b} + \mathbf{C}_b)\mathbf{V}_b]_{(j,:)}\|^2 \leq \lambda_b, \forall j = 1, 2, \dots, N_b$ , and  $P_K \|[(\widehat{\mathbf{H}}_{k,k} + \mathbf{C}_k)]_{(j,:)}\|^2 \leq \lambda_k, \forall j = 1, 2, \dots, K$  **then**
  - 16:     Output  $\mathbf{V}_b$ ,  $\mathbf{C}_b$ ,  $\mathbf{C}_K$ ,  $\mathbf{D}_b = -(\widehat{\mathbf{H}}_{b,b} + \mathbf{C}_b)$ ,  $\mathbf{D}_K = -(\widehat{\mathbf{H}}_{K,K} + \mathbf{C}_K)$ , and stop the algorithm.
  - 17: **else**
  - 18:     Output that the  $\mathbf{C}_b$  realizations or  $\mathbf{C}_K$  do not meet the receive RF saturation constraints.
  - 19: **end if**
- 

tion of the training symbols by all  $N_b$  RX RF chains of the BS, which means that the UL channel can be efficiently estimated using Equation 4.7. The second constraint enforces the saturation threshold  $\lambda_K$  at the  $K$  UEs assuring feasible decoding of BS's information data symbols. The final two constraints in Equation 4.12 refer to the nodes' average transmit powers.

The optimization problem in Equation 4.12 is quite difficult to tackle, since it is non-convex including couplings among the optimization variables. In this chapter, we suboptimally solve it using an alternating optimization approach, leaving other possibilities for future work. To this end, we start with an allowable  $\mathbf{C}_b$  realization given the available number of analog canceller taps  $N$ , where the tap values are set to be the respective amplitude elements of the estimated SI channel  $\widehat{\mathbf{H}}_{b,b}$ . Based on the chosen  $\mathbf{C}_b$ , we seek for the precoding matrix  $\mathbf{V}_b$  maximizing the DL rate, while meeting the first constraint for the BS analog SI cancellation threshold  $\lambda_b$ . This procedure is repeated for all allowable realizations of  $\mathbf{C}_b$  to find the best pair of  $\mathbf{C}_b$  and  $\mathbf{V}_b$ . Adopting the approach in [59], the BS precoder for DL data communication is constructed as  $\mathbf{V}_b = \mathbf{F}_b \mathbf{G}_b$ , where  $\mathbf{F}_b \in \mathbb{C}^{N_b \times \alpha}$  aims at reducing the residual SI after analog cancellation and  $\mathbf{G}_b \in \mathbb{C}^{\alpha \times m_b}$  is the Zero-Forcing (ZF) beamformer maximizing the rate of the effective DL channel  $\widehat{\mathbf{H}} \mathbf{F}_b$ . The parameter  $\alpha$  is a positive integer taking the values  $1 \leq \alpha \leq N_b$ . At each of the UE nodes, a single-tap analog canceller is employed resulting in a diagonal analog SI canceller matrix  $\mathbf{C}_K = -\widehat{\mathbf{H}}_{K,K}$ . To maximize the signal-to-interference-plus-noise ratio, the residual SI is further reduced by setting the digital cancellation signal at both FD nodes as their respective complementary residual SI channels after analog SI cancellation. For each allowable realization of  $\mathbf{C}_b$ , the proposed solution for the considered optimization problem Equation 4.12 is summarized in Algorithm 4.

#### 4.5 Evaluation of SCDC Scheme for Single-user FD MIMO System

In this section, we investigate the performance of the proposed FD-enabled simultaneous DL information data and UL training data transmission scheme for single-user FD MIMO sys-

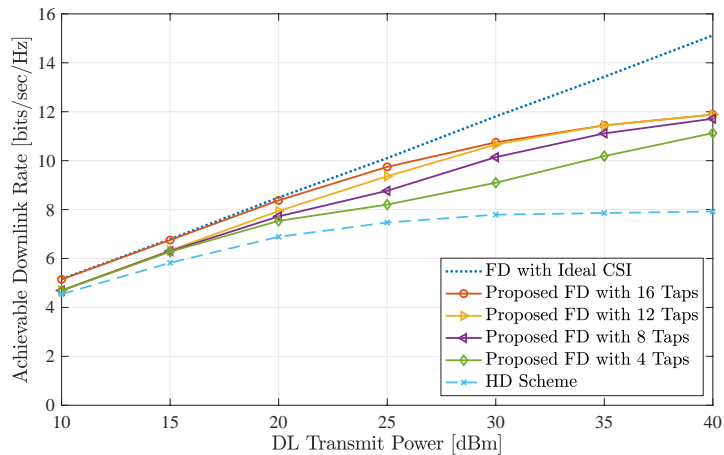


Figure 20. Achievable DL rate of the proposed FD SCDC scheme for a single-user versus the DL transmit power in dBm for the case of limited UL transmit power at 5dBm.

tems. The simulation parameters and assumptions are detailed in the following Sec. 4.5.1, while Sec. 4.5.2 presents representative results on the achievable DL rate and UL channel estimation.

#### 4.5.1 Simulation Parameters

We perform an extensive simulation following the FD MIMO architecture illustrated in Fig. Figure 18. We have considered a  $4 \times 4$  (i.e.,  $N_b = 4$ ) FD MIMO BS node  $b$  serving a FD single-antenna UE node  $u$ . Both DL and UL channels are assumed as block Rayleigh fading channels with a pathloss of 110dB. The SI channels at both FD nodes  $b$  and  $u$  are simulated as Rician fading channel with a  $K$ -factor of 35dB and pathloss of 40dB [24]. We have considered a narrowband communication system with a bandwidth of 1.4MHz, which is a supported bandwidth for LTE. RX noise floors at both nodes were assumed to be  $-110$ dBm. To this end, the RXs have effective dynamic range of 62.24dB provided by the 14-bit ADC for

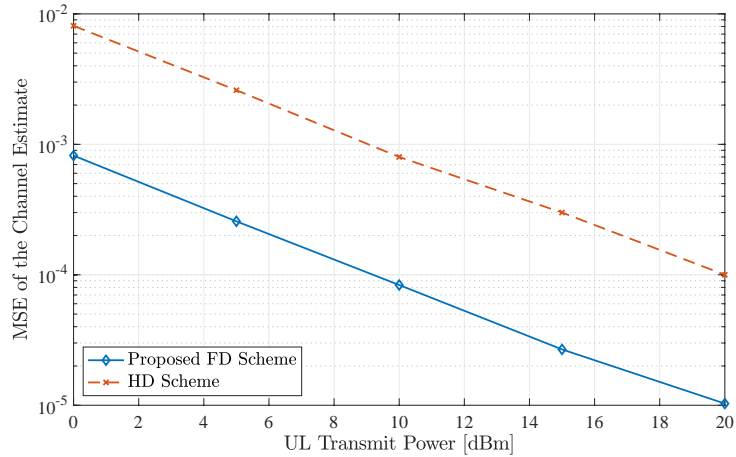


Figure 21. MSE of UL channel estimation versus the UL transmit power for the case where the DL transmit power is 40dBm.

a PAPR of 10 dB [98]. Therefore, the residual SI power after analog SI cancellation at the input of each RX chain has to be below  $-47.76\text{dBm}$  to avoid saturation. Furthermore, non-ideal multi-tap analog canceller is considered with steps of  $0.02\text{dB}$  for attenuation and  $0.13^\circ$  for phase as in [59]. We have used 1000 independent Monte Carlo simulation runs to calculate the performance of all considered designs. In each run, a total number of  $T = 400$  symbols were considered in every transmission packet. For the compared HD scheme, 10% the packet's symbols (i.e.,  $T_{\text{HD}} = 40$ ) were dedicated for UL channel sounding.

#### 4.5.2 Achievable DL Rate and CSI Estimation Performances

Figure 20 depicts the achievable DL rate performance of the single-user FD SCDC scheme as a function of the DL transmit power in dBm for the case where the UL transmit power for training data is 5dBm with 50dB digital SI cancellation. We have considered different

numbers for the analog canceller taps  $N$  for the proposed FD MIMO architecture at BS node  $b$ , and also sketched the performance of the ideal CSI case with  $N = 16$  together with the HD-based transmission scheme discussed in 4.5.1. It is shown in the figure that, for low to moderate transmit powers ( $\leq 20\text{dBm}$ ), the proposed FD-based transmission scheme exhibits similar performance to the ideal CSI case. The performance gap in large transmit powers is a consequence of practical CSI estimation error and residual SI at the FD RXs. For the highest considered transmit power of  $40\text{dBm}$ , Algorithm 1 results in less than  $1\text{bit}/\text{sec}/\text{Hz}$  DL rate gap between 4 and 16 taps for analog SI cancellation, leading to 75% reduction in the hardware complexity for the analog canceller. It is also evident that, for all DL transmit powers, the proposed scheme outperforms HD-based transmissions. For example, when the DL transmit power is  $40\text{dBm}$ , the DL data rate with FD-based transmissions is  $1.4\times$  the HD-based one. The MSE of CSI estimation versus the UL transmit power in dBm is shown in Figure 21 for the case where the DL transmit power is  $40\text{dBm}$ . It is noted that the proposed FD-based scheme provides similar MSE performance irrespective of  $N$ , since it targets reducing SI at BS's RX below the noise floor for all cases. Despite the residual SI, the proposed scheme exhibits substantially smaller MSE compared to the HD scheme, since the former supports simultaneous communication of 400 ( $T = 400 \gg T_{\text{HD}} = 40$ ) UL training symbols together with 400 DL information data symbols. Finally, Figure 22 plots the achievable DL rate for different UL transmit powers and DL transmit power of  $40\text{dBm}$ . It is shown that with increasing UL transmit power, the DL rate of the proposed FD-based scheme with CSI estimation approaches that of the ideal CSI case, which witnesses that the CSI error decreases. The same trend happens for

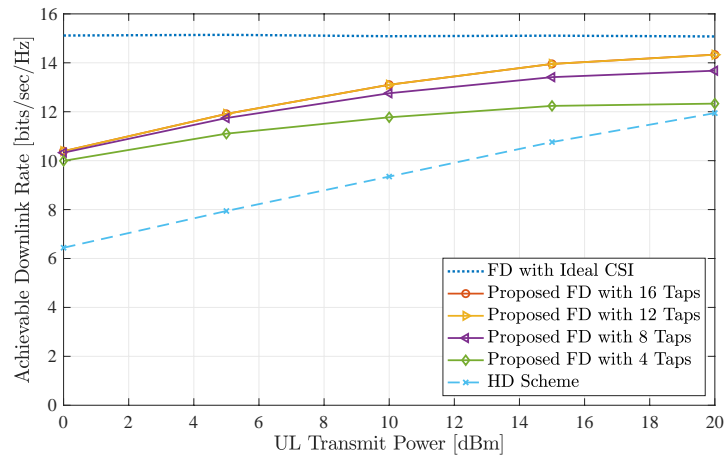


Figure 22. Achievable DL rate versus the UL transmit power for the case where the DL transmit power is 40dBm.

the HD-based transmission scheme, whose DL rate performance is however outperformed from the proposed scheme with only 4 analog SI cancellation taps. For UL transmit powers larger than 12.5dB, the DL rate performance of the proposed scheme is around 1bit/sec/Hz close to the ideal CSI case with 50% reduction in the number of the analog taps.

#### 4.6 Evaluation of SCDC Scheme for Multi-user FD MIMO System

In this section, we provide representative simulation results of the proposed FD-based MU MIMO simultaneous data communication and channel estimation approach. In Section 4.6.1, we describe the existing FD and HD MIMO solutions to be compared with our proposed approach. The simulations parameters and assumptions are detailed in Section 4.6.2, whereas the hardware complexity, and achievable DL rate results are presented in Section 4.6.3.

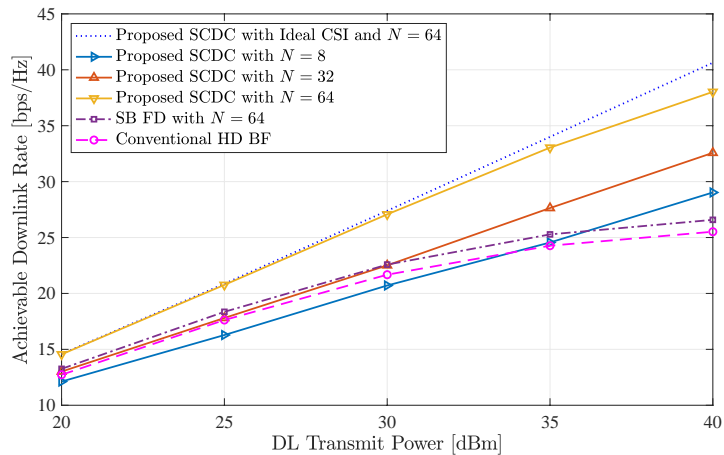


Figure 23. Achievable DL Rate w.r.t DL transmit power for  $N_b = 8$ ,  $K = 4$ ,  $f_d = 50\text{Hz}$  and different analog canceller taps  $N$ .

#### 4.6.1 Compared FD and HD MIMO Designs

We compare our novel FD SCDC scheme with the Sequential Beamforming (SB) FD approach presented in [104], where the UEs send their training symbols using TDMA. Contrary to the conventional HD MIMO approach, which is also illustrated here for comparison, in SB FD approach, the BS node does not wait for all the UEs to finish training. In SB FD, the BS starts transmitting to the UE with available CSI at the BS node, while receiving training from other UEs. The SB FD approach considers perfect analog SI cancellation, which includes full-tap analog SI canceller. In addition, we also illustrate the proposed FD approach with ideal CSI and full-tap analog SI canceller.

### 4.6.2 Simulation Parameters

We perform an extensive simulation following the FD MIMO architecture illustrated in Fig. Figure 18. We have considered an  $8 \times 8$  (i.e.,  $N_b = 8$ ) FD MIMO BS node  $b$  serving  $K = 4$  single-antenna FD UE nodes. DL, UL, and inter-node interference channels are assumed as block Rayleigh fading channels with a pathloss of 110dB. The SI channels at the BS and all UE nodes are simulated as Rician fading channels with a  $\kappa$ -factor of 30dB and pathloss of 40dB [24]. We have considered a narrowband communication system with a bandwidth and carrier frequency of 1.4MHz and 2.4GHz, respectively. RX noise floors at all nodes were assumed to be  $-100$ dBm. To this end, the RXs have effective dynamic range of 50dB provided by the 12-bit ADC for a PAPR of 10 dB [98]. Therefore, the residual SI power after analog SI cancellation at the input of each RX chain has to be below  $-50$ dBm to avoid RX RF chain saturation. Furthermore, non-ideal multi-tap analog canceller is considered with steps of 0.02dB for attenuation and  $0.13^\circ$  for phase as in [59]. All the user nodes employ single-tap SI canceller, where the MIMO BS node requires an  $N$ -tap analog SI canceller. We have used 1000 independent Monte Carlo simulation runs to calculate the performance of all considered designs. Every transmission time slot is considered to be 1ms with  $T = 400$  symbols. For the compared HD and SB FD scheme, 10% of the total symbols were dedicated for UL channel sounding. The UL transmit power of each UE node is limited to 10dBm for all considered designs.

### 4.6.3 Analog Canceller Complexity and Achievable DL Rate

We illustrate the DL rate performance of the proposed and other considered designs in Figure 23 with respect to DL transmit power for  $K = 4$ ,  $f_d = 50$ Hz and varying analog

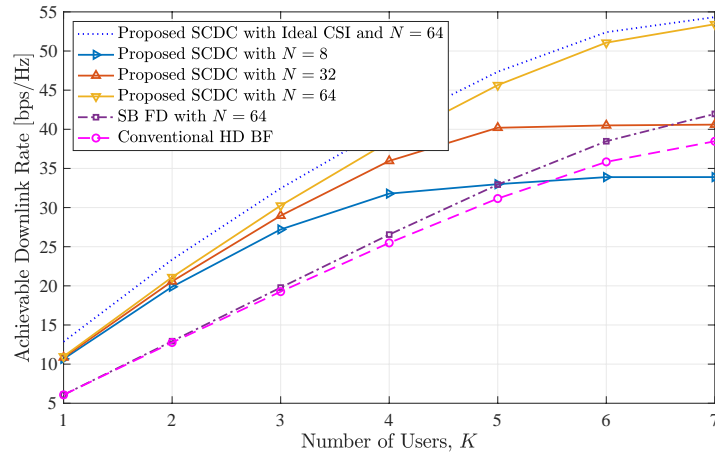


Figure 24. Achievable DL Rate of FD MU system w.r.t number of UEs  $K$  for  $N_b = 8$ ,  $P_b = 40\text{dBm}$ ,  $f_d = 50\text{Hz}$  and different analog canceller taps  $N$ .

canceller taps  $N$ . The proposed SCDC scheme with full-tap analog canceller with  $N = 64$  provides DL rate close to the ideal case for transmit power below 30dBm and outperforms all other considered designs for all transmit powers. After 50% reduction of analog canceller taps, the proposed approach with  $N = 32$  still provides  $1.25\times$  DL rate compared to the SB FD [104] and conventional HD approach for transmit power of 40dBm, while achieving identical DL rate performance for low transmit powers. Furthermore, we consider a more extreme case with  $N = 8$ , which results in an analog SI canceller with only 12.5% taps. Although, such low-complexity SCDC approach provides less DL rate compared to the SB FD approach, it can achieve higher performance for high transmit powers above 35dBm. In Figure 24, we plotted the achievable DL rate of the considered transmission schemes with respect to the the number of UEs  $K$  being served by the FD BS node for a fixed DL transmit power of 40dBm. It is

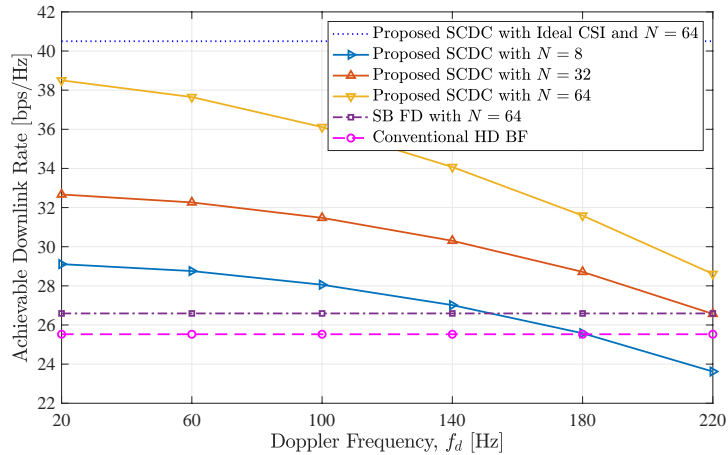


Figure 25. Achievable DL Rate w.r.t Doppler frequency  $f_d$  for  $N_b = 8$ ,  $P_b = 40\text{dBm}$ ,  $K = 4$  and different analog canceller taps  $N$ .

evident from the figure that, the proposed SCDC scheme with  $N = 64$  provides substantial DL rate increment compared to the SB FD [104] and the conventional FD design for any number of UEs. However, the proposed approach with  $N = 32$  can efficiently serve 6 UEs providing better DL rate than the SB FD approach. For a further reduction of canceller taps, the proposed SCDC approach with  $N = 8$  achieves higher rate than SB FD and conventional HD scheme up to 5 UEs. Therefore, the proposed SCDC scheme provides a flexible design with an important trade-off between number of UEs and analog SI canceller taps that achieves higher DL rate performance compared to the full-tap SB FD approach.

We showcase the DL rate performance of the considered design with respect to the Doppler frequency  $f_d$  in Figure 25 for  $K = 4$  UEs and fixed DL transmit power of 40dBm. As described in 4.3.2, the successive time slots are correlated and the correlation coefficient is measured using

$f_d$  given  $T_c = 1\text{ms}$ . It is evident from Figure 25 that the increment of  $f_d$  only affects the proposed scheme, as it estimates the DL channel based on the training symbols acquired in the preceding time slot. However, it is shown that the proposed schemes with  $N = 64$  and  $N = 32$  taps provide superior rate compared to the SB FD [104] and the conventional HD approach for a high Doppler frequency of 220Hz, which for our considered communication parameter represents a relative velocity 100km/h between BS and UE nodes. The proposed SCDC scheme with  $N = 8$  can achieve higher rate for  $f_d$  up to 140Hz. Therefore, we conclude that, compared to the SB FD and conventional HD scheme, the proposed SCDC approach can achieve higher rates with 50% less taps.

#### 4.7 Concluding Remarks

In this chapter, we proposed single- and multi-user FD MIMO communication systems for simultaneous DL information data transmission and UL CSI estimation with reduced complexity multi-tap analog SI cancellation. Considering an MMSE-based channel estimation error model, we presented a unified optimization framework for the joint design of digital TX precoding and A/D SI cancellation. Our performance evaluation results demonstrated that the proposed SCDC protocol is capable of achieving improved achievable DL rates for both single- and multi-user systems compared to the existing FD and conventional HD systems, requiring reduced complexity analog cancellation compared to conventional FD MIMO architectures.

## CHAPTER 5

### SELF-INTERFERENCE CANCELLATION FOR FULL DUPLEX MASSIVE MIMO SYSTEMS WITH HYBRID BEAMFORMERS

Current wireless systems, and visions for 6G, adopt the massive MIMO technologies [6], which rely on multiple TX and RX antennas and beamforming techniques to offer highly reliable and high throughput communication links. Naturally, if SI can be suppressed below the reception noise floor, combining FD with MIMO communication will further boost the spectral efficiency of FD operation compared to the case of FD SISO systems. Hybrid A/D beamforming architectures have been lately considered as a candidate technology for realizing massive MIMO transceivers with very large number of antenna elements, but with much fewer numbers of RF chains. However, as the number of TX and/or RX antennas increases, mitigating SI becomes more challenging, since more antennas result in more interference components. In this chapter, we present a novel architecture for full duplex hybrid A/D transceivers including multi-tap analog cancellation with reduced number of taps and simple multiplexers for efficient signal routing among the transceiver RF chains. Capitalizing on the proposed transceiver architec-

---

Part of this chapter is based on our published and submitted articles in [102] and [108], respectively. Copyright © 2020, 2022 IEEE.

ture, we present a joint design of analog cancellation and A/D beamforming with the objective to maximize the full duplex rate performance.

## 5.1 Introduction

The FD technology has been lately theoretically combined with Hybrid analog and digital BeamForming (HBF) [109] to enable simultaneous UL and DL communications in massive MIMO systems operating in the millimeter wave frequency bands [110–112]. These works mainly assigned the role of SI mitigation to the hybrid beamformers and/or deployed analog SI cancellation that scales with the number of TX/RX antennas.

Recently, in [110–114], hybrid beamforming SI mitigation approach has been introduced for FD massive MIMO systems. Specifically, these studies achieves SI suppression through both analog RF precoding and digital baseband beamforming. In [113], authors provide a suboptimal solution for analog RF beamformers suppressing the SI, whereas a multi-user hybrid beamforming cancellation approach is presented in [110]. More recently, the authors in [111] proposed a fully-digital hybrid beamforming solution for SI mitigation. However, all these approaches assume an RF hardware based analog SI cancellation where the hardware requirements scale with the number of TX/RX antennas.

### 5.1.1 Contributions

The contribution of this chapter is as follows.

- We present a novel hardware architecture for FD HBF systems enabling the joint design of A/D TX/RX beamformers with reduced complexity tap-based analog cancellation.

- The proposed analog canceller interconnects a subset of the outputs of the TX RF chains to a subset of the inputs to the RX RF chains in order to ensure that the residual SI signal after A/D TX precoding and analog RX combining remains below the noise floor.
- We also derive a novel sub-rate based RF TX/RX beamforming design that remove the computational complexity of analog beam selection compared to a conventional exhaustive search approach.
- Our indicative simulation results with the proposed architecture and an example FD HBF algorithmic framework showcase a 1.7 times rate improvement over HD HBF communication.

## 5.2 System Model and Proposed Architecture

In this section, the considered FD MIMO communication system is introduced and the proposed FD HBF hardware architecture is detailed together with the received signal models.

### 5.2.1 System Model

We consider the 3-user bidirectional communication system in Figure 26 comprising of a FD MIMO node  $k$  equipped with  $N_k$  TX and  $M_k$  RX antenna elements, and two half duplex multi-antenna nodes  $q$  and  $m$  having  $M_q$  and  $N_m$  antennas, respectively. Without loss of generality, it is assumed that node  $k$  communicates simultaneously (in the same time and frequency resources) with node  $q$  in the DL and node  $m$  in the UL directions. All nodes are considered capable of performing digital beamforming, which for simplicity we assume hereinafter to be realized with linear filters. Node  $k$  is also capable of analog TX/RX beamforming using the partially connected HBF architecture [109], as will be detailed in the sequel.

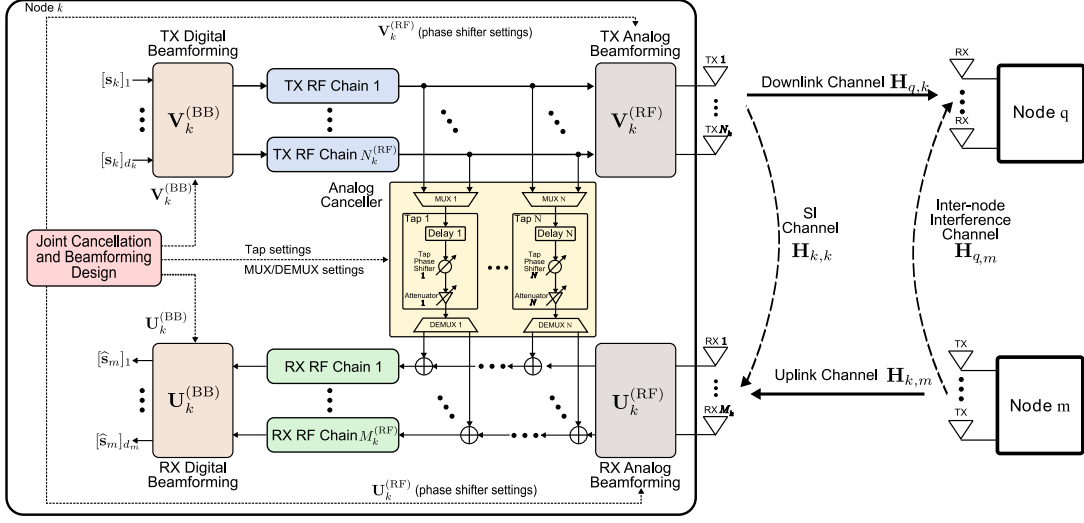


Figure 26. The considered bidirectional communication system with the proposed FD HBF architecture in the MIMO node  $k$  including  $N$ -tap analog cancellation and A/D TX/RX beamforming. The HD multi-antenna nodes  $q$  and  $m$  communicate with node  $k$  in the DL and UL directions, respectively.

It is assumed that node  $m$  makes use of the digital precoding matrix  $\mathbf{V}_m^{(\text{BB})} \in \mathbb{C}^{N_m \times d_m}$  for processing in BB its unit power symbol vector  $\mathbf{s}_m \in \mathbb{C}^{d_m \times 1}$  (chosen from a discrete modulation set) before UL transmission. The dimension of  $\mathbf{s}_m$  satisfies  $d_m \leq \min\{M_k^{(\text{RF})}, N_m\}$  with  $M_k^{(\text{RF})}$  (it holds  $M_k^{(\text{RF})} \leq M_k$ , although in practice  $M_k^{(\text{RF})} \ll M_k$ ) denoting the number of RX RF chains at node  $k$ . The latter constraint certifies data decodability for the considered UL communication. It additionally holds that  $\mathbb{E}\{\|\mathbf{V}_m^{(\text{BB})} \mathbf{s}_m\|^2\} \leq P_m$ , where  $P_m$  is the total TX power of node  $m$ . On the DL direction, the reception node  $q$  applies the digital combining matrix  $\mathbf{U}_q^{(\text{BB})} \in \mathbb{C}^{N_q \times d_k}$  in the BB received signal that includes the unit power symbol vector  $\mathbf{s}_k \in \mathbb{C}^{d_k \times 1}$  (chosen from a discrete modulation set) transmitted from node  $k$  such that  $d_k \leq \min\{M_q, N_k^{(\text{RF})}\}$  with  $N_k^{(\text{RF})}$

( $N_k^{(\text{RF})} \leq N_k$ , but practically  $N_k^{(\text{RF})} \ll N_k$ ) denoting the number of TX RF chains at node  $k$ . Similarly, the latter constraint verifies the spatial DoF of the effective  $M_q \times N_k^{(\text{RF})}$  DL MIMO channel between the TX RF chains of node  $k$  and the RX RF chains of node  $q$ ; recall that each antenna at node  $q$  is connected to a dedicated RF chain.

### 5.2.2 Proposed FD HBF Hardware Architecture

The proposed FD HBF hardware architecture comprising of  $N$ -tap analog cancellation for the SI signal as well as A/D precoding and combining for the outgoing and incoming signals is adopted for the MIMO node  $k$ , as depicted in the left part of Figure 26. Differently from [59]'s architecture that considered only fully digital TX/RX beamforming, node  $k$  is capable of HBF through its partially connected beamforming architecture. As shown in the figure, the analog canceller interconnects the  $N_k^{(\text{RF})}$  inputs of the analog TX precoder to the  $M_k^{(\text{RF})}$  outputs of the analog RX combiner. Evidently, the complexity of the analog canceller expressed in the number of taps  $N$  is independent of the numbers  $N_k$  and  $M_k$  of the TX and RX antennas, respectively, and as it will be shown in the results' section scales with the product  $\lambda N_k^{(\text{RF})} M_k^{(\text{RF})}$  with  $\lambda < 1$ . This is in contrast to [59] where the analog canceller interconnects the  $N_k$  TX antenna inputs to the  $M_k$  RX antenna outputs, and hence  $N$  scales as  $\lambda N_k M_k$  with  $0.5 \leq \lambda < 1$ .

### 5.2.3 Partially Connected HBF

Each of the  $N_k^{(\text{RF})}$  TX and  $M_k^{(\text{RF})}$  RX RF chains of node  $k$  is connected to a separate subset of the available TX antenna elements. As shown in Figure 26, the  $i$ -th TX RF chain with  $i = 1, 2, \dots, N_k^{(\text{RF})}$  is connected via phase shifters with  $N_k^{(\text{A})}$  TX antenna elements, each denoted as  $\text{TX}(i, j) \forall j = 1, 2, \dots, N_k^{(\text{A})}$ . Clearly, it holds  $N_k = N_k^{(\text{RF})} N_k^{(\text{A})}$  for the total number

of TX antennas at node  $k$ . Stacking the values of the  $N_k^{(A)}$  phase shifters that connect each  $i$ -th TX RF chain with its antenna elements in a complex-valued  $N_k^{(A)} \times 1$  vector  $\mathbf{v}_i$ , we can formulate the complex-valued  $N_k \times N_k^{(\text{RF})}$  analog TX precoder, as follows:

$$\mathbf{V}_k^{(\text{RF})} = \begin{bmatrix} \mathbf{v}_1 & \mathbf{0}_{N_k^{(A)}} & \cdots & \mathbf{0}_{N_k^{(A)}} \\ \mathbf{0}_{N_k^{(A)}} & \mathbf{v}_2 & \cdots & \mathbf{0}_{N_k^{(A)}} \\ \vdots & \vdots & \ddots & \vdots \\ \mathbf{0}_{N_k^{(A)}} & \mathbf{0}_{N_k^{(A)}} & \cdots & \mathbf{v}_{N_k^{(\text{RF})}} \end{bmatrix}. \quad (5.1)$$

The elements of each  $\mathbf{v}_i$  are assumed to have constant magnitude, i.e.,  $|\mathbf{v}_i|_n|^2 = 1/N_k^{(A)} \forall n = 1, 2, \dots, N_k^{(A)}$ . In addition, we assume that  $\mathbf{v}_i \in \mathbb{F}_{\text{TX}} \forall i$ , which means that all analog TX precoding vectors belong in a predefined beam codebook  $\mathbb{F}_{\text{TX}}$  including  $\text{card}(\mathbb{F}_{\text{TX}})$  distinct vectors (or analog beams). Apart from applying  $\mathbf{V}_k^{(\text{RF})}$  in the analog domain to the information bearing signal before transmission, the symbol vector  $\mathbf{s}_k$  is also processed in BB with the digital TX precoder  $\mathbf{V}_k^{(\text{BB})} \in \mathbb{C}^{N_k^{(\text{RF})} \times d_k}$  (recall that  $d_k \leq \min\{M_k, N_k^{(\text{RF})}\}$ ) before entering into the  $N_k^{(\text{RF})}$  TX RF chains, as shown in Figure 26. Similar to the UL communication from node  $m$  to  $k$ , we assume that the DL transmission from node  $k$  to  $q$  is power limited according to  $\mathbb{E}\{\|\mathbf{V}_k^{(\text{RF})}\mathbf{V}_k^{(\text{BB})}\mathbf{s}_k\|^2\} \leq P_k$  with  $P_k$  being the total available TX power at node  $k$ .

The RX side of node  $k$  is composed of an analog combiner connecting the RX antenna elements with the inputs of the RX RF chains, and a digital combiner that processes the outputs of the RX RF chains in BB before signal decoding. In particular, the  $n$ -th RX RF chain with  $n = 1, 2, \dots, M_k^{(\text{RF})}$  is connected through phase shifters with  $M_k^{(A)}$  RX antenna

elements; each such component is denoted as  $\text{RX}(n, \ell) \forall \ell = 1, 2, \dots, M_k^{(A)}$ . It should hold that  $M_k = M_k^{(\text{RF})} M_k^{(A)}$  for the total number of RX antennas at node  $k$ . Similar to Equation 5.1, we define the complex-valued  $M_k \times M_k^{(\text{RF})}$  analog RX combiner as:

$$\mathbf{U}_k^{(\text{RF})} = \begin{bmatrix} \mathbf{u}_1 & \mathbf{0}_{M_k^{(A)}} & \cdots & \mathbf{0}_{M_k^{(A)}} \\ \mathbf{0}_{M_k^{(A)}} & \mathbf{u}_2 & \cdots & \mathbf{0}_{M_k^{(A)}} \\ \vdots & \vdots & \ddots & \vdots \\ \mathbf{0}_{M_k^{(A)}} & \mathbf{0}_{M_k^{(A)}} & \cdots & \mathbf{u}_{M_k^{(\text{RF})}} \end{bmatrix}, \quad (5.2)$$

where each  $\mathbf{u}_n$  contains the constant magnitude values of the  $M_k^{(A)}$  phase shifters (i.e.,  $|\mathbf{u}_n[j]|^2 = 1/M_k^{(A)} \forall j = 1, 2, \dots, M_k^{(A)}$ ) connecting each  $n$ -th RX RF chain with its antenna elements. We further assume that  $\mathbf{u}_n \in \mathbb{F}_{\text{RX}} \forall n$ , implying that all analog RX combining vectors belong in a predefined beam codebook  $\mathbb{F}_{\text{RX}}$  having  $\text{card}(\mathbb{F}_{\text{RX}})$  distinct vectors. Finally,  $\mathbf{U}_k^{(\text{BB})} \in \mathbb{C}^{M_k^{(\text{RF})} \times d_m}$  with  $d_m \leq \min\{M_k^{(\text{RF})}, N_m\}$  represents the digital RX combiner at node  $k$ .

#### 5.2.4 Multi-Tap Analog Cancellation

The analog canceller at node  $k$  consists of  $N$  taps with each tap connected via a  $N_k^{(\text{RF})}$ -to-1 MUltipleXer (MUX) to all  $N_k^{(\text{RF})}$  outputs of the respective TX RF chains. A tap includes a fixed delay, a variable phase shifter, and a variable attenuator [59, 115]. The output of each tap is connected to a 1-to- $M_k^{(\text{RF})}$  DEMUltipleXer (DEMUX), which routes the cancellation signal at the output of the tap to one of the adders located just before the RX RF chains. There are a total of  $NM_k^{(\text{RF})}$  such adders and we use the notation ‘‘Adder  $(i, j)$ ’’ to label the adder that connects DEMUX  $j$  to RX RF chain  $i$ , where  $i = 1, 2, \dots, M_k^{(\text{RF})}$  and  $j = 1, 2, \dots, N$ . The adders before

the RX RF chains can be implemented via power combiners or directional couplers, while the analog RF MUXs/DEMUXs can be implemented with RF switches. Similar to [59], we model in BB the analog processing realized by the analog canceller with  $\mathbf{C}_k \triangleq \mathbf{L}_3 \mathbf{L}_2 \mathbf{L}_1 \in \mathbb{C}^{M_k^{(\text{RF})} \times N_k^{(\text{RF})}}$ , where  $\mathbf{L}_1 \in \mathbb{R}^{N \times N_k^{(\text{RF})}}$ ,  $\mathbf{L}_2 \in \mathbb{C}^{N \times N}$ , and  $\mathbf{L}_3 \in \mathbb{R}^{M_k^{(\text{RF})} \times N}$ . The elements  $[\mathbf{L}_1]_{j,\ell}$  and  $[\mathbf{L}_3]_{i,j}$  with  $j = 1, 2, \dots, N$ ,  $\ell = 1, 2, \dots, N_k^{(\text{RF})}$ , and  $i = 1, 2, \dots, M_k^{(\text{RF})}$  take the binary values 0 or 1, and it must hold that

$$\sum_{\ell=1}^{N_k^{(\text{RF})}} [\mathbf{L}_1]_{j,\ell} = \sum_{i=1}^{M_k^{(\text{RF})}} [\mathbf{L}_3]_{i,j} = 1 \quad \forall j = 1, 2, \dots, N. \quad (5.3)$$

The  $\mathbf{L}_2$  in  $\mathbf{C}_k$  is a diagonal matrix whose complex entries represent the attenuation and phase shift of the canceller taps; the magnitude and phase of the element  $[\mathbf{L}_2]_{i,i}$  with  $i = 1, 2, \dots, N$  specify the attenuation and phase of the  $i$ -th tap. Recall that the tap delays in each canceller tap are fixed and since we focus on a narrowband system, we model the effects of the  $i$ -th tap delay as a phase shift that is incorporated to the phase of  $[\mathbf{L}_2]_{i,i}$ .

The use of MUXs/DEMUXs for signal routing in the analog canceller and then subtraction of the analog cancellation signal from the received RF signal has been first proposed in [59] as an effective means to reduce the hardware complexity of multi-tap analog cancellation. As previously discussed, the analog canceller in the proposed FD HBF architecture interconnects the  $N_k^{(\text{RF})}$  inputs of the analog TX precoder to the  $M_k^{(\text{RF})}$  outputs of the analog RX combiner, hence, its complexity  $N$  depends on the number of TX/RX RF chains, and not on the number of TX/RX antenna elements, as in [59]. Note that, in the special case of  $N_k^{(\text{RF})} = M_k^{(\text{RF})} = 1$  and arbitrary numbers for  $N_k$  and  $M_k$  (i.e., only analog TX/RX beamforming is feasible), the analog

canceller is comprised of only a single tap. The tap settings (i.e., values for the phase shifters and attenuators), the configuration of the  $N$  MUXs and  $N$  DEMUXs, as well the values for the A/D TX precoders and A/D RF combiners are jointly designed to meet certain performance and complexity indicators, as will be discussed in Section 5.3. The joint design splits the burden of SI cancellation between the TX/RX HBF and the analog canceller, thus allowing the use of smaller  $N$  for the latter unit. It is noted that the choice for  $N$  can be decided offline in a flexible way as a function of size constraints, cost per tap, or other constraints on the analog canceller hardware. The A/D TX/RX beamformers and the analog canceller will adapt to each others capabilities via their joint design.

### 5.2.5 Received Signal Models

Using the previously described system configuration, the baseband received signal  $\mathbf{y}_q \in \mathbb{C}^{M_q \times 1}$  at node  $q$  in the DL communication can be mathematically expressed as

$$\mathbf{y}_q \triangleq \mathbf{H}_{q,k} \mathbf{V}_k^{(\text{RF})} \mathbf{V}_k^{(\text{BB})} \mathbf{s}_k + \mathbf{H}_{q,m} \mathbf{V}_m \mathbf{s}_m + \mathbf{n}_q, \quad (5.4)$$

where  $\mathbf{H}_{q,k} \in \mathbb{C}^{M_q \times N_k}$  is the DL channel gain matrix (i.e., between nodes  $q$  and  $k$ ),  $\mathbf{H}_{q,m} \in \mathbb{C}^{M_q \times N_m}$  denotes the channel gain matrix for inter-node interference (i.e., between nodes  $q$  and  $m$ ), and  $\mathbf{n}_q \in \mathbb{C}^{M_q \times 1}$  represents the AWGN at node  $q$  with variance  $\sigma_q^2$ . In the UL communi-

cation, the symbol vector  $\hat{\mathbf{s}}_m \in \mathbb{C}^{d_m \times 1}$  used for the estimation of  $\mathbf{s}_m$  at the FD HBF node  $k$  is derived as

$$\begin{aligned} \hat{\mathbf{s}}_m \triangleq & \left( \mathbf{U}_k^{(\text{BB})} \right)^{\text{H}} \left( \left( \mathbf{U}_k^{(\text{RF})} \right)^{\text{H}} \mathbf{H}_{k,k} \mathbf{V}_k^{(\text{RF})} + \mathbf{C}_k \right) \mathbf{V}_k^{(\text{BB})} \mathbf{s}_k \\ & + \left( \mathbf{U}_k^{(\text{BB})} \right)^{\text{H}} \left( \mathbf{U}_k^{(\text{RF})} \right)^{\text{H}} \left( \mathbf{H}_{k,m} \mathbf{V}_m \mathbf{s}_m + \mathbf{n}_k \right), \end{aligned} \quad (5.5)$$

where  $\mathbf{H}_{k,k} \in \mathbb{C}^{M_k \times N_k}$  denotes the SI channel seen at the RX antennas of node  $k$  due to its own DL transmission,  $\mathbf{H}_{k,m} \in \mathbb{C}^{M_k \times N_m}$  is the UL channel gain matrix (i.e., between nodes  $k$  and  $m$ ), and  $\mathbf{n}_k \in \mathbb{C}^{M_k \times 1}$  denotes the received AWGN at node  $k$  with variance  $\sigma_k^2$ . The first term in Equation 5.5 describes the residual SI signal after analog cancellation and A/D TX/RX beamforming (all performed by node  $k$  using the proposed architecture), while its second term contains the A/D RX combined signal transmitted from node  $m$  plus the AWGN. In contrast to [59],  $\mathbf{C}_k$  needs to cancel the effective SI channel  $\left( \mathbf{U}_k^{(\text{RF})} \right)^{\text{H}} \mathbf{H}_{k,k} \mathbf{V}_k^{(\text{RF})}$ , which is a matrix of dimension  $M_k^{(\text{RF})} \times N_k^{(\text{RF})}$  and not the actual  $M_k \times N_k$  SI channel  $\mathbf{H}_{k,k}$ . This fact witnesses the reduced analog cancellation complexity offered by the proposed FD HBF architecture as well as the interplay among the  $N$ -tap analog canceller, the analog TX precoder  $\mathbf{V}_k^{(\text{RF})}$ , and the analog RX combiner  $\mathbf{U}_k^{(\text{RF})}$ , which can be further configured using the digital TX precoder  $\mathbf{V}_k^{(\text{BB})}$  and the digital RX combiner  $\mathbf{U}_k^{(\text{BB})}$ . It is finally noted that if the residual SI signal at the output of the digital RX combiner, as expressed by the first term in Equation 5.5, does not meet the cancellation requirements, further digital cancellation can be used [85].

### 5.3 Joint Design Problem Formulation

As shown in Figure 26 with the proposed FD HBF hardware architecture, the components of the analog canceller are jointly designed with the A/D TX/RX beamforming blocks in order to satisfy certain performance objectives. In this section, we focus on the massive MIMO node  $k$  and present a sum-rate optimization framework for the joint design of  $\mathbf{C}_k$ ,  $\mathbf{V}_k^{(\text{RF})}$ ,  $\mathbf{V}_k^{(\text{BB})}$ ,  $\mathbf{U}_k^{(\text{RF})}$ , and  $\mathbf{U}_k^{(\text{BB})}$ . Using the notation  $\mathbf{V}_k \triangleq \mathbf{V}_k^{(\text{RF})}\mathbf{V}_k^{(\text{BB})}$  and assuming capacity-achieving combining at node  $q$  like the non-linear minimum mean squared error successive interference cancellation, the achievable DL rate that is a function of the A/D TX precoding matrices  $\mathbf{V}_k^{(\text{RF})}$  and  $\mathbf{V}_k^{(\text{BB})}$  of node  $k$  as well as the digital TX precoder  $\mathbf{V}_m$  of node  $m$ , is given by

$$\mathcal{R}_{\text{DL}} = \log_2 \left( \det \left( \mathbf{I}_{M_q} + \mathbf{H}_{q,k} \mathbf{V}_k \mathbf{V}_k^H \mathbf{H}_{q,k}^H \mathbf{Q}_q^{-1} \right) \right), \quad (5.6)$$

where  $\mathbf{Q}_q \in \mathbb{C}^{M_q \times M_q}$  denotes the covariance matrix of the IpN at node  $q$  that is obtained as

$$\mathbf{Q}_q \triangleq \mathbf{H}_{q,m} \mathbf{V}_m \mathbf{V}_m^H \mathbf{H}_{q,m}^H + \sigma_q^2 \mathbf{I}_{M_q}. \quad (5.7)$$

We hereinafter assume that there is no inter-node interference between the half duplex nodes  $q$  and  $m$  due to, for example, appropriate node scheduling [96, 116] for the FD operation at node  $k$ . The latter assumption translates to setting the channel matrix between the involved nodes in Equation 5.4 as  $\mathbf{H}_{q,m} = \mathbf{0}_{M_q \times N_k}$ , which means that Equation 5.7 simplifies to  $\mathbf{Q}_q = \sigma_q^2 \mathbf{I}_{M_q}$ .

For the computation of the achievable UL rate, we use the notation  $\mathbf{U}_k \triangleq \mathbf{U}_k^{(\text{RF})} \mathbf{U}_k^{(\text{BB})}$  to express this rate as a function of the A/D RX combiners  $\mathbf{U}_k^{(\text{RF})}$  and  $\mathbf{U}_k^{(\text{BB})}$ , the A/D TX precoders  $\mathbf{V}_k^{(\text{RF})}$  and  $\mathbf{V}_k^{(\text{BB})}$ , and the analog cancellation matrix  $\mathbf{C}_k$  of node  $k$  as well as of the digital TX precoder  $\mathbf{V}_m$  of node  $m$ . Using Equation 5.5, the UL rate is given by

$$\mathcal{R}_{\text{UL}} = \log_2 \left( \det \left( \mathbf{I}_{d_m} + \mathbf{U}_k^{\text{H}} \mathbf{H}_{k,m} \mathbf{V}_m \mathbf{V}_m^{\text{H}} \mathbf{H}_{k,m}^{\text{H}} \mathbf{U}_k \mathbf{Q}_k^{-1} \right) \right). \quad (5.8)$$

where  $\mathbf{Q}_k \in \mathbb{C}^{d_m \times d_m}$  denotes the IpN covariance matrix after A/D RX combining at node  $q$  which can be expressed as

$$\begin{aligned} \mathbf{Q}_k \triangleq & \left( \mathbf{U}_k^{(\text{BB})} \right)^{\text{H}} \tilde{\mathbf{H}}_{k,k} \mathbf{V}_k^{(\text{BB})} \left( \mathbf{V}_k^{(\text{BB})} \right)^{\text{H}} \tilde{\mathbf{H}}_{k,k}^{\text{H}} \mathbf{U}_k^{(\text{BB})} \\ & + \sigma_k^2 \left( \mathbf{U}_k^{(\text{BB})} \right)^{\text{H}} \left( \mathbf{U}_k^{(\text{RF})} \right)^{\text{H}} \mathbf{U}_k^{(\text{RF})} \mathbf{U}_k^{(\text{BB})}. \end{aligned} \quad (5.9)$$

In the latter expression,  $\tilde{\mathbf{H}}_{k,k} \in \mathbb{C}^{M_k^{(\text{RF})} \times N_k^{(\text{RF})}}$  denotes the effective SI channel after performing analog TX/RX beamforming and analog cancellation, which is defined as

$$\tilde{\mathbf{H}}_{k,k} \triangleq \left( \mathbf{U}_k^{(\text{RF})} \right)^{\text{H}} \mathbf{H}_{k,k} \mathbf{V}_k^{(\text{RF})} + \mathbf{C}_k. \quad (5.10)$$

Using the latter expressions Equation 5.6 and Equation 5.8 for the achievable DL and UL rates, respectively, the sum-rate optimization problem for the joint design of the analog canceller and the A/D TX/RX beamformers is mathematically expressed as

$$\mathcal{OP} : \max_{\mathbf{C}_k, \mathbf{V}_k^{(\text{RF})}, \mathbf{V}_k^{(\text{BB})}, \mathbf{U}_k^{(\text{RF})}, \mathbf{U}_k^{(\text{BB})}} \mathcal{R}_{\text{DL}} + \mathcal{R}_{\text{UL}} \quad (5.11)$$

$$\text{s.t} \quad \text{tr}\{\mathbf{V}_k^{(\text{RF})} \mathbf{V}_k^{(\text{BB})} (\mathbf{V}_k^{(\text{BB})})^{\text{H}} (\mathbf{V}_k^{(\text{RF})})^{\text{H}}\} \leq P_k, \quad (\text{C1})$$

$$\mathbf{C}_k = \mathbf{L}_3 \mathbf{L}_2 \mathbf{L}_1 \text{ with Equation 5.3 and } [\mathbf{L}_2]_{i,j} = 0 \text{ for } i \neq j, \quad (\text{C2})$$

$$\left\| \left[ \tilde{\mathbf{H}}_{k,k} \mathbf{V}_k^{(\text{BB})} \right]_{(j,:)} \right\|^2 \leq \lambda_A, \quad \forall j = 1, 2, \dots, M_k^{(\text{RF})}, \quad (\text{C3})$$

$$\mathbf{u}_j \in \mathbb{F}_{\text{RX}} \quad \forall j \text{ and } \mathbf{v}_n \in \mathbb{F}_{\text{TX}} \quad \forall n = 1, 2, \dots, N_k^{(\text{RF})}, \quad (\text{C4})$$

where constraint (C1) relates to the average transmit power at node  $k$  and constraint (C2) refers to the hardware capabilities of the analog canceller. Constraint (C3) imposes the threshold  $\lambda_A \in \mathbb{R}$  on the average power of the residual SI signal after analog cancellation and analog TX/RX beamforming. The averaging in the latter constraint is being taken over all transmitted symbols within a coherent channel block. Finally, constraint (C4) refers to the predefined TX and RX beam codebooks. To tackle  $\mathcal{OP}$ , which is a nonconvex problem with nonconvex constraints, we adopt a similar to [59] decoupled way that in this case requires at most  $\alpha_{\text{max}} \triangleq N_k^{(\text{RF})} - 1$  iterations including closed form expressions for the design parameters. We first solve for  $\mathbf{C}_k$ ,  $\mathbf{V}_k^{(\text{RF})}$ ,  $\mathbf{V}_k^{(\text{BB})}$ , and  $\mathbf{U}_k^{(\text{RF})}$  maximizing the DL rate, and then find  $\mathbf{U}_k^{(\text{BB})}$  maximizing the UL

rate. Specifically, we formulate the following optimization subproblem for the design of  $\mathbf{C}_k$ ,  $\mathbf{V}_k^{(\text{RF})}$ ,  $\mathbf{V}_k^{(\text{BB})}$ , and  $\mathbf{U}_k^{(\text{RF})}$ :

$$\mathcal{OP1} : \max_{\substack{\mathbf{C}_k, \mathbf{V}_k^{(\text{RF})}, \\ \mathbf{V}_k^{(\text{BB})}, \mathbf{U}_k^{(\text{RF})}}} \mathcal{R}_{\text{DL}} \quad \text{s.t.} \quad (\text{C1}), (\text{C2}), (\text{C3}), \text{ and } (\text{C4}). \quad (5.12)$$

### 5.3.1 Exhaustive Search

Given RF precoder and combiner codebooks, we can solve the optimization problem  $\mathcal{OP1}$  using an exhaustive search approach. First, considering each combination of the RF precoder  $\mathbf{V}_k^{(\text{RF})}$  and combiner  $\mathbf{U}_k^{(\text{RF})}$  of node  $k$ , we seek for  $\mathbf{V}_k^{(\text{BB})}$  maximizing the DL rate while meeting constraints (C1) and (C3). This procedure is repeated for all allowable realizations of  $\mathbf{C}_k$  satisfying the constraint (C2) for the given number of analog canceller taps  $N$  in order to find the best  $\mathbf{V}_k^{(\text{BB})}$  solving  $\mathcal{OP1}$ .

Given each combination of  $\mathbf{V}_k^{(\text{RF})}$  and  $\mathbf{U}_k^{(\text{RF})}$ , the digital precoder  $\mathbf{V}_k^{(\text{BB})}$  design procedure is summarized in Algorithm 5, which is a generalization of [59, Algorithm 1] for the FD HBF case. As shown in the algorithm, the digital TX beamformer is constructed as  $\mathbf{V}_k^{(\text{BB})} = \mathbf{F}_k \mathbf{G}_k$  with  $\mathbf{F}_k \in \mathbb{C}^{N_k^{(\text{RF})} \times \alpha}$  and  $\mathbf{G}_k \in \mathbb{C}^{\alpha \times d'_k}$ , where  $\alpha$  is a positive integer taking the values  $1 \leq \alpha \leq \alpha_{\max}$  and  $d'_k \leq \min\{M_q, \alpha\}$ . We note that, for large transmission powers and strictly small values for  $\lambda_A$ , one could set  $\alpha_{\max} = \min\{M_q, N_k^{(\text{RF})}\}$ . Moreover, it holds that the larger the  $\alpha$  value is, the higher the DL rate but also SI. Finally, as shown in the algorithm, we adopt a similar approach to [86] for the design of  $\mathbf{V}_k^{(\text{BB})}$  for each feasible  $\alpha$  value.

Given codebook  $\mathbb{F}_{\text{TX}}$ , the TX RF precoder  $\mathbf{V}_k^{(\text{RF})}$  has  $\text{card}(\mathbb{F}_{\text{TX}})^{N_k^{(\text{RF})}}$  distinct combinations, while the RX RF combiner  $\mathbf{U}_k^{(\text{RF})}$  renders  $\text{card}(\mathbb{F}_{\text{RX}})^{M_k^{(\text{RF})}}$  combinations given RX codebook  $\mathbb{F}_{\text{RX}}$ . Therefore, Algorithm 5 is required to run for  $\text{card}(\mathbb{F}_{\text{TX}})^{N_k^{(\text{RF})}} \times \text{card}(\mathbb{F}_{\text{RX}})^{M_k^{(\text{RF})}}$  times given one realization of  $\mathbf{C}_k$  to solve for  $\mathbf{V}_k^{(\text{RF})}$ ,  $\mathbf{U}_k^{(\text{RF})}$ ,  $\mathbf{V}_k^{(\text{BB})}$  that maximizes the  $\mathcal{R}_{\text{DL}}$ . This exhaustive search procedure renders high computational complexity that is impractical for real-time implementations. Therefore, in the following subsection, we provide a low-complexity subrate optimization based RF precoder and combiner solution that suboptimally solves  $\mathcal{OP}1$ .

### 5.3.2 Sub-rate Optimization Based RF Precoder and Combiner

We propose to find  $\mathbf{V}_k^{(\text{RF})}$  and  $\mathbf{U}_k^{(\text{RF})}$  that potentially maximizes the DL rate and minimizes the SI channel power. Using this suboptimal solution for the precoder and combiner, we use Algorithm 5 to find digital precoder  $\mathbf{V}_k^{(\text{BB})}$  that maximizes the DL rate while meeting constraints (C1) and (C3).

First, we decompose the achievable DL rate in Equation 5.6 into summation of sub-rate of each sub-antenna array.

**Proposition 1.** *The total achievable DL rate in Equation 5.6*

$$\mathcal{R}_{\text{DL}} = \log_2 \left( \det \left( \mathbf{I}_{M_q} + \sigma_q^{-2} \mathbf{H}_{q,k} \mathbf{V}_k \mathbf{V}_k^H \mathbf{H}_{q,k}^H \right) \right),$$

*is equivalent to*

$$\mathcal{R}_{\text{DL}} = \sum_{n=1}^{N_k^{(\text{RF})}} \log_2 \left( 1 + \frac{P_k}{N_k^{(\text{RF})} \sigma_q^2} \mathbf{v}_n^H \mathbf{R}_n \mathbf{G}_{n-1} \mathbf{R}_n^H \mathbf{v}_n \right), \quad (5.13)$$

---

**Algorithm 5** Digital TX Precoder Design for FD massive MIMO systems
 

---

- Input:**  $P_k$ ,  $\mathbf{V}_k^{(\text{RF})}$  and  $\mathbf{U}_k^{(\text{RF})}$  solving  $\mathcal{OP}2$ ,  $\mathbf{H}_{k,k}$ , and  $\mathbf{H}_{q,k}$  as well as a realization of  $\mathbf{C}_k$  for a given  $N$  satisfying constraint (C2).
- 1: Set  $\tilde{\mathbf{H}}_{k,k} = \left(\mathbf{U}_k^{(\text{RF})}\right)^{\text{H}} \mathbf{H}_{k,k} \mathbf{V}_k^{(\text{RF})} + \mathbf{C}_k$ .
  - 2: Obtain  $\mathbf{D}_k$  including the  $N_k^{(\text{RF})}$  right-singular vectors of  $\tilde{\mathbf{H}}_{k,k}$  corresponding to the singular values in descending order.
  - 3: **for**  $\alpha = \alpha_{\max}, \alpha_{\max} - 1, \dots, 2$  **do**
  - 4:     Set  $\mathbf{F}_k = [\mathbf{D}_k]_{(:, N_k^{(\text{RF})} - \alpha + 1 : N_k^{(\text{RF})})}$ .
  - 5:     Set  $\mathbf{G}_k$  as the optimum precoding for the effective DL MIMO channel  $\mathbf{H}_{q,k} \mathbf{V}_k^{(\text{RF})} \mathbf{F}_k$  given  $P_k$ .
  - 6:     **if**  $\|[\tilde{\mathbf{H}}_{k,k} \mathbf{F}_k \mathbf{G}_k]_{(i,:)}\|^2 \leq \lambda_A \forall i = 1, \dots, M_k^{(\text{RF})}$ , **then**
  - 7:         Output  $\mathbf{V}_k^{(\text{BB})} = \mathbf{F}_k \mathbf{G}_k$  and stop the algorithm.
  - 8:     **end if**
  - 9: **end for**
  - 10: Set  $\mathbf{F}_k = [\mathbf{D}_k]_{(:, N_k^{(\text{RF})})}$  and  $\mathbf{G}_k = \mathbf{P}_k^{1/2}$ .
  - 11: **if**  $\|[\tilde{\mathbf{H}}_{k,k} \mathbf{F}_k \mathbf{G}_k]_i\|^2 \leq \lambda_A \forall i = 1, \dots, M_k^{(\text{RF})}$ , **then**
  - 12:     Output  $\mathbf{V}_k^{(\text{BB})} = \mathbf{F}_k \mathbf{G}_k$  and stop the algorithm.
  - 13: **else**
  - 14:     Output that the  $\mathbf{C}_k$  realization does not meet the residual SI constraint.
  - 15: **end if**
- 

where  $\mathbf{R}_n = [\mathbf{0}_{N_k^{(\text{A})} \times N_k^{(\text{A})} (n-1)} \quad \mathbf{I}_{N_k^{(\text{A})}} \quad \mathbf{0}_{N_k^{(\text{A})} \times N_k^{(\text{A})} (N_k^{(\text{RF})} - n)}]$ ,  $\mathbf{G}_0 = \mathbf{H}_{q,k}^{\text{H}} \mathbf{H}_{q,k}$ , and

$$\mathbf{G}_n = \mathbf{G}_{n-1} - \frac{\frac{P_k}{N_k^{(\text{RF})} \sigma_q^2} \mathbf{G}_{n-1} \mathbf{R}_n^{\text{H}} \mathbf{v}_n \mathbf{v}_n^{\text{H}} \mathbf{R}_n \mathbf{G}_{n-1}}{1 + \frac{P_k}{N_k^{(\text{RF})} \sigma_q^2} \mathbf{v}_n^{\text{H}} \mathbf{R}_n \mathbf{G}_{n-1} \mathbf{R}_n^{\text{H}} \mathbf{v}_n}. \quad (5.14)$$

*Proof.* See Appendix C. □

Based on  $\mathbf{1}$ , we find  $\mathbf{v}_n, \forall n = 1, \dots, N_k^{(\text{RF})}$  that maximizes the DL rate, while minimizing the SI. Therefore, we formulate the optimization problem as

$$\mathbf{v}_n^* = \underset{\mathbf{v}_j \in \mathbb{F}_{\text{TX}}, \forall j}{\operatorname{argmax}} \frac{\mathbf{v}_j^H \mathbf{R}_n \mathbf{G}_{n-1} \mathbf{R}_n^H \mathbf{v}_j}{\mathbf{v}_j^H \mathbf{R}_n \mathbf{H}_{k,k}^H \mathbf{H}_{k,k} \mathbf{R}_n^H \mathbf{v}_j}. \quad (5.15)$$

Solving for the optimization problem in Equation 5.15, we form the  $\mathbf{V}_k^{(\text{RF})}$  using the RF precoding vectors  $\mathbf{v}_n^*, \forall n = 1, \dots, N_k^{(\text{RF})}$  as shown in Equation 5.1.

Now, we seek the RF combiner vectors  $\mathbf{u}_n, \forall n = 1, \dots, M_k^{(\text{RF})}$  of each sub-antenna array of the node  $k$  RX that minimizes the SI channel  $\overline{\mathbf{H}}_{k,k} = \mathbf{H}_{k,k} \mathbf{V}_k^{(\text{RF})}$ . Therefore, we formulate the following optimization problem

$$\mathbf{u}_n^* = \underset{\mathbf{u}_j \in \mathbb{F}_{\text{RX}} \forall j}{\operatorname{argmin}} \mathbf{u}_j^H \mathbf{R}_m^H \overline{\mathbf{H}}_{k,k} \overline{\mathbf{H}}_{k,k}^H \mathbf{R}_m \mathbf{u}_j, \quad (5.16)$$

where  $\mathbf{R}_m = [\mathbf{0}_{M_k^{(\text{A})} \times M_k^{(\text{A})} (m-1)} \quad \mathbf{I}_{M_k^{(\text{A})}} \quad \mathbf{0}_{M_k^{(\text{A})} \times M_k^{(\text{A})} (M_k^{(\text{RF})} - m)}]$  is the RX sub-antenna array selection matrix.

**Proposition 2.** *Considering very large number of RX antenna elements  $M_k^{(\text{A})}$  in each array, RF combiner vector  $\mathbf{u}_n, \forall n$  can be found solving Equation 5.16 that suppresses the SI channel norm  $\|\overline{\mathbf{H}}_{k,k}\|_{\text{F}}$  to zero.*

*Proof.* See Appendix D. □

---

**Algorithm 6** Sub-rate Optimization based RF TX Precoder and RX Combiner Design
 

---

**Input:**  $\mathbf{H}_{k,k}$ ,  $\mathbf{H}_{q,k}$ ,  $\mathbb{F}_{\text{TX}}$ , and  $\mathbb{F}_{\text{RX}}$ .

- 1: Set  $\mathbf{G}_0 = \mathbf{H}_{q,k}^H \mathbf{H}_{q,k}$ .
  - 2: **for**  $n = 1, 2, \dots, N_k^{(\text{RF})}$  **do**
  - 3:   Set  $\mathbf{R}_n = [\mathbf{0}_{N_k^{(\text{A})} \times N_k^{(\text{A})} (n-1)} \quad \mathbf{I}_{N_k^{(\text{A})}} \quad \mathbf{0}_{N_k^{(\text{A})} \times N_k^{(\text{A})} (N_k^{(\text{RF})} - n)]$ .
  - 4:   Set  $\mathbf{v}_n = \underset{\mathbf{v}_j \in \mathbb{F}_{\text{TX}} \forall j}{\text{argmax}} \frac{\mathbf{v}_j^H \mathbf{R}_n \mathbf{G}_{n-1} \mathbf{R}_n^H \mathbf{v}_j}{\mathbf{v}_j^H \mathbf{R}_n \mathbf{H}_{k,k}^H \mathbf{H}_{k,k} \mathbf{R}_n^H \mathbf{v}_j}$ .
  - 5:   Set  $\mathbf{G}_n = \mathbf{G}_{n-1} - \frac{\frac{P_k}{N_k^{(\text{RF})} \sigma_q^2} \mathbf{G}_{n-1} \mathbf{R}_n^H \mathbf{v}_n \mathbf{v}_n^H \mathbf{R}_n \mathbf{G}_{n-1}}{1 + \frac{P_k}{N_k^{(\text{RF})} \sigma_q^2} \mathbf{v}_n^H \mathbf{R}_n \mathbf{G}_{n-1} \mathbf{R}_n^H \mathbf{v}_n}$ .
  - 6: **end for**
  - 7: Set  $\bar{\mathbf{H}}_{k,k} = \mathbf{H}_{k,k} \mathbf{V}_k^{(\text{RF})}$ .
  - 8: **for**  $m = 1, 2, \dots, M_k^{(\text{RF})}$  **do**
  - 9:   Set  $\mathbf{R}_m = [\mathbf{0}_{M_k^{(\text{A})} \times M_k^{(\text{A})} (m-1)} \quad \mathbf{I}_{M_k^{(\text{A})}} \quad \mathbf{0}_{M_k^{(\text{A})} \times M_k^{(\text{A})} (M_k^{(\text{RF})} - m)]$ .
  - 10:   Set  $\mathbf{u}_m = \underset{\mathbf{u}_j \in \mathbb{F}_{\text{RX}} \forall j}{\text{argmin}} \mathbf{u}_j^H \mathbf{R}_m^H \bar{\mathbf{H}}_{k,k} \bar{\mathbf{H}}_{k,k}^H \mathbf{R}_m \mathbf{u}_j$
  - 11: **end for**
- 

Solving for the optimization problem in Equation 5.16, we form the analog combiner  $\mathbf{U}_k^{(\text{RF})}$  using the RF combining vectors  $\mathbf{u}_n^*$ ,  $\forall n = 1, \dots, M_k^{(\text{RF})}$  as shown in Equation 5.2. The procedure for designing RF precoder and combiner is summarized in Algorithm 6.

Now using the analog precoder  $\mathbf{V}_k^{(\text{RF})}$  and combiner  $\mathbf{U}_k^{(\text{RF})}$  derived from Algorithm 6, we run the Algorithm 5 to seek the digital precoder  $\mathbf{V}_k^{(\text{BB})}$  for all allowable realization of  $\mathbf{C}_k$  given the number of analog cancellation taps  $N$ .

The values for  $\mathbf{C}_k$ ,  $\mathbf{V}_k^{(\text{RF})}$ ,  $\mathbf{V}_k^{(\text{BB})}$ , and  $\mathbf{U}_k^{(\text{RF})}$  solving  $\mathcal{OP}1$  are finally substituted into the achievable UL rate expression  $\mathcal{R}_{\text{UL}}$  in Equation 5.8. The  $\mathbf{U}_k^{(\text{BB})}$  maximizing this point-to-point MIMO rate is obtained in closed form using [117, Sec. 4.2].

### 5.3.3 Complexity Analysis

In this subsection, we provide the complexity evaluation of the proposed low complexity sub-rate base RF beamforming and combining solution of the optimization problem in  $\mathcal{OP}1$  in terms of the required numbers of complex multiplications along with the exhaustive search procedure. First, we derive the complexity of the DL baseband precoder design described in Algorithm 5.

The computational complexity originates from the following steps of Algorithm 5:

1. Step 1 residual SI channel matrix  $\tilde{\mathbf{H}}_{k,k}$  requires  $N_k^{(\text{RF})} M_k \left( M_k^{(\text{RF})} + N_k \right)$  numbers of multiplication.
2. The number of multiplications for the SVD operation in step 2 is  $\left( M_k^{(\text{RF})} \right)^2 N_k^{(\text{RF})}$ .
3. The SVD operation in Step 5 along with the conditional operation in Step 6 require  $\left( M_q^2 + M_k^{(\text{RF})} N_k^{(\text{RF})} \right) \sum_{\alpha=1}^{\alpha_{\max}} \alpha$  numbers of multiplication.

Therefore, Algorithm 5 requires in total  $\mathbf{N}_{\text{Alg1}} = N_k^{(\text{RF})} M_k \left( M_k^{(\text{RF})} + N_k \right) + \left( M_k^{(\text{RF})} \right)^2 N_k^{(\text{RF})} + \left( M_q^2 + M_k^{(\text{RF})} N_k^{(\text{RF})} \right) \sum_{\alpha=1}^{\alpha_{\max}} \alpha$  multiplications.

Now, we evaluate the complexity of the sub-rate based RF precoder and combiner designing procedure. From Algorithm 6, we observe that the complexity of each iteration renders from:

1. First, matrix  $\mathbf{G}_0$  requires  $N_k^2 M_q$  times of multiplications.
2. Selection of the RF precoder vectors for all the sub-antenna arrays requires in total  $\text{card}(\mathbb{F}_{\text{TX}}) N_k^{(\text{RF})} N_k^{(\text{A})} \left( N_k^{(\text{A})} + 1 \right)$  number of multiplications.

TABLE IV  
COMPUTATIONAL COMPLEXITY OF PROPOSED SCHEME AND EXHAUSTIVE SEARCH

	No. of Multiplications
Proposed Scheme	$\mathcal{O}(N_k^2 M_q + N_k^{(\text{RF})} (\text{card}(\mathbb{F}_{\text{TX}}) N_k^{(\text{A})} (N_k^{(\text{A})} + 1) + N_k (2N_k^{(\text{A})} + N_k) + M_k N_k) + \text{card}(\mathbb{F}_{\text{RX}}) M_k^{(\text{RF})} M_k^{(\text{A})} (M_k^{(\text{A})} N_k^{(\text{RF})} + M_k^{(\text{A})} + 1) + \mathbf{N}_{\text{Alg1}})$
Exhaustive Search	$\mathcal{O}(\text{card}(\mathbb{F}_{\text{TX}})^{N_k^{(\text{RF})}} \text{card}(\mathbb{F}_{\text{RX}})^{M_k^{(\text{RF})}} \mathbf{N}_{\text{Alg1}})$

3. Updating matrix  $\mathbf{G}_n$  at step 5 requires  $N_k^{(\text{RF})} N_k (2N_k^{(\text{A})} + N_k)$  times of multiplications.
4. Calculating matrix  $\overline{\mathbf{H}}_{k,k}$  in step 7 needs  $M_k N_k N_k^{(\text{RF})}$  multiplications.
5. Finally selection of combining vectors of all receiver arrays at step 10 requires  $\text{card}(\mathbb{F}_{\text{RX}}) M_k^{(\text{RF})} M_k^{(\text{A})} (M_k^{(\text{A})} N_k^{(\text{RF})} + M_k^{(\text{A})} + 1)$  times of multiplications.

The total computational complexity of the proposed scheme and the exhaustive search method is given in Table IV. For comparison of computational complexity between the exhaustive search and proposed sub-rate based solution of  $\mathcal{OP}1$ , we consider an example model with  $N_k^{(\text{RF})} = M_q = 4$ ,  $M_k^{(\text{RF})} = 2$ ,  $N_m = 1$ ,  $N_k^{(\text{A})} = M_k^{(\text{A})} = \text{card}(\mathbb{F}_{\text{TX}}) = \text{card}(\mathbb{F}_{\text{RX}}) = 16$ . Based on the example parameters, exhaustive search approach would require  $1.46 \times 10^{11}$  multiplications. In comparison, the proposed sub-rate based solution in Algorithm 6 requires only 116736 times of multiplications, which is a very small fraction of the exhaustive search procedure.

## 5.4 Simulation Results and Discussion

In this section, we provide the representative simulation results of our proposed full-duplex design with hybrid A/D beamforming.

### 5.4.1 Channel Models

The FD node  $k$  and the HD node  $q$  and  $m$  are separated in a far-field manner. Therefore, we follow the narrowband clustered channel model for the DL and UL channels  $\mathbf{H}_{q,k}$  and  $\mathbf{H}_{k,m}$ , respectively. Explicitly, channels  $\mathbf{H}_{q,k}$  and  $\mathbf{H}_{k,m}$  are modeled as follows, where  $i, j \in \{q, k, m\}$ ,

$$\mathbf{H}_{i,j} = \sqrt{\frac{M_i N_j}{N_{\text{cl}} N_{\text{ray}}}} \sum_{k=1}^{N_{\text{cl}}} \sum_{l=1}^{N_{\text{ray}}} \beta_{k,l} \mathbf{a}_i(\phi_{k,l}) \mathbf{a}_j^{\text{H}}(\theta_{k,l}), \quad (5.17)$$

Here,  $N_{\text{cl}}$  is the number of scattering clusters in the respective channel each contributing  $N_{\text{ray}}$  propagation paths. The complex gain of ray  $l$  from cluster  $k$  is given as  $\beta_{k,l} \sim \mathcal{CN}(0, 1)$ , while  $\phi_{k,l}$  and  $\theta_{k,l}$  are angle-of-arrival (AoA) and angle-of-departure (AoD), respectively. Considering Uniform Linear Array (ULA), the array response vectors  $\mathbf{a}_i$  and  $\mathbf{a}_j$  are expressed as

$$\begin{aligned} \mathbf{a}_i(\phi_{k,l}) &= [1 \quad e^{j\frac{2\pi}{\lambda}d \cos(\phi_{k,l})}, \dots, e^{j\frac{2\pi}{\lambda}(M_i-1)d \cos(\phi_{k,l})}]^{\text{T}}, \\ \mathbf{a}_j(\theta_{k,l}) &= [1 \quad e^{j\frac{2\pi}{\lambda}d \cos(\theta_{k,l})}, \dots, e^{j\frac{2\pi}{\lambda}(N_j-1)d \cos(\theta_{k,l})}]^{\text{T}}. \end{aligned} \quad (5.18)$$

The Rician SI channel  $\mathbf{H}_{k,k}$  is modeled as

$$\mathbf{H}_{k,k} = \sqrt{\frac{K}{K+1}} \mathbf{H}_{k,k}^{\text{LOS}} + \sqrt{\frac{1}{K+1}} \mathbf{H}_{k,k}^{\text{NLOS}}, \quad (5.19)$$

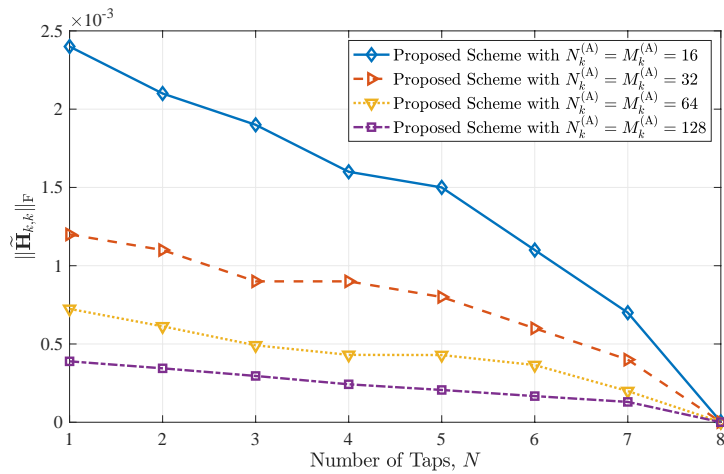


Figure 27. Frobenius Norm of  $\tilde{\mathbf{H}}_{k,k}$  vs Number of Analog Cancellation Taps for different Antenna Elements per RF Chain at Node  $k$

where  $K$  is the Rician factor of the SI channel. Here,  $\mathbf{H}_{k,k}^{\text{LOS}}$  and  $\mathbf{H}_{k,k}^{\text{NLOS}}$  are the line-of-sight (LOS) and non-line-of-sight (NLOS) components of the SI channel, respectively. The LOS channel component is described in a near-field fashion as

$$[\mathbf{H}_{k,k}^{\text{LOS}}]_{m,n} = \frac{1}{r_{m,n}} \exp(-j \frac{2\pi r_{m,n}}{\lambda}), \quad (5.20)$$

where  $r_{m,n}$  is the distance between  $m$ -th receive antenna and  $n$ -th transmit antenna of the SI node  $k$  defined as [111, eq. (9)]. The NLOS component  $\mathbf{H}_{k,k}^{\text{NLOS}}$  is modeled in a far-field fashion using Equation 5.17.

### 5.4.2 Simulation Parameters

We perform an extensive simulation following the FD MIMO architecture illustrated in Figure 26 with  $N_k^{(\text{RF})} = M_q = 4$ ,  $M_k^{(\text{RF})} = 2$ , and  $N_m = 1$ . The FD node  $k$  has its antennas arranged in ULAs with  $\lambda/2$  separation between adjacent elements, where  $\lambda$  is the wavelength. The distance and angle between the TX and RX ULAs of each node are respectively  $d = 2\lambda$  and  $\omega = \pi/6$  in both cases, see [110, Fig. 2]. Each of the RF chain in node  $k$  TX/RX is connected to a ULA with  $N_k^{(\text{A})} = M_k^{(\text{A})} = \{16, 32, 64, 128\}$ . The DL and UL channels are simulated mmWave channels using Equation 5.17 with pathloss of 110 dB. The mmWave SI channel at node  $k$  is assumed to be Rician fading channel with a  $K$ -factor of 35 dB and a pathloss of 40 dB and modeled as Equation 5.19. RX noise floors at both nodes  $k$  and  $q$  are assumed to be  $-110$  dBm and  $-90$  dBm, respectively. Therefore, the RXs have effective dynamic range of 62dB provided by the 14-bit ADC for a PAPR of 10 dB [98]. Therefore, the residual SI power after analog cancellation at the input of each RX RF chain has to be below  $-47$  dBm to avoid saturation. Furthermore, non-ideal multi-tap analog canceller is considered with steps of 0.02 dB for attenuation and  $0.13^\circ$  for phase as in [59]. For TX and RX analog beamforming, we consider Discrete Fourier Transform (DFT) based predefined beam codebooks with lengths equalling to the antenna elements  $N_k^{(\text{A})}$  and  $M_k^{(\text{A})}$ , respectively. The entries of DFT codebooks are defined as [118]. We have used 1000 Monte Carlo simulation runs (1000 independent set of channels) to calculate the performance of all proposed FD MIMO design.

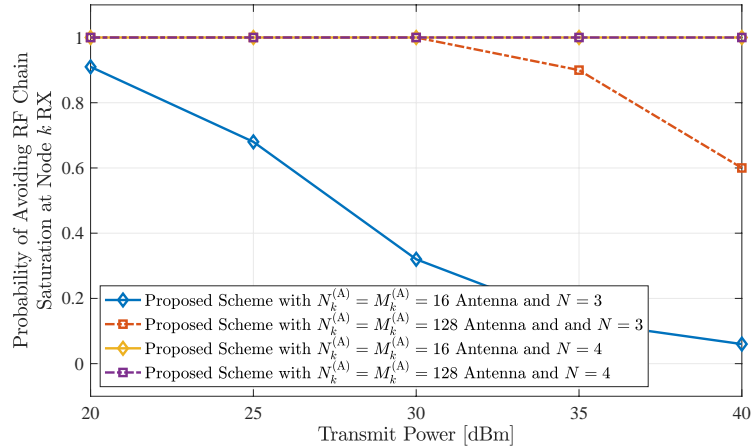


Figure 28. Probability of avoiding RX RF chain saturation vs transmit power for different Antenna Elements per RF Chain at Node  $k$  with  $\alpha = 3$

#### 5.4.3 Hardware Complexity, Self-Interference Mitigation Capability, and Achievable Rates

Using the proposed sub-rate based optimization in Algorithm 6, we find the beamformers  $\mathbf{V}_k^{(\text{RF})}$  and  $\mathbf{U}_k^{(\text{RF})}$  based on the DFT beam codebook given antenna elements  $N_k^{(A)} = M_k^{(A)} = \{16, 32, 64, 128\}$ . Using the analog TX/RX beamformers, the effective SI channel  $\tilde{\mathbf{H}}_{k,k}$  in Equation 5.10 is derived. Figure 27 represents the Frobenius norm of  $\tilde{\mathbf{H}}_{k,k}$  with respect to the number of analog taps  $N$  for different antenna elements  $N_k^{(A)} = M_k^{(A)} = \{16, 32, 64, 128\}$ . We observe that the SI channel Frobenius norm reduces, as the number of antenna elements increases. This trait further proves Proposition 2. As an example, in Figure 27, with only 3 analog taps the SI for 128 antenna elements is almost 5 times lower than that of 16 antenna elements. Therefore,

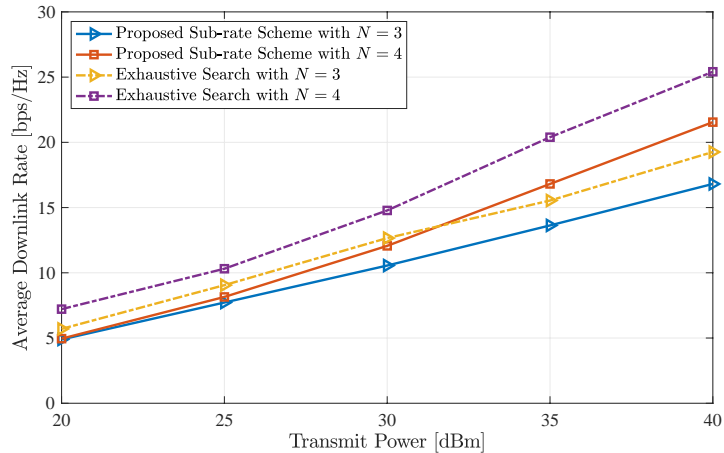


Figure 29. Achievable DL rates vs the transmit powers in dBm for Proposed Sub-rate and Exhaustive Search Scheme with  $N_k^{(A)} = M_k^{(A)} = 16$  antenna elements

we can decrease number of analog cancellation hardware with larger antenna arrays for the proposed FD MIMO system.

Figure 28 shows the probability of RF chain saturation at node  $k$  RX with respect to transmit power for different taps and antenna elements  $N_k^{(A)} = M_k^{(A)} = \{16, 128\}$ . We run the Algorithm 5, based on analog beamformers and analog canceller given number of taps  $N$  with  $\alpha = 3$ . Although, the system with 128 antenna elements and 3 taps analog canceller avoids RF saturation for low transmit powers, the 16 antenna elements approach results in saturation in all power cases. As shown, for 4 analog taps the proposed FD system avoids RF saturation resulting residual SI below threshold  $\lambda_A = -48$  dBm irrespective of the antenna elements. Therefore, the proposed system achieves effective UL reception suppressing SI for an analog canceller of  $0.5 \times N_k^{(\text{RF})} M_k^{(\text{RF})}$  hardware taps.

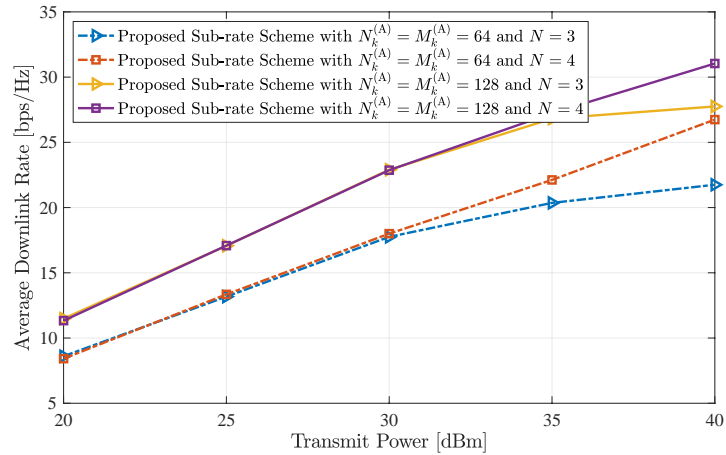


Figure 30. Achievable DL rates vs the transmit powers in dBm of Proposed Sub-rate Scheme with  $N_k^{(A)} = M_k^{(A)} = \{64, 128\}$  antenna elements

Figure 29 exhibits the DL rate performance for the proposed sub-rate based scheme and exhaustive search with 3 and 4 analog taps with respect to transmit power for different antenna elements for 16 antenna elements for each sub-antenna array at node  $k$ . As shown, using exhaustive search to solve  $\mathcal{OP}1$  achieves around 3 bps/Hz higher DL rate than the proposed sub-rate scheme. However, the proposed scheme is still preferable because of its low-complexity instead of this small DL rate trade-off.

The achievable DL rate for  $N_k^{(A)} = M_k^{(A)} = \{64, 128\}$  with respect to transmit power is presented in Figure 30. The proposed system with 128 antenna elements provides the highest DL rate considering 4 tap analog canceller. Although the 3 tap FD architecture provides similar performance for low transmit powers, the DL rate degrades as more DoFs are required for suppress the SI at high transmit power.

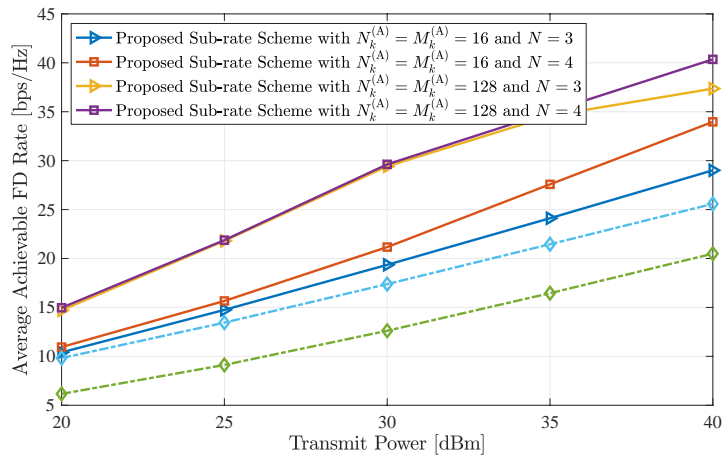


Figure 31. Average FD and HD rates vs. the transmit powers in dBm for  $N_k^{(A)} = M_k^{(A)} = \{16, 128\}$  antenna elements and different analog canceller taps at node  $k$ .

The achievable FD rate as a function of the transmit powers of nodes  $k$  and  $m$  is illustrated in Figure 31 for  $N = \{3, 4\}$  taps for the proposed analog canceller, which translates to 50% – 62% reduction in the number of taps compared to a case that connects all outputs of the TX RF chains to every input to the RX RF chains. It is shown in the figure that all rates increase with increasing transmit power, and no rate saturation is exhibited for the proposed FD HBF technique for  $N = 4$ . The latter trend witnesses the effective adaptability of Algorithm 5 to the SI conditions for both considered pairs of  $N_k^{(A)}$  and  $M_k^{(A)}$ . Although, for  $N = 3$  taps, the FD rate reduces at high transmit power, it provides comparable performance to  $N = 4$  taps case in limited transmit power cases while large antenna elements are considered. As an indicative example, it is shown that for 40dBm transmit powers, the proposed approach with 128 antenna

elements results in a 40bps/Hz achievable rate, which is around 1.6 times more than the HD rate.

## 5.5 Concluding Remarks

In this chapter, we presented a hybrid A/D beamforming architecture realizing FD massive MIMO transceivers with large antenna elements and much fewer RF chains. We proposed a novel multi-tap analog canceller where the complexity is independent of number of antenna elements. We also derived a novel sub-rate based RF TX/RX beamforming design that remove the computational complexity of analog beam selection compared to a conventional exhaustive search approach. Our representative simulation with millimeter wave channel model exhibits achievable rate superiority of the proposed FD design compared to the HD system.

## CHAPTER 6

### DIRECTION-ASSISTED BEAM MANAGEMENT IN FULL DUPLEX MILLIMETER WAVE MASSIVE MIMO SYSTEMS

Recent applications of the Full Duplex (FD) technology focus on enabling simultaneous control communication and data transmission to reduce the control information exchange overhead, which impacts end-to-end latency and spectral efficiency. In this chapter, we present a simultaneous direction estimation and data transmission scheme for millimeter Wave (mmWave) massive MIMO systems, enabled by a recent FD MIMO technology with reduced hardware complexity SI cancellation. We apply the proposed framework in the mmWave analog beam management problem, considering a base station equipped with a large transmit antenna array realizing downlink analog beamforming and few digitally controlled receive antenna elements used for uplink Direction of Arrival (DoA) estimation. A joint optimization framework for designing the DoA-assisted analog beamformer and the analog as well as digital SI cancellation is presented with the objective to maximize the achievable downlink rate.

---

The content of this chapter is based on our published article in [119]. Copyright © 2021 IEEE.

## 6.1 Introduction

Recently in [102, 110, 120], FD MIMO systems operating at mmWave frequencies were introduced, where SI suppression was achieved through a combination of propagation domain isolation, analog domain suppression, and digital SI cancellation techniques.

Wireless communications at mmWave frequencies are mainly realized via highly directional BF, which is enabled by massive MIMO transceivers [121] that are capable of analog or hybrid A/D beamforming [122]. To alleviate the hardware cost in those transceiver architectures, the large-scale antenna arrays are connected to small numbers of RF chains via analog preprocessing networks comprised of phase shifters [123]. However, the selection of the adequate analog beams from the predefined codebooks and the design of the digital beamformers require CSI knowledge, which is hard to acquire with realistically affordable latency, especially under mobility conditions (see, e.g., [124] and references therein). This challenge will be naturally more pronounced in the envisioned FD massive MIMO systems operating at mmWave frequencies, where multiple UL and DL channels need to be estimated. In practice, the analog BF in mmWave massive MIMO systems is designed via beam switching between the communicating nodes in order to find a pair of beams from their available beam codebooks meeting a link performance indicator threshold [125, 126]. However, such time-consuming beam training procedures incur significant configuration overhead deprived of data transmission. Hence, beam misalignment may yield poor performance under mobility scenarios [127]. Alternatively, exploiting UL/DL reciprocity or position information, the DL BF can be performed in the direction of the UL dominant Direction of Arrival (DoA), thus, reducing the beam sweeping overhead [121, 128].

### 6.1.1 Contributions

The contribution of our work is as follows.

- We present a DoA-assisted beam management framework for FD mmWave massive MIMO systems, where the BS is equipped with a large antenna array realizing DL analog BF and few digitally controlled receive antenna elements used for UL DoA estimation.
- Capitalizing on our presented FD hardware architecture for hybrid A/D BF in Chapter 5, we propose a Simultaneous DoA estimation and Data Transmission (SDDT) scheme for boosting beam management in FD mmWave massive MIMO communications.
- Enabled by FD and leveraging channel reciprocity, we simultaneously estimate the UL dominant DoA and transmit analog beamformed data in the DL direction.
- We present a joint design of the DoA-assisted analog BF as well as the A/D SI cancellation units, targeting the maximization of the achievable DL rate.
- Our extensive simulation results considering a mmWave channel model showcase the FD-enabled gains of DoA-assisted beam management under various user mobility conditions.

## 6.2 System and Signal Models

We consider an FD mmWave massive MIMO BS node  $b$  equipped with  $N_b$  TX and  $M_b$  RX antenna elements communicating with a mobile single-antenna FD UE node  $u$ . In particular, in the TX of the BS node  $b$ , a single RF chain is connected via phase shifters with a large antenna array of  $N_b$  elements, whereas each of the few  $M_b$  RX antennas is connected to a dedicated RF

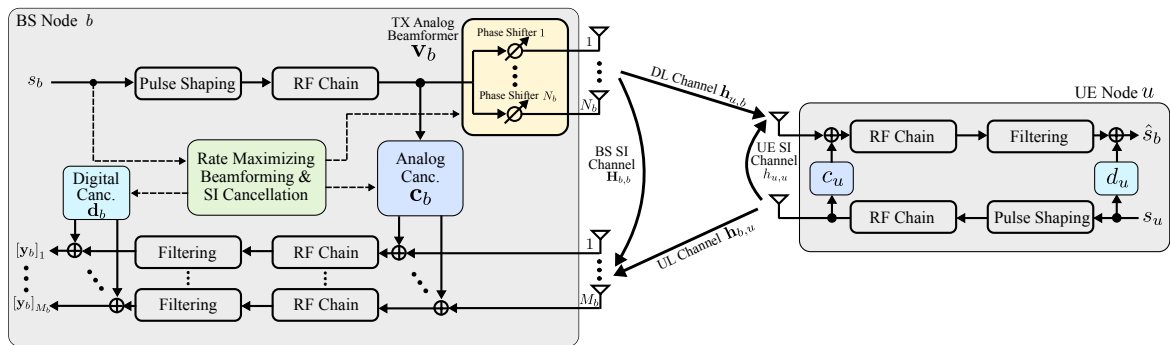


Figure 32. The considered FD massive MIMO communication system operating at mmWave frequencies: an FD massive MIMO BS capable of analog BF communicates with a mobile single-antenna FD UE, where the latter node transmits training signals in the UL for DoA estimation.

chain. In this work, a small number for  $M_b$  is sufficient for UL DoA estimation; extension for large  $M_b$  and analog combining is left for future work. Using the values of the  $N_b$  phase shifters, we can formulate the TX analog beamforming vector  $\mathbf{v}_b \in \mathbb{C}^{N_b \times 1}$ , whose elements are assumed to have constant magnitude, i.e.,  $|\mathbf{v}_b[n]|^2 = 1/N_b \forall n = 1, 2, \dots, N_b$ . Besides, we assume that the angles of the analog phase shifters are quantized and have a finite set of possible values. Therefore,  $\mathbf{v}_b \in \mathbb{F}_{\text{TX}}$ , where  $\mathbb{F}_{\text{TX}}$  represents the predefined beam codebook including  $\text{card}(\mathbb{F}_{\text{TX}})$  distinct vectors (or analog beams) [124,129]. We assume that, for every channel use, the BS node  $b$  transmits the complex-valued information data symbol  $s_b$  (chosen from a discrete modulation set) after analog BF with  $\mathbf{v}_b$ . Similarly, the single-antenna FD UE node  $u$  sends the training symbol  $s_u$  through the UL channel. The signal transmissions at both node  $b$  and node  $u$  are power limited according to  $\mathbb{E}\{\|\mathbf{v}_b s_b\|^2\} \leq P_b$  and  $\mathbb{E}\{|s_u|^2\} \leq P_u$ , respectively.

### 6.2.1 Channel Model

All the considered mmWave UL/DL channels consist of multiple propagation paths. In the spatial domain, each propagation path can be characterized by its DoA/DoD and the corresponding power as well as phase components [130]. For a certain coherence block, the UL channel  $\mathbf{h}_{b,u} \in \mathbb{C}^{M_b \times 1}$  including a LoS component and  $L_p - 1$  nLoS paths is mathematically expressed as

$$\mathbf{h}_{b,u} \triangleq \beta_{\text{LoS}} \mathbf{a}_{M_b}(\theta_{\text{LoS}}) + \sum_{\ell=1}^{L_p-1} \beta_{\text{nLoS},\ell} \mathbf{a}_{M_b}(\theta_{\text{nLoS},\ell}), \quad (6.1)$$

where  $\beta_{\text{LoS}} \in \mathbb{C}$  and  $\theta_{\text{LoS}} \in [0, 2\pi]$  represent the complex gain and the DoA of the LoS path, respectively. Here,  $\beta_{\text{nLoS},\ell} \in \mathbb{C}$  and  $\theta_{\text{nLoS},\ell} \in [0, 2\pi] \forall \ell = \{1, 2, \dots, L_p - 1\}$  are the complex gains and the DoAs of the nLoS path, respectively. Considering a ULA, the response vector  $\mathbf{a}_{M_b}(\theta)$  for  $M_b$  antenna elements and any DoA  $\theta$  is formulated as [129]

$$\mathbf{a}_{M_b}(\theta) \triangleq \frac{1}{\sqrt{M_b}} [1, e^{j\frac{2\pi}{\lambda} d \sin(\theta)}, \dots, e^{j\frac{2\pi}{\lambda} (M_b-1) d \sin(\theta)}]^T, \quad (6.2)$$

where  $\lambda$  is the propagation signal wavelength and  $d$  denotes the distance between adjacent antenna elements.

For the considered FD system, the UL and DL channels are reciprocal resulting in similar complex gains and DoAs/DoDs [121, 129]. Therefore, similar to Equation 6.1, the DL channel  $\mathbf{h}_{u,b}^T \in \mathbb{C}^{1 \times N_b}$  can be expressed as follows:

$$\mathbf{h}_{u,b}^T \triangleq \beta_{\text{LoS}} \mathbf{a}_{N_b}^H(\theta_{\text{LoS}}) + \sum_{\ell=1}^{L_p-1} \beta_{\text{nLoS},\ell} \mathbf{a}_{N_b}^H(\theta_{\text{nLoS},\ell}). \quad (6.3)$$

In this work, our goal is to estimate the LoS DoA  $\theta_{\text{LoS}}$  using the UL training symbols and find the DoA-assisted analog beamformer  $\mathbf{v}_b$  that maximizes the DL rate. However, due to the FD operation at both nodes, the simultaneous DL data and UL training transmission induce SI signal in the RXs of the BS and UE. Following [102, 111], we consider the mmWave clustered model for the SI channels denoted by  $\mathbf{H}_{b,b} \in \mathbb{C}^{M_b \times N_b}$  for the BS node  $b$  and  $h_{u,u} \in \mathbb{C}$  for the UE node  $u$ , where  $\kappa$  represent the Rician factor.

### 6.2.2 Received Signal Model

At the RX of the BS node  $b$ , the training symbols transmitted from the UE node  $u$  are received along with the SI signal induced by the simultaneous data and training signal transmissions. Due to limited propagation attenuation, the strong SI signal is capable of driving the RX RF chains into saturation. Therefore, as shown in Figure 32, an  $N$ -tap analog SI canceller is utilized to suppress the SI at the inputs of the RX RF chains, which is based on the TX RF chain output. Exploiting the low-complexity cancellation in Chapter 5, we employ the canceller taps at the TX RF chain output at the BS node  $b$  resulting in an analog SI canceller where the number of taps does not scale with the number of antenna elements. To suppress the residual SI

signal after analog cancellation, a digital SI canceller is utilized at the BS baseband. Denoting  $\mathbf{c}_b, \mathbf{d}_b \in \mathbb{C}^{M_b \times 1}$  as the analog and digital SI cancellers, respectively, the baseband received signal at the BS node  $b$ ,  $\mathbf{y}_b \in \mathbb{C}^{M_b \times 1}$ , is given by

$$\mathbf{y}_b \triangleq \mathbf{h}_{b,u} s_u + (\mathbf{H}_{b,b} \mathbf{v}_b + \mathbf{c}_b + \mathbf{d}_b) s_b + \mathbf{n}_b, \quad (6.4)$$

where  $\mathbf{n}_b \in \mathbb{C}^{M_b \times 1}$  is the zero-mean AWGN with variance  $\sigma_b^2 \mathbf{I}_{M_b}$ . Similarly, the DL signal  $y_u \in \mathbb{C}$  received at the UE node  $u$  after analog and digital SI cancellation can be expressed as

$$y_u \triangleq \mathbf{h}_{u,b}^T \mathbf{v}_b s_b + (h_{u,u} + c_u + d_u) s_u + n_u, \quad (6.5)$$

where  $n_u \in \mathbb{C}$  represents the AWGN with variance  $\sigma_u^2$ . As previously mentioned, for proper FD-based reception, the RXs' RF chains need to be unsaturated from any residual SI stemming out analog SI cancellation at both nodes  $b$  and  $u$  [59, 85]. Denoting the residual SI power thresholds as  $\lambda_b$  and  $\lambda_u$  at node  $b$  and node  $u$ , respectively, the residual SI power constraints  $P_b |[(\mathbf{H}_{b,b} \mathbf{v}_b + \mathbf{c}_b)]_{(j,:)}|^2 \leq \lambda_b \forall j = 1, 2, \dots, M_b$  and  $P_u |(h_{u,u} + c_u)|^2 \leq \lambda_u$  are necessary to be satisfied for successful reception after analog SI suppression.

### 6.3 DoA Estimation and DL Data Transmission

In this section, we introduce the proposed DoA-assisted analog beam management protocol along with the DoA tracking scheme for the considered UL/DL mmWave channel with the proposed FD massive MIMO system.

### 6.3.1 UL/DL Channel Evolution Properties

We assume wireless communications in TDD manner, where the considered channels remain constant for all the channel uses in a time slot, and the channel properties (i.e., DoAs/DoDs, complex path gains) of the successive time slots are temporally correlated. Each time slot of  $T_s$  time units contains  $L$  symbols (i.e.,  $L$  channel uses). For any consecutive  $(i-1)$  and  $i$  time slots, the evolution of LoS DoA component is expressed similar to [131] as

$$\theta_{\text{LoS}}[i] \triangleq \theta_{\text{LoS}}[i-1] + \Delta\theta, \quad (6.6)$$

where  $\Delta\theta$  depends on the velocity of the UE node  $u$  and the time slot duration  $T_s$ . We also assume that the UE node is moving with the constant velocity  $v$ , hence,  $\Delta\theta \triangleq \arctan\left(\frac{vT_s}{d_{\text{BS}}}\right)$  with  $d_{\text{BS}}$  being the distance between the UE and the BS nodes. The evolution model for the LoS complex path gain  $\beta_{\text{LoS}}$  is given by the first-order Gauss-Markov model as [131]

$$\beta_{\text{LoS}}[i] \triangleq \rho\beta_{\text{LoS}}[i-1] + \epsilon[i-1], \quad (6.7)$$

where  $\rho$  is the correlation coefficient, and  $\epsilon[i-1]$  is the zero-mean complex Gaussian noise distributed as  $\mathcal{CN}(0, 1 - \rho^2)$ . The DoAs and complex path gains of the nLoS components are assumed to change randomly between consecutive time slots. In this chapter, we propose to track only the LoS DoA component for each time slot, and then use it analog beam selection.

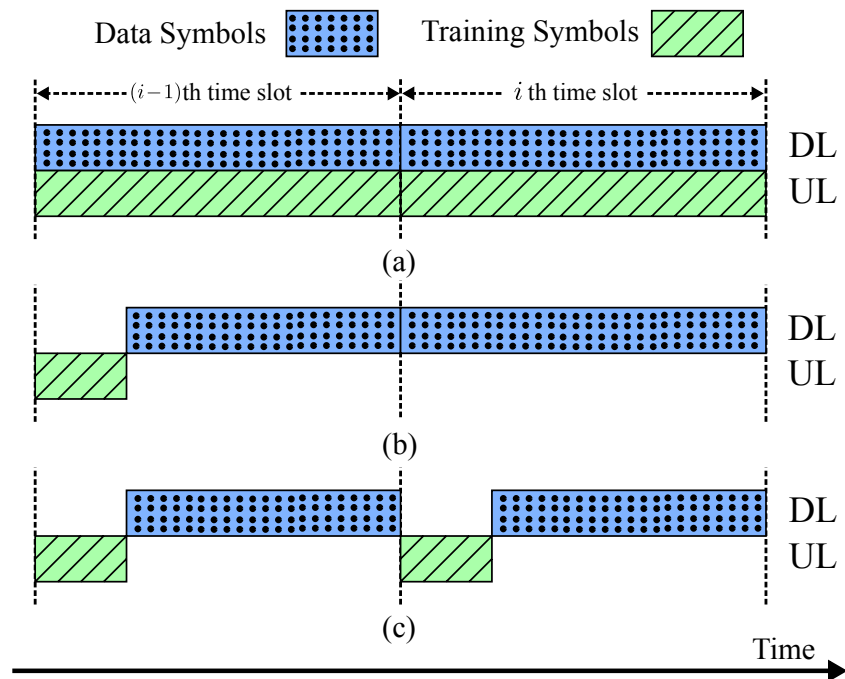


Figure 33. (a) Proposed FD SDDT Scheme, (b) Conventional HD DoA with update after threshold, and (c) Conventional HD DoA estimation in each slot.

The estimation of all complex path gains and their correlation coefficients is left for future investigation.

### 6.3.2 Proposed FD-Based SDDT Protocol

The proposed protocol for simultaneous DoA estimation and data transmission is illustrated in Figure 33(a), where the DL channel is dedicated for data transmission, while the UL is accessed to transmit training symbols. The procedures of DoA-based tracking and transmission are described as follows:

1. DL Data transmission at any  $i$ th time slot leverages the DOA estimation for the previous  $(i-1)$ th time slot, which is realized via simultaneous UL transmission of  $L$  orthogonal training symbols sent from the UE node  $u$ .
2. Capitalizing on the UL/DL reciprocity, any LoS component estimation  $\hat{\theta}_{\text{LoS}}[i-1]$  is used during the next  $i$ th time slot for the DL data transmission precoding.
3. The DL analog beamformer  $\mathbf{v}_b[i] \in \mathbb{F}_{\text{TX}}$  at each  $i$ th time slot is chosen according to  $\hat{\theta}_{\text{LoS}}[i-1]$  subject to the satisfaction of the residual SI power constraints.

In Figure 33(b), a conventional HD DoA-assisted analog beamforming scheme is illustrated, where, contrary to the FD case, a fraction of the available symbols in a time slot is dedicated for DoA estimation. Once the DoA of a time slot is estimated, its analog beamforming and that of the succeeding ones utilizes the same DoA estimation, unless the received SNR falls below a certain threshold; in this case, a DoA estimation update occurs. An HD data transmission protocol with DoA estimation at each time slot is shown in Figure 33(c).

### 6.3.3 UL DoA Estimation

As previously discussed, the UL training symbols at any  $(i-1)$ th time slot are used for this slot's LoS DoA estimation, which is leveraged for analog BF at the  $i$ th time slot. For this estimation, we deploy the MULTiple SIGNAL Classification (MUSIC) algorithm; other DoA estimation techniques can be used as well [132]. Starting from Equation 6.4, the received  $L$

training symbols at any  $(i-1)$ th time slot can be grouped in  $\mathbf{Y}_b[i-1] \in \mathbb{C}^{M_b \times L}$ . For the MUSIC DoA estimation, the received signal covariance matrix  $\mathbf{R}_b \in \mathbb{C}^{M_b \times M_b}$  can be estimated as

$$\mathbf{R}_b \triangleq \mathbb{E}\{\mathbf{Y}_b[i-1]\mathbf{Y}_b[i-1]^H\}, \hat{\mathbf{R}}_b \triangleq \frac{1}{L}\mathbf{Y}_b[i-1]\mathbf{Y}_b^H[i-1]. \quad (6.8)$$

By taking the eigenvalue decomposition of the estimated sample covariance matrix  $\hat{\mathbf{R}}_b$ , it is deduced that:

$$\hat{\mathbf{R}}_b \triangleq \mathbf{U}\text{diag}\{\eta_1, \eta_2, \dots, \eta_{M_b}\}\mathbf{U}^H, \quad (6.9)$$

where  $\eta_1 \geq \eta_2 \geq \dots \geq \eta_{M_b}$  are the eigenvalues of  $\hat{\mathbf{R}}_b$  and  $\mathbf{U} \in \mathbb{C}^{M_b \times M_b}$  contains their corresponding eigenvectors. Since we are interested in estimating the DoA of the LoS component, the matrix  $\mathbf{U}$  can be partitioned as  $\mathbf{U} = [\mathbf{u}_s | \mathbf{U}_n]$ , where the columns in  $\mathbf{U}_n \in \mathbb{C}^{M_b \times M_b - 1}$  are the eigenvectors spanning the noise subspace and  $\mathbf{u}_s$  is the signal space eigenvector. We next project the search vector  $\mathbf{a}_{M_b}(\theta) \forall \theta \in [0, 2\pi]$  onto the noise subspace  $\mathbf{U}_n$  and calculate the spectral peak as

$$S(\theta) \triangleq \frac{1}{\mathbf{a}_{M_b}^H(\theta)\mathbf{U}_n\mathbf{U}_n^H\mathbf{a}_{M_b}(\theta)}. \quad (6.10)$$

Finally, the position  $\theta$  of the spectral peak is the estimated LoS DoA  $\hat{\theta}_{\text{LoS}}[i-1]$  corresponding to this  $(i-1)$ th time slot.

### 6.3.4 DoA-Assisted Analog Beamforming and DL Rate

Capitalizing on the UL/DL reciprocity and the estimated LoS DoA component, we propose to approximate the DL channel at each  $i$ th time slot as follows:

$$\widehat{\mathbf{h}}_{u,b}^T[i] \triangleq \mathbf{a}_{N_b}^H(\widehat{\theta}_{\text{LoS}}[i-1]). \quad (6.11)$$

This approximation is further used during this  $i$ th time slot to find the best analog beamformer  $\mathbf{v}_b[i]$  at the BS node  $b$ , via searching in the available beam codebook  $\mathbb{F}_{\text{TX}}$ . Therefore, the instantaneous achievable DL rate per channel use for the proposed FD-based SDDT scheme at this time slot is given by

$$\mathcal{R}_{\text{DL}}[i] = \log_2 \left( 1 + \frac{P_b |\widehat{\mathbf{h}}_{u,b}^T[i] \mathbf{v}_b[i]|^2}{\sigma_u^2 + \sigma_{r,u}^2[i]} \right), \quad (6.12)$$

where  $\sigma_{r,u}^2[i] \triangleq P_u |h_{u,u}[i] + c_u[i] + d_u[i]|^2$  is the residual signal power after both A/D SI cancellation at the UE node  $u$ .

## 6.4 Proposed SDDT Optimization Framework

In this section, we focus on the joint design of the analog beamformer  $\mathbf{v}_b$ , the analog SI cancellers  $\mathbf{c}_b$  and  $c_u$ , as well as the digital canceller  $d_b$  and  $d_u$  at the BS node  $b$  and the UE node  $u$ , which maximize the estimated achievable DL rate in Equation 6.12 at each  $i$ th time

slot. Based on the availability of the DL channel estimation  $\widehat{\mathbf{h}}_{u,b}[i]$ , as well as the SI estimations  $\widehat{\mathbf{H}}_{b,b}[i]$  and  $\widehat{h}_{u,u}[i]$ , we consider the optimization problem:

$$\begin{aligned}
& \max_{\substack{\mathbf{v}_b[i], \mathbf{c}_b[i], d_b[i] \\ c_u[i], d_u[i]}} \log_2 \left( 1 + \frac{P_b |\widehat{\mathbf{h}}_{u,b}^T[i] \mathbf{v}_b[i]|^2}{\sigma_u^2 + \sigma_{r,u}^2[i]} \right) \\
& \text{s.t. } P_b |[(\widehat{\mathbf{H}}_{b,b}[i] \mathbf{v}_b[i] + \mathbf{c}_b[i])]_{(j,:)}|^2 \leq \lambda_b \forall j = 1, \dots, M_b, \\
& P_u |(\widehat{h}_{u,u}[i] + c_u[i])|^2 \leq \lambda_u, \\
& \mathbb{E}\{\|\mathbf{v}_b[i] s_b[i]\|^2\} \leq P_b, \text{ and } \mathbb{E}\{|s_u[i]|^2\} \leq P_u, \\
& \mathbf{v}_b[i] \in \mathbb{F}_{\text{TX}}. \tag{6.13}
\end{aligned}$$

The first and second constraints impose the RX RF chain saturation thresholds  $\lambda_b$  and  $\lambda_u$  after analog cancellation at nodes  $b$  and  $u$ , respectively. These saturation thresholds ensure successful reception of the training symbols and decoding of BS's data symbols. The next two constraints in Equation 6.13 refer to the nodes' average transmit powers. The final constraint enforces the predefined analog codebook for the BS beamformer.

The optimization problem in Equation 6.13 is a non-convex problem with coupling variables, hence, quite difficult to tackle. In this work, we solve it suboptimally using alternating optimization, leaving other possibilities for future work. First, we find the BS analog beamformer  $\mathbf{v}_b[i]$  via the following problem:

$$\mathbf{v}_b[i] = \arg \max_{\mathbf{v} \in \mathbb{F}_{\text{TX}}} \frac{|\widehat{\mathbf{h}}_{u,b}^T[i] \mathbf{v}|^2}{\|\widehat{\mathbf{H}}_{b,b}[i] \mathbf{v}\|^2}. \tag{6.14}$$

---

**Algorithm 7** Proposed FD massive MIMO SDDT Design
 

---

**Input:**  $\widehat{\mathbf{H}}_{b,b}[i]$ ,  $\widehat{h}_{u,u}[i]$ ,  $P_b$ ,  $P_u$ ,  $\widehat{\theta}_{\text{LoS}}[i-1]$ , and  $M_b$ .

**Output:**  $\mathbf{v}_b[i]$ ,  $\mathbf{c}_b[i]$ ,  $c_u[i]$ ,  $\mathbf{d}_b[i]$ , and  $d_u[i]$ .

- 1: Obtain the DL channel estimate  $\widehat{\mathbf{h}}_{u,b}[i]$  using  $\widehat{\theta}_{\text{LoS}}[i-1]$  as described in Equation 6.11.
  - 2: Obtain the analog beamformer  $\mathbf{v}_b[i] = \arg \max_{\mathbf{v} \in \mathbb{F}_{\text{TX}}} \frac{|\widehat{\mathbf{h}}_{u,b}^T[i]\mathbf{v}|^2}{\|\widehat{\mathbf{H}}_{b,b}[i]\mathbf{v}\|^2}$  using exhaustive search.
  - 3: **for**  $n = 1, 2, \dots, M_b - 1$  **do**
  - 4:     Set analog SI canceller  $\mathbf{c}_b[i] = \begin{bmatrix} -[\widehat{\mathbf{H}}_{b,b}[i]\mathbf{v}_b[i]]_{1:n} \\ \mathbf{0}_{(M_b-n):M_b} \end{bmatrix}$ .
  - 5:     Set  $c_u[i] = -\widehat{h}_{u,u}[i]$ .
  - 6:     **if**  $P_b|[(\widehat{\mathbf{H}}_{b,b}[i]\mathbf{v}_b[i] + \mathbf{c}_b[i])_{(j,:)}]|^2 \leq \lambda_b \forall j = 1, \dots, M_b$ , and  $P_u|(\widehat{h}_{u,u}[i] + c_u[i])|^2 \leq \lambda_u$  **then**
  - 7:         Output  $\mathbf{v}_b[i]$ ,  $\mathbf{c}_b[i]$ ,  $c_u[i]$ ,  $\mathbf{d}_b[i] = -(\widehat{\mathbf{H}}_{b,b}[i]\mathbf{v}_b[i] + \mathbf{c}_b[i])$ ,  $d_u[i] = -(\widehat{h}_{u,u}[i] + c_u[i])$ , and terminate the iterations.
  - 8:     **end if**
  - 9: **end for**
  - 10: Set  $\mathbf{c}_b[i] = -\widehat{\mathbf{H}}_{b,b}[i]\mathbf{v}_b[i]$  and  $c_u[i] = -\widehat{h}_{u,u}[i]$ .
  - 11: **if**  $P_b|[(\widehat{\mathbf{H}}_{b,b}[i]\mathbf{v}_b[i] + \mathbf{c}_b[i])_{(j,:)}]|^2 \leq \lambda_b \forall j = 1, 2, \dots, M_b$ , and  $P_u|(\widehat{h}_{u,u}[i] + c_u[i])|^2 \leq \lambda_u$  **then**
  - 12:     Output  $\mathbf{v}_b[i]$ ,  $\mathbf{c}_b[i]$ ,  $c_u[i]$ ,  $\mathbf{d}_b[i] = -(\widehat{\mathbf{H}}_{b,b}[i]\mathbf{v}_b[i] + \mathbf{c}_b[i])$ ,  $d_u[i] = -(\widehat{h}_{u,u}[i] + c_u[i])$ , and stop the algorithm.
  - 13: **else**
  - 14:     Output that the  $\mathbf{c}_b[i]$  realizations or  $c_u[i]$  do not meet the RX RF saturation constraints.
  - 15: **end if**
- 

The exhaustive search for this problem can be easily implemented by a simple look-up table given the estimated SI channel  $\widehat{\mathbf{H}}_{b,b}[i]$  and the estimated DL channel  $\widehat{\mathbf{h}}_{u,b}[i]$ . Following the analog SI canceller structure in Chapter 5 and using  $\mathbf{v}_b[i]$ , we next seek the  $N$ -tap analog canceller  $\mathbf{c}_b[i]$  with  $1 \leq N \leq M_b$  that satisfies the first threshold constraint. The single-tap canceller at node  $u$  is obtained as  $c_u[i] = -\widehat{h}_{u,u}[i]$ . To maximize the signal-to-interference-plus-noise ratio, the digital cancellers  $\mathbf{d}_b$  and  $d_u$  are set as the respective complementary residual SI channels after

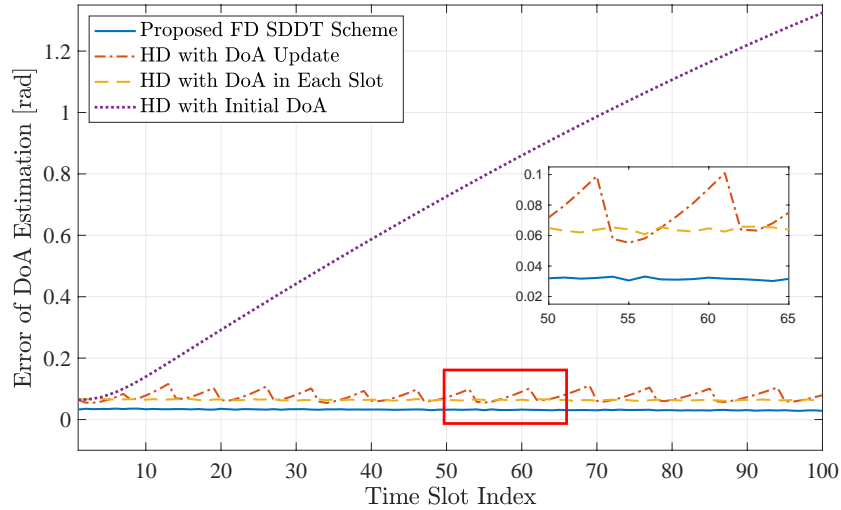


Figure 34. Error of LoS DoA estimation w.r.t the time slot index for the  $64 \times 2$  FD massive MIMO node  $b$  communicating with the mobile single-antenna FD UE  $u$  transmitting UL training symbols with 10dBm transmit power.

analog SI cancellation. Our solution for the optimization problem Equation 6.13 is summarized in Algorithm 7.

## 6.5 Numerical Results

In this section, we present simulation results for the performance of the proposed SDDT scheme for FD mmWave massive systems in comparison with HD counterparts.

### 6.5.1 Simulation Parameters

We perform an extensive waveform simulation following the FD massive MIMO architecture illustrated in Figure 32 when operating at mmWave frequencies, where a  $64 \times 2$  FD massive MIMO node  $b$  is communicating with a single-antenna FD UE node  $u$ . We have assumed that

the single TX RF chain at the BS node  $b$  is connected to a ULA consisting of  $N_b = 64$  antenna elements. In contrast, on the RX side,  $M_b = 2$  RX antennas are connected to their dedicated RX RF chains. The UE node  $u$  employs a non-ideal single-tap SI canceller, where the FD massive MIMO BS node  $b$  deploys an  $N = 2$  taps analog SI canceller [102]. The multipath UL and DL channels are simulated as mmWave channels at 28 GHz each with one LoS and 4 nLoS channel paths. Considering the distance  $d_{BS} = 100m$  of the BS node  $b$  from the UE, the pathloss of the both UL and DL channels is assumed to be 100dB with a 25 dB Rician factor between the LoS and nLoS paths [130]. In addition, the SI channels are modeled as Rician fading channels with a  $\kappa$ -factor of 35dB and pathloss 40dB [59]. The RX noise floors at all nodes were assumed to be  $-100\text{dBm}$ . To this end, the RXs have an effective dynamic range of 60dB provided by 14-bit ADC for a PAPR of 10 dB. Therefore, the residual SI power after analog SI cancellation at the input of each RX RF chain has to be below  $-40\text{dBm}$  to avoid signal saturation. For the considered FD massive MIMO architecture, we have assumed that the UE  $u$  is moving at a constant velocity of 120km/h for a duration of 100 time slots, where each time slot is considered to be  $T_s = 10\text{msec}$  with  $L = 400$  symbols. For the BS analog beamformer, we have used a 6-bit beam codebook based on the DFT matrix. We have used 1000 independent Monte Carlo simulation runs to calculate the performance of all considered DoA estimation and data transmission designs.

### 6.5.2 Compared HD Massive MIMO Designs

We compare the performance of the proposed FD-based SDDT scheme with three HD DoA-assisted DL analog beam management techniques. First, we consider the “HD with Initial DoA”

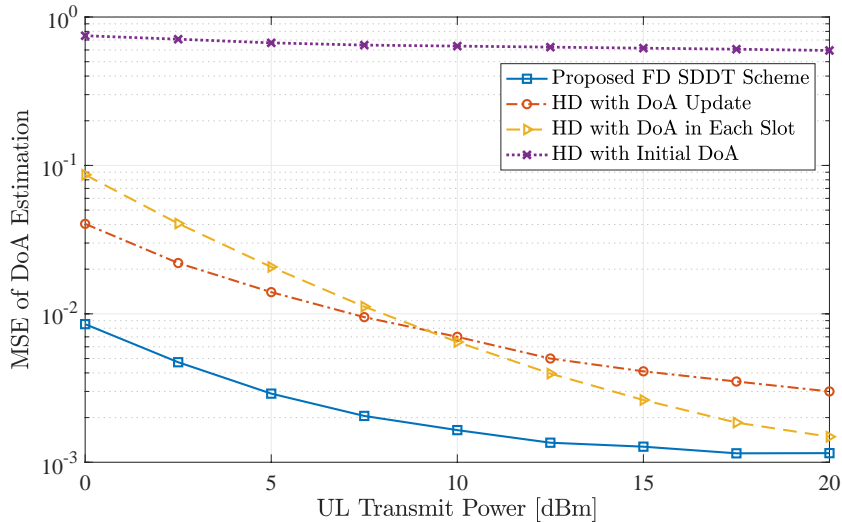


Figure 35. MSE of the DoA estimation with respect to UL transmit power in dBm for the  $64 \times 2$  FD massive MIMO node  $b$  communicating with the single-antenna FD UE  $u$  transmitting training symbols in the UL direction.

case, where DoA is estimated using the UL training symbols only in the first time slot, and for the rest of the 99 time slots, the same DoA is utilized for finding the DL analog beam. Secondly, we simulate the “HD DoA in Each Slot” scheme, where, for every time slot, a fraction of the UL training symbols is utilized for DoA estimation, and the rest of the symbols are dedicated for data transmission with analog BF. Finally, we consider the “HD DoA with Update” technique, where DL analog BF in each time slot is performed using the DoA estimation of the previous time slot, unless more than 3dB SNR loss occurs in the received DL signal, which triggers the initialization of a DoA-based analog beamformer update. In addition to the latter HD cases,

we have simulated the achievable DL rate for the proposed FD-based SDDT scheme with ideal DoA estimation.

### 6.5.3 DoA Estimation Error and Average DL Rate

In Figure 34, the LoS DoA estimation error in radians is illustrated with respect to the time slot index. We have considered that the FD massive MIMO node  $b$  communicates with the mobile single-antenna FD UE  $u$ , while the latter sends training symbols in the UL for DoA estimation with power 10dBm. It is shown in the figure that the “HD with Initial DoA” scheme provides higher DoA estimation error with increasing time slot index. This happens because it only estimates the DoA in the first time slot. As the UE moves, the initial DoA becomes outdated, and hence, a DoA estimation as well as an analog beam update are required. As illustrated in the inset plot, the “HD DoA with Update” scheme performs an LoS DoA update after reaching approximately 0.1rad estimation error, while the “HD DoA in Each Slot” results in a steady error as the estimation is performed in each time slot. It is, however, evident from Figure 34 that the proposed FD-based SDDT scheme with a 2-tap analog canceller provides substantially lower DoA estimation error compared to the HD cases across all time slots for the considered 10dBm UL transmit power. In Figure 35, we plot the Mean Squared Error (MSE) of the DoA estimation for all considered schemes as a function of the UL transmit power in the range 0 – 20dBm. It is clear from the figure that the MSE of the DoA estimation reduces with increasing UL transmit power. This happens because the received SNR at the BS increases. It is also shown that the proposed scheme outperforms all considered HD-based counterparts.

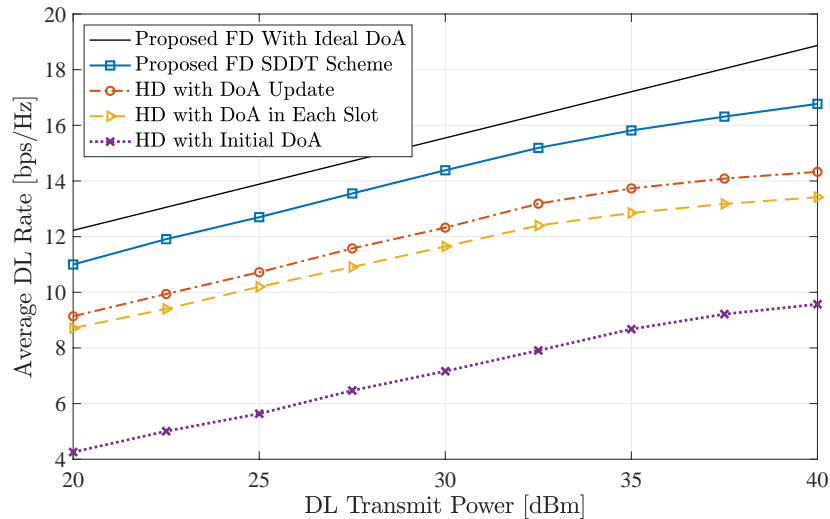


Figure 36. Achievable DL rate with respect to DL transmit power in dBm for the  $64 \times 2$  FD massive MIMO node  $b$  communicating with the mobile single-antenna FD UE  $u$  sending training symbols with 10dBm transmit power.

Figure 36 illustrates the achievable DL rate of the proposed SDDT scheme as a function of the DL transmit power, considering that the  $64 \times 2$  BS node  $b$  is transmitting data in the DL via analog BF to the constant-velocity mobile UE node  $u$ , while receiving UL training symbols with 10dBm transmit power. It is demonstrated that the “HD with Initial DoA” provides the lowest DL rate for all DL transmit power levels, as it suffers from the highest DoA estimation error. It is also shown that, although the “HD DoA with Update” scheme achieves higher DoA estimation error compared to the “HD DoA in Each Slot” approach, as depicted in Figure 34, it achieves higher DL rate across all DL transmit powers. This is due to the fact that the later HD DoA-assisted beam management scheme utilizes 10% symbols in each time slot for DoA

estimation, whereas the “HD DoA with Update” approach is capable of sending data symbols for the whole time slot when it doesn’t have to update the DoA estimation. It is finally evident that the proposed scheme with 2-tap analog cancellation achieves a higher DL rate compared to all the HD-based schemes for all DL transmit powers. In particular, for the large DL transmit power of 40dB, the proposed scheme for FD mmWave massive MIMO systems results in 120% of the achievable DL rate with the best HD-based counterpart.

## 6.6 Concluding Remarks

In this chapter, we presented a novel DoA-assisted analog beam management scheme for FD mmWave massive MIMO systems. We considered an FD massive MIMO BS with an analog beamformer serving a mobile single-antenna FD user moving at a constant velocity. By adopting the MUSIC DoA estimation technique as an example, we presented a joint design of the DoA-assisted analog beamformer and A/D SI cancellation at the BS node maximizing the DL rate. Our performance evaluation results considering a realistic mmWave channel model demonstrated the superior achievable rates of the proposed FD-based SDDT scheme.

## CHAPTER 7

### INTEGRATED SENSING AND COMMUNICATION WITH MILLIMETER WAVE FULL DUPLEX HYBRID BEAMFORMING

Integrated Sensing and Communication (ISAC) has attracted substantial attraction in recent years for spectral efficiency improvement, enabling hardware and spectrum sharing for simultaneous sensing and signaling operations. In-band FD is being considered as a key enabling technology for ISAC applications due to its simultaneous transmission and reception capability. In this chapter, we present an FD-based ISAC system operating at mmWave frequencies, where a massive MIMO BS node employing hybrid A/D beamforming is communicating with DL multi-antenna users and the same waveform is utilized at the BS receiver for sensing the radar targets in its coverage environment. We develop a sensing algorithm that is capable of estimating DoA, range, and relative velocity of the radar targets. A joint optimization framework for designing the A/D transmit and receive beamformers as well as the SI cancellation is presented with the objective to maximize the achievable DL rate and the accuracy of the radar target sensing performance.

---

Part of this chapter is based on our published and submitted articles in [133] and [134], respectively. Copyright © 2022 IEEE.

## 7.1 Introduction

Integrated sensing and communication is an emerging concept for future wireless networks, where the previously competing sensing and communication operations are jointly optimized in the same hardware platform using a unified signal processing framework [13–17]. Recently, FD massive MIMO communications have been considered a key enabler for ISAC applications due to their simultaneous UL and DL transmission capability within the entire frequency band [90, 102, 119, 135]. Furthermore, FD massive MIMO ISAC applications at millimeter Wave frequencies have the potential to provide high capacity communication links while simultaneously achieving high-resolution sensing, e.g., direction of arrival, range, and relative speed of radar targets/scatterers.

The performance of the FD ISAC systems relies on the in-band SI signal suppression capability that stems from the TX to the RX side during FD operation. Recently in [102, 110, 119, 120], SI cancellation was achieved for the FD massive MIMO systems operating at mmWave, utilizing a combination of propagation domain isolation, analog domain suppression, and digital SI cancellation techniques. To alleviate the hardware cost in mmWave massive MIMO transceivers, hybrid A/D beamformers are usually employed, where large-scale antenna arrays are usually connected to a small number of RF chains via analog preprocessing networks comprised of phase shifters [123]. Such systems require appropriate beam selection for analog TX/RX beamformers, chosen from predefined codebooks, to maximize DL rate and sensing accuracy. Moreover, in the envisioned FD ISAC with massive MIMO radios, the transmit waveform will be utilized for both DL data transmission and sensing of the radar targets [13]. Therefore, a joint design of the

A/D beamformers and SI cancellation along with sensing techniques is required for maximizing the performance of FD ISAC systems.

Very recently in [18, 19], joint radar communication and sensing frameworks, leveraging FD operation, were considered for single-antenna systems, where both communication and radar waveforms were optimized for sensing performance. In [20, 21], the FD ISAC operation was proposed for mmWave frequency bands considering a massive MIMO FD BS, where the signal power is maximized in the radar target direction, while maintaining a threshold DL rate performance. Although the considered FD ISAC approach estimated the DoA two radar targets, the range was only calculated for one target due to its disassociated DoA and range estimation technique.

### 7.1.1 Contributions

The contribution of this chapter is as follows:

1. We present a novel FD massive MIMO ISAC system operating at mmWave frequencies and realizing hybrid A/D beamforming, where OFDM waveforms are utilized for both DL communication and radar target sensing.
2. Unlike state-of-the-art works, we devise an ISAC optimization framework that is capable of estimating the DoA, range, and relative velocity of multiple radar targets, while maximizing the DL communication rate.
3. Our numerical results, considering the 5G NR OFDM waveform, verify the high sensing accuracy and the increased communication rate of the proposed optimization design.

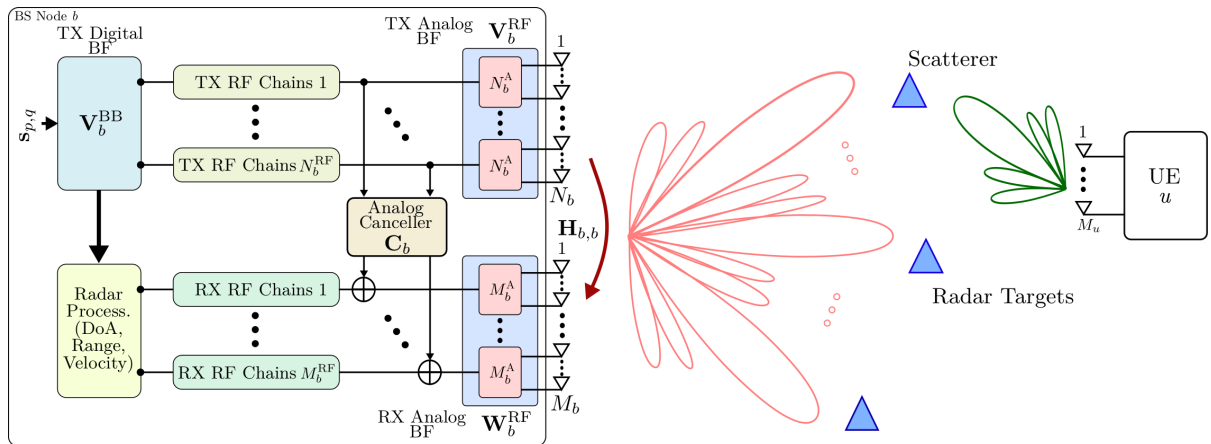


Figure 37. The considered FD massive MIMO ISAC system: the FD hybrid A/D beamforming BS communicates in the downlink with a mobile half duplex UE, while its reflected transmitted signals from radar targets/scatterers in the environment are received via hybrid combining and processed for DoA, range, and relative velocity estimations of the radar targets/scatterers.

4. We also employ the ISAC system for a multi-user DL communication, where we propose a joint design of the A/D beamformers and a reduced complexity SI cancellation for the FD ISAC system, which target at maximizing the multi-user DL communication rate and the precision of the radar target tracking.
5. Our extensive waveform simulation exhibits the radar tracking performance of the proposed multi-user FD ISAC system.

## 7.2 System and Signal Models

We consider an FD ISAC system comprising of an FD mmWave massive MIMO BS node  $b$  equipped with  $N_b$  TX and  $M_b$  RX antenna elements communicating in the DL direction with

an RX UE node  $u$  with  $M_u$  antenna elements, while the reflected DL signal is utilized to detect radar targets/scatterers randomly distributed within the communication/sensing environment at the RX of BS node  $b$ , as depicted in Figure 37. To reduce the number of RF chains and phase shifters, the BS node  $b$  employs a partially-connected Hybrid beamforming structure with A/D TX and RX beamformers, where each of the  $N_b^{\text{RF}}$  and  $M_b^{\text{RF}}$  TX/RX RF chains is connected to a ULA of  $N_b^{\text{A}}$  and  $M_b^{\text{A}}$  antenna elements, respectively, via phase shifters. Therefore, it holds  $N_b = N_b^{\text{A}}N_b^{\text{RF}}$  and  $M_b = M_b^{\text{A}}M_b^{\text{RF}}$  for total number of TX and RX antennas, respectively, at the BS node  $b$ . Since the size of the antenna array at the UE node  $u$  is typically much smaller than at the FD massive MIMO BS  $b$ , we assume that the UE adopts a fully digital beamforming structure.

It is assumed that BS node  $b$  transmits mmWave OFDM waveforms in the DL direction containing  $Q$  OFDM symbols with  $P$  active subcarriers. In the BB, the unit power frequency-domain symbol vector  $\mathbf{s}_{p,q} \in \mathbb{C}^{d_b \times 1}$  at the  $p$ th subcarrier of  $q$ th OFDM symbol is precoded using digital beamforming matrix  $\mathbf{V}_b^{\text{BB}} \in \mathbb{C}^{N_b^{\text{RF}} \times d_b}$ , where  $d_b \leq \min\{N_b^{\text{RF}}, M_u\}$ . Following the BB precoder, the DL signal is processed by the analog beamformer  $\mathbf{V}_b^{\text{RF}} \in \mathbb{C}^{N_b \times N_b^{\text{RF}}}$  containing the configurations of the phase shifters as follows:

$$\mathbf{V}_b^{\text{RF}} \triangleq \begin{bmatrix} \mathbf{v}_1 & \mathbf{0}_{N_b^{\text{A}} \times 1} & \cdots & \mathbf{0}_{N_b^{\text{A}} \times 1} \\ \mathbf{0}_{N_b^{\text{A}} \times 1} & \mathbf{v}_2 & \cdots & \mathbf{0}_{N_b^{\text{A}} \times 1} \\ \vdots & \vdots & \ddots & \vdots \\ \mathbf{0}_{N_b^{\text{A}} \times 1} & \mathbf{0}_{N_b^{\text{A}} \times 1} & \cdots & \mathbf{v}_{N_b^{\text{RF}}} \end{bmatrix}. \quad (7.1)$$

The elements of each  $\mathbf{v}_i$  are assumed to have constant magnitude, i.e.,  $|\mathbf{v}_i[n]|^2 = 1/N_b^A \forall n = 1, 2, \dots, N_b^A$ . We also assume that  $\mathbf{v}_i \in \mathbb{F}_{\text{TX}} \forall i = 1, 2, \dots, N_b^{\text{RF}}$ , which means that all analog TX precoding vectors belong in a predefined beam codebook  $\mathbb{F}_{\text{TX}}$  including  $\text{card}(\mathbb{F}_{\text{TX}})$  distinct vectors (or analog beams). Applying both A/D beamforming, the TX frequency-domain symbols at the antenna elements are expressed as

$$\mathbf{x}_{p,q} \triangleq \mathbf{V}_b^{\text{RF}} \mathbf{V}_b^{\text{BB}} \mathbf{s}_{p,q}, \quad (7.2)$$

where  $\mathbf{x}_{p,q} \in \mathbb{C}^{N_b \times 1}$ . The signal transmissions is power limited. Therefore,  $\mathbb{E}\{\|\mathbf{V}_b^{\text{RF}} \mathbf{V}_b^{\text{BB}} \mathbf{s}_{p,q}\|^2\} \leq P_b$ .

### 7.2.1 Radar Signal Reception Model

For sensing operation, we consider that a collection of  $K$  radar targets/scatterers are randomly distributed within the communication/sensing environment and are to be detected by the BS node  $b$ . All the  $K$  targets reflect DL signal back to the RX of the BS node, while only a subset of them ( $L$  out of  $K$ ) contributes to the DL communication scattering paths between the BS node  $b$  and the RX UE node  $u$ . The purpose of the sensing operation is to estimate the DoA, range, and relative velocity of each radar targets.

We consider that the DoAs of the  $K$  targets are defined as  $\Theta = [\theta_1, \theta_2, \dots, \theta_K]$ , while the distance and the relative speed of  $k$ th target correspond to a delay  $\tau_k$  and a Doppler shift  $f_{D,k}$ ,

respectively. Enabled by FD, the received signal  $\mathbf{y}_{p,q} \in \mathbb{C}^{M_b \times 1}$  at the RX of the BS node  $b$  combining the SI and the reflected signal by the Radar targets is expressed as

$$\mathbf{y}_{p,q} \triangleq \sum_{k=1}^K \alpha_k e^{j2\pi(qT_s f_{D,k} - p\tau_k \Delta f)} \mathbf{a}_{M_b}(\theta_k) \mathbf{a}_{N_b}^H(\theta_k) \mathbf{x}_{p,q} + \mathbf{H}_{b,b} \mathbf{x}_{p,q} + \mathbf{n}_{p,q}, \quad (7.3)$$

where  $\alpha_k \in \mathbb{C}$  and  $\mathbf{n}_{p,q} \sim \mathcal{CN}(0, \sigma_b^2 \mathbf{I}_{M_b})$  represent the reflection coefficient of the  $k$ th radar target and the receiver noise floor, respectively. Here,  $\Delta f$  and  $T_s \triangleq 1/\Delta f + T_{cp}$  denote the subcarrier spacing and the total OFDM symbol duration (including the cyclic prefix). The propagation delay causes the phase shift  $e^{-j2\pi p\tau_k \Delta f}$  across subcarriers, while the Doppler shift contributes a row-wise oscillation across different OFDM symbols [136]. Considering ULA, the steering vector  $\mathbf{a}_{N_b}(\theta)$  for  $N_b$  antenna elements and any DoA  $\theta$  is formulated as [129]

$$\mathbf{a}_{M_b}(\theta) \triangleq \frac{1}{\sqrt{N_b}} [1, e^{j\frac{2\pi}{\lambda} d \sin(\theta)}, \dots, e^{j\frac{2\pi}{\lambda} (N_b-1) d \sin(\theta)}]^T, \quad (7.4)$$

where  $\lambda$  is the propagation signal wavelength and  $d$  denotes the distance between adjacent antenna elements. Here,  $\mathbf{H}_{b,b} \in \mathbb{C}^{M_b \times N_b}$  is the SI channel path at the BS node  $b$ , which is modeled as a Rician fading mmWave channel as [111, eq. (9)].

The received signal at the node  $b$  RX is first processed by the RF combiner  $\mathbf{W}_b^{\text{RF}} \in \mathbb{C}^{M_b \times M_b^{\text{RF}}}$ , where the structure of the combiner is formulated similarly as Equation 7.1. Here, the analog

RX combining vectors belong in a predefined beam codebook  $\mathbb{F}_{\text{RX}}$  including  $\text{card}(\mathbb{F}_{\text{RX}})$  distinct vectors. After RF combination and A/D SI cancellation, the received signal is expressed as

$$\begin{aligned} \tilde{\mathbf{y}}_{p,q} \triangleq & (\mathbf{W}_b^{\text{RF}})^{\text{H}} \sum_{k=1}^K \alpha_k e^{j2\pi(qT_s f_{D,k} - p\tau_k \Delta f)} \mathbf{a}_{M_b}(\theta_k) \mathbf{a}_{N_b}^{\text{H}}(\theta_k) \mathbf{x}_{p,q} \\ & + (\tilde{\mathbf{H}}_{b,b} + \mathbf{C}_b + \mathbf{D}_b) \mathbf{V}_b^{\text{BB}} \mathbf{s}_{p,q} + (\mathbf{W}_b^{\text{RF}})^{\text{H}} \mathbf{n}_{p,q}, \end{aligned} \quad (7.5)$$

where  $\tilde{\mathbf{H}}_{b,b} \triangleq (\mathbf{W}_b^{\text{RF}})^{\text{H}} \mathbf{H}_{b,b} \mathbf{V}_b^{\text{RF}}$  is the effective SI channel after analog TX/RX beamforming. Here,  $\mathbf{C}_b$  and  $\mathbf{D}_b$  represent the analog and digital SI cancellation, respectively, that are designed following the structure presented in Chapter 5.

### 7.2.2 DL Signal Reception Model

As mentioned above,  $L$  out of  $K$  scatterers contributes to the DL channel  $\mathbf{H}_{u,b} \in \mathbb{C}^{M_u \times N_b}$ . As the principal focus of the work is to estimate Radar target parameters, we ignore the delay and Doppler shift parameters for the DL channel. Now, the received DL signal vector  $\mathbf{r}_{p,q} \in \mathbb{C}^{M_u \times d_b}$  at the UE RX is expressed as

$$\begin{aligned} \mathbf{r}_{p,q} \triangleq & \mathbf{W}_u^{\text{H}} \left( \sum_{\ell=1}^L \beta_{\ell} \mathbf{a}_{M_u}(\theta_{\ell}) \mathbf{a}_{N_b}^{\text{H}}(\theta_{\ell}) \mathbf{x}_{p,q} + \mathbf{z}_{p,q} \right) \\ & = \mathbf{W}_u^{\text{H}} \left( \mathbf{H}_{u,b} \mathbf{x}_{p,q} + \mathbf{z}_{p,q} \right), \end{aligned} \quad (7.6)$$

where  $\beta_{\ell} \in \mathbb{C}$  and  $\mathbf{z}_{p,q} \sim \mathcal{CN}(0, \sigma_u^2 \mathbf{I}_{M_u})$  represent the complex reflection coefficient of  $\ell$ th scatterer path and the noise floor at RX node  $u$ , respectively.

The achievable DL rate of the FD ISAC system can be expressed as

$$\mathcal{R}_{\text{DL}} \triangleq \log_2 \left( \det \left( \mathbf{I}_{d_b} + \mathbf{W}_u^H \mathbf{H}_{u,b} \mathbf{V}_b^{\text{RF}} \mathbf{V}_b^{\text{BB}} (\mathbf{V}_b^{\text{RF}} \mathbf{V}_b^{\text{BB}})^H \mathbf{H}_{u,b}^H \mathbf{W}_u (\mathbf{W}_u^H \mathbf{W}_u \sigma_u^2)^{-1} \right) \right), \quad (7.7)$$

### 7.3 DoA, Delay, and Doppler Shift Estimation

In this section, we present the estimations of the DoA, delay, and Doppler shift parameters of the Radar targets, which are realized by the BS's RX using the reflected signals.

#### 7.3.1 Radar Target DoA Estimation

For DoA estimation, we deploy the MUSIC algorithm; other DoA estimation techniques can be used as well [132]. First, we estimate the covariance matrix of the radar target reflected signal. Across all subcarriers and OFDM symbols of the communication slot, the covariance matrix  $\mathbf{R}_b \in \mathbb{C}^{M_b^{\text{RF}} \times M_b^{\text{RF}}}$  can be estimated as

$$\mathbf{R}_b \triangleq \mathbb{E}\{\tilde{\mathbf{y}}_{p,q} \tilde{\mathbf{y}}_{p,q}^H\}, \quad \hat{\mathbf{R}}_b \triangleq \frac{1}{PQ} \sum_{q=0}^{Q-1} \sum_{p=0}^{P-1} \tilde{\mathbf{y}}_{p,q} \tilde{\mathbf{y}}_{p,q}^H. \quad (7.8)$$

By taking the eigenvalue decomposition of the estimated sample covariance matrix  $\hat{\mathbf{R}}_b$ , it is deduced that:

$$\hat{\mathbf{R}}_b \triangleq \mathbf{U} \text{diag}\{\eta_1, \eta_2, \dots, \eta_{M_b}\} \mathbf{U}^H, \quad (7.9)$$

where  $\eta_1 \geq \eta_2 \geq \dots \geq \eta_{M_b^{\text{RF}}}$  are the eigenvalues of  $\hat{\mathbf{R}}_b$  and  $\mathbf{U} \in \mathbb{C}^{M_b^{\text{RF}} \times M_b^{\text{RF}}}$  contains their corresponding eigenvectors. Since we are interested in estimating the DoAs of  $K$  radar targets,

---

**Algorithm 8** Delay and Doppler Shift Estimation
 

---

**Input:**  $\mathbf{x}_{p,q}, \tilde{\mathbf{y}}_{p,q}, \forall p, q, \mathbf{W}_b^{\text{RF}}$ , and  $\hat{\theta}_k \forall k$ .

**Output:**  $\hat{\tau}_k, \hat{f}_{D,k}, \forall k$ .

- 1: Set  $n = 0, \dots, P-1$  and  $m = -\frac{Q}{2}, \dots, \frac{Q}{2} - 1$ .
  - 2: **for**  $k = 1, 2, \dots, K$  **do**
  - 3:   Set  $\mathbf{g}_{p,q} \triangleq \mathbf{a}_{M_b}(\hat{\theta}_k) \mathbf{a}_{N_b}^H(\hat{\theta}_k) \mathbf{x}_{p,q}$ .
  - 4:   Set  $z_{p,q} \triangleq \frac{1}{M_b} \sum_{i=1}^{M_b} [\mathbf{W}_b^{\text{RF}} \tilde{\mathbf{y}}_{p,q}]_i / [\mathbf{g}_{p,q}]_i, \forall p, q$ .
  - 5:   Set  $A(n, m) \triangleq \sum_{p=0}^{P-1} \left( \sum_{q=0}^{Q-1} z_{p,q} e^{-j2\pi \frac{qm}{Q}} \right) e^{j2\pi \frac{pn}{P}}$ .
  - 6:   Set  $(n^*, m^*) = \arg \max_{n,m} |A(n, m)|^2$ .
  - 7:   Set the estimated delay  $\hat{\tau}_k = \frac{n^*}{P\Delta f}$ .
  - 8:   Set the Doppler frequency of  $k$ th target  $\hat{f}_{D,k} = \frac{m^*}{QT_s}$ .
  - 9: **end for**
- 

the matrix  $\mathbf{U}$  can be partitioned as  $\mathbf{U} = [\mathbf{U}_s | \mathbf{U}_n]$ , where the columns in  $\mathbf{U}_n \in \mathbb{C}^{M_b^{\text{RF}} \times M_b^{\text{RF}} - K}$  are the eigenvectors spanning the noise subspace and  $\mathbf{U}_s \in \mathbb{C}^{M_b^{\text{RF}} \times K}$  contains the signal space eigenvectors. The MUSIC spectrum for the considered HBF architecture can be thus formulated as:

$$S(\theta) \triangleq (\mathbf{a}_{M_b}^H(\theta) \mathbf{W}_b^{\text{RF}} \mathbf{U}_n \mathbf{U}_n^H (\mathbf{W}_b^{\text{RF}})^H \mathbf{a}_{M_b}(\theta))^{-1}, \quad (7.10)$$

whose  $K$  peaks correspond to the  $K$  estimated DoAs  $\hat{\theta}_k, \forall k$ .

### 7.3.2 Delay and Doppler Shift Estimation

The next step is to estimate the delay and Doppler shift parameters associated with the  $K$  estimated DoAs. Using the estimate DoA  $\hat{\theta}_k$  and the known transmit signal  $\mathbf{x}_{p,q}$ , we formulate a reference signal in the DoA direction as

$$\mathbf{g}_{p,q} \triangleq \mathbf{a}_{M_b}(\hat{\theta}_k) \mathbf{a}_{N_b}^H(\hat{\theta}_k) \mathbf{x}_{p,q}. \quad (7.11)$$

Now, we utilize the received signal  $\tilde{\mathbf{y}}_{p,q}$  to derive the quotient averaged across all RX antennas that includes the effect of delay and Doppler shift in the direction of  $\hat{\theta}_k$  as

$$z_{p,q} \triangleq \frac{1}{M_b} \sum_{i=1}^{M_b} [\mathbf{W}_b^{\text{RF}} \tilde{\mathbf{y}}_{p,q}]_i / [\mathbf{g}_{p,q}]_i, \quad \forall p, q. \quad (7.12)$$

To estimate  $\hat{\tau}_k$  and  $\hat{f}_{D,k}$ , we formulate the likelihood function:

$$A(n, m) \triangleq \sum_{p=0}^{P-1} \left( \sum_{q=0}^{Q-1} z_{p,q} e^{-j2\pi \frac{qm}{Q}} \right) e^{j2\pi \frac{pn}{P}}, \quad (7.13)$$

where  $n = 0, \dots, P-1$  and  $m = -Q/2, \dots, Q/2-1$ . Finally, we find the best quantized delay and Doppler shift that maximizes the likelihood function norm. The delay and Doppler shift estimation procedure is provided in Algorithm 8.

## 7.4 Proposed ISAC Optimization Framework

In this section, we present a joint optimization framework deriving A/D beamformers and SI cancellation matrices with the objective to maximize the DL rate and the radar estimation accuracy.

We consider a time division duplexing communication protocol, where the DoAs estimated in one communication time slot is utilized to derive the beamformers and SI cancellation matrices for the successive slot. To optimize the DL rate and radar target parameter estimation accuracy, we propose to maximize the SNR in both the DL and radar target direction. Given the estimated DoAs  $\hat{\theta}_k, \forall k$ , the SNR in the direction of all radar targets can be written as

$$\hat{\Gamma}_{\text{Radar}} \triangleq \left\| (\mathbf{W}_b^{\text{RF}})^{\text{H}} \sum_{k=1}^K \mathbf{a}_{M_b}(\hat{\theta}_k) \mathbf{a}_{N_b}^{\text{H}}(\hat{\theta}_k) \mathbf{V}_b^{\text{RF}} \mathbf{V}_b^{\text{BB}} \right\|_{\Sigma_b^{-1}}^2, \quad (7.14)$$

where  $\Sigma_b = \|(\hat{\mathbf{H}}_{b,b} + \mathbf{C}_b + \mathbf{D}_b) \mathbf{V}_b^{\text{BB}}\|^2 + \|\mathbf{W}_b^{\text{RF}}\|^2 \sigma_b^2$  is the interference plus noise covariance matrix at the RX of node  $b$ . Similarly, the estimated DL SNR is expressed as

$$\hat{\Gamma}_{\text{DL}} = \left\| \mathbf{W}_u^{\text{H}} \sum_{\ell=1}^L \mathbf{a}_{M_u}(\hat{\theta}_\ell) \mathbf{a}_{N_b}^{\text{H}}(\hat{\theta}_\ell) \mathbf{V}_b^{\text{RF}} \mathbf{V}_b^{\text{BB}} \right\|_{\Sigma_u^{-1}}^2, \quad (7.15)$$

where  $\Sigma_u = \|\mathbf{W}_u\|^2 \sigma_u^2$  is the noise covariance matrix at the RX node  $u$ .

The optimization problem to maximize the Radar target and DL SNR can be written as

$$\begin{aligned}
\mathcal{OP} : \quad & \max_{\mathbf{V}_b^{\text{RF}}, \mathbf{V}_b^{\text{BB}}, \mathbf{W}_b^{\text{RF}}, \mathbf{C}_b, \mathbf{D}_b, \mathbf{W}_u} \hat{\Gamma}_{\text{Radar}} + \hat{\Gamma}_{\text{DL}} \\
\text{s.t.} \quad & \left\| [(\hat{\mathbf{H}}_{b,b} + \mathbf{C}_b) \mathbf{V}_b^{\text{BB}}]_{(j,:)} \right\|^2 \leq \lambda_b, \forall j = 1, \dots, M_b^{\text{RF}}, \\
& \mathbb{E}\{\|\mathbf{V}_b^{\text{RF}} \mathbf{V}_b^{\text{BB}}\|^2\} \leq P_b, \\
& \mathbf{w}_j \in \mathbb{F}_{\text{RX}} \quad \forall j \text{ and } \mathbf{v}_n \in \mathbb{F}_{\text{TX}} \quad \forall n = 1, 2, \dots, N_b^{(\text{RF})}
\end{aligned} \tag{7.16}$$

The optimization problem in Equation 7.16 is a non-convex problem with coupling variables, hence, quite difficult to tackle. In this work, we solve it suboptimally using alternating optimization, leaving other possibilities for future work.

First, using the estimated DoAs, we formulate a virtual channel of in the radar target direction as  $\hat{\mathbf{H}}_{\text{R}} \triangleq \sum_{k=1}^K \mathbf{a}_{M_b}(\hat{\theta}_k) \mathbf{a}_{N_b}^{\text{H}}(\hat{\theta}_k)$ . Now to maximize the radar SNR, we find the TX analog beams solving the following suboptimization problem:

$$\mathcal{OP1} : \quad \mathbf{V}_b^{\text{RF}} \triangleq \underset{\mathbf{v}_j \in \mathbb{F}_{\text{TX}}}{\text{argmax}} \quad \|\hat{\mathbf{H}}_{\text{R}} \mathbf{V}_b^{\text{RF}}\|^2 \tag{7.17}$$

The solution of  $\mathcal{OP1}$  requires a simple search through the beam codebook  $\mathbb{F}_{\text{TX}}$ . Using the TX analog beamformer  $\mathbf{V}_b^{\text{RF}}$ , we derive the analog combiner solving the suboptimization problem  $\mathcal{OP2}$ , where we simultaneously maximize the radar SNR and suppress SI signal as follows:

$$\mathcal{OP2} : \quad \mathbf{W}_b^{\text{RF}} \triangleq \underset{\mathbf{w}_j \in \mathbb{F}_{\text{TX}}}{\text{argmax}} \quad \frac{\|(\mathbf{W}_b^{\text{RF}})^{\text{H}} \hat{\mathbf{H}}_{\text{R}} \mathbf{V}_b^{\text{RF}}\|^2}{\|(\mathbf{W}_b^{\text{RF}})^{\text{H}} \hat{\mathbf{H}}_{b,b} \mathbf{V}_b^{\text{RF}}\|^2} \tag{7.18}$$

---

**Algorithm 9** FD ISAC Optimization
 

---

**Input:**  $\widehat{\mathbf{H}}_{b,b}$ ,  $N$ ,  $P_b$  and  $\widehat{\theta}_k \forall k$ .

**Output:**  $\mathbf{V}_b^{\text{RF}}$ ,  $\mathbf{V}_b^{\text{BB}}$ ,  $\mathbf{W}_b^{\text{RF}}$ ,  $\mathbf{C}_b$ ,  $\mathbf{D}_b$ , and  $\mathbf{W}_u$ .

- 1: Set  $\widehat{\mathbf{H}}_{\text{R}} \triangleq \sum_{k=1}^K \mathbf{a}_{M_b}(\widehat{\theta}_k) \mathbf{a}_{N_b}^{\text{H}}(\widehat{\theta}_k)$ .
  - 2: Set  $\widehat{\mathbf{H}}_{\text{u,b}} \triangleq \sum_{\ell=1}^L \mathbf{a}_{M_u}(\widehat{\theta}_\ell) \mathbf{a}_{N_b}^{\text{H}}(\widehat{\theta}_\ell)$ .
  - 3: Set  $\mathbf{W}_u$  as the  $d_b$  left-singular vectors of  $\widehat{\mathbf{H}}_{\text{u,b}}$  corresponding to the singular values in descending order.
  - 4: Set  $\mathbf{V}_b^{\text{RF}} \triangleq \arg \max_{\mathbf{v}_j \in \mathbb{F}_{\text{TX}}} \|\widehat{\mathbf{H}}_{\text{R}} \mathbf{V}_b^{\text{RF}}\|^2$ .
  - 5: Set  $\mathbf{W}_b^{\text{RF}} \triangleq \arg \max_{\mathbf{w}_j \in \mathbb{F}_{\text{TX}}} \frac{\|(\mathbf{W}_b^{\text{RF}})^{\text{H}} \widehat{\mathbf{H}}_{\text{R}} \mathbf{V}_b^{\text{RF}}\|^2}{\|(\mathbf{W}_b^{\text{RF}})^{\text{H}} \widehat{\mathbf{H}}_{\text{u,b}} \mathbf{V}_b^{\text{RF}}\|^2}$ .
  - 6: Set  $\widehat{\mathbf{H}}_{b,b} = (\mathbf{W}_b^{\text{RF}})^{\text{H}} \widehat{\mathbf{H}}_{b,b} \mathbf{V}_b^{\text{RF}}$  and  $\widehat{\mathbf{H}}_{u,b} = \widehat{\mathbf{H}}_{u,b} \mathbf{V}_b^{\text{RF}}$ .
  - 7: Set  $\mathbf{C}_b = \begin{bmatrix} -[\widehat{\mathbf{H}}_{b,b}]_{:,1:\frac{N}{M_b}^{\text{RF}}} & \mathbf{0}_{:,(N_b^{\text{RF}} - \frac{N}{M_b}^{\text{RF}}:N_b^{\text{RF}})} \end{bmatrix}$  and  $\mathbf{D}_b = -(\widehat{\mathbf{H}}_{b,b} + \mathbf{C}_b)$ .
  - 8: Obtain  $\mathbf{B}$  with the  $N_b^{\text{RF}}$  right-singular vectors of  $(\widehat{\mathbf{H}}_{b,b} + \mathbf{C}_b)$  corresponding to the singular values in descending order.
  - 9: **for**  $\alpha = N_b^{\text{RF}}, N_b^{\text{RF}} - 1, \dots, 2$  **do**
  - 10:     Set  $\mathbf{F} = [\mathbf{B}]_{(:,N_b^{\text{RF}} - \alpha + 1:N_b^{\text{RF}})}$ .
  - 11:     Set  $\mathbf{G}$  as the optimum precoding for the effective DL MIMO channel  $\widehat{\mathbf{H}}_{u,b} \mathbf{F}$  given  $P_b$ .
  - 12:     **if**  $\left\| [(\widehat{\mathbf{H}}_{b,b} + \mathbf{C}_b) \mathbf{F} \mathbf{G}]_{(j,:)} \right\|^2 \leq \lambda_b, \forall j = 1, \dots, M_b^{\text{RF}}$ , **then**
  - 13:         Output  $\mathbf{V}_b^{\text{BB}} = \mathbf{F} \mathbf{G}$  and stop the algorithm.
  - 14:     **else**
  - 15:         Output that the  $\mathbf{C}_b$  realization does not meet the residual SI constraint.
  - 16:     **end if**
  - 17: **end for**
- 

Similar to  $\mathcal{OP}1$ , the solution of  $\mathcal{OP}2$  requires a simple search through the available beam codebook  $\mathbb{F}_{\text{RX}}$ . Given the analog SI cancellation taps  $N \leq N_b^{\text{RF}} M_b^{\text{RF}}$  and the analog TX/RX beamformer at the BS, we follow a similar procedure to Chapter 5, aiming to find the digital beamforming matrix  $\mathbf{V}_b^{\text{BB}}$  and the SI cancellation matrices maximizing the DL rate and

suppressing the SI signal power below the RF saturation level of  $\lambda_b$ . The latter will ensure proper reception of the Radar target reflected signal. Our solution for the optimization problem Equation 7.16 is summarized in Algorithm 9.

## 7.5 Numerical Results and Discussion

In this section, we present numerical results for the radar sensing and DL rate performance of the proposed FD massive MIMO ISAC system operating at mmWave frequencies.

### 7.5.1 Simulation Parameters

We perform an extensive waveform simulation following the FD massive MIMO architecture illustrated in Figure 37 when operating at mmWave frequencies, where a  $128 \times 128$  FD massive MIMO node  $b$  is communicating in the DL direction with 4 antenna RX UE node  $u$ . The BS node  $b$  employs  $N_b^{\text{RF}} = M_b^{\text{RF}} = 8$  TX/RX RF chains with each of them connected to a ULA of  $N_b^{\text{A}} = M_b^{\text{A}} = 16$  antenna elements via phase shifters. The communication is performed using mmWave frequency of 28GHz and a 5G NR OFDM waveform with 100MHz BW and  $\Delta f = 120\text{KHz}$  subcarrier spacing. According to the 5G NR specifications, we have 66 Physical Resource Blocks (PRBs) resulting in  $P = 792$  active subcarriers and  $Q = 14$  OFDM symbols in each communication slot. Total OFDM symbol duration is defined as  $T_s = 8.92\mu\text{s}$ . We have considered a radio subframe of 1ms for DL communication. The RX noise floors at all nodes were assumed to be  $-90\text{dBm}$  for 100MHz BW OFDM signal. To this end, the RXs have an effective dynamic range of 60dB provided by 14-bit ADC for a PAPR of 10 dB. Therefore, the residual SI power after analog SI cancellation at the input of each RX RF chain has to be below  $-30\text{dBm}$  to avoid signal saturation. The pathloss of the clustered DL channel is assumed to

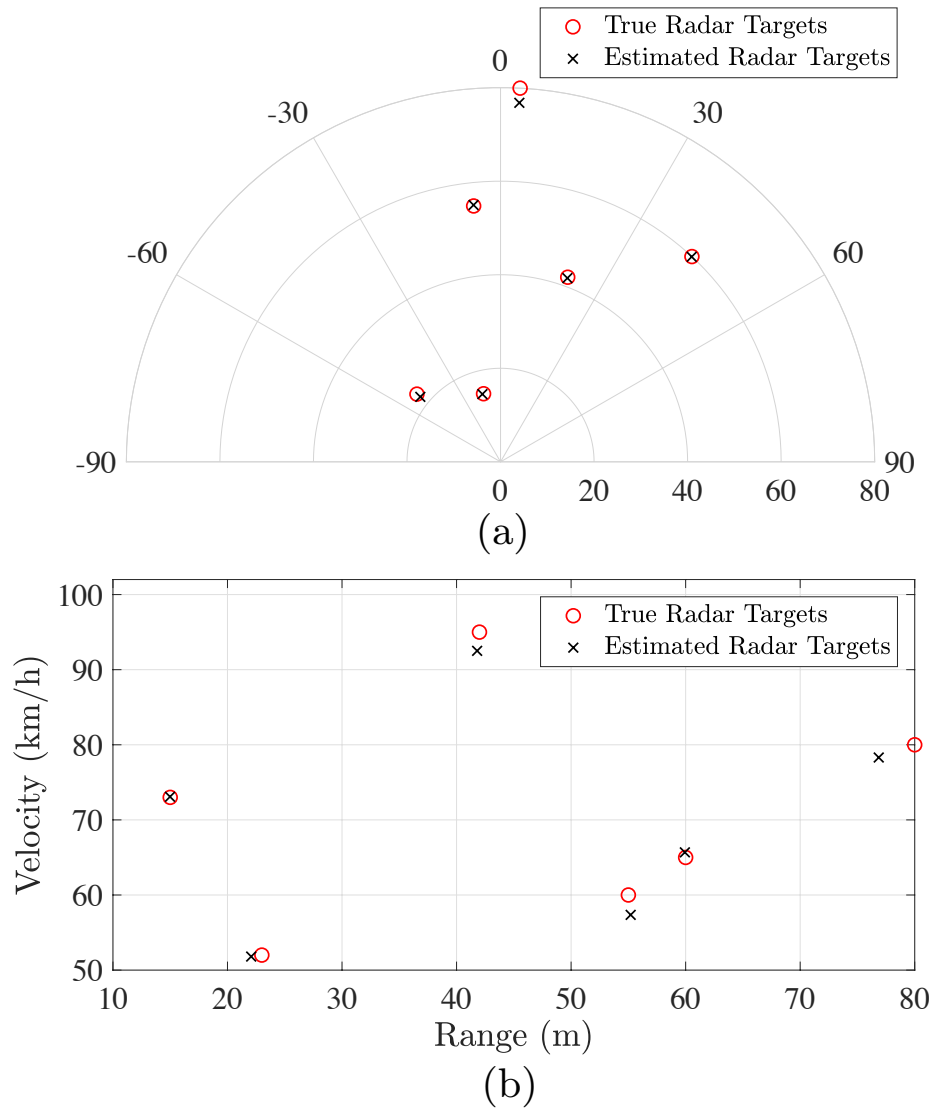


Figure 38. Sensing parameter estimation performance for 6 radar targets with  $N_b^{\text{RF}} = M_b^{\text{RF}} = 8$ ,  $N_b^{\text{A}} = N_b^{\text{AF}} = 16$  and transmit power of 30dBm. (a) DoA and range estimation, (b) Range and relative velocity estimation.

be 100dB, whereas the SI channels are modeled as Rician fading channels with a  $\kappa$ -factor of 35dB and pathloss 40dB [59]. For the BS analog TX/RX beamformer, we consider a 5-bit beam codebook based on the DFT matrix. We have used 1000 independent Monte Carlo simulation runs to calculate the Radar sensing and DL rate performance.

### 7.5.2 Radar Target Parameters

We have considered  $K = 6$  radar targets randomly distributed in the sensing/communication environment with DoAs  $\theta_k \in [-90^\circ \quad 90^\circ], \forall k$ . For communication scatters,  $L = 2$  out of  $K = 6$  targets are chosen randomly. Each of the radar targets the range and relative velocity is selected randomly with a maximum range of 80m and maximum velocity of 100km/h.

### 7.5.3 Radar Target Sensing performance

In Figure 38, We have depicted the sensing performance of the proposed FD ISAC system with a  $128 \times 128$  massive MIMO node transmitting DL signal with a transmit power of 30dBm. The DoA and range estimation is plotted in contrast to the true target parameters in Figure 38(a), where it is evident that the proposed FD ISAC system can detect all 6 targets successfully with high precision. Even for really close target ( $10^\circ$  and  $12^\circ$ ) with only  $2^\circ$  angle and less than 5m range difference, the estimation performance is highly accurate. The superior sensing performance is provided by the proposed associated delay estimation approach with high-resolution MUSIC DoA estimation unlike previous FD ISAC work in [21], where range estimation for such close targets was not possible. In Figure 38(b), the relative velocity is plotted with respect to the range estimation for 30dBm DL transmit power. The figure shows that the

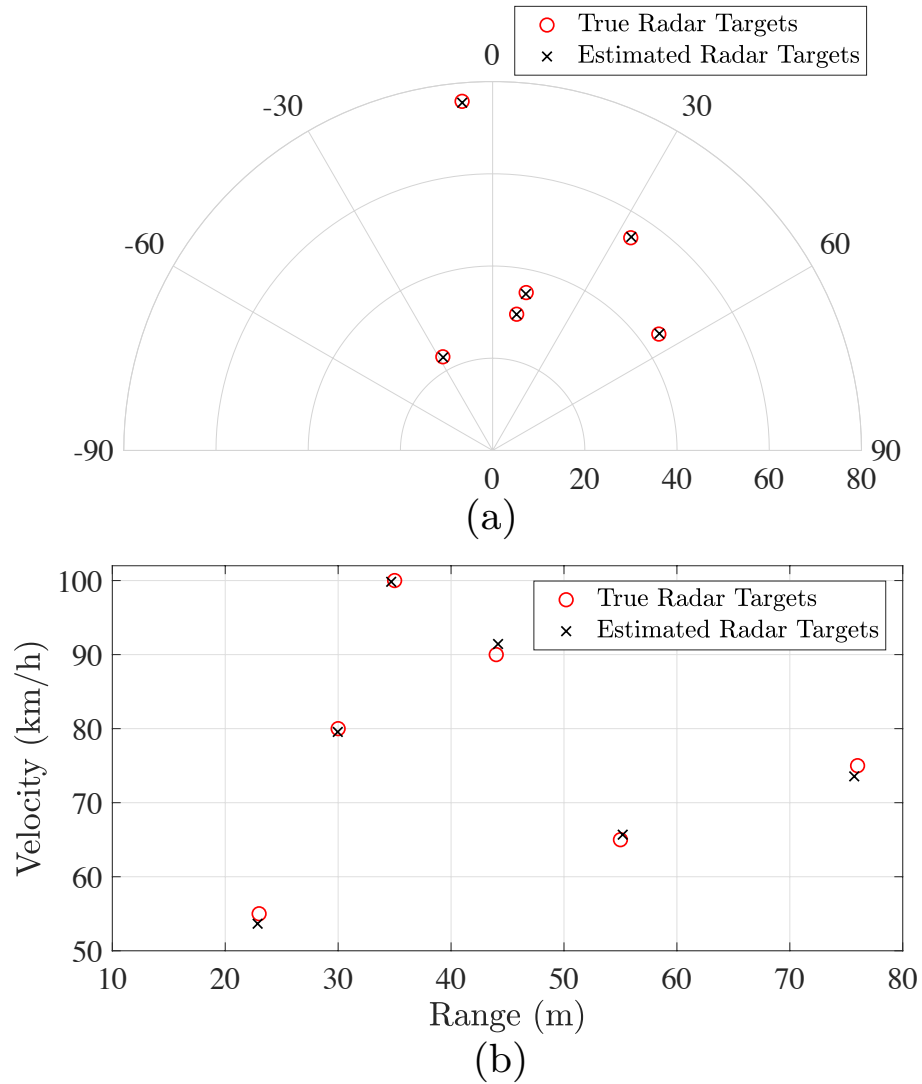


Figure 39. Sensing parameter estimation performance for 6 radar targets with  $N_b^{\text{RF}} = M_b^{\text{RF}} = 8$ ,  $N_b^{\text{A}} = N_b^{\text{A}} = 16$  and DL transmit power of 10dBm. (a) DoA and range estimation, (b) Range and relative velocity estimation.

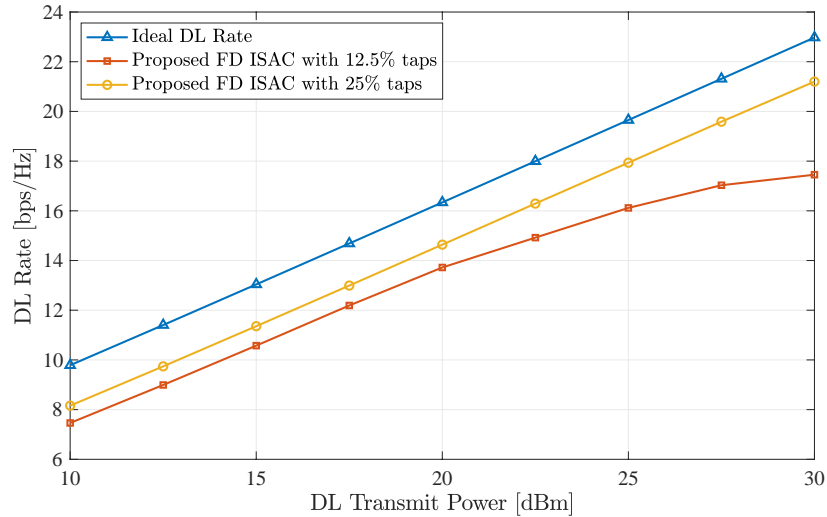


Figure 40. DL rate with respect to transmit power in dBm for the  $128 \times 128$  massive MIMO FD BS communicating with a 4 antenna UE RX node.

proposed FD ISAC system is capable of estimating the relative velocity of all 6 targets with less than 1.5% estimation error.

In Figure 39, radar target sensing performance of the proposed FD ISAC system is presented for 10dBm DL transmit power. It is evident from Figure 39(a) that the DoA estimation is almost accurate even at a low transmit power of 10dBm. However, for the target at  $3^\circ$ , the estimated range is around 3m away the actual value of 80m. This is due to the low transmit power and higher path loss of the furthest target. In Figure 39(b), the relative velocity estimation is showcased, where the proposed approach achieved sensing performance with less than 5% estimation error for a low transmit power of 10dBm.

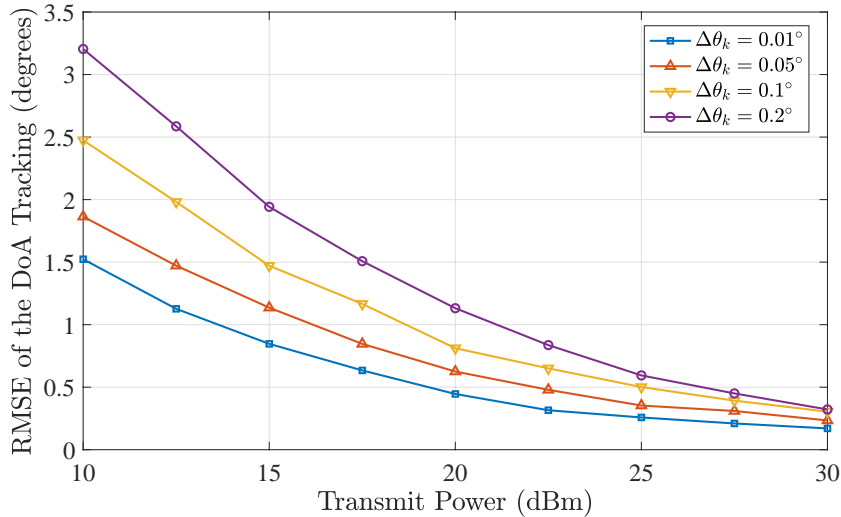


Figure 41. RMSE of the DoA Tracking for 4 radar targets with  $N_{\text{RF}} = M_{\text{RF}} = 8$ ,  $N_{\text{A}} = M_{\text{A}} = 16$  and DL transmit power of 30dBm.

The DL rate performance of the proposed FD ISAC system with a  $128 \times 128$  massive MIMO BS node transmitting to a 4 antenna UE RX node is depicted in Figure 40 with respect to transmit power. It is evident from the figure that the proposed FD ISAC approach is capable of providing DL rate very close (1.5bps/Hz) to the ideal rate in addition to the high radar sensing performance at the RX of BS node for  $N = 16$  (25%) analog SI cancellation taps at the FD massive MIMO node. For even smaller hardware complexity (12.5%) taps, the DL rate performance is comparable up to 20 dB transmit power. However, as transmit power increases the impact of SI signal worsens, for DL transmit power of 30dBm, the FD ISAC system is capable of providing 75% of the ideal DL rate with only  $N = 8$  SI cancellation taps.

In Figure 41, we have plotted the Root Mean Square Error (RMSE) of the DoA tracking in degrees for  $K = 4$  the radar targets across 20 5G NR radio subframes with different DoA evolution  $\Delta\theta_k = [0.01^\circ \ 0.05^\circ \ 0.1^\circ \ 0.2^\circ]$  between consecutive subframes. For a range of 20m, an angle evolution of  $0.2^\circ$  corresponds to a velocity of 250km/h for radar targets. Therefore, the proposed FD ISAC approach is capable of tracking multiple radar targets moving at very high speed. For a moderate transmit power of 20dBm, the proposed approach provides less than  $1^\circ$  RMSE for most of the DoA evolution cases. However, the RMSE of DoA tracking for all different  $\Delta\theta_k$  cases is around  $0.25^\circ$  for 30dBm transmit power exhibiting precise target tracking performance. Therefore, the proposed FD ISAC technique exhibits superior precision of radar tracking

## 7.6 Concluding Remarks

In this chapter, we presented an FD-based ISAC optimization framework, where an FD massive MIMO BS node is transmitting DL signals and concurrently performing radar target sensing utilizing the reflected signals. We devised a DoA, delay, and Doppler shift estimation algorithm for multiple radar target sensing considering hybrid A/D beamforming at the BS node. Adopting a limited complexity analog SI cancellation architecture, we presented a joint design of the A/D beamformer and SI cancellation that maximizes the DL rate together with the target sensing performance. Our performance results for a mmWave channel model demonstrated the high precision DoA, range, velocity estimation and tracking of multiple radar targets while providing maximized DL rate.

## CHAPTER 8

### CONCLUSION

This thesis investigated FD systems for future wireless networks through the co-design of low-complexity SI suppression techniques and optimized transceiver architecture for various performance objectives.

Chapter 2 studied the single-antenna FD systems. We provided a comprehensive signal modeling of the single-antenna FD node considering practical hardware impairments of the TX/RX RF components. Utilizing the model, we devised an orthogonalized QR decomposition based digital cancellation algorithm. It was shown the proposed scheme can achieve superior SI suppression performance compared to the conventional SI cancellation techniques under limited analog cancellation. We, furthermore, designed a Transfer Learning based DNN architecture to perform nonlinear digital SI cancellation which outperforms the traditional approaches without prior knowledge of the nonlinearity order of the SI components.

In Chapter 3, we presented a reduced complexity wideband analog SI canceller jointly designed with digital TX/RX beamforming for practical FD MIMO systems maximizing the FD sum-rate performance. To suppress the SI signal at the FD node, we proposed a novel adaptive digital SI cancellation technique to reduce the number of estimation parameters. We showed that the proposed optimization framework provided higher achievable rate performance with reduced hardware complexity for analog SI cancellation and computational resources of digital SI cancellation compared to the full-tap wideband FD MIMO radios. Building on the

low-complexity FD MIMO architecture, we proposed a novel SCDC scheme for simultaneous channel acquisition and DL transmission in Chapter 4.

Exploiting our low-complexity analog cancellation solution, we presented FD massive MIMO systems with hybrid beamforming operating at mmWave frequencies in Chapter 5. A unified FD massive MIMO transceiver architecture is proposed comprising A/D TX/RX BF as well as A/D SI cancellation, which is jointly optimized for various performance objectives and complexity requirements. The proposed scheme outperformed the state-of-the-art approaches providing a superior FD sum rate, while radically reducing the analog beam selection complexity. In Chapter 6, we designed a direction-Assisted beam management technique for mmWave FD massive MIMO systems utilizing its simultaneous transmission and reception capability and thus, reducing the beam training overhead.

Finally, in Chapter 7, we investigated mmWave FD massive MIMO radios as the key enabler for the emerging ISAC systems, where an FD massive MIMO BS node is transmitting DL signals and concurrently performing radar target sensing utilizing the reflected signals. We devised a DoA, delay, and Doppler shift estimation algorithm for multiple radar target sensing considering hybrid A/D beamforming at the BS node. Through an indicative mmWave waveform simulation, it was demonstrated the proposed FD ISAC approach achieves high precision parameter estimation and tracking of multiple radar targets while providing maximized DL rate.

As 5G NR has adopted mmWave frequencies to accommodate high data rate communications, its successors, 6G and beyond, are expected to support wireless links at TeraHertz (THz) (i.e., 0.1 – 10 THz). Therefore, a promising future extension of this thesis is the combina-

tion of the proposed low-complexity FD massive MIMO system with THz communication to compensate for the high path loss of higher frequencies. Additionally, the SCDC features of the presented FD massive MIMO framework can be used for low latency analog beam tracking, paving the way for beyond 5G standalone mmWave and THz communications. For example, the beam refinement for multiple UEs can take place in the UL simultaneously with their DL data communication from the FD massive MIMO BS. Recently, the incorporation of reconfigurable metasurfaces in wireless networks has been advocated as a revolutionary means to transform any naturally passive wireless propagation environment into a dynamically programmable one. This can be accomplished by deploying cost-effective and easy-to-coat metasurfaces to the environment's objects, thus, offering increased environmental intelligence for the scope of diverse wireless networking objectives. Interesting directions of research are the investigation of FD massive MIMO operation in networks empowered by passive metasurfaces, and the design of FD MIMO architectures with massive numbers of metasurface-based antennas. In the former direction, efficient NOMA techniques to manage FD-based reflections need to be devised, whereas, in the latter, hybrid A/D TX/RX BF schemes will be required. Metasurface antenna based FD massive MIMO systems operating in THz frequencies can further enable a new paradigm in ISAC systems providing extreme data rates with millimeter-level precision in radar sensing performance.

## APPENDICES

## Appendix A

### Proof of Equation 2.6

Necessary proofs for Equation 2.6 are provided here.

Let  $\omega_c t + \theta_{Rx}(t) = \omega_c t + \theta_{Tx}(t) = \Delta(t)$  as  $\theta_{Rx}(t) = \theta_{Tx}(t)$ .

Now,

$$\begin{aligned}
& \text{LPF} \left\{ \left( \sum_{q=1,3} \beta_{LNA,q} \left( \sum_{p=1,3} h_p(t) * (x_{IQ}(t))^p \right)^q + c(t) \right) e^{-j\Delta(t)} \right\} \\
&= \text{LPF} \left\{ \sum_{q=1,3} \beta_{LNA,q} \left( (h_1(t) * z(t) + h_3(t) * 3z^2(t)\bar{z}(t)) e^{j\Delta(t)} \right. \right. \\
&\quad \left. \left. + (h_1(t) * \bar{z}(t) + h_3(t) * 3z(t)\bar{z}(t)^2) e^{-j\Delta(t)} \right)^q e^{-j\Delta(t)} \right\} \\
&= \text{LPF} \left\{ \sum_{q=1,3} \beta_{LNA,q} \sum_{k=0}^q \binom{q}{k} (h_1(t) * z(t) + h_3(t) * 3z^2(t)\bar{z}(t))^{q-k} \right. \\
&\quad \left. (h_1(t) * \bar{z}(t) + h_3(t) * 3z(t)\bar{z}(t)^2)^k e^{j\Delta(t)(q-2k-1)} \right\} \tag{A.1} \\
&\stackrel{(c)}{=} \sum_{q=1,3} \beta_{LNA,q} \binom{q}{\frac{q-1}{2}} (h_1(t) * z(t) + h_3(t) * 3z^2(t)\bar{z}(t))^{\frac{q+1}{2}} \\
&\quad (h_1(t) * \bar{z}(t) + h_3(t) * 3z(t)\bar{z}(t)^2)^{\frac{q-1}{2}}.
\end{aligned}$$

Here, (c) is achieved if

$$q - 2k - 1 = 0 \Rightarrow k = \frac{q-1}{2}. \tag{A.2}$$

## Appendix B

### Derivation of Equation 3.9

The linearly processed estimated symbol vector  $\widehat{\mathbf{s}}_{b,n}$  is derived as

$$\begin{aligned}
\widehat{\mathbf{s}}_{b,n} &= \mathbf{u}_{m_1,n} \left( \frac{1}{\sqrt{N_c}} \sum_{k=0}^{N_c-1} \left( \sum_{\ell=0}^{L_{\text{DL}}-1} \mathbf{H}_{\text{DL}}[\ell] \widetilde{\mathbf{x}}_b[k-\ell] + \mathbf{w}_{m_1}[k] \right) e^{-\frac{j2\pi kn}{N_c}} \right) \\
&\stackrel{(a)}{=} \mathbf{u}_{m_1,n} \left( \frac{1}{\sqrt{N_c}} \sum_{k=0}^{N_c-1} \left( \sum_{\ell=0}^{L_{\text{DL}}-1} \mathbf{H}_{\text{DL}}[\ell] (\mathbf{G}_{1,b} \mathbf{x}_b[k-\ell] + \mathbf{z}[k-\ell]) \right. \right. \\
&\quad \left. \left. + \mathbf{w}_{m_1}[k] \right) e^{-\frac{j2\pi kn}{N_c}} \right) \\
&\stackrel{(b)}{=} \mathbf{u}_{m_1,n} \left( \frac{1}{\sqrt{N_c}} \sum_{k=0}^{N_c-1} \left( \sum_{\ell=0}^{L_{\text{DL}}-1} \mathbf{H}_{\text{DL}}[\ell] \left( \mathbf{G}_{1,b} \frac{1}{\sqrt{N_c}} \sum_{p=0}^{N_c-1} \mathbf{v}_{b,p} \right. \right. \right. \\
&\quad \left. \left. \times \mathbf{s}_{b,p} e^{\frac{j2\pi p(k-\ell)}{N_c}} + \mathbf{z}[k-\ell] \right) + \mathbf{w}_{m_1}[k] \right) e^{-\frac{j2\pi kn}{N_c}} \right) \\
&= \mathbf{u}_{m_1,n} \left( \sum_{\ell=0}^{L_{\text{DL}}-1} \mathbf{H}_{\text{DL}}[\ell] e^{-\frac{j2\pi \ell n}{N_c}} \left( \mathbf{G}_{1,b} \left( \frac{1}{N_c} \sum_{k=0}^{N_c-1} \sum_{p=0}^{N_c-1} \mathbf{v}_{b,p} \right. \right. \right. \\
&\quad \left. \left. \times \mathbf{s}_{b,p} e^{\frac{j2\pi(p-n)k}{N_c}} e^{-\frac{j2\pi \ell p}{N_c}} \right) + \frac{1}{\sqrt{N_c}} \sum_{k=0}^{N_c-1} \mathbf{z}[k-\ell] e^{-\frac{j2\pi(k-\ell)n}{N_c}} \right) \right. \\
&\quad \left. + \frac{1}{\sqrt{N_c}} \sum_{k=0}^{N_c-1} \mathbf{w}_{m_1}[k] e^{-\frac{j2\pi kn}{N_c}} \right) \\
&\stackrel{(c)}{=} \mathbf{u}_{m_1,n} \left( \mathcal{H}_{\text{DL},n} (\mathbf{G}_{1,b} \mathbf{v}_{b,n} \mathbf{s}_{b,n} + \mathbf{z}_{b,n}) + \mathbf{w}_{m_1,n} \right),
\end{aligned}$$

### Appendix B (Continued)

where (a) and (b) are obtained from Equation 3.5 and Equation 3.1, respectively. Here, (c) is derived using the identities

$$\frac{1}{N_c} \sum_{k=0}^{N_c-1} e^{\frac{j2\pi(p-n)k}{N_c}} = \begin{cases} 1, & \text{if } p = n, \\ 0, & \text{if } p \neq n, \end{cases}$$

$$\mathbf{z}_{b,n} = \frac{1}{\sqrt{N_c}} \sum_{k=0}^{N_c-1} \mathbf{z}[k] e^{-\frac{j2\pi kn}{N_c}}, \text{ and}$$

$$\mathbf{w}_{m_1,n} = \frac{1}{\sqrt{N_c}} \sum_{k=0}^{N_c-1} \mathbf{w}_{m_1}[k] e^{-\frac{j2\pi kn}{N_c}}.$$

Similarly, the proof of Equation 3.12 can be obtained using Equation 3.13 and the above mentioned identities.

## Appendix C

### Proof of Proposition 1

From Equation 5.6, the achievable DL rate is expressed as

$$\mathcal{R}_{\text{DL}} = \log_2 \left( \det \left( \mathbf{I}_{M_q} + \sigma_q^{-2} \mathbf{H}_{q,k} \mathbf{V}_k^{(\text{RF})} \mathbf{V}_k^{(\text{BB})} \left( \mathbf{V}_k^{(\text{BB})} \right)^{\text{H}} \left( \mathbf{V}_k^{(\text{RF})} \right)^{\text{H}} \mathbf{H}_{q,k}^{\text{H}} \right) \right).$$

Here  $\mathbf{V}_k^{(\text{BB})}$  is the digital basedband precoding matrix which will be obtained using the right singular vectors of the effective DL channel  $\mathbf{H}_{q,k} \mathbf{V}_k^{(\text{RF})}$ . Therefore  $\mathbf{V}_k^{(\text{BB})} \left( \mathbf{V}_k^{(\text{BB})} \right)^{\text{H}} = \frac{P_k}{N_k^{(\text{RF})}} \mathbf{I}_{N_k^{(\text{RF})}}$ .

$$\mathcal{R}_{\text{DL}} = \log_2 \left( \det \left( \mathbf{I}_{M_q} + \frac{P_k}{N_k^{(\text{RF})} \sigma_q^2} \mathbf{H}_{q,k} \mathbf{V}_k^{(\text{RF})} \left( \mathbf{V}_k^{(\text{RF})} \right)^{\text{H}} \mathbf{H}_{q,k}^{\text{H}} \right) \right). \quad (\text{C.1})$$

We can divide the RF precoder  $\mathbf{V}_k^{(\text{RF})}$  as  $\mathbf{V}_k^{(\text{RF})} = [\mathbf{P}_{N_k^{(\text{RF})-1} \mathbf{p}_{N_k^{(\text{RF})}}}]$ , where  $\mathbf{p}_{N_k^{(\text{RF})}}$  is the  $N_k^{(\text{RF})}$ th column of the precoder matrix  $\mathbf{V}_k^{(\text{RF})}$ , and  $\mathbf{P}_{N_k^{(\text{RF})-1}$  is an  $N_k \times N_k^{(\text{RF})} - 1$  matrix containing the first  $N_k^{(\text{RF})} - 1$  columns of  $\mathbf{V}_k^{(\text{RF})}$ .

$$\begin{aligned} \mathcal{R}_{\text{DL}} &= \log_2 \left( \det \left( \mathbf{I}_{M_q} + \frac{P_k}{N_k^{(\text{RF})} \sigma_q^2} \mathbf{H}_{q,k} [\mathbf{P}_{N_k^{(\text{RF})-1} \mathbf{p}_{N_k^{(\text{RF})}}}] [\mathbf{P}_{N_k^{(\text{RF})-1} \mathbf{p}_{N_k^{(\text{RF})}}}]^{\text{H}} \mathbf{H}_{q,k}^{\text{H}} \right) \right), \\ &= \log_2 \left( \det \left( \mathbf{I}_{M_q} + \frac{P_k}{N_k^{(\text{RF})} \sigma_q^2} \mathbf{H}_{q,k} \mathbf{P}_{N_k^{(\text{RF})-1} \mathbf{P}_{N_k^{(\text{RF})-1}^{\text{H}} \mathbf{H}_{q,k}^{\text{H}} + \frac{P_k}{N_k^{(\text{RF})} \sigma_q^2} \mathbf{H}_{q,k} \mathbf{p}_{N_k^{(\text{RF})} \mathbf{p}_{N_k^{(\text{RF})}^{\text{H}} \mathbf{H}_{q,k}^{\text{H}} \right) \right), \\ &\stackrel{\text{(a)}}{=} \log_2 \left( \det \left( \mathbf{T}_{N_k^{(\text{RF})-1} \right) \right) + \log_2 \left( \det \left( \mathbf{I}_{M_q} + \frac{P_k}{N_k^{(\text{RF})} \sigma_q^2} \mathbf{T}_{N_k^{(\text{RF})-1}^{-1} \mathbf{H}_{q,k} \mathbf{p}_{N_k^{(\text{RF})} \mathbf{p}_{N_k^{(\text{RF})}^{\text{H}} \mathbf{H}_{q,k}^{\text{H}} \right) \right) \\ &\stackrel{\text{(b)}}{=} \log_2 \left( \det \left( \mathbf{T}_{N_k^{(\text{RF})-1} \right) \right) + \log_2 \left( 1 + \frac{P_k}{N_k^{(\text{RF})} \sigma_q^2} \mathbf{p}_{N_k^{(\text{RF})}^{\text{H}} \mathbf{H}_{q,k}^{\text{H}} \mathbf{T}_{N_k^{(\text{RF})-1}^{-1} \mathbf{H}_{q,k} \mathbf{p}_{N_k^{(\text{RF})} \right) \end{aligned} \quad (\text{C.2})$$

### Appendix C (Continued)

where (a) is obtained by  $\mathbf{T}_{N_k^{(\text{RF})-1}} = \mathbf{I}_{M_q} + \frac{P_k}{N_k^{(\text{RF})}\sigma_q^2} \mathbf{H}_{q,k} \mathbf{P}_{N_k^{(\text{RF})-1}} \mathbf{P}_{N_k^{(\text{RF})-1}}^H \mathbf{H}_{q,k}^H$  and (b) is true due to the fact that  $\det(\mathbf{I} + \mathbf{X}\mathbf{Y}) = \det(\mathbf{I} + \mathbf{Y}\mathbf{X})$  by defining  $\mathbf{X} = \mathbf{T}_{N_k^{(\text{RF})-1}}^{-1} \mathbf{H}_{q,k} \mathbf{P}_{N_k^{(\text{RF})}}$  and  $\mathbf{Y} = \mathbf{P}_{N_k^{(\text{RF})}}^H \mathbf{H}_{q,k}^H$ . The second term on the right side of Equation C.2 is the DL rate of  $N_k^{(\text{RF})}$ th sub-antenna array, while the first term  $\log_2 \left( \det \left( \mathbf{T}_{N_k^{(\text{RF})-1} \right) \right)$  shares the same form as Equation C.1. This observation implies that we can further decompose  $\log_2 \left( \det \left( \mathbf{T}_{N_k^{(\text{RF})-1} \right) \right)$  using the similar method in Equation C.2 as

$$\begin{aligned} \log_2 \left( \det \left( \mathbf{T}_{N_k^{(\text{RF})-1} \right) \right) &= \log_2 \left( \det \left( \mathbf{T}_{N_k^{(\text{RF})-2} \right) \right) + \log_2 \left( 1 + \frac{P_k}{N_k^{(\text{RF})}\sigma_q^2} \mathbf{P}_{N_k^{(\text{RF})-1}}^H \right. \\ &\quad \left. \times \mathbf{H}_{q,k}^H \mathbf{T}_{N_k^{(\text{RF})-2}^{-1}} \mathbf{H}_{q,k} \mathbf{P}_{N_k^{(\text{RF})-1}} \right) \end{aligned} \quad (\text{C.3})$$

Then, after  $N_k^{(\text{RF})}$  such decomposition, the total achievable DL rate in Equation C.1 can be presented as

$$\begin{aligned} \mathcal{R}_{\text{DL}} &= \sum_{n=1}^{N_k^{(\text{RF})}} \log_2 \left( 1 + \frac{P_k}{N_k^{(\text{RF})}\sigma_q^2} \mathbf{P}_n^H \mathbf{H}_{q,k}^H \mathbf{T}_{n-1}^{-1} \mathbf{H}_{q,k} \mathbf{P}_n \right) \\ &= \sum_{n=1}^{N_k^{(\text{RF})}} \log_2 \left( 1 + \frac{P_k}{N_k^{(\text{RF})}\sigma_q^2} \mathbf{P}_n^H \mathbf{G}_{n-1} \mathbf{P}_n \right) \end{aligned} \quad (\text{C.4})$$

where we have

$$\begin{aligned} \mathbf{T}_n &= \mathbf{I}_{M_q} + \frac{P_k}{N_k^{(\text{RF})}\sigma_q^2} \mathbf{H}_{q,k} \mathbf{P}_n \mathbf{P}_n^H \mathbf{H}_{q,k}^H, \quad \mathbf{T}_0 = \mathbf{I}_{N_k^{(\text{RF})}} \\ \mathbf{G}_n &= \mathbf{H}_{q,k}^H \mathbf{T}_n^{-1} \mathbf{H}_{q,k} \end{aligned}$$

### Appendix C (Continued)

From Equation C.4, we observe that the total achievable rate optimization problem can be transformed into a series of sub-rate optimization problems of sub-antenna arrays, which can be optimized one by one.

The  $n$ th precoding vector  $\mathbf{p}_n$  only has  $N_k^{(A)}$  non-zero elements  $\mathbf{v}_n$  from the  $(N_k^{(A)}(n-1)+1)$ th one to the  $(N_k^{(A)}n)$ th one. Therefore the total achievable DL rate can be written as

$$\mathcal{R}_{\text{DL}} = \sum_{n=1}^{N_k^{(\text{RF})}} \log_2 \left( 1 + \frac{P_k}{N_k^{(\text{RF})} \sigma_q^2} \mathbf{v}_n^H \mathbf{R}_n \mathbf{G}_{n-1} \mathbf{R}_n^H \mathbf{v}_n \right) \quad (\text{C.5})$$

where  $\mathbf{R}_n = [\mathbf{0}_{N_k^{(A)} \times N_k^{(A)}(n-1)} \quad \mathbf{I}_{N_k^{(A)}} \quad \mathbf{0}_{N_k^{(A)} \times N_k^{(A)}(N_k^{(\text{RF})} - n)}]$  is the corresponding sub-array selection matrix. For each sub-array, updating  $\mathbf{G}_n$  involves the matrix inversion of  $\mathbf{T}_n$  large size, which leads to high computational complexity. To avoid the matrix inversion, partitioning  $\mathbf{P}_n = [\mathbf{P}_{n-1} \quad \mathbf{p}_n]$ ,  $\mathbf{T}_n$  can be written as

$$\begin{aligned} \mathbf{T}_n &= \mathbf{I}_{M_q} + \frac{P_k}{N_k^{(\text{RF})} \sigma_q^2} \mathbf{H}_{q,k} \mathbf{P}_n \mathbf{P}_n^H \mathbf{H}_{q,k}^H = \mathbf{I}_{M_q} + \frac{P_k}{N_k^{(\text{RF})} \sigma_q^2} \mathbf{H}_{q,k} [\mathbf{P}_{n-1} \quad \mathbf{p}_n] [\mathbf{P}_{n-1} \quad \mathbf{p}_n]^H \mathbf{H}_{q,k}^H \\ &= \mathbf{I}_{M_q} + \frac{P_k}{N_k^{(\text{RF})} \sigma_q^2} \mathbf{H}_{q,k} \mathbf{P}_{n-1} \mathbf{P}_{n-1}^H \mathbf{H}_{q,k}^H + \frac{P_k}{N_k^{(\text{RF})} \sigma_q^2} \mathbf{H}_{q,k} \mathbf{p}_n \mathbf{p}_n^H \mathbf{H}_{q,k}^H \\ &= \mathbf{T}_{n-1} + \frac{P_k}{N_k^{(\text{RF})} \sigma_q^2} \mathbf{H}_{q,k} \mathbf{p}_n \mathbf{p}_n^H \mathbf{H}_{q,k}^H. \end{aligned} \quad (\text{C.6})$$

Then,  $\mathbf{T}_n^{-1}$  can be presented as

$$\begin{aligned} \mathbf{T}_n^{-1} &= \left( \mathbf{T}_{n-1} + \frac{P_k}{N_k^{(\text{RF})} \sigma_q^2} \mathbf{H}_{q,k} \mathbf{p}_n \mathbf{p}_n^H \mathbf{H}_{q,k}^H \right)^{-1} \\ &= \mathbf{T}_{n-1}^{-1} - \frac{\frac{P_k}{N_k^{(\text{RF})} \sigma_q^2} \mathbf{T}_{n-1}^{-1} \mathbf{H}_{q,k} \mathbf{p}_n \mathbf{p}_n^H \mathbf{H}_{q,k}^H \mathbf{T}_{n-1}^{-1}}{1 + \frac{P_k}{N_k^{(\text{RF})} \sigma_q^2} \mathbf{p}_n^H \mathbf{H}_{q,k}^H \mathbf{T}_{n-1}^{-1} \mathbf{H}_{q,k} \mathbf{p}_n}}, \end{aligned} \quad (\text{C.7})$$

## Appendix C (Continued)

using the Sherman-Morrison formula  $(\mathbf{A} + \mathbf{u}\mathbf{v}^H)^{-1} = \mathbf{A}^{-1} - \frac{\mathbf{A}^{-1}\mathbf{u}\mathbf{v}^H\mathbf{A}^{-1}}{1 + \mathbf{v}^H\mathbf{A}^{-1}\mathbf{u}}$ . Now substituting

Equation C.7 into  $\mathbf{G}_n = \mathbf{H}_{q,k}^H \mathbf{T}_n^{-1} \mathbf{H}_{q,k}$ ,

$$\begin{aligned}
\mathbf{G}_n &= \mathbf{H}_{q,k}^H \mathbf{T}_n^{-1} \mathbf{H}_{q,k} \\
&= \mathbf{H}_{q,k}^H \left( \mathbf{T}_{n-1}^{-1} - \frac{\frac{P_k}{N_k^{(\text{RF})} \sigma_q^2} \mathbf{T}_{n-1}^{-1} \mathbf{H}_{q,k} \mathbf{p}_n \mathbf{p}_n^H \mathbf{H}_{q,k}^H \mathbf{T}_{n-1}^{-1}}{1 + \frac{P_k}{N_k^{(\text{RF})} \sigma_q^2} \mathbf{p}_n^H \mathbf{H}_{q,k}^H \mathbf{T}_{n-1}^{-1} \mathbf{H}_{q,k} \mathbf{p}_n}} \right) \mathbf{H}_{q,k} \\
&= \mathbf{G}_{n-1} - \frac{\frac{P_k}{N_k^{(\text{RF})} \sigma_q^2} \mathbf{G}_{n-1} \mathbf{p}_n \mathbf{p}_n^H \mathbf{G}_{n-1}}{1 + \frac{P_k}{N_k^{(\text{RF})} \sigma_q^2} \mathbf{p}_n^H \mathbf{G}_{n-1} \mathbf{p}_n}} \\
&= \mathbf{G}_{n-1} - \frac{\frac{P_k}{N_k^{(\text{RF})} \sigma_q^2} \mathbf{G}_{n-1} \mathbf{R}_n^H \mathbf{v}_n \mathbf{v}_n^H \mathbf{R}_n \mathbf{G}_{n-1}}{1 + \frac{P_k}{N_k^{(\text{RF})} \sigma_q^2} \mathbf{v}_n^H \mathbf{R}_n \mathbf{G}_{n-1} \mathbf{R}_n^H \mathbf{v}_n}}.
\end{aligned} \tag{C.8}$$

## Appendix D

### Proof of Proposition 2

According to the optimization problem in Equation 5.16, we seek for the RF combining vectors  $\mathbf{u}_n$  that minimizes the SI channel  $\overline{\mathbf{H}}_{k,k}$ . Now, we reformulate the optimization problem into a codebook free system as

$$\mathbf{u}_n^* = \underset{\mathbf{u}_n \in \mathcal{F}}{\operatorname{argmin}} |\mathbf{u}_n^H \mathbf{H}_n|^2, \quad (\text{D.1})$$

where  $\mathcal{F} = \{\mathbf{u} \mid |[\mathbf{u}]_j| = 1/\sqrt{M_k^{(A)}}, \forall j = 1, \dots, M_k^{(A)}\}$  and  $\mathbf{H}_n = \mathbf{R}_n^H \overline{\mathbf{H}}_{k,k}$ . Now, the unconstrained solution of the combiner vector is  $\mathbf{a}_n \in \mathbb{C}^{M_k^{(A)} \times 1}$  such that  $\langle \mathbf{a}_n, \mathbf{H}_n \rangle = 0$ .

There, the combining vector optimization problem can be formulated as

$$\mathbf{u}_n^{\text{opt}} = \underset{\mathbf{u}_n \in \mathcal{F}}{\operatorname{argmin}} \|\mathbf{a}_n - \mathbf{u}_n\|^2. \quad (\text{D.2})$$

Here,  $\mathbf{a}_n$  can be expressed as  $\mathbf{a}_n = |\mathbf{a}_n| \circ e^{j\angle \mathbf{a}_n}$ . Therefore, the optimal solution  $\mathbf{u}_n^{\text{opt}} = \frac{1}{\sqrt{M_k^{(A)}}} e^{j\angle \mathbf{a}_n}$ . Given this specific choice of matrices, the residual error of the combining vector selection can be expressed as

$$\begin{aligned} \|\mathbf{a}_n - \mathbf{u}_n^{\text{opt}}\|^2 &= \left\| \mathbf{a}_n - \frac{1}{\sqrt{M_k^{(A)}}} e^{j\angle \mathbf{a}_n} \right\|^2 = \left\| |\mathbf{a}_n| \circ e^{j\angle \mathbf{a}_n} - \frac{1}{\sqrt{M_k^{(A)}}} e^{j\angle \mathbf{a}_n} \right\|^2 \\ &= \left\| \left( |\mathbf{a}_n| - \frac{1}{\sqrt{M_k^{(A)}}} \right) \circ e^{j\angle \mathbf{a}_n} \right\|^2 = \left\| \left( |\mathbf{a}_n| - \frac{1}{\sqrt{M_k^{(A)}}} \right) \right\|^2 \end{aligned}$$

## Appendix D (Continued)

$$\begin{aligned}
&= \sum_{j=1}^{M_k^{(A)}} |[\mathbf{a}_n]_j|^2 + \sum_{j=1}^{M_k^{(A)}} \frac{1}{M_k^{(A)}} - \frac{2}{\sqrt{M_k^{(A)}}} \sum_{j=1}^{M_k^{(A)}} |[\mathbf{a}_n]_j| \\
&\stackrel{(a)}{=} 2 \left( 1 - \frac{1}{\sqrt{M_k^{(A)}}} \sum_{j=1}^{M_k^{(A)}} |[\mathbf{a}_n]_j| \right) \\
&\stackrel{(b)}{\leq} 2 \left( 1 - \frac{1}{\sqrt{M_k^{(A)}}} \right),
\end{aligned} \tag{D.3}$$

where (a) is obtained as  $\sum_{j=1}^{M_k^{(A)}} |[\mathbf{a}_n]_j|^2 = 1$  and (b) is formed exploiting the fact that  $\sum_{j=1}^{M_k^{(A)}} |[\mathbf{a}_n]_j| \leq \sqrt{\sum_{j=1}^{M_k^{(A)}} |[\mathbf{a}_n]_j|^2}$ . Since the error is distributed over the  $M_k^{(A)}$  antenna elements, therefore average per-element error is formulated as

$$\frac{\|\mathbf{a}_n - \mathbf{u}_n^{\text{opt}}\|^2}{M_k^{(A)}} \leq \frac{2 \left( 1 - \frac{1}{\sqrt{M_k^{(A)}}} \right)}{M_k^{(A)}} < \frac{2}{M_k^{(A)}}. \tag{D.4}$$

It is evident from Equation D.4 that for large values of  $M_k^{(A)}$ , the error is negligible, therefore the SI effective channel power  $\left| \left( \mathbf{u}_n^{\text{opt}} \right)^H \mathbf{H}_n \right|^2$  gets close to 0 and suppress the SI in the node  $k$  receiver.

## Appendix E

### COPYRIGHT PERMISSIONS

In this appendix, we include the copyright permissions for the articles, whose contents were used for the production of this thesis. The permissions follow the same order as the appearance of the articles in the thesis.

## Appendix E (Continued)



Home



Help ▾



Email Support



Sign in



Create Account



### A Comprehensive Self-Interference Model for Single-Antenna Full-Duplex Communication Systems

Conference Proceedings:

ICC 2019 - 2019 IEEE International Conference on Communications (ICC)

Author: [::Md::] [::Atiquil::] [::Islam::]; Besma Smida

Publisher: IEEE

Date: 20-24 May 2019

Copyright © 2019, IEEE

#### Thesis / Dissertation Reuse

The IEEE does not require individuals working on a thesis to obtain a formal reuse license, however, you may print out this statement to be used as a permission grant:

*Requirements to be followed when using any portion (e.g., figure, graph, table, or textual material) of an IEEE copyrighted paper in a thesis:*

- 1) In the case of textual material (e.g., using short quotes or referring to the work within these papers) users must give full credit to the original source (author, paper, publication) followed by the IEEE copyright line © 2011 IEEE.
- 2) In the case of illustrations or tabular material, we require that the copyright line © [Year of original publication] IEEE appear prominently with each reprinted figure and/or table.
- 3) If a substantial portion of the original paper is to be used, and if you are not the senior author, also obtain the senior author's approval.

*Requirements to be followed when using an entire IEEE copyrighted paper in a thesis:*

- 1) The following IEEE copyright/ credit notice should be placed prominently in the references: © [year of original publication] IEEE. Reprinted, with permission, from [author names, paper title, IEEE publication title, and month/year of publication]
- 2) Only the accepted version of an IEEE copyrighted paper can be used when posting the paper or your thesis online.
- 3) In placing the thesis on the author's university website, please display the following message in a prominent place on the website: In reference to IEEE copyrighted material which is used with permission in this thesis, the IEEE does not endorse any of [university/educational entity's name goes here]'s products or services. Internal or personal use of this material is permitted. If interested in reprinting/republishing IEEE copyrighted material for advertising or promotional purposes or for creating new collective works for resale or redistribution, please go to [http://www.ieee.org/publications\\_standards/publications/rights/rights\\_link.html](http://www.ieee.org/publications_standards/publications/rights/rights_link.html) to learn how to obtain a License from RightsLink.

If applicable, University Microfilms and/or ProQuest Library, or the Archives of Canada may supply single copies of the dissertation.

BACK

CLOSE WINDOW

## Appendix E (Continued)



Home



Help ▾



Email Support



Sign in



Create Account



### On Deep Learning Assisted Self-Interference Estimation in a Full-Duplex Relay Link

Author: Konstantin Muranov; [::Md:] [::Atiqu:] [::Islam::]; Besma Smida; Natasha Devroye

Publication: IEEE Wireless Communications Letters

Publisher: IEEE

Date: Dec. 2021

Copyright © 2021, IEEE

#### Thesis / Dissertation Reuse

The IEEE does not require individuals working on a thesis to obtain a formal reuse license, however, you may print out this statement to be used as a permission grant:

*Requirements to be followed when using any portion (e.g., figure, graph, table, or textual material) of an IEEE copyrighted paper in a thesis:*

- 1) In the case of textual material (e.g., using short quotes or referring to the work within these papers) users must give full credit to the original source (author, paper, publication) followed by the IEEE copyright line © 2011 IEEE.
- 2) In the case of illustrations or tabular material, we require that the copyright line © [Year of original publication] IEEE appear prominently with each reprinted figure and/or table.
- 3) If a substantial portion of the original paper is to be used, and if you are not the senior author, also obtain the senior author's approval.

*Requirements to be followed when using an entire IEEE copyrighted paper in a thesis:*

- 1) The following IEEE copyright/ credit notice should be placed prominently in the references: © [year of original publication] IEEE. Reprinted, with permission, from [author names, paper title, IEEE publication title, and month/year of publication]
- 2) Only the accepted version of an IEEE copyrighted paper can be used when posting the paper or your thesis online.
- 3) In placing the thesis on the author's university website, please display the following message in a prominent place on the website: In reference to IEEE copyrighted material which is used with permission in this thesis, the IEEE does not endorse any of [university/educational entity's name goes here]'s products or services. Internal or personal use of this material is permitted. If interested in reprinting/republishing IEEE copyrighted material for advertising or promotional purposes or for creating new collective works for resale or redistribution, please go to [http://www.ieee.org/publications\\_standards/publications/rights/rights\\_link.html](http://www.ieee.org/publications_standards/publications/rights/rights_link.html) to learn how to obtain a License from RightsLink.

If applicable, University Microfilms and/or ProQuest Library, or the Archives of Canada may supply single copies of the dissertation.

BACK

CLOSE WINDOW

## Appendix E (Continued)



Home



Help ▾



Email Support



Sign in



Create Account



### A Unified Beamforming and A/D Self-Interference Cancellation Design for Full Duplex MIMO Radios

Conference Proceedings:

2019 IEEE 30th Annual International Symposium on Personal, Indoor and Mobile Radio Communications (PIMRC)

Author: [::Md:] [::Atiqu:] [::Islam:]; George C. Alexandropoulos; Besma Smida

Publisher: IEEE

Date: 8-11 Sept. 2019

Copyright © 2019, IEEE

#### Thesis / Dissertation Reuse

The IEEE does not require individuals working on a thesis to obtain a formal reuse license, however, you may print out this statement to be used as a permission grant:

*Requirements to be followed when using any portion (e.g., figure, graph, table, or textual material) of an IEEE copyrighted paper in a thesis:*

- 1) In the case of textual material (e.g., using short quotes or referring to the work within these papers) users must give full credit to the original source (author, paper, publication) followed by the IEEE copyright line © 2011 IEEE.
- 2) In the case of illustrations or tabular material, we require that the copyright line © [Year of original publication] IEEE appear prominently with each reprinted figure and/or table.
- 3) If a substantial portion of the original paper is to be used, and if you are not the senior author, also obtain the senior author's approval.

*Requirements to be followed when using an entire IEEE copyrighted paper in a thesis:*

- 1) The following IEEE copyright/ credit notice should be placed prominently in the references: © [year of original publication] IEEE. Reprinted, with permission, from [author names, paper title, IEEE publication title, and month/year of publication]
- 2) Only the accepted version of an IEEE copyrighted paper can be used when posting the paper or your thesis on-line.
- 3) In placing the thesis on the author's university website, please display the following message in a prominent place on the website: In reference to IEEE copyrighted material which is used with permission in this thesis, the IEEE does not endorse any of [university/educational entity's name goes here]'s products or services. Internal or personal use of this material is permitted. If interested in reprinting/republishing IEEE copyrighted material for advertising or promotional purposes or for creating new collective works for resale or redistribution, please go to [http://www.ieee.org/publications\\_standards/publications/rights/rights\\_link.html](http://www.ieee.org/publications_standards/publications/rights/rights_link.html) to learn how to obtain a License from RightsLink.

If applicable, University Microfilms and/or ProQuest Library, or the Archives of Canada may supply single copies of the dissertation.

BACK

CLOSE WINDOW

## Appendix E (Continued)



Home



Help ▾



Email Support



Sign in



Create Account



### Simultaneous Downlink Data Transmission and Uplink Channel Estimation with Reduced Complexity Full Duplex MIMO Radios

Conference Proceedings:

2020 IEEE International Conference on Communications Workshops (ICC Workshops)

Author: [::Md::] [::Atiqu::] [::Islam::]; George C. Alexandropoulos; Besma Smida

Publisher: IEEE

Date: 7-11 June 2020

Copyright © 2020, IEEE

### Thesis / Dissertation Reuse

The IEEE does not require individuals working on a thesis to obtain a formal reuse license, however, you may print out this statement to be used as a permission grant:

*Requirements to be followed when using any portion (e.g., figure, graph, table, or textual material) of an IEEE copyrighted paper in a thesis:*

- 1) In the case of textual material (e.g., using short quotes or referring to the work within these papers) users must give full credit to the original source (author, paper, publication) followed by the IEEE copyright line © 2011 IEEE.
- 2) In the case of illustrations or tabular material, we require that the copyright line © [Year of original publication] IEEE appear prominently with each reprinted figure and/or table.
- 3) If a substantial portion of the original paper is to be used, and if you are not the senior author, also obtain the senior author's approval.

*Requirements to be followed when using an entire IEEE copyrighted paper in a thesis:*

- 1) The following IEEE copyright/ credit notice should be placed prominently in the references: © [year of original publication] IEEE. Reprinted, with permission, from [author names, paper title, IEEE publication title, and month/year of publication]
- 2) Only the accepted version of an IEEE copyrighted paper can be used when posting the paper or your thesis online.
- 3) In placing the thesis on the author's university website, please display the following message in a prominent place on the website: In reference to IEEE copyrighted material which is used with permission in this thesis, the IEEE does not endorse any of [university/educational entity's name goes here]'s products or services. Internal or personal use of this material is permitted. If interested in reprinting/republishing IEEE copyrighted material for advertising or promotional purposes or for creating new collective works for resale or redistribution, please go to [http://www.ieee.org/publications\\_standards/publications/rights/rights\\_link.html](http://www.ieee.org/publications_standards/publications/rights/rights_link.html) to learn how to obtain a License from RightsLink.

If applicable, University Microfilms and/or ProQuest Library, or the Archives of Canada may supply single copies of the dissertation.

BACK

CLOSE WINDOW

## Appendix E (Continued)



### Simultaneous Data Communication and Channel Estimation in Multi-User Full Duplex MIMO Systems

Conference Proceedings: 2020 54th Asilomar Conference on Signals, Systems, and Computers

Author: [::Md::] [::Atiqul::] [::Islam::]; George C. Alexandropoulos; Besma Smida

Publisher: IEEE

Date: 1-4 Nov. 2020

Copyright © 2020, IEEE

### Thesis / Dissertation Reuse

The IEEE does not require individuals working on a thesis to obtain a formal reuse license, however, you may print out this statement to be used as a permission grant:

*Requirements to be followed when using any portion (e.g., figure, graph, table, or textual material) of an IEEE copyrighted paper in a thesis:*

- 1) In the case of textual material (e.g., using short quotes or referring to the work within these papers) users must give full credit to the original source (author, paper, publication) followed by the IEEE copyright line © 2011 IEEE.
- 2) In the case of illustrations or tabular material, we require that the copyright line © [Year of original publication] IEEE appear prominently with each reprinted figure and/or table.
- 3) If a substantial portion of the original paper is to be used, and if you are not the senior author, also obtain the senior author's approval.

*Requirements to be followed when using an entire IEEE copyrighted paper in a thesis:*

- 1) The following IEEE copyright/ credit notice should be placed prominently in the references: © [year of original publication] IEEE. Reprinted, with permission, from [author names, paper title, IEEE publication title, and month/year of publication]
- 2) Only the accepted version of an IEEE copyrighted paper can be used when posting the paper or your thesis online.
- 3) In placing the thesis on the author's university website, please display the following message in a prominent place on the website: In reference to IEEE copyrighted material which is used with permission in this thesis, the IEEE does not endorse any of [university/educational entity's name goes here]'s products or services. Internal or personal use of this material is permitted. If interested in reprinting/republishing IEEE copyrighted material for advertising or promotional purposes or for creating new collective works for resale or redistribution, please go to [http://www.ieee.org/publications\\_standards/publications/rights/rights\\_link.html](http://www.ieee.org/publications_standards/publications/rights/rights_link.html) to learn how to obtain a License from RightsLink.

If applicable, University Microfilms and/or ProQuest Library, or the Archives of Canada may supply single copies of the dissertation.

BACK

CLOSE WINDOW

## Appendix E (Continued)



Home



Help ▾



Email Support



Sign in



Create Account



### Full Duplex Hybrid A/D Beamforming with Reduced Complexity Multi-Tap Analog Cancellation

#### Conference Proceedings:

2020 IEEE 21st International Workshop on Signal Processing Advances in Wireless Communications (SPAWC)

Author: George C. Alexandropoulos; [::Md::] [::Atiquil::] [::Islam::]; Besma Smida

Publisher: IEEE

Date: 26-29 May 2020

Copyright © 2020, IEEE

### Thesis / Dissertation Reuse

The IEEE does not require individuals working on a thesis to obtain a formal reuse license, however, you may print out this statement to be used as a permission grant:

*Requirements to be followed when using any portion (e.g., figure, graph, table, or textual material) of an IEEE copyrighted paper in a thesis:*

- 1) In the case of textual material (e.g., using short quotes or referring to the work within these papers) users must give full credit to the original source (author, paper, publication) followed by the IEEE copyright line © 2011 IEEE.
- 2) In the case of illustrations or tabular material, we require that the copyright line © [Year of original publication] IEEE appear prominently with each reprinted figure and/or table.
- 3) If a substantial portion of the original paper is to be used, and if you are not the senior author, also obtain the senior author's approval.

*Requirements to be followed when using an entire IEEE copyrighted paper in a thesis:*

- 1) The following IEEE copyright/ credit notice should be placed prominently in the references: © [year of original publication] IEEE. Reprinted, with permission, from [author names, paper title, IEEE publication title, and month/year of publication]
- 2) Only the accepted version of an IEEE copyrighted paper can be used when posting the paper or your thesis online.
- 3) In placing the thesis on the author's university website, please display the following message in a prominent place on the website: In reference to IEEE copyrighted material which is used with permission in this thesis, the IEEE does not endorse any of [university/educational entity's name goes here]'s products or services. Internal or personal use of this material is permitted. If interested in reprinting/republishing IEEE copyrighted material for advertising or promotional purposes or for creating new collective works for resale or redistribution, please go to [http://www.ieee.org/publications\\_standards/publications/rights/rights\\_link.html](http://www.ieee.org/publications_standards/publications/rights/rights_link.html) to learn how to obtain a License from RightsLink.

If applicable, University Microfilms and/or ProQuest Library, or the Archives of Canada may supply single copies of the dissertation.

BACK

CLOSE WINDOW

## Appendix E (Continued)



Home



Help ▾



Email Support



Sign in



Create Account



### Direction-Assisted Beam Management in Full Duplex Millimeter Wave Massive MIMO Systems

Conference Proceedings: 2021 IEEE Global Communications Conference (GLOBECOM)

Author: [::Md::] [::Atiquil::] [::Islam::]; George C. Alexandropoulos; Besma Smida

Publisher: IEEE

Date: 7-11 Dec. 2021

Copyright © 2021, IEEE

#### Thesis / Dissertation Reuse

The IEEE does not require individuals working on a thesis to obtain a formal reuse license, however, you may print out this statement to be used as a permission grant:

*Requirements to be followed when using any portion (e.g., figure, graph, table, or textual material) of an IEEE copyrighted paper in a thesis:*

- 1) In the case of textual material (e.g., using short quotes or referring to the work within these papers) users must give full credit to the original source (author, paper, publication) followed by the IEEE copyright line © 2011 IEEE.
- 2) In the case of illustrations or tabular material, we require that the copyright line © [Year of original publication] IEEE appear prominently with each reprinted figure and/or table.
- 3) If a substantial portion of the original paper is to be used, and if you are not the senior author, also obtain the senior author's approval.

*Requirements to be followed when using an entire IEEE copyrighted paper in a thesis:*

- 1) The following IEEE copyright/ credit notice should be placed prominently in the references: © [year of original publication] IEEE. Reprinted, with permission, from [author names, paper title, IEEE publication title, and month/year of publication]
- 2) Only the accepted version of an IEEE copyrighted paper can be used when posting the paper or your thesis online.
- 3) In placing the thesis on the author's university website, please display the following message in a prominent place on the website: In reference to IEEE copyrighted material which is used with permission in this thesis, the IEEE does not endorse any of [university/educational entity's name goes here]'s products or services. Internal or personal use of this material is permitted. If interested in reprinting/republishing IEEE copyrighted material for advertising or promotional purposes or for creating new collective works for resale or redistribution, please go to [http://www.ieee.org/publications\\_standards/publications/rights/rights\\_link.html](http://www.ieee.org/publications_standards/publications/rights/rights_link.html) to learn how to obtain a License from RightsLink.

If applicable, University Microfilms and/or ProQuest Library, or the Archives of Canada may supply single copies of the dissertation.

BACK

CLOSE WINDOW

## CITED LITERATURE

1. Andrews, J. G., Buzzi, S., Choi, W., Hanly, S. V., Lozano, A., Soong, A. C., and Zhang, J. C.: What will 5G be? IEEE Journal on Selected Areas in Communications, 32(6):1065–1082, Jun. 2014.
2. Osseiran, A., Monserrat, J. F., and Marsch, P.: 5G mobile and wireless communications technology. Cambridge University Press, 2016.
3. Sabharwal, A., Schniter, P., Guo, D., Bliss, D. W., Rangarajan, S., and Wichman, R.: In-Band Full-Duplex Wireless: Challenges and Opportunities. IEEE Journal on Selected Areas in Communications, 32(9):1637–1652, Sep. 2014.
4. Zhang, Z., Long, K., Vasilakos, A. V., and Hanzo, L.: Full-Duplex Wireless Communications: Challenges, Solutions, and Future Research Directions. Proceedings of the IEEE, 104(7):1369–1409, Feb. 2016.
5. Kolodziej, K. E., Perry, B. T., and Herd, J. S.: In-Band Full-Duplex Technology: Techniques and Systems Survey. IEEE Transactions on Microwave Theory and Techniques, 67(7):3025–3041, Feb. 2019.
6. The next hyper-Connected experience for all. White Paper, June 2020.
7. Kim, D., Park, S., Ju, H., and Hong, D.: Transmission capacity of full-duplex-based two-way ad hoc networks with arq protocol. IEEE Transactions on Vehicular Technology, 63(7):3167–3183, 2014.
8. Muranov, K., Smida, B., and Devroye, N.: On channel equalization for full-duplex relay networks. In Proceedings of the IEEE International Conference on Communications (ICC), pages 1–6, May 2017.
9. Ju, H., Lim, S., Kim, D., Poor, H. V., and Hong, D.: Full duplexity in beamforming-based multi-hop relay networks. IEEE Journal on Selected Areas in Communications, 30(8):1554–1565, 2012.

10. Hong, S., Brand, J., Choi, J. I., Jain, M., Mehlman, J., Katti, S., and Levis, P.: Applications of self-interference cancellation in 5G and beyond. IEEE Communications Magazine, 52(2):114–121, 2014.
11. Riihonen, T., Korpi, D., Rantula, O., Rantanen, H., Saarelainen, T., and Valkama, M.: Inband full-duplex radio transceivers: A paradigm shift in tactical communications and electronic warfare? IEEE Communications Magazine, 55(10):30–36, 2017.
12. Talwar, S., Choudhury, D., Dimou, K., Aryafar, E., Bangerter, B., and Stewart, K.: Enabling technologies and architectures for 5G wireless. In Proceedings of the IEEE MTT-S International Microwave Symposium, pages 1–4, Jun 2014.
13. Liu, F., Masouros, C., Petropulu, A. P., Griffiths, H., and Hanzo, L.: Joint radar and communication design: Applications, state-of-the-art, and the road ahead. IEEE Transactions on Communications, 68(6):3834–3862, Feb. 2020.
14. Alamzadeh, I., Alexandropoulos, G. C., Shlezinger, N., and Imani, M. F.: A reconfigurable intelligent surface with integrated sensing capability. Scientific Reports, 11(20737):1–10, Oct. 2021.
15. Alexandropoulos, G. C., Shlezinger, N., Alamzadeh, I., Imani, M. F., Zhang, H., and Eldar, Y. C.: Hybrid reconfigurable intelligent metasurfaces: Enabling simultaneous tunable reflections and sensing for 6G wireless communications. [online] <https://arxiv.org/abs/2104.04690>, 2021.
16. Mishra, K. V., Shankar, M. B., Koivunen, V., Ottersten, B., and Vorobyov, S. A.: Toward millimeter-wave joint radar communications: A signal processing perspective. IEEE Signal Processing Magazine, 36(5):100–114, Sep. 2019.
17. Paul, B., Chiriyath, A. R., and Bliss, D. W.: Survey of RF communications and sensing convergence research. IEEE Access, 5:252–270, Jan. 2016.
18. Barneto, C. B., Riihonen, T., Turunen, M., Anttila, L., Fleischer, M., Stadius, K., Rynänen, J., and Valkama, M.: Full-duplex OFDM radar with LTE and 5G NR waveforms: Challenges, solutions, and measurements. IEEE Transactions on Microwave Theory and Techniques, 67(10):4042–4054, Aug. 2019.

19. Liyanaarachchi, S. D., Riihonen, T., Barneto, C. B., and Valkama, M.: Optimized waveforms for 5G–6G communication with sensing: Theory, simulations and experiments. IEEE Transactions on Wireless Communications, Jun. 2021.
20. Barneto, C. B., Liyanaarachchi, S. D., Riihonen, T., Heino, M., Anttila, L., and Valkama, M.: Beamforming and waveform optimization for OFDM-based joint communications and sensing at mm-waves. In Proceedings of the IEEE ASILOMAR, pages 895–899, Pacific Grove, USA, Nov. 2020.
21. Liyanaarachchi, S. D., Barneto, C. B., Riihonen, T., Heino, M., and Valkama, M.: Joint multi-user communication and MIMO radar through full-duplex hybrid beamforming. In IEEE International Symposium on Joint Communications & Sensing (JC&S), pages 1–5, Feb. 2021.
22. Duarte, M. and Sabharwal, A.: Full-duplex wireless communications using off-the-shelf radios: Feasibility and first results. In Proceedings of the IEEE Asilomar Conference on Signals, Systems and Computers, pages 1558 – 1562, 2010.
23. Bliss, D. W., Parker, P. A., and Margetts, A. R.: Simultaneous transmission and reception for improved wireless network performance. In Proceedings of the IEEE Workshop on Statistical Signal Processing, pages 478 – 482, Aug. 2007.
24. Duarte, M., Dick, C., and Sabharwal, A.: Experiment-driven characterization of full-duplex wireless systems. IEEE Transactions on Wireless Communications, 11(12):4296–4307, Dec. 2012.
25. Duarte, M., Sabharwal, A., Aggarwal, V., Jana, R., Ramakrishnan, K. K., Rice, C., and Shankaranarayanan, N. K.: Design and characterization of a full-duplex multiantenna system for WiFi networks. IEEE Transactions on Vehicular Technology, 63(3):1160–1177, Nov. 2013.
26. Anderson, C., Krishnamoorthy, S., Ranson, C., Lemon, T., Newhall, W., Kummetz, T., and Reed, J.: Antenna isolation, wideband multipath propagation measurements, and interference mitigation for on-frequency repeaters. In Proceedings of the IEEE SoutheastCon, pages 110–114, March 2004.
27. Korpi, D., Heino, M., Icheln, C., Haneda, K., and Valkama, M.: Compact inband full-duplex relays with beyond 100 dB self-interference suppression: Enabling

- techniques and field measurements. IEEE Transactions on Antennas and Propagation, 65(2):960–965, Nov. 2017.
28. Alrabadi, O. N., Tatomirescu, A. D., Knudsen, M. B., Pelosi, M., and Pedersen, G. F.: Breaking the Transmitter–Receiver Isolation Barrier in Mobile Handsets With Spatial Duplexing. IEEE Transactions on Antennas and Propagation, 61(4):2241–2251, Dec. 2013.
  29. Everett, E., Duarte, M., Dick, C., and Sabharwal, A.: Empowering full-duplex wireless communication by exploiting directional diversity. In Proceedings of the IEEE Asilomar Conference on Signals, Systems and Computers, pages 2002 – 2006, 2011.
  30. Choi, J. I., Jain, M., Srinivasan, K., Levis, P., and Katti, S.: Achieving single channel, full duplex wireless communication. In Proceedings of the International Conference on Mobile Computing and Networking (MobiCom), pages 1 – 12, Sep. 2010.
  31. Khandani, A. K.: Shaping the future of wireless: Two-way connectivity. [http://www.nortel-institute.uwaterloo.ca/content/Shaping Future of Wireless Two-way Connectivity 18ne2012.pdf](http://www.nortel-institute.uwaterloo.ca/content/Shaping%20Future%20of%20Wireless%20Two-way%20Connectivity%2018ne2012.pdf), Jun. 2012.
  32. Aryafar, E., Khojastepour, M. A., Sundaresan, K., Rangarajan, S., and Chiang, M.: MIDU: enabling MIMO full duplex. In Proceedings of the International Conference on Mobile Computing and Networking (MobiCom), pages 1 – 12, Sep. 2012.
  33. Cryan, M. J. and Hall, P. S.: Integrated active antenna with simultaneous transmit-receive operation. Electronics Letters, 32(4):286–287, Feb 1996.
  34. Sharma, S. K., Shafai, L., and Jacob, N.: Investigation of wide-band microstrip slot antenna. IEEE Transactions on Antennas and Propagation, 52(3):865–872, Apr. 2004.
  35. Li, Y., Zhang, Z., Chen, W., Feng, Z., and Iskander, M. F.: A Dual-Polarization Slot Antenna Using a Compact CPW Feeding Structure. IEEE Antennas and Wireless Propagation Letters, 9:191–194, Mar. 2010.

36. Nguyen, N. A., Le, V. H., Nguyen-Trong, N., Radfar, M., Ebrahimi, A., Phan, K., and Desai, A.: Dual-Polarized Slot Antenna for Full-Duplex Systems with High Isolation. IEEE Transactions on Antennas and Propagation, Jul. 2020.
37. Mao, C. X., Zhou, Y., Wu, Y., Soewardiman, H., Werner, D. H., and Jur, J. S.: Low-Profile Strip-Loaded Textile Antenna With Enhanced Bandwidth and Isolation for Full-Duplex Wearable Applications. IEEE Transactions on Antennas and Propagation, 68(9):6527–6537, 2020.
38. Everett, E., Sahai, A., and Sabharwal, A.: Passive Self-Interference Suppression for Full-Duplex Infrastructure Nodes. IEEE Transactions on Wireless Communications, 13(2):680–694, 2014.
39. Elmansouri, M. A. and Filipovic, D. S.: Realization of ultra-wideband bistatic simultaneous transmit and receive antenna system. In Proceedings of the IEEE International Symposium on Antennas and Propagation (APSURSI), pages 2115–2116, 2016.
40. Prasannakumar, P. V., Elmansouri, M. A., and Filipovic, D. S.: Wideband Decoupling Techniques for Dual-Polarized Bi-Static Simultaneous Transmit and Receive Antenna Subsystem. IEEE Transactions on Antennas and Propagation, 65(10):4991–5001, 2017.
41. Nawaz, H. and Tekin, I.: Double-Differential-Fed, Dual-Polarized Patch Antenna With 90 dB Interport RF Isolation for a 2.4 GHz In-Band Full-Duplex Transceiver. IEEE Antennas and Wireless Propagation Letters, 17(2):287–290, 2018.
42. Lian, R., Shih, T. Y., Yin, Y., and Behdad, N.: A High-Isolation, Ultra-Wideband Simultaneous Transmit and Receive Antenna With Monopole-Like Radiation Characteristics. IEEE Transactions on Antennas and Propagation, 66(2):1002–1007, Feb. 2018.
43. Makar, G., Tran, N., and Karacolak, T.: A High-Isolation Monopole Array With Ring Hybrid Feeding Structure for In-Band Full-Duplex Systems. IEEE Antennas and Wireless Propagation Letters, 16:356–359, 2017.
44. Khaledian, S., Farzami, F., Smida, B., and Erricolo, D.: Robust self-interference cancellation for microstrip antennas by means of phase reconfigurable cou-

- pler. IEEE Transactions on Antennas and Propagation, 66(10):5574–5579, Jul. 2018.
45. Debaillie, B., van den Broek, D. J., Lavin, C., van Liempd, B., Klumperink, E., Palacios, C., Craninckx, J., Nauta, B., and Pärssinen, A.: Analog/RF solutions enabling compact full-duplex radios. IEEE Journal on Selected Areas in Communications, 32(9):1662, 2014.
  46. Wang, X., Che, W., Yang, W., Feng, W., and Gu, L.: Self-Interference Cancellation Antenna Using Auxiliary Port Reflection for Full-Duplex Application. IEEE Antennas and Wireless Propagation Letters, 16:2873–2876, 2017.
  47. Deng, C., Yektakhah, B., and Sarabandi, K.: Series-Fed Dual-Polarized Single-Layer Linear Patch Array With High Polarization Purity. IEEE Antennas and Wireless Propagation Letters, 18(9):1746–1750, 2019.
  48. Hernández, C. A. M., Boskovic, L. B., Elmansouri, M. A., Ignatenko, M., and Filipovic, D. S.: Fixed and Steerable Beam Dual-Polarized Lens Antenna with High Tx to Rx Isolation. IEEE Transactions on Antennas and Propagation, 2021.
  49. Smida, B. and Khaledian, S.: ReflectFX: In-band full-duplex wireless communication by means of reflected power. IEEE Transactions on Communications, 65(5):2207–2219, Feb. 2017.
  50. Khaledian, S., Farzami, F., Smida, B., and Erricolo, D.: Inherent Self-Interference Cancellation for In-Band Full-Duplex Single-Antenna Systems. IEEE Transactions on Microwave Theory and Techniques, 66(6):2842–2850, Jun. 2018.
  51. Bharadia, D., McMilin, E., and Katti, S.: Full duplex radios. In Proceedings of the ACM SIGCOMM, pages 375–386, Aug. 2013.
  52. Zhou, J., Chuang, T.-H., Dinc, T., and Krishnaswamy, H.: Integrated wideband self-interference cancellation in the RF domain for fdd and full-duplex wireless. IEEE Journal of Solid-State Circuits, 50(12):3015–3031, Oct. 2015.

53. Kolodziej, K. E., McMichael, J. G., and Perry, B. T.: Multitap RF canceller for in-band full-duplex wireless communications. IEEE Transactions on Wireless Communications, 15(6):4321–4334, Mar. 2016.
54. Korpi, D., Tamminen, J., Turunen, M., Huusari, T., Choi, Y.-S., Anttila, L., Talwar, S., and Valkama, M.: Full-duplex mobile device: Pushing the limits. IEEE Communications Magazine, 54(9):80–87, Sep. 2016.
55. Chen, T., Baraani Dastjerdi, M., Zhou, J., Krishnaswamy, H., and Zussman, G.: Wideband full-duplex wireless via frequency-domain equalization: Design and experimentation. In Proceedings of the ACM MobiCom, pages 1–16, Aug. 2019.
56. Antonio-Rodriguez, E., Lopez-Valcarce, R., Riihonen, T., Werner, S., and Wichman, R.: Adaptive self-interference cancellation in wideband full-duplex decode-and-forward MIMO relays. In Proceedings of the IEEE PIMRC, pages 370–374, Darmstadt, Germany, Jun. 2013.
57. Bharadia, D. and Katti, S.: Full duplex MIMO radios. In Proceedings of the USENIX NSDI, pages 359–372, Seattle, WA, 2-4 Apr. 2014.
58. Riihonen, T., Werner, S., and Wichman, R.: Mitigation of loopback self-interference in full-duplex MIMO relays. IEEE Transactions on Signal Processing, 59(12):5983–5993, Dec. 2011.
59. Alexandropoulos, G. C. and Duarte, M.: Joint design of multi-tap analog cancellation and digital beamforming for reduced complexity full duplex MIMO systems. In Proceedings of the IEEE ICC, pages 1–7, Paris, France, May 2017.
60. Huberman, S. and Le-Ngoc, T.: MIMO full-duplex precoding: A joint beamforming and self-interference cancellation structure. IEEE Transactions on Wireless Communications, 14(4):2205–2217, Dec. 2014.
61. Duarte, M. and Alexandropoulos, G. C.: Full duplex MIMO digital beamforming with reduced complexity AUXTX analog cancellation. In Proceedings of the IEEE ICC, pages 1–6, Jun. 2020.

62. Lee, D. and Min, B.-W.: Analysis of self-interference cancellation and experimental results of  $2 \times 2$  MIMO in-band full-duplex radio front-end. In Proceedings of the IEEE Symposium on Personal, Indoor and Mobile Radio Communications (PIMRC Workshops), pages 1–6, Sep. 2019.
63. Le, A. T., Huang, X., Guo, Y. J., et al.: Beam-based analog self-interference cancellation in full-duplex MIMO systems. IEEE Transactions on Wireless Communications, 19(4):2460–2471, Apr. 2020.
64. Cao, Y. and Zhou, J.: Integrated self-adaptive and power-scalable wideband interference cancellation for full-duplex MIMO wireless. IEEE Journal of Solid-State Circuits, 55(11):2984–2996, Nov. 2020.
65. Ahmed, E. and Eltawil, A. M.: All-digital self-interference cancellation technique for full-duplex systems. IEEE Transactions on Wireless Communications, 14(7):3519–3532, 2015.
66. Korpi, D., Anttila, L., Syrjala, V., and Valkama, M.: Widely linear digital self-interference cancellation in direct-conversion full-duplex transceiver. IEEE Journal on Selected Areas in Communications, 32(9):1674–1687, Sep. 2014.
67. Islam, M. A. and Smida, B.: A comprehensive self-interference model for single-antenna full-duplex communication systems. In Proceedings of the IEEE International Conference on Communications (ICC), pages 1–7, Shanghai, China, May 2019.
68. Anttila, L., Korpi, D., Antonio-Rodriguez, E., Wichman, R., and Valkama, M.: Modeling and efficient cancellation of nonlinear self-interference in MIMO full-duplex transceivers. In Proceedings of the IEEE GLOBECOM, pages 777–783, Austin, USA, Dec. 2014.
69. Korpi, D., Anttila, L., and Valkama, M.: Nonlinear self-interference cancellation in MIMO full-duplex transceivers under crosstalk. EURASIP Journal on Wireless Communications and Networking, 2017(1):24, Dec. 2017.
70. Muranov, K., Islam, M. A., Smida, B., and Devroye, N.: On deep learning assisted self-interference estimation in a full-duplex relay link. IEEE Wireless Communications Letters, 10(12):2762–2766, Sep. 2021.

71. Quan, X., Liu, Y., Shao, S., Huang, C., and Tang, Y.: Impacts of phase noise on digital self-interference cancellation in full-duplex communications. IEEE Transactions on Signal Processing, 65(7):1881–1893, 2017.
72. Balatsoukas-Stimming, A., Austin, A. C., Belanovic, P., and Burg, A.: Baseband and RF hardware impairments in full-duplex wireless systems: experimental characterisation and suppression. EURASIP Journal on Wireless Communications and Networking, 2015(1):142, 2015.
73. Jain, M., Choi, J. I., Kim, T. M., D.Bharadia, Seth, S., Srinivasan, K., Levis, P., Katti, S., and Sinha, P.: Practical, real-time, full duplex wireless. In Proceedings of the International Conference on Mobile Computing and Networking (MobiCom), pages 301 – 312, Sep. 2011.
74. Korpi, D., Choi, Y. S., Huusari, T., Anttila, L., Talwar, S., and Valkama, M.: Adaptive nonlinear digital self-interference cancellation for mobile inband full-duplex radio: Algorithms and RF measurements. In Proceedings of the IEEE Global Communications Conference (GLOBECOM), pages 1–7, Dec. 2015.
75. Gu, Q.: RF system design of transceivers for wireless communications. Springer Science & Business Media, 2005.
76. Schenk, T.: RF imperfections in high-rate wireless systems: impact and digital compensation. Springer Science & Business Media, 2008.
77. Sahai, A., Patel, G., Dick, C., and Sabharwal, A.: On the impact of phase noise on active cancellation in wireless full-duplex. IEEE Transactions on Vehicular Technology, 62(9):4494–4510, 2013.
78. Analog Devices: AD9361: 2 × 2 RF Agile Transceiver, Rev. F. <http://www.analog.com/media/en/technical-documentation/data-sheets/AD9361.pdf>.
79. Zhang, Z., Shen, Y., Shao, S., Pan, W., and Tang, Y.: Full duplex 2×2 MIMO radios. In Proceedings of the International Conference on Wireless Communications and Signal Processing, pages 1–6, Hefei, China, Oct. 2014.

80. Balatsoukas-Stimming, A.: Non-linear digital self-interference cancellation for in-band full-duplex radios using neural networks. In Proceedings of the IEEE International Workshop on Signal Processing Advances in Wireless Communications (SPAWC), pages 1–5, 2018.
81. Guo, H., Wu, S., Wang, H., and Daneshmand, M.: Dsic: Deep learning based self-interference cancellation for in-band full duplex wireless. In Proceedings of the IEEE Global Communications Conference (GLOBECOM), pages 1–6, 2019.
82. Kurzo, Y., Burg, A., and Balatsoukas-Stimming, A.: Design and implementation of a neural network aided self-interference cancellation scheme for full-duplex radios. In Proceedings of the IEEE Asilomar Conference on Signals, Systems, and Computers, pages 589–593, 2018.
83. Goodfellow, I., Bengio, Y., Courville, A., and Bengio, Y.: Deep learning, volume 1. MIT press Cambridge, 2016.
84. Islam, M. A., Alexandropoulos, G. C., and Smida, B.: Joint analog and digital transceiver design for wideband full duplex MIMO systems. IEEE Transactions on Wireless Communications, Jun. 2022.
85. Islam, M. A., Alexandropoulos, G. C., and Smida, B.: A unified beamforming and A/D self-interference cancellation design for full duplex MIMO radios. In Proceedings of the IEEE Annual International Symposium on Personal, Indoor and Mobile Radio Communications (PIMRC), pages 1–7, Istanbul, Turkey, Sep. 2019.
86. Everett, E., Shepard, C., Zhong, L., and Sabharwal, A.: Softnull: Many-antenna full-duplex wireless via digital beamforming. IEEE Transactions on Wireless Communications, 15(12):8077–8092, Dec. 2016.
87. Masmoudi, A. and Le-Ngoc, T.: Channel estimation and self-interference cancellation in full-duplex communication systems. IEEE Transactions on Vehicular Technology, 66(1):321–334, Jan. 2017.
88. Islam, M. A., Alexandropoulos, G. C., and Smida, B.: Simultaneous downlink data transmission and uplink channel estimation with reduced complexity full duplex MIMO radios. In Proceedings of the IEEE International Conference on

Communications Workshops (ICC Workshops), pages 1–6, Dublin, Ireland, Jun. 2020.

89. Mirza, J., Zheng, G., Wong, K.-K., Lambotaran, S., and Hanzo, L.: On the performance of multi-user MIMO systems relying on full-duplex CSI acquisition. IEEE Transactions on Wireless Communications, 66(10):4563–4577, Oct. 2018.
90. Islam, M. A., Alexandropoulos, G. C., and Smida, B.: Simultaneous data communication and channel estimation in multi-user full duplex MIMO systems. In Proceedings of the IEEE Asilomar Conference on Signals, Systems and Computers, pages 1–6, Pacific Grove, USA, Nov. 2020.
91. Ng, D. W. K., Lo, E. S., and Schober, R.: Dynamic resource allocation in MIMO-OFDMA systems with full-duplex and hybrid relaying. IEEE Transactions on Communications, 60(5):1291–1304, Apr. 2012.
92. Taghizadeh, O., Radhakrishnan, V., Cirik, A. C., Mathar, R., and Lampe, L.: Hardware impairments aware transceiver design for bidirectional full-duplex MIMO OFDM systems. IEEE Transactions on Vehicular Technology, 67(8):7450–7464, May 2018.
93. Radhakrishnan, V., Taghizadeh, O., and Mathar, R.: Hardware impairments-aware transceiver design for multi-carrier full-duplex MIMO relaying. IEEE Transactions on Vehicular Technology, 70(2):1109–1121, Jan. 2021.
94. Korpi, D., Riihonen, T., Syrjälä, V., Anttila, L., Valkama, M., and Wichman, R.: Full-duplex transceiver system calculations: Analysis of ADC and linearity challenges. IEEE Transactions on Wireless Communications, 13(7):3821–3836, Jul. 2014.
95. Zhou, G. T., Qian, H., Ding, L., and Raich, R.: On the baseband representation of a bandpass nonlinearity. IEEE Transactions on Signal Processing, 53(8):2953–2957, Aug. 2005.
96. Alexandropoulos, G. C., Kountouris, M., and Atzeni, I.: User scheduling and optimal power allocation for full-duplex cellular networks. In Proceedings of the IEEE SPAWC, pages 1–6, Edinburgh, UK, July 2016.

97. Atzeni, I., Kountouris, M., and Alexandropoulos, G. C.: Performance evaluation of user scheduling for full-duplex small cells in ultra-dense networks. In Proceedings of the EuCNC, pages 1–6, Oulu, Finland, May 2016.
98. Texas Instruments: Analog-to-Digital Converters, 2016.
99. Wu, X., Shen, Y., and Tang, Y.: The power delay profile of the single-antenna full-duplex self-interference channel in indoor environments at 2.6 GHz. IEEE Antennas and Wireless Propagation Letters, 13:1561–1564, Aug. 2014.
100. Askar, R., Undi, F., Rezende, R. S., Peter, M., and Keusgen, W.: Polarimetric characterization of sub-6-GHz self-interference indoor radio channels. In Proceedings of the IEEE ICC, pages 1–6, Shanghai, China, May 2019.
101. Chen, F., Morawski, R., and Le-Ngoc, T.: Self-interference channel characterization for wideband  $2 \times 2$  MIMO full-duplex transceivers using dual-polarized antennas. IEEE Transactions on Antennas and Propagation, 66(4):1967–1976, Jan. 2018.
102. Alexandropoulos, G. C., Islam, M. A., and Smida, B.: Full duplex hybrid A/D beamforming with reduced complexity multi-tap analog cancellation. In Proceedings of the IEEE International Workshop on Signal Processing Advances in Wireless Communications (SPAWC), pages 1–5, Atlanta, USA, Jun. 2020.
103. Du, X., Tadrous, J., Dick, C., and Sabharwal, A.: MU-MIMO beamforming with full-duplex open-loop training. In Proceedings of the IEEE SPAWC, pages 301–305, Stockholm, Sweden, Jun. 2015.
104. Du, X., Tadrous, J., and Sabharwal, A.: Sequential beamforming for multi-user MIMO with full-duplex training. IEEE Transactions on Wireless Communications, 15(12):8551–8564, Dec. 2016.
105. Kobayashi, M., Jindal, N., and Caire, G.: Training and feedback optimization for multi-user MIMO downlink. IEEE Transactions on Communications, 59(8):2228–2240, May 2011.
106. Tse, D. and Viswanath, P.: Fundamentals of wireless communication. Cambridge university press, 2005.

107. Iimori, H., de Abreu, G. T. F., and Alexandropoulos, G. C.: MIMO beamforming schemes for hybrid SIC FD radios with imperfect hardware and CSI. IEEE Transactions on Wireless Communications, 18(10):4816–4830, Oct. 2019.
108. Alexandropoulos, G. C., Islam, M. A., and Smida, B.: Full duplex massive MIMO architectures: Recent advances, applications, and future directions. [online] <https://arxiv.org/abs/2205.08393>, 2022.
109. Molisch, A. F. et al.: Hybrid beamforming for massive MIMO: A survey. IEEE Communications Magazine, 55(9):134–141, September 2017.
110. Xiao, Z. et al.: Full-duplex millimeter-wave communication. IEEE Wireless Communications, 24(6):136–143, Dec. 2017.
111. Satyanarayana, K. et al.: Hybrid beamforming design for full-duplex millimeter wave communication. IEEE Transactions on Vehicular Technology, 68(2):1394–1404, Dec. 2018.
112. Cai, Y. et al.: Robust joint hybrid transceiver design for millimeter wave full-duplex MIMO relay systems. IEEE Transactions on Wireless Communications, 18(2):1199–1215, Jan. 2019.
113. Liu, X., Xiao, Z., Bai, L., Choi, J., Xia, P., and Xia, X.-G.: Beamforming based full-duplex for millimeter-wave communication. Sensors, 16(7):1130, Jul. 2016.
114. López-Valcarce, R. and González-Prelcic, N.: Analog beamforming for full-duplex millimeter wave communication. In Proceedings of the ISWCS, pages 687–691, Aug. 2019.
115. Kolodziej, K. E. et al.: Multitap RF canceller for in-band full-duplex wireless communications. IEEE Transactions on Wireless Communications, 15(6):4321–4334, Jun. 2016.
116. Atzeni, I. et al.: Performance evaluation of user scheduling for full-duplex small cells in ultra-dense networks. In Proceedings of the European Wireless Conference, pages 1–6, Oulu, Finland, 18-20 May 2016.

117. Alexandropoulos, G. C. and Papadias, C. B.: A reconfigurable iterative algorithm for the  $K$ -user MIMO interference channel. Signal Processing (Elsevier), 93(12):3353–3362, December 2013.
118. He, S., Wang, J., Huang, Y., Ottersten, B., and Hong, W.: Codebook-based hybrid precoding for millimeter wave multiuser systems. IEEE Transactions on Signal Processing, 65(20):5289–5304, Jul. 2017.
119. Islam, M. A. et al.: Direction-assisted beam management in full duplex millimeter wave massive MIMO systems. In Proceedings of the IEEE Global Communications Conference (GLOBECOM), Madrid, Spain, Dec. 2021.
120. Roberts, I. P., Jain, H. B., and Vishwanath, S.: Equipping millimeter-wave full-duplex with analog self-interference cancellation. In Proceedings of the IEEE ICC, Dublin, Ireland, Jun. 2020.
121. Björnson, E., Larsson, E. G., and Marzetta, T. L.: Massive MIMO: Ten myths and one critical question. IEEE Communications Magazine, 54(2):114–123, Feb. 2016.
122. Vlachos, E., Alexandropoulos, G. C., and Thompson, J.: Wideband MIMO channel estimation for hybrid beamforming millimeter wave systems via random spatial sampling. IEEE Journal on Selected Areas in Communications, 13(5):1136–1150, Sep. 2019.
123. Venkateswaran, V. and van der Veen, A.-J.: Analog beamforming in MIMO communications with phase shift networks and online channel estimation. IEEE Transactions on Signal Processing, 58(8):4131–4143, Aug. 2010.
124. Alexandropoulos, G. C., Vinieratou, I., Rebato, M., Rose, L., and Zorzi, M.: Uplink beam management for millimeter wave cellular MIMO systems with hybrid beamforming. In Proceedings of the IEEE WCNC, Nanjing, China, Apr. 2021.
125. Giordani, M., Polese, M., Roy, A., Castor, D., and Zorzi, M.: A tutorial on beam management for 3GPP NR at mmWave frequencies. IEEE Communications Surveys & Tutorials, 21(1):173–196, 2019.

126. Aykin, I. and Krunz, M.: Efficient beam sweeping algorithms and initial access protocols for millimeter-wave networks. IEEE Transactions on Wireless Communications, 19(4):2504–2514, Apr. 2020.
127. Palacios, J., De Donno, D., and Widmer, J.: Tracking mm-Wave channel dynamics: Fast beam training strategies under mobility. In Proceedings of the IEEE INFOCOM, pages 1–9, Atlanta, USA, May 2017.
128. Alexandropoulos, G. C.: Position aided beam alignment for millimeter wave backhaul systems with large phased arrays. In Proceedings of the IEEE CAMSAP, pages 1–5, Curacao, Dutch Antilles, Dec. 2017.
129. González-Coma, J. P. et al.: Channel estimation and hybrid precoding for frequency selective multiuser mmWave MIMO systems. IEEE Journal on Selected Topics in Signal Processing, 12(2):353–367, Mar. 2018.
130. Akdeniz, M. R. et al.: Millimeter wave channel modeling and cellular capacity evaluation. IEEE Journal on Selected Areas in Communications, 32(6):1164–1179, Jun. 2014.
131. Va, V., Vikalo, H., and Heath, R. W.: Beam tracking for mobile millimeter wave communication systems. In Proceedings of the IEEE GlobalSIP, pages 743–747, Dec. 2016.
132. Krim, H. and Viberg, M.: Two decades of array signal processing research: the parametric approach. IEEE Signal Processing Magazine, 13(4):67–94, Jul. 1996.
133. Islam, M. A. et al.: Integrated sensing and communication with millimeter wave full duplex hybrid beamforming. In Proceedings of the IEEE International Conference on Communications (ICC), Seoul, South Korea, May. 2022.
134. Islam, M. A., Alexandropoulos, G. C., and Smida, B.: Simultaneous multi-user MIMO communications and multi-target tracking with full duplex radios. [online] <https://arxiv.org/abs/2205.08402>, 2022.
135. Alves, H., Riihonen, T., and Suraweera, H. A.: Full-Duplex Communications for Future Wireless Networks. Singapore, Springer, 2020.

136. Braun, M., Sturm, C., and Jondral, F. K.: Maximum likelihood speed and distance estimation for OFDM radar. In IEEE Radar Conference, pages 256–261, May 2010.

## VITA

# MD ATIQUUL ISLAM

### EDUCATION

Ph.D., University of Illinois at Chicago, IL, USA, 2022  
M.S., University of Illinois at Chicago, IL, USA, 2021  
B.S., Islamic University of Technology, Bangladesh, 2015

### EXPERIENCE

Research Assistant, Electrical and Computer Engineering Department, UIC, Chicago, IL, USA

Aug. 2017 – Present

Teaching Assistant, Electrical and Computer Engineering Department, UIC, Chicago, IL, USA

Aug. 2017 – May 2022

Research Intern - 5G Next Generation Radio Access Networks, Futurewei Technologies, Inc., Chicago, IL, USA

May 2021 – Dec. 2021

Lecturer and Program Coordinator, Green University of Bangladesh, Dhaka, Bangladesh

Feb. 2016 – July 2017

### PUBLICATIONS

#### **Journal Publications**

Md Atiqul Islam, G. C. Alexandropoulos, and B. Smida, "Joint Analog and Digital Transceiver Design for Wideband Full Duplex MIMO Systems," in *IEEE Transactions on Wireless Communications*, Jun. 2022.

K. Muranov, Md Atiqul Islam, B. Smida, N. Devroye, "On Deep Learning Assisted Self-Interference Estimation in a Full-Duplex Relay Link," *IEEE Wireless Communications Letters*, 2021 Sep 29;10(12):2762-6.

George C. Alexandropoulos, Md Atiqul Islam, and B. Smida, "Full Duplex Massive MIMO Architectures: Recent Advances, Applications, and Future Directions," Under review in the *IEEE Vehicular Technology Magazine*, 2022.

Smida, S. Khaledian, F. Farzami, Md Atiqul Islam, and D. Erricolo, "Single-Antenna In-Band Full-Duplex Communications," Accepted to be published in the Wiley Encyclopedia of Electrical and Electronics Engineering, 2023.

### Conference Publications

Md Atiqul Islam, G. C. Alexandropoulos, and B. Smida, "Simultaneous Multi-User MIMO Communications and Multi-Target Tracking with Full Duplex Radios," Submitted in the IEEE Global Communications Conference (GLOBECOM), Dec. 2022, Rio de Janeiro, Brazil, pp. 1–6.

Md Atiqul Islam, G. C. Alexandropoulos, and B. Smida, "Integrated Sensing and Communication with Millimeter Wave Full Duplex Hybrid Beamforming," in Proceedings of the IEEE International Conference on Communications (ICC), Seoul, South Korea, May 2022, pp. 1–6.

Md Atiqul Islam, G. C. Alexandropoulos, and B. Smida, "Direction-Assisted Beam Management in Full Duplex Millimeter Wave Massive MIMO Systems," in Proceedings of the IEEE Global Communications Conference (GLOBECOM), Madrid, Spain, Dec. 2021, pp. 1–6.

Md Atiqul Islam, G. C. Alexandropoulos, and B. Smida, "Simultaneous Data Communication and Channel Estimation in Multi-User Full Duplex MIMO Systems," in Proceedings of the IEEE ASILOMAR Conference on Signals, Systems and Computers, Pacific Grove, USA, Nov. 2020, pp. 1–6.

G. C. Alexandropoulos, Md Atiqul Islam, and B. Smida, "Full duplex hybrid A/D beamforming with reduced complexity multi-tap analog cancellation," in Proceedings of the IEEE International Workshop on Signal Processing Advances in Wireless Communications (SPAWC), Atlanta, USA, Jun. 2020, pp. 1–5.

Md Atiqul Islam, G. C. Alexandropoulos, and B. Smida, “Simultaneous downlink data transmission and uplink channel estimation with reduced complexity full duplex MIMO radios,” in Proceedings of the IEEE International Conference on Communications (ICC), Dublin, Ireland, Jun. 2020, pp. 1–6.

Md Atiqul Islam, G. C. Alexandropoulos, and B. Smida, “A unified beamforming and A/D self-interference cancellation design for full duplex MIMO radios,” in Proceedings of the IEEE Annual International Symposium on Personal, Indoor and Mobile Radio Communications (PIMRC), Istanbul, Turkey, Sep. 2019, pp. 1–7.

Md Atiqul Islam and B. Smida, “A comprehensive self-interference model for single-antenna full-duplex communication systems,” in Proceedings of the IEEE International Conference on Communications (ICC), Shanghai, China, May 2019, pp. 1–7.

### **Patents**

Md Atiqul Islam, J. Liu, N. Prasad, W. Xiao, G. Yue, “Advanced Beamforming and Transmission Techniques for MIMO URLLC Applications,” Submitted Provisional Patent.

## **PRESENTATIONS**

### **Conference Presentations**

2022 IEEE International Conference on Communications (ICC), Seoul, South Korea

2021 IEEE Global Communications Conference (GLOBECOM), Madrid, Spain

2020 IEEE ASILOMAR Conference on Signals, Systems and Computers, Pacific Grove, USA

2020 IEEE International Workshop on Signal Processing Advances in Wireless Communications (SPAWC), Atlanta, USA

2019 IEEE Annual International Symposium on Personal, Indoor and Mobile Radio Communications (PIMRC), Istanbul, Turkey

2019 IEEE International Conference on Communications (ICC), Shanghai, China

### Poster Presentations

2019 IEEE ComSoc Summer School, Austin, USA

2018 IEEE North American School of Information Theory, College Station, USA

### AWARDS

2022 Exceptional Research Promise Award from the College of Engineering, University of Illinois at Chicago, USA

May 2022

Best Paper Award for the Selected Areas in Communications Symposium of the IEEE Global Communications Conference (GLOBECOM), Madrid, Spain

Dec. 2021

IEEE ComSoc Summer School Travel Grant, National Instruments Campus, Texas

Jul. 2019

IEEE North American School of Information Theory (NASIT) Travel Grant, Texas A & M University, Texas

May 2018

### MEMBERSHIPS

IEEE Communication Society (ComSoc)

Student Member

Aug. 2017 – Present

### SERVICES

Journal Article Referee at

IEEE Transaction on Wireless Communications

2018 – Present

IEEE Journal on Selected Areas in Communications

2018 – Present

IEEE Transaction on Communications

2018 – Present

IEEE Open Journal of the Communication Society

2020 – Present

IEEE Wireless Communication Letters

2019 – Present

Conference Article Referee at

IEEE ICC 2022, 2021, 2019, 2018

IEEE IWCMC 2021, IEEE ICT 2020

IEEE SPAWC 2020, IEEE PIMRC 2019

IEEE WCNC 2019, IEEE GC 2019

Vice Chair, IEEE Communication Society, Chicago Chapter

Aug. 2021 – May 2022

President & Treasurer, Bangladeshi Students' Association at  
UIC

May 2019 – May 2022